PHD

Impact on Hybrid Composite Materials

Rizzo, Francesco

Award date:
2020

Awarding institution:
University of Bath

Impact on Hybrid Composite Materials

Francesco Rizzo

Department of Mechanical Engineering

University of Bath

Thesis submitted for the degree of

Doctor of Philosophy

Copyright

Signature of Author 

Francesco Rizzo

Per aspera ad astra
To the stars through difficulties
(Cicero)

Acknowledgements

Firstly, I would like to express all my gratitude to my Supervisors, Prof Michele Meo and Dr Fulvio Pinto for giving me this life changing opportunity. Throughout the last 3 years, they have gone above and beyond to provide me with support, and guidance and it is thanks to them that I am the engineer that I am today.

A special mention also goes to Stephen Thomas, who has patiently guided me through the composite manufacturing process and constantly supported me over these years.

I also thank the people in the office who it has been a pleasure to work with; Gian Piero Malfense Fierro, Mario Emanuele De Simone, Salvatore Boccardi, Fabrizio Bucciarelli, Christos Andreades, Francesco Flora, Marco Boccaccio, Stefano Cuomo, Mario Rapisarda and Kostas Myronidis. I am pleased to call them not only my colleagues but my friends.

An important mention goes to my Home Friends Agostino Ciriello, Arcangelo Rao, Davide Cardella, Dario Corvino, Francesco Sciaudone, Gennaro Zevoli and Antonio Morrone who supported and tolerated me throughout these years. Thank you, guys, for all your help!

I would also like to express my thanks to Charlotte, Richard, Dave, Jo, Janet, Roger, Sophie and Dan who have made being away from home that little bit easier.

Un speciale e sentito ringraziamento, a mio fratello Gianluca, mio zio Giovanni, mia nonna Michelina, ma zia Amalia e I miei cugini Anna, Mario, Francesco ed Andrea per il loro continuo supporto e incoraggiamento nel proseguire questo percorso. Anche se a parecchi chilometri di distanza. Ai miei genitori Maria e Giuseppe va il mio piu profondo ringraziamento. Grazie per tutto quello che avete fatto per me nel corso della mia vita. Spero un giorno di riuscire a diventare come voi.

Finally, I would like to thank my partner Rebecca, whose love, support and belief in me has pushed me through the difficult periods. I couldn't have done this without her. Thank you from the deepest of my heart for all the love and kindness you have for me.

Abstract

Over the last 60 years, laminated composite materials have attracted the attention of several advanced industries including aerospace, motorsport and energy due to the excellent ratio between in-plane mechanical properties and low density. However, due to the fragile nature and the lack of reinforcement along their through-the-thickness direction, these materials are sensitive to impact loading conditions and are prone to damage generation within the composite structure leading to the decreased performance and eventual catastrophic failure of the structure. The original contribution of this thesis is the systematic presentation of three different hybridisation processes aiming to improve the impact properties of laminated composite materials through the introduction of an additional phase or reinforcement within the composite structure and, at the same time, to enable important non-structural properties which can significantly increase reliability of the structure and the appeal of these materials for advanced sectors. Three were investigated in this work. The first consisted of the introduction of metal wires as secondary reinforcement to improve maximum tolerated contact force whilst enabling structural monitoring (sensing ability and IR damage detection), de-icing and anti-icing safety procedures. The second investigated the effect of the introduction of resin pockets along fibres length creating a 3D discontinuities pattern whilst activating additional failure mechanisms typical of biological organisms to increase the toughness of the laminate and enhance drapability. The final hybridisation process investigated was the introduction of polymeric coating on the impact surface to mitigate the impact damage generated within the structure by increasing the amount of dissipated impact energy via damping mechanisms whilst increasing erosion resistance. Experimental impact testing was carried out to characterise and evaluate the benefits of hybridisation on laminated materials and reported improvement in each of the evaluated properties demonstrating the potential of these materials to be used in increasing performance, reliability and safety for advanced applications.

Contents

List of Figures

2 Chapter: Background of impact behaviour of composite materials and failure mechanisms

3 Chapter: Literature review on hybridisation for improvement of mechanical and impact properties

4 Chapter: Impact resistance enhancement and enabled SHM features via metal array hybridisation

5 Chapter: Toughness improvement via the introduction of a 3D discontinuity pattern

6 Chapter: Damage mitigation for Hybrid CFRP composites under Low Velocity Impact Loading

7 Chapter: Damage mitigation for CFRP structures against High Velocity Impact events

8 Chapter: Conclusions and Future Works

List of Tables

1 Chapter: Introduction

2 Chapter: Background of impact behaviour of composite materials and failure mechanisms

4 Chapter: Impact resistance enhancement and enabled SHM features via metal array hybridisation

5 Chapter: Toughness improvement via the introduction of a 3D discontinuity pattern

Nomenclature

FRP	Fibre Reinforced Polymer
CFRP	Carbon Fibre Reinforced Polymer
LVI	Low Velocity Impact
LVID	Low Velocity Impact Damage
HVID	High Velocity Impact Damage
SHM	Structural Health Monitoring
IR	InfraRed
TPU	Thermoplastic Polyurethane
FEM	Finite Element Modelling
HVI	High Velocity Impact
CLT	Classical Lamination Theory
CT	Computed Tomography
CTBN	Carboxyl-Terminated Butadiene-Acrylonitrile
ARALL	Aramid Reinforced Aluminium Laminate
GLARE	Glass Laminated Aluminium Reinforced Epoxy
CARALL	Carbon Reinforced Aluminium Laminate
SMA	Shape Memory Alloys
SMAHC	Shape Memory Alloy Hybrid Composite
DMA	Dynamic Mechanical Analysis
DSC	Differential Scanning Calorimetry
FML	Fibre-Metal Laminates

PTFE	Polytetrafluoroethylene
PS	Pulsed Thermography
PPT	Pulsed Phase Thermography
LIT	Lock-In Thermography
SHT	Step Heating Thermography
DCFRP	Discontinuous Carbon Fibre Reinforced Polymers
RVE	Representative Volume Element
CP	Cross-Ply
CNT	Carbon Nano Tubes
FEA	Finite Element Analysis
NDT	Non-Destructive techniques
FOD	Foreign Object Debris

1 CHAPTER: Introduction

1.1 Overview

Throughout the last 60 years, research within the engineering sector has been dominated by the development of cutting-edge materials which satisfy the demand of industries including aerospace, automotive and energy for structures with high-level performance combined with low density. In this context, Fibre Reinforced Polymers (FRPs) have drawn much attention due to their excellent specific properties, high corrosion [1] and fatigue [2] resistance and high tailorability [3] which enable these materials to adapt to extreme applications and harsh environments. The increasing importance of FRPs within the global market is clear with the demand for carbon fibres set to grow from 70,500 tonnes in 2017 to 120,500 tonnes in 2022 [4]. Whilst the rising application of FRPs within the industry presents the opportunity for revolutionary advancements across industries, its use is not currently without limitations. Crucially, in contrast with traditional metal structural materials which show plastic deformation prior to a catastrophic failure with a high absorption of strain energy, FRPs show no signs of failure prior to a catastrophic brittle collapse with an elastic deformation of only 1-3% leading to limited absorbed strain energy.

Among the possible causes of critical damage to composite structures, the most severe loading scenarios occurs when dynamic loading is applied through the thickness direction of the laminate where no reinforcement is present. Impacts are the most common threat within this loading scenario. Indeed, one of the well-known consequences of impacts is the significant internal damage associated with the reduction of residual mechanical properties and fatigue resistance which threaten the overall structural reliability and integrity. The higher the kinetic energy involved in the impact event, the higher the damage extension generated within the

laminate. Thus, a significant overdesign of FRPs is required to guarantee the absence of the catastrophic failure of a global system whilst maintaining its specific mechanical properties. Due to the aforementioned intrinsic anisotropy and brittle behaviour of composite materials, regulatory authorities require the application of a safety factor of 2.0 on the ultimate force used as input for the part dimensioning [6] within aircraft applications, in contrast to the standard safety factor of 1.5 [5], used in the design of metal structures.

In order to overcome these issues, hybridisation is the process used to alter the properties of a traditional laminated material in this work. It consists of the introduction of an additional reinforcement within the laminated material which enables both the improvement of the structural response of the FRP towards external dynamic loading and also the activation of additional non-structural features to increase the reliability and the appeal of the material in advanced applications.

1.2 Scope and Objectives

This thesis focuses on the design and characterisation of laminated composite materials with improved impact properties obtained via the hybridisation of the traditional structure of Carbon Fibre Reinforced Polymers (CFRPs). Carbon-based composites were chosen among those available in the realisation of composite laminates due to their superior performance from advanced sectors including aerospace, motorsport and energy. As previously mentioned, the crucial issue reported in the use of FRP in modern industry is the generation of significant damage as a consequence of an impact event which reduces the reliability and the performance of the structure. The scope of this thesis is to investigate the potentialities of hybridisation via several approaches and techniques to improve certain impact properties of FRP structures and, at the same time, provide other non-structural benefits including Structural Health Monitoring (SHM), improved drapability or erosion resistance. This work paves the way for the use of hybrid

composite materials with increased general safety and reduced maintenance costs in many advanced applications.

Three main questions have arisen from this process, and these are the focus of this research:

1) What are the processes available to carry out hybridisation on FRP?
2) Do the hybridisation processes increase the out of plane properties of the FRP?
3) What are the non-structural features enabled by the hybridisation processes?

These questions are answered in the context section of each of the peer-reviewed manuscripts included into this work and in its conclusions. Four research manuscripts have been included in this thesis investigating three different approaches to improve the impact behaviour of the CFRP material. It is important to underline that each manuscript investigates a specific hybridisation process aiming to improve single specific impact properties on the global performances of the hybrid laminate. The label of the paper, the hybridisation process used, the impact property that has been improved and the non-structural benefits obtained are reported in the Table 1 below:

Table 1- Specs of papers used as chapter in this thesis work

PAPER	MODIFICATION	ENHANCED IMPACT PROP.	NON-STRUCTURAL BENEFITS
PAPER A	Introduction of metal wires array	Maximum Contact Force	SHM abilities: strain sensing, IR damage detection and de-icing
PAPER B	Introduction of a brick and mortar internal structure	Toughness	Drapability
PAPER C	Introduction of a protective polymeric layer	Damage mitigation LVID	Erosion protection
PAPER D	Introduction of a protective polymeric layer	Damage mitigation HVID	Erosion protection

In Paper A, the hybridisation process was carried out by introducing an array of metal wires in order to increase the maximum tolerated force by the material when the material was subject to Low Velocity Impacts (LVIs). In addition, the presence of the wires enabled several non-structural abilities such as strain sensing, IR damage detection and de-icing. Due to the complex nature of non-structural features that were enabled in this process, this work required an in-depth analysis of each of the non-structural features reporting in the paper's body the relative background.

In Paper B, the CFRP structure was hybridised through the introduction of a pattern of discontinuities during the manufacturing process which created a brick and mortar-based material. This enabled several failure mechanisms that increased the toughness of the material as verified under flexural and impact conditions. Additionally, the presence of discontinuities prior to the curing process, increased

the drapability of the material, its ability to adjust itself to complex shapes with high curvatures.

In Paper C, the CFRP structure was hybridised using a Thermoplastic Polyurethane (TPU) coating placed on the impact surface. This led to increased damage resistance towards LVI and at the same time, the protection of the external surface from erosion due to the intrinsic properties of the coating polymer. The hybrid material was characterised under LVI conditions and residual properties were investigated. A Finite Element Model (FEM) was also developed and validated to predict the TPU/CFRP response.

Finally, Paper D extended the content of Paper C by applying the characterised hybrid material to a common aerospace structure (T-Stiffened panel) which was significantly more complex than the structure used during the impact investigation in Paper C (rectangular samples). Rectangular samples were impacted using high velocity projectile (HVI) to evaluate the reliability of this approach in mitigating impact damage under high-velocity impact conditions. A FEM model was then developed modelling the aerospace structure and validated in order to optimise the TPU thickness for minimal impact damage generation.

The original contribution of this thesis is that it represents the first systematic investigation which focuses on hybridisation as a solution to improve the single impact properties of FRP materials whilst non-structural benefits are enabled to increase the reliability and industrial appeal for the use of the material in advanced applications. To enhance the readability of this work, the contextualisation of the hybridisation processes used in each research manuscript and their effectiveness are reported in the dedicated section of each chapter.

1.3 Outline of the Thesis

This thesis is structured following the alternative format (by publications).

1 Chapter contains the introduction of this work illustrating their advantages and disadvantages of FRP materials and hybridisation process. The Scope and Objectives of this thesis is also illustrated in this chapter highlighting the research questions, novelty and the context in which each paper included in this work lies.

2 Chapter explores the background of the mechanical and impact properties of laminated composite materials. The chapter focuses on the theoretical description of composite mechanical behaviour reporting both micromechanical and macromechanical theory. Impact response of composite materials and their failure criteria and mechanisms of laminated composites are also reported in this chapter.

3 Chapter contains the literature review of hybridisation processes analysing previous research works and their approach to solve the impact issue on composite structures.

From 4 Chapter to 7 Chapter, peer-reviewed papers comprise the thesis body, illustrating the solutions developed during the duration of this PhD programme. At the beginning of each chapter a brief introduction is presented where the original contribution, scope and overall results of the work are summarised.

4 Chapter explores Paper A, which focusses on a hybridisation process involving the integration of an array of metal wires within a Carbon Fibre Reinforced Polymer (CFRP) structure to increase the tolerated contact force and enable several non-structural functions such as strain sensing, IR damage detection and de-icing creating a multifunctional (hybrid) composite material.

5 Chapter (Paper B) describes the hybridisation process used to create a bioinspired hierarchical laminate from traditional CFRP material by introducing a pattern of discontinuities within the material creating a brick and mortar inner structure characterised by soft and tough elements.

6 Chapter (Paper C) describes the process of hybridisation used to improve the damage and erosion resistance of CFRP panels through the introduction of an additional protecting layer of Thermoplastic Polyurethane (TPU) on the impact surface.

In 7 Chapter, Paper D tests the hybrid material designed and characterised in Paper C by using it to create a common aircraft structure. The effectiveness of this hybrid material to reduce the generated damage in real-world conditions is evaluated.

Conclusions, considerations, and future works are explored in 8 Chapter and the global activities carried out within this PhD programme are summarised.

2 CHAPTER: Background of impact behaviour of composite materials and failure mechanisms

In this Chapter, an overview of the theory of mechanical properties of composite material and impacts is provided. The first part of the chapter consists of traditional composite mechanics in which micromechanics of lamina and macromechanics of laminate will be reported. Following this, the theory of impacts on composite materials will be illustrated, with a focus on the failure mechanisms that intervene during an impact event. A brief summary of damage detection techniques will be included in this section.

2.1 Overview

"Composite" is a term used to describe a material that is created by the combination of two or more different materials that have different intrinsic properties (termed "phases") to obtain a macroscopically homogeneous third material with properties that are different from the first two [4]. Historically, the origin and the temporal collocation of the first composite materials used by humans remains largely unknown. There is evidence [5, 6] which dates the use of composites back to circa 3400 B.C., during which time Mesopotamians used glued wood strips at different angles to create plywood. In circa 1500 B.C. both Mesopotamians and early Egyptians created sturdy and durable buildings by mixing straw and clay. Later on, in 1200 A.D., the Mongolis invented a composite bow (Figure 1.a) using a combination of wood, bone and animal glue pressed together and wrapped in birch bark. These bows aided Genghis Khan's military supremacy

during the Yuan Era and became the most feared weapons prior to the invention of firearms. A further development and diffusion of composite material use began in the late 1800's, when plastics including vinyl, polystyrene, phenolic, and polyester made available by the industrial revolution began substituting natural resins from animal and plant sources. These materials however had limited structural use due to their low strength and rigidity and thus required reinforcement prior to their use in a range of advanced applications.

The appearance of modern composite materials occurred in 1935 with the development of Fibre Reinforced Composite materials (FRPs) by Owens Corning [5, 6]. These materials combined fibre glass (Figure 1.b) with one of the aforementioned resins to create a lightweight yet strong material. The significance of FRPs rapidly increased during the II World War (WWII) due the necessity for lightweight and high-performance materials for military aircraft and weapons [5, 6]. Furthermore, it was discovered that fiberglass was invisible to radiofrequencies, and was consequently used to manufacture the shelters [7, 8] where strategic radio station instrumentations were located (radomes). After WWII, the demand for advanced military equipment decreased, however these top-tier materials began to be introduced into other industrial sectors and markets. In 1946 the first full composite boat hull (Figure 1.c) was produced [9].

Figure 1-Composites across history: a) Mongolian Bow, b) glass fibre production (from picryl) and c) boat hull made of glass fibre reinforced polymers (image from [5, 6]).

A fundamental step which increased the efficiency of the production of composite materials was the invention of the pultrusion process by Brandt Goldsworthy in 1976 [10, 11]. This process enabled the high-volume manufacturing of composite forms of common engineering products such as pipes, rails and medical rods. Furthermore, the polymer industry was mature and able to produce adaptable resins and plastics by tuning different properties in function of the application required. Several new reinforcements also started to appear on the market around this period including aramid fibres [12] (which are today used to build body armours due to their high tensile strength, low density and light weight) and carbon fibre (which is today the ultimate reinforcement for plastics able to replace steel in certain structural applications). The knowledge acquired during the last 60 years of research has led to the characterisation and classification of composite materials which can be defined as made up of two (or more) components: the matrix and the reinforcement.

The matrix is a polymeric materials (resin) which gives geometrical shape, shields the fibres by external environment and, it is responsible of transferring the load applied on the structure to the fibres, maximising the stiffness and resistance of the

composite structure. Some of the available resin on the market are reported in Table 2:

Table 2-Mechanical properties and maximum operating temperature of matrix.

Resin	E [MPa]	S [MPa]	P [g/cm3]	Tmax °C
Epoxy	3500	80	1.15	200
Polyester	4500	30	1.15	80
Phenolic	6900	50	1.3	>200
Polyimide	4000	120	4.46	260-425
Torloc*(Amoco)	4800	193	1.35	275
PEEK*(ICI)	4500	92	1.3	180

Reinforcement can be classified into two main categories, continuous and discontinuous, depending on the critical length parameter which is calculated using the formula [13] $l_c = \sigma_{fu} d_f \backslash 2\tau_i$ where σ_{fu} is the failure stress of the fibres, τ_i is the interface shear strength between fibre and matrix and d_f is the fibres diameter. Based on this premise, the fibrous reinforcement is considered continuous when the actual length of the fibres is bigger than the critical one and discontinuous when the length of fibres is smaller (Figure 2).

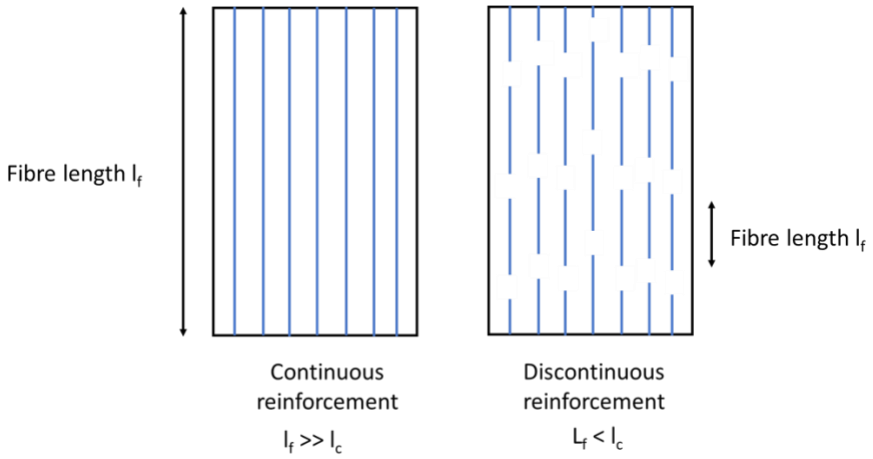

Figure 2-Schematic representation of continuous and discontinuous fibrous reinforcement.

Considering continuous reinforcements, several typologies of fibres are available on the market including carbon fibres, glass fibres, aramid (Kevlar) fibres and boron

fibres which show unique properties that influence the final properties of the laminate (Table 3).

Table 3-Summary of typologies of fibrous reinforcement and their respective properties.

	E (N/mm^2) **Elastic Modulus**	**σ_f** (N/mm^2) **Strength at failure**	**ρ** (g/cm^3) **Density**	**E/ρ** ($10^3 J/g$) **Specific Elasticity**	**σt/ ρ** ($10^2 J/g$) **Specific Strength**
Carbon C1	385000	2000	1.9	202	10.5
Carbon C2	260000	2500	1.9	136	13.1
Glass E	70000	3000	2.5	28	12
Glass S	80000	4500	2.5	32	18
Kevlar 49	131000	3600	1.44	91	25
Boron	420000	2400	2.4	175	10
Beryllium	315000	1300	1.8	175	7.2
Tungsten	350000	2500	19	18	1.3
Steel	210000	2500	7.8	27	3.2

The arrangement of unidirectional fibres (oriented in one direction) and the matrix is called lamina, ply or layer. The laminate (Figure 3) is the structure which is made of layers stacked up together using the same matrix material and oriented at different angles to provide strength in each direction [4].

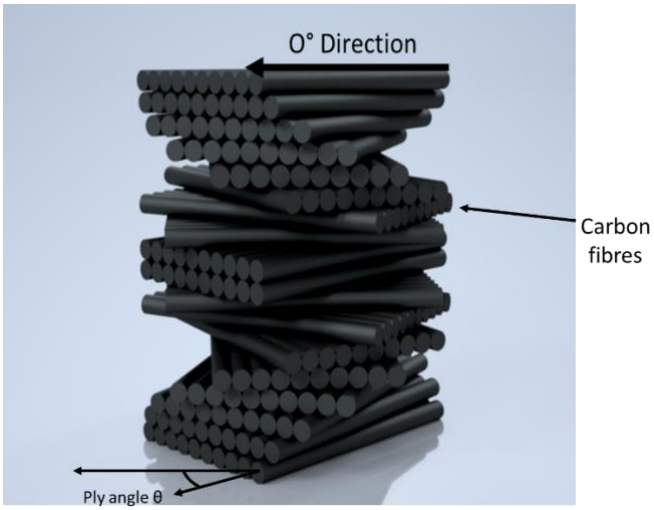

Figure 3-Schematic representation of composite laminate. Black cylinders represent carbon fibres reinforcement in each layer (ply) that composes the laminate. Layers have different orientation (θ) with the reference ply oriented at 0º angle.

These principles lead to the possibility of tailoring certain properties including stiffness and strength in function of specific loading conditions. In this work, the attention will be focussed on laminated fibrous composite materials and, carbon fibres were chosen due to their high stiffness, strength and light weight (Table 3).

Hybrid composite materials are introduced as an evolution of standard composite. A composite is considered "hybrid" when a secondary layer of reinforcement different from the primary one is embedded within the composite in order to improve one or more specific properties. It is possible to carry out hybridisation in using different approaches and these will be discussed in the literature review paragraph of this chapter.

2.2 Mechanical properties of composite material

2.2.1 Overview

The aim of this chapter is to provide background regarding the mechanical properties of laminated composite materials. Three different theories will be presented which analyse three different aspects of composite mechanics: micromechanics of lamina, macromechanics of lamina and macromechanics of

laminate. Micromechanics of the lamina deals with the prediction of the mechanical properties of a lamina when the relative amount (volume fraction) and properties of the single components, i.e. matrix and fibres, used to create the layer are known. The macromechanics of lamina presents the global mechanical response that the single lamina shows when a determined stress is applied, with no focus on the interactions between the single components. This theory is required in the description of the macromechanics of the laminate which analyses the global structural response of a laminated material created by bonding several laminae together with different fibre orientation. It is important to note that modifications of these theories are present in the literature and are reported (where applicable) in the relative chapters.

2.2.2 Terminology

The aim of this paragraph is to define the basic terminology used in the following section. Common structural materials such as metal are generally considered isotropic and homogeneous [13]. A body is homogeneous when its properties are uniform and independent of the location of the evaluation point in the body itself. It is instead heterogeneous when the properties are influenced by the position. A body is defined as isotropic when its material properties are uniform and independent of orientation and direction and there are infinite planes of symmetry. A body is considered anisotropic instead when the material properties are a function of the direction and orientation and no symmetry planes can be identified. A body is called orthotropic if its properties are different along three principal directions (conventionally 1,2 and 3) and in reference to three orthogonal symmetry planes (Figure 4).

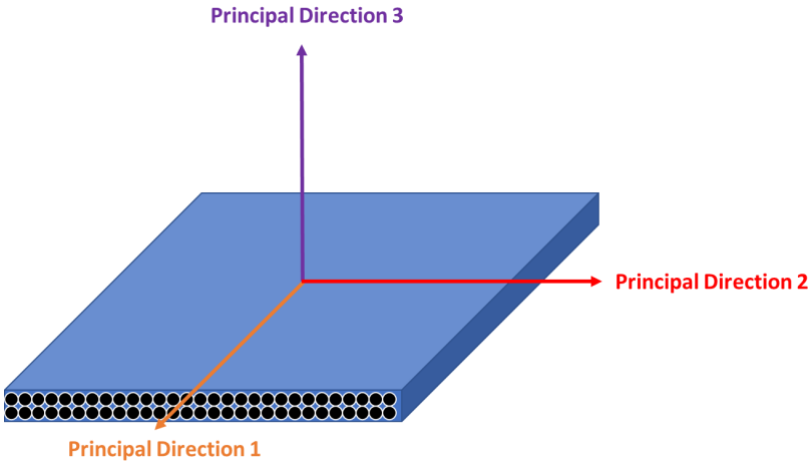

Figure 4-Layout of an orthotropic material indicating the principal direct 1 (fibre direction), principal direction 2 (in-plane transverse direction of fibres) and principal direction 3 (out-of-plane direction of fibres).

When the properties along two of the three principal directions can be considered the same, then, the material can be considered transversally orthotropic[4].

2.2.3 Micromechanics of lamina

This area of composite mechanics focuses on analysing the composite material layer as a heterogeneous material where the reinforcement and matrix components are considered separately. It is clear that a great difference in terms of intrinsic properties (e.g. Young's Modulus, Poisson's coefficient, density) exists between the two components. Therefore, an understanding of the relationship between the material properties of the two materials and the resultant properties of the final lamina is critical. Based on these relationships, it is possible to predict the properties of the final lamina when varying the typologies of the two components and this is fundamental during the design and material selection phase of the structures production.

The aim of micromechanics is principally the determination of the elastic moduli of the lamina in function of Young's Moduli of fibres and matrix. Fewer works have focused on the prediction of lamina strength since it is highly influenced by

manufacturing, aging and environmental effects which reduce the reliability of the predicted values against the experimental ones.

Several assumptions are made in the description of the micromechanics of lamina. Firstly, the lamina is assumed linearly elastic, macroscopically homogeneous and initially stress-free. The fibre and matrix are also idealised as linearly elastic, homogeneous, isotropic and perfectly aligned, perfectly bonded and uniformly spaced. Based on these assumptions, it is possible to consider a representative volume as the smallest region where the stresses can be considered macroscopically uniform (Figure 5). Consequently, it is possible to analyse the representative volume case and extend the results to the global volume. It is important to note that conventionally three principal directions of a laminated composite are used. Direction 1 is oriented parallel to the fibres' length, direction 2 perpendicular to direction 1 and in the same plane, and direction 3 oriented along the through the thickness direction of the laminate as shown in Figure 5.

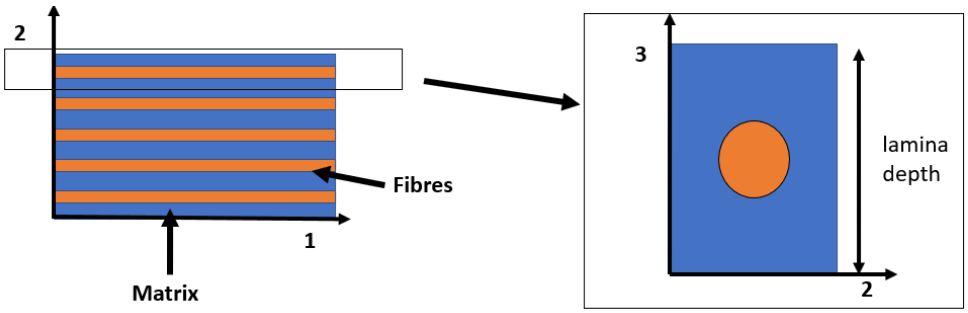

Figure 5-Representative volume of single lamina of laminated composite material: fibres (orange lines) and matrix (blue). Principal direction 1 parallel to the fibre.

Using this volume element, it is possible to determine the longitudinal elastic modulus E_1 using the *rule of mixture* when applying a uniform stress σ_1 on the lamina along the fibre direction (conventionally considered the principal direction 1) as shown in Figure 6.

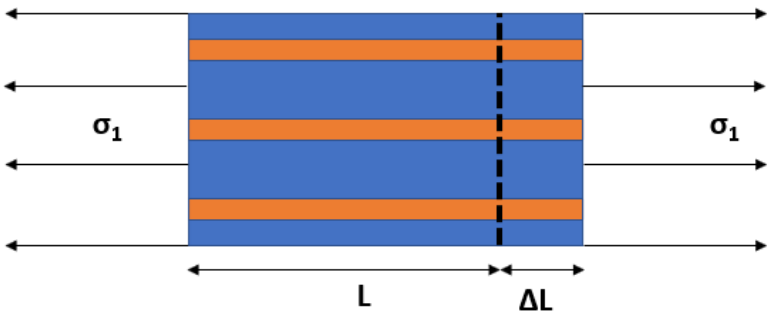

Figure 6-Representative element loaded along direction 1where L is the initial length of the volume and ΔL is the elongation generated by the stressed applied.

Since perfect bonding between fibres and matrix is assumed, the strain ε_1 ($\Delta L/L$) must be the same on both components. Also, since the materials are linearly elastic, it is possible to describe its longitudinal modulus using the equation:

$$E_{11} = E_f V_f + E_m V_m \quad (1)$$

where E_f is the elastic modulus of fibres, E_m is the elastic modulus of matrix, and V_f and V_m are the volume fraction of fibres and matrix respectively. Generally, the maximum percentage of fibres in a lamina can be around 0.65.

To determine E_{22} the elastic modulus in the transverse direction of the lamina (direction 2), it is not possible to assume that the strain ε_2 is uniform between fibres and matrix when a stress σ_2 is applied on the element.

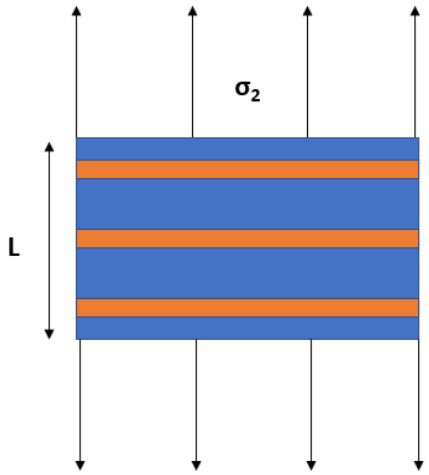

Figure 7-Representative element loaded along direction 2.

However, since the stress applied is the same for both fibres and matrix (Figure 7), it is possible to use the equation to determine the transversal modulus:

$$E_{22} = \frac{E_f E_m}{V_m E_f + E_m V_f}. \quad (2)$$

Other equations are available to describe other parameters including Poisson's ratios and shear modulus and are obtained using the same assumptions [4]:

$$G_{12} = \frac{G_f G_m}{V_m G_f + G_m V_f} \quad (3)$$

$$\nu_{12} = \nu_f V_f + \nu_m V_m. \quad (4)$$

Where: G_f is the shear modulus of fibres, G_m is the shear modulus of matrix, and ν_f and ν_m are the Poisson's coefficients of the fibres and matrix respectively.

Modifications of these equations are also available in the literature where it is possible to extend the micromechanics to predict mechanical properties in different cases including discontinuous fibre reinforced laminates [14, 15] and angle-ply laminates [16].

2.2.4 Macromechanics of lamina

This element of composite mechanics focuses on understanding the macroscopic lamina response towards applied stresses. No interactions between constituents on a microscopic level are considered. The basic restriction of this area is that the lamina shows only linear elastic behaviour. Considering an elemental volume, it is possible to characterise its three-dimensional mechanical response in the cartesian reference system using the generalised Hooke's law [4] which relates stresses to strains:

$$\sigma_k = C_{ki}\varepsilon_i \qquad i,j = 1,2\ldots,6. \tag{5}$$

Where: σi is the stress component, Cki is the stiffness matrix and ε is the strain component. The distribution of these components on the volume element is reported in Figure 8

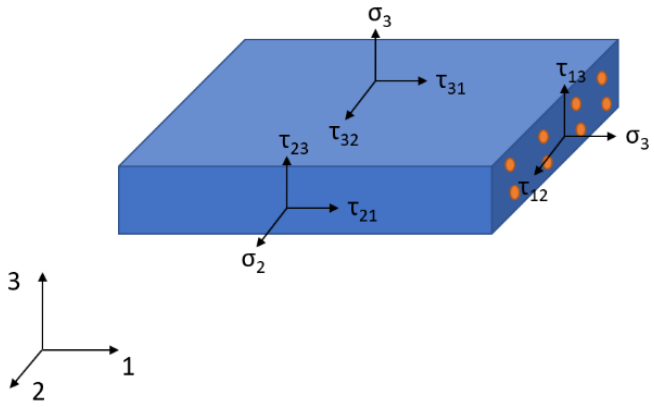

Figure 8-Stress distribution on the element volume.

Another way to show this equation is using the matrix representation:

$$\begin{bmatrix}\sigma_1\\ \sigma_2\\ \sigma_3\\ \tau_{23}\\ \tau_{31}\\ \tau_{12}\end{bmatrix} = \begin{bmatrix}C_{11} & C_{12} & C_{13} & C_{14} & C_{15} & C_{16}\\ C_{21} & C_{22} & C_{33} & C_{24} & C_{25} & C_{26}\\ C_{31} & C_{32} & C_{33} & C_{34} & C_{35} & C_{36}\\ C_{41} & C_{42} & C_{43} & C_{44} & C_{45} & C_{46}\\ C_{51} & C_{52} & C_{53} & C_{54} & C_{55} & C_{56}\\ C_{61} & C_{62} & C_{63} & C_{64} & C_{65} & C_{66}\end{bmatrix}\begin{bmatrix}\varepsilon_1\\ \varepsilon_2\\ \varepsilon_3\\ \gamma_{23}\\ \gamma_{31}\\ \gamma_{12}\end{bmatrix} \tag{6}$$

Conventionally, the engineering shear strain γ is used considering the relationship γ=2ε as well as the engineering shear stress τ. This notation is typical of an anisotropic material where 36 constants are required to fully describe the mechanical response of the material. However, only 21 independent constants are

required since the stiffness matrix is symmetrical [4]. Furthermore, it is possible to reduce the number of required constants by introducing materials with orthotropic symmetry planes which require only 9 independent constants. Indeed, orthotropic materials have three principal directions where no correlation between shear strains and normal stresses is reported. In this case, the matrix representation for an orthotropic lamina can be written as:

$$\begin{bmatrix}\sigma_1\\ \sigma_2\\ \sigma_3\\ \tau_{23}\\ \tau_{31}\\ \tau_{12}\end{bmatrix}=\begin{bmatrix}C_{11} & C_{12} & C_{13} & 0 & 0 & 0\\ C_{12} & C_{22} & C_{23} & 0 & 0 & 0\\ C_{13} & C_{23} & C_{33} & 0 & 0 & 0\\ 0 & 0 & 0 & C_{44} & 0 & 0\\ 0 & 0 & 0 & 0 & C_{55} & 0\\ 0 & 0 & 0 & 0 & 0 & C_{66}\end{bmatrix}\begin{bmatrix}\varepsilon_1\\ \varepsilon_2\\ \varepsilon_3\\ \gamma_{23}\\ \gamma_{31}\\ \gamma_{12}\end{bmatrix} \tag{7}$$

The constants are generally measured using either experimental tests or micromechanics equations. It is possible to substitute the stiffness constants with the relative engineering property obtaining the following expression:

$$\begin{bmatrix}\sigma_1\\ \sigma_2\\ \sigma_3\\ \tau_{23}\\ \tau_{31}\\ \tau_{12}\end{bmatrix}=\begin{bmatrix}E_{11} & \nu_{12} & \nu_{13} & 0 & 0 & 0\\ \nu_{12} & E_{22} & \nu_{23} & 0 & 0 & 0\\ \nu_{13} & \nu_{23} & E_{33} & 0 & 0 & 0\\ 0 & 0 & 0 & G_{23} & 0 & 0\\ 0 & 0 & 0 & 0 & G_{31} & 0\\ 0 & 0 & 0 & 0 & 0 & G_{12}\end{bmatrix}\begin{bmatrix}\varepsilon_1\\ \varepsilon_2\\ \varepsilon_3\\ \gamma_{23}\\ \gamma_{31}\\ \gamma_{12}\end{bmatrix} \tag{8}$$

Based on this expression, it is possible to fully characterise the mechanical behaviour of a single lamina and, as explained in the next section, its response when bonded together in a laminate. Applications involving a single lamina are very rare.

2.2.5 Macromechanics of laminate

In this section, the macroscopic mechanical behaviour of several laminae bonded together acting as whole is described. No interactions between single components are considered in this theory. The main reason for laminae being stacked up together in a lamination sequence or stacking sequence is the very small thickness that a lamina offers and the necessity to increase this to improve the overall stiffness and the strength. A particularity of this structure is that the orientation of the single laminae can vary in the stacking sequence, allowing the creation of several typologies of laminates with different global mechanical

properties. The understanding of the mechanical response when the lamination sequence is known is indeed one of the main aims of this theory. The basic assumptions used to analyse this aspect of composite mechanics are presented by the Classical Lamination Theory (CLT). CLT imposes a plane stress behaviour on the laminae bonded within the laminate. This leads to the expression of the stress-strain relationship of an orthotropic lamina as:

$$\begin{bmatrix}\sigma_1\\ \sigma_2\\ \tau_{12}\end{bmatrix}=\begin{bmatrix}Q_{11} & Q_{12} & 0\\ Q_{12} & Q_{22} & 0\\ 0 & 0 & Q_{66}\end{bmatrix}\begin{bmatrix}\varepsilon_1\\ \varepsilon_2\\ \gamma_{12}\end{bmatrix}. \tag{9}$$

Where: Q_{ki} terms are the reduced stiffness coefficient for the 1-2 plane stress state and are determined using the formulas in terms of engineering constants [4]:

$$\begin{aligned} Q_{11} &= \frac{E_{11}}{1-\nu_{12}\nu_{21}} & Q_{22} &= \frac{E_{22}}{1-\nu_{12}\nu_{21}}\\ Q_{12} &= \frac{\nu_{21}E_{11}}{1-\nu_{12}\nu_{21}} & Q_{66} &= G_{12}\\ \nu_{21} &= \frac{\nu_{12}E_{22}}{E_{11}} \end{aligned} \tag{10}$$

Since it is necessary to have this relationship also when the reinforcement is oriented in a different direction to the applied solicitation, it is possible to generalise this expression. For every mutual orientation of fibres and stresses, and using a polar transformation tensor, it possible to transform the stresses from a 1-2 *local* reference system into an x-y *global* reference system following the expression:

$$\begin{bmatrix}\sigma_x\\ \sigma_y\\ \tau_{xy}\end{bmatrix}=\begin{bmatrix}cos^2\theta & sin^2\theta & -2cos\theta sin\theta\\ sin^2\theta & cos^2\theta & 2cos\theta sin\theta\\ cos\theta sin\theta & -cos\theta sin\theta 0 & cos^2\theta-sin^2\theta\end{bmatrix}\begin{bmatrix}\sigma_1\\ \sigma_2\\ \tau_{12}\end{bmatrix}$$
$$\begin{bmatrix}\sigma_x\\ \sigma_y\\ \tau_{xy}\end{bmatrix}=[T]^{-1}\begin{bmatrix}\sigma_1\\ \sigma_2\\ \tau_{12}\end{bmatrix} \tag{11}$$

Using (9) and (7), it is possible to write:

$$\begin{bmatrix}\sigma_x\\ \sigma_y\\ \tau_{xy}\end{bmatrix}=\begin{bmatrix}\overline{Q_{11}} & \overline{Q_{12}} & \overline{Q_{16}}\\ \overline{Q_{12}} & \overline{Q_{22}} & \overline{Q_{26}}\\ \overline{Q_{16}} & \overline{Q_{26}} & \overline{Q_{66}}\end{bmatrix}\begin{bmatrix}\varepsilon_x\\ \varepsilon_y\\ \gamma_{xy}\end{bmatrix}$$
$$[\sigma]=[\bar{Q}][\varepsilon] \tag{12}$$
$$[\bar{Q}]=[T]^{-1}[\mathrm{Q}][\mathrm{T}]$$

Using this stress-strain relationship, it is possible to describe the behaviour of any arbitrary layer that is part of a multilayer laminate. Thus, it is possible to rewrite this expression for a laminate with kth layers as:

$$[\sigma]_k = [\bar{Q}]_k[\varepsilon]_k \tag{13}$$

Knowing the stress distribution and via an integration process, the resultant forces and moments can be obtained from equation 13. Before illustrating the procedure used to calculate these results, it necessary to assume that the bond between the laminae must be considered perfect, that non-shear deformation occurs during the loading and that laminae have small thicknesses. The results forces and moments acting on the laminate can then be calculated using the formulas in which the laminate is considered as the collection of kth layers[4]:

$$\begin{bmatrix} N_x \\ N_y \\ N_{xy} \end{bmatrix} = \int_{-\frac{t}{2}}^{\frac{t}{2}} \begin{bmatrix} \sigma_x \\ \sigma_y \\ \tau_{xy} \end{bmatrix} dz = \sum_{k=1}^{N} \int_{z_{k-1}}^{z_k} \begin{bmatrix} \sigma_x \\ \sigma_y \\ \tau_{xy} \end{bmatrix}_k dz \tag{14}$$

$$\begin{bmatrix} M_x \\ M_y \\ M_{xy} \end{bmatrix} = \int_{-\frac{t}{2}}^{\frac{t}{2}} \begin{bmatrix} \sigma_x \\ \sigma_y \\ \tau_{xy} \end{bmatrix} z\, dz = \sum_{k=1}^{N} \int_{z_{k-1}}^{z_k} \begin{bmatrix} \sigma_x \\ \sigma_y \\ \tau_{xy} \end{bmatrix}_k z\, dz. \tag{15}$$

Where N_x, N_y and N_{xy} are the force for unit of width of the laminate section while M_x, M_y and M_{xy} are the moment for unit of width, t is the tackiness of the laminate and z_k and z_{k-1} are the distances of the top and bottom surface of the ply from the reference system located on the middle plane of the laminate as reported in Figure 9. The positive direction of z is considered downwards.

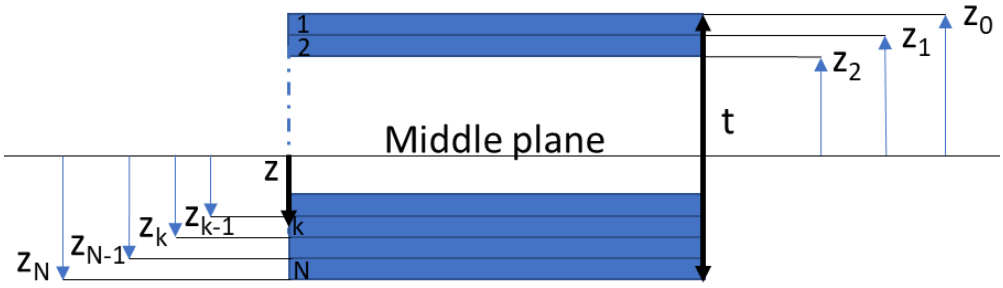

Figure 9-Geometrical representation of a laminated made of N layers.

The representation of forces and moments are reported in Figure 10.

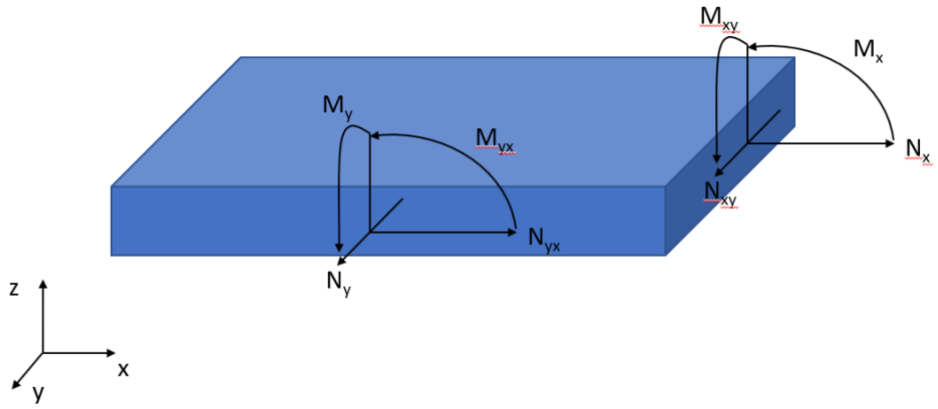

Figure 10-Representation of forces and moments on laminate.

Substituting equation 10 into equation 13 and using equation 14 and equation 15, it is possible to correlate the resultant forces and moments to the reduced stiffness' coefficients. The reduced stiffness matrix is considered constant within the lamina, and therefore can be written outside the integral [4]. Moreover, it is possible to decompose the strain components [4] in longitudinal strain ε0 (strain of the middle plane) and curvature strain κ (deflection during bending) considering the cinematics of plate deformation:

$$\begin{bmatrix} N_x \\ N_y \\ N_{xy} \end{bmatrix} = \sum_{k=1}^{N} \begin{bmatrix} \overline{Q_{11}} & \overline{Q_{12}} & \overline{Q_{16}} \\ \overline{Q_{12}} & \overline{Q_{22}} & \overline{Q_{26}} \\ \overline{Q_{16}} & \overline{Q_{26}} & \overline{Q_{66}} \end{bmatrix}_k \int_{z_{k-1}}^{z_k} \left[\begin{bmatrix} \varepsilon_x \\ \varepsilon_y \\ \gamma_{xy} \end{bmatrix} dz \right] \tag{14}$$

$$\begin{bmatrix} M_x \\ M_y \\ M_{xy} \end{bmatrix} = \sum_{k=1}^{N} \begin{bmatrix} \overline{Q_{11}} & \overline{Q_{12}} & \overline{Q_{16}} \\ \overline{Q_{12}} & \overline{Q_{22}} & \overline{Q_{26}} \\ \overline{Q_{16}} & \overline{Q_{26}} & \overline{Q_{66}} \end{bmatrix}_k \int_{z_{k-1}}^{z_k} \left[\begin{bmatrix} \varepsilon_x \\ \varepsilon_y \\ \gamma_{xy} \end{bmatrix} z dz \right] \tag{15}$$

$$\begin{bmatrix} \varepsilon_x \\ \varepsilon_y \\ \gamma_{xy} \end{bmatrix} = \left[\begin{bmatrix} {\varepsilon_x}^0 \\ {\varepsilon_y}^0 \\ {\gamma_{xy}}^0 \end{bmatrix} + z \begin{bmatrix} \kappa_x \\ \kappa_y \\ \kappa_{xy} \end{bmatrix} \right]. \tag{16}$$

Using (14) in (12) and (13), the resultant forces and moments can be calculated in function of the applied strains:

$$\begin{bmatrix} N_x \\ N_y \\ N_{xy} \end{bmatrix} = \sum_{k=1}^{N} \begin{bmatrix} \overline{Q_{11}} & \overline{Q_{12}} & \overline{Q_{16}} \\ \overline{Q_{12}} & \overline{Q_{22}} & \overline{Q_{26}} \\ \overline{Q_{16}} & \overline{Q_{26}} & \overline{Q_{66}} \end{bmatrix}_k \int_{z_{k-1}}^{z_k} \left[\begin{bmatrix} {\varepsilon_x}^0 \\ {\varepsilon_y}^0 \\ {\gamma_{xy}}^0 \end{bmatrix} + z \begin{bmatrix} \kappa_x \\ \kappa_y \\ \kappa_{xy} \end{bmatrix} \right] dz \tag{17}$$

$$\begin{bmatrix} M_x \\ M_y \\ M_{xy} \end{bmatrix} = \sum_{k=1}^{N} \begin{bmatrix} \overline{Q_{11}} & \overline{Q_{12}} & \overline{Q_{16}} \\ \overline{Q_{12}} & \overline{Q_{22}} & \overline{Q_{26}} \\ \overline{Q_{16}} & \overline{Q_{26}} & \overline{Q_{66}} \end{bmatrix}_k \int_{z_{k-1}}^{z_k} \left[\begin{bmatrix} {\varepsilon_x}^0 \\ {\varepsilon_y}^0 \\ {\gamma_{xy}}^0 \end{bmatrix} + z \begin{bmatrix} \kappa_x \\ \kappa_y \\ \kappa_{xy} \end{bmatrix} \right] z dz \qquad (18)$$

Since the strain terms are not a function of z, they can be written outside the sum operator. Rearranging the equations and solving the integrals as reported in [4], it is possible to obtain the final equations that are used to describe the resultant force and moments:

$$\begin{bmatrix} N_x \\ N_y \\ N_{xy} \end{bmatrix} = \begin{bmatrix} A_{11} & A_{12} & A_{16} \\ A_{12} & A_{22} & A_{26} \\ A_{16} & A_{26} & A_{66} \end{bmatrix} \begin{bmatrix} {\varepsilon_x}^0 \\ {\varepsilon_y}^0 \\ {\gamma_{xy}}^0 \end{bmatrix} + \begin{bmatrix} B_{11} & B_{12} & B_{16} \\ B_{12} & B_{22} & B_{26} \\ B_{16} & B_{26} & B_{66} \end{bmatrix} \begin{bmatrix} \kappa_x \\ \kappa_y \\ \kappa_{xy} \end{bmatrix} \qquad (19)$$

$$\begin{bmatrix} M_x \\ M_y \\ M_{xy} \end{bmatrix} = \begin{bmatrix} B_{11} & B_{12} & B_{16} \\ B_{12} & B_{22} & B_{26} \\ B_{16} & B_{26} & B_{66} \end{bmatrix} \begin{bmatrix} {\varepsilon_x}^0 \\ {\varepsilon_y}^0 \\ {\gamma_{xy}}^0 \end{bmatrix} + \begin{bmatrix} D_{11} & D_{12} & D_{16} \\ D_{12} & D_{22} & D_{26} \\ D_{16} & D_{26} & D_{66} \end{bmatrix} \begin{bmatrix} \kappa_x \\ \kappa_y \\ \kappa_{xy} \end{bmatrix} \qquad (20)$$

where

$$\begin{aligned} A_{ij} &= \textstyle\sum_{k=1}^{N} \left(\overline{Q_{ij}}\right)_k (z_k - z_{k-1}) \, (\\ B_{ij} &= \frac{1}{2} \sum_{k=1}^{N} (\overline{Q_{ij}})_k \, ({z_k}^2 - {z_{k-1}}^2) \\ D_{ij} &= \frac{1}{3} \sum_{k=1}^{N} \left(\overline{Q_{ij}}\right)_k \, ({z_k}^3 - {z_{k-1}}^3). \end{aligned} \qquad (21)$$

Analysing these expressions, it is possible to define the different components that describe a different aspect of the microscopical behaviour of the laminate. A_{ij} is the extensional stiffness matrix that relates the longitudinal strain to the normal forces where diagonal terms (i=j) are the ones which are linked to normal extension while the terms out-of-diagonal (i≠j) are the ones related to in-plane shear. Similarly, D_{ij} is the bending stiffness of the laminate which relates the curvature strain components to the moments where the terms on the diagonal are related to the pure bending and the ones out-of-diagonal are related to twisting. B_{ij} conversely, is the coupling matrix which generates coupling between extensional and bending terms and is the reason for the unique mechanical response of composites. Indeed, when a normal force is applied on the material, it is not possible to avoid the generation of bending/twisting in addition to the longitudinal strain of the middle plane.

These phenomena represent an issue for the use of composite materials in structural applications. Consequently, the materials must be designed following certain guidelines to avoid the coupling between extensional and bending components. By using a symmetrical design for the lamination sequence, it is possible to eliminate all the B_{ij} terms from the matrix (these terms are responsible for this coupling). This can be achieved by symmetrically introducing a pair of laminae with the same material, thickness, and orientation at the same distance across the middle plane. Consequently, their contribution in the B matrix is exactly opposite and they cancel each other. However, the coupling between bending and twisting is still present. This phenomenon can be eliminated by designing the laminates as balanced. Balanced laminates are a special category of symmetric laminates where alongside the symmetric characteristics, the plies are introduced in pairs oriented at opposite angles. In other words, if two laminae at +45° are introduced into the laminate, they must be balanced by introducing two other plies at -45° respecting the symmetric laminate definition. Therefore, the use of balanced laminates is very common due to the elimination of shear-extension, bending-extension and bending-twisting. However, it is important to underline that either the introduction of additional layers of reinforcement or the use of laminae with hybrid fibrous reinforcement modify this theory as discussed in detail in the literature review of reinforcement hybridisation in the next chapter (Section 3.2).

Cases in which fabrics are considered are out of the scope of this thesis works since only unidirectional carbon fibres were used to manufacture the analysed hybrid composites. Several works are available in literature analysing the mechanical [17-19] and micromechanical [20-22] aspects of laminae using fabrics as reinforcement.

2.3 Impact behaviour of composite materials

2.3.1 Overview

Following the description of the mechanical behaviour of these materials, it is necessary to analyse their behaviour when subjected to dynamic loading - an impact - and evaluate the parameters that are critical for the material's integrity. An impact is defined as an interaction between a body and a foreign object which occurs in a short period of time. Generally, it is possible to classify impacts in two broad categories: Low Velocity Impacts (LVIs) and High Velocity Impacts (HVIs), even though the separation between these two categories is not well defined. Some authors [23, 24] use a range between 0-10 ms to define the interval during which LVIs occur, since the contact duration between the impacting object and the structure is long and the stress waves are able to reach the boundaries of the part. Conversely, for HVIs contact time is short and consequently, the phenomenon is dominated by the stress wave propagation. The material is not able to react since the impact event is terminated before the stress waves reach the boundaries. Other researchers [25] suggest classification of impacts according to the typology of damage found after the impact occurs. This is because LVIs mostly generate matrix cracking and delamination while HVIs generate penetration and fibre breakage. Another classification [26] was developed which categorises impacts in function of the through-the-thickness stress wave that are generated during the impact event. The impact is considered LV if wave propagation has no influence on the stress distribution while it is considered HV if the stress distribution is influenced by the through-the-thickness stress wave propagation.

The most common causes of impacts can be identified in several different phenomena which can occur at different stages of the life of a part. These include tool drops during maintenance of aerospace structures, flying ballasts for railways and runway debris in the case of aircrafts application. Unlike metals which have a limited criticality towards impact damage due to the plastic deformation which limits the risks to the structure's safety, composite materials are characterised by

brittle behaviour which can cause severe inner damage and a consequent reduction in the mechanical properties of the part. It is therefore paramount to understand the impact dynamics, the damage typologies and the failure mechanisms involved during impact events.

2.3.2 Impact Mechanics

The impact phenomenon can be studied using the equation of motion for two-degree of freedom systems [27] illustrated in Figure 11 :

$$M_p\ddot{\alpha} + K_{bs}\alpha + K_m\alpha^{3/2} + P(\alpha) = 0 \qquad (22)$$

where M_p is the mass of the impacted body, K_{bs} is the resultant stiffness between bending and shear stiffnesses (usually k_s is small enough to be neglected), K_m is membrane stiffness and α is the indentation (displacement) of the body.

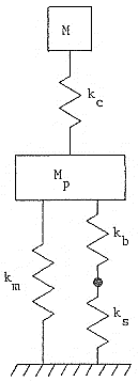

Figure 11-Impact model considering a two degrees of freedom system spring-mass model. M is the mass of the impacting object and k_c is the stiffness of the contact. Image from [27].

The expressions for the bending and membrane stiffness' under different boundary conditions such as clamped and simply supported, and different plate reactions such as immovable and movable can be written as (Table 4):

Table 4- Expressions for bending stiffness and membrane stiffnesses. Table from [27].

Boundary Conditions	**Bending Stiffness K_b**		**Membrane stiffness parameters K_f**	
Clamped	Immovable	$\frac{4\pi E_r h^3}{3(1-v_r^2)a^2}$	Immovable	$\frac{(353-191v_r)\pi E_r h}{648(1-v_r)a^2}$
	Movable	$\frac{4\pi E_r h^3}{3(1-v_r^2)a^2}$	Movable	$\frac{191\pi E_r h}{648a^2}$
Simply supported	Immovable	$\frac{4\pi E_r h^3}{3(1-v_r)(3+v_r)a^2}$	Immovable	$\frac{\pi E_r h}{(3+v_r)^4 a^2}\left\{\frac{191}{648}(1+v_r)^4+\frac{41}{27}(1+v_r)^3+\frac{32}{9}(1+v_r)^2+\frac{40}{9}(1+v_r)+\frac{8}{3}+\frac{1}{1-v_r}\left[\frac{(1+v_r)^4}{4}+2(1+v_r)^3+8(1+v_r)^2+16(1+v_r)+16\right]\right\}$
	Movable	$\frac{4\pi E_r h^3}{3(1-v_r)(3+v_r)a^2}$	Movable	$\frac{\pi E_r h}{(3+v_r)^4 a^2}\left[\frac{191}{648}(1+v_r)^4+\frac{41}{27}(1+v_r)^3+\frac{32}{9}(1+v_r)^2+\frac{40}{9}(1+v_r)+\frac{8}{3}\right]$

Abrate [28, 29] proposed several semiempirical contact laws to define the force P as a function of the indentation α and predicted the impact response of composite materials. Furthermore, Yang and Sun [30] proposed an elastoplastic contact law to describe the contact force applied to the composite structure:

$$P_{loading} = \frac{\pi R_i E}{h}\alpha^2 \qquad \alpha \leq \alpha_{cr} \qquad (23)$$

$$P_{loading} = \pi R_i Z_c(2\alpha - \alpha_{cr}) \qquad \alpha > \alpha_{cr} \qquad (24)$$

$$P_{unloading} = \frac{\pi R_i E}{h}(\alpha^2 - \alpha_0^2) \qquad \alpha > \alpha_0 \qquad (25)$$

$$\alpha_{cr} = \frac{Z_c h}{E}$$

$$\alpha_0 = \alpha_m - \alpha_{cr}$$

Where Z_c is the strength of the material, E is the transverse modulus of the laminate, R_i is the radius of the impacting object, α_m is the maximum indentation during the loading phase, α_{cr} is the minimum indentation required to generate permanent indentation considered as a material property and α is the indentation applied on the plate. Equations 23 and 24 describe the elastic part of the force-indentation curve during the loading phase of the impact before critical indentation is reached. Equation 25 describes the curve during the unloading behaviour of the material.

Both curves can be merged to obtain the full description of the impact event on the laminate as shown in Figure 12.

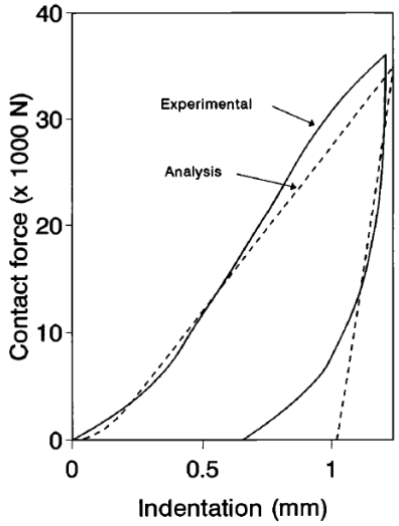

Figure 12-Experimental and analytical force-indentation curves in comparison. Image from [29].

To fully understand the impact on composite plates, numerical integration is required to obtain the solution to the differential equation (equation 22). To analyse the impact event from an experimental perspective however, it is important to consider that the force history is generally recorded by a sensor connected to the impacting object. A schematic representation of the three curves (force, velocity and displacement) is shown in Figure 13.

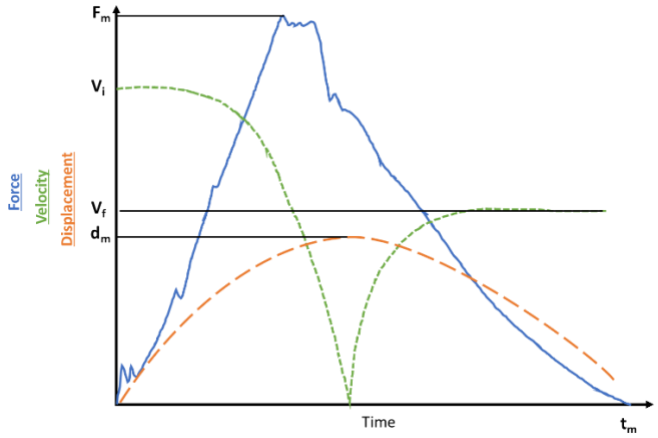

Figure 13-Example of force-time (blue), velocity (absolute value)-time (green) and displacement-time (orange) curves.

The analysis of this curve gives raw information about the time of contact t_c, maximum contact time t_m and the maximum contact force F_m. It is possible to obtain more information by integrating the force-time curve and calculating the velocity of the impacting object and the rebound velocity. From these, initial information about the amount of energy lost during the impact event is evaluated. Equation 26 is used to carry out this operation:

$$v(t) = v_i + gt - \int_0^t \frac{F(t)}{m} dt \tag{26}$$

where v_i is the initial velocity of the impacting body, g is the gravitational acceleration, F(t) is the force history in function of time, v(t) is the velocity history over time, m is the impacting mass and t is the time instant in which the specific results are evaluated. The velocity-time curve is also shown in Figure 13. Processing the velocity-time curve using a further numerical integration shown in equation 27, it possible to obtain data about the displacement withstood by the material obtaining the maximum displacement d_m (Figure 13) reached during the impact event.

$$d(t) = d_i + v_i t + \frac{gt^2}{2} + \int_0^t \left(\int_0^t \frac{F(t)}{m} dt \right) dt \tag{27}$$

Where d_i is the initial displacement and d(t) is the displacement history over time. It is important to notice that maximum displacement and maximum force are not obtained at the same time value.

Impact energy is another important parameter to consider when evaluating impact events. It is the kinetic energy of the impacting object that that is transferred entirely to the composite during the dynamic event. Composites can store this energy as elastic energy and transfer it back to the impacting object after the point of maximum displacement, or dissipate it via damage generation, vibrations and other non-linear components. It is possible to evaluate the energy dissipated during the impact event considering the difference between impact energy E_{imp} and rebound energy E_r. These energies can be directly associated to the impact v_{imp} and rebound v_r velocities of the velocity-time plot using the equation:

$$E_{dis} = E_{imp} - E_r = \frac{1}{2} m\left({v_{imp}}^2 - {v_r}^2\right). \quad (28)$$

Where m is the mass of the impacting object.

Another important plot that can be obtained from these datasets is the force-displacement plot, fundamental to assess the energy that the composite absorbed during the impact event. The curve also gives information about the impact nature and damage topology. In Figure 14, different impact curves are shown.

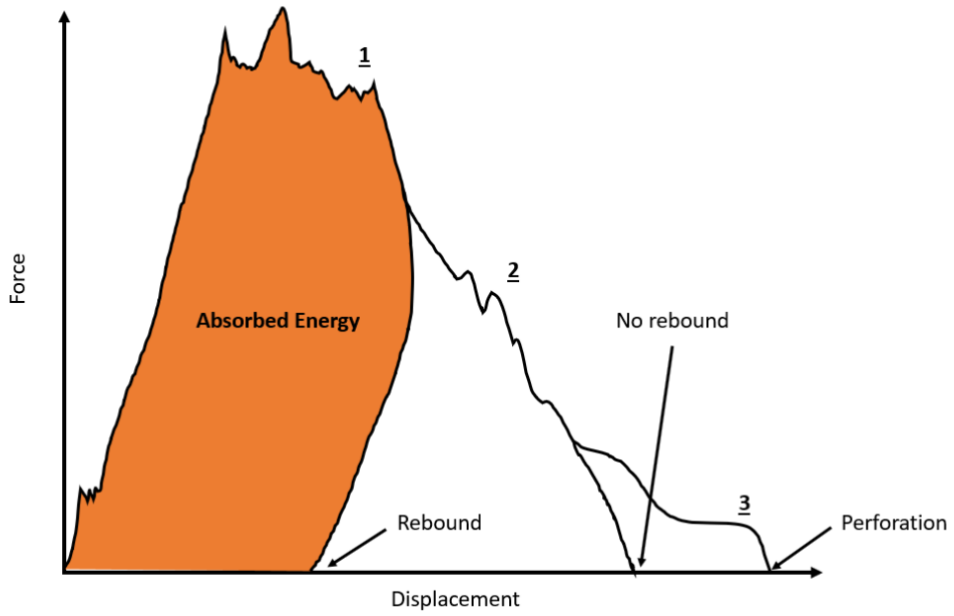

Figure 14-Example of a force-displacement curve indicating several characteristics typical of a specific impact response.

Curve 1 is a force-displacement curve which can typically be obtained from LVIs where mainly matrix cracking and delamination are identified. These failure mechanisms are unable to absorb enough energy to stop the impactor that bounces back using the elastic energy accumulated in the composite. Curve 2 is obtained by processing the impact response of an impact event with a higher energy level in which fibre failure, severe matrix cracking and wide delamination are typically generated. The impactor is stopped, and no rebound is observed. Curve 3 is the representation of an impact event in which penetration is involved because the material is not able to absorb all the applied impact energy, resulting in severe fibre failure, matrix collapse and wide delamination. This response is common in cases where the material is subject to High Velocity Impact (HVI) conditions.

2.3.3 Impact damage

Internal damage generated as consequence of an impact event can be categorised into three main categories: fibre failure, interlaminar matrix failure and intralaminar matrix failure (Figure 15).

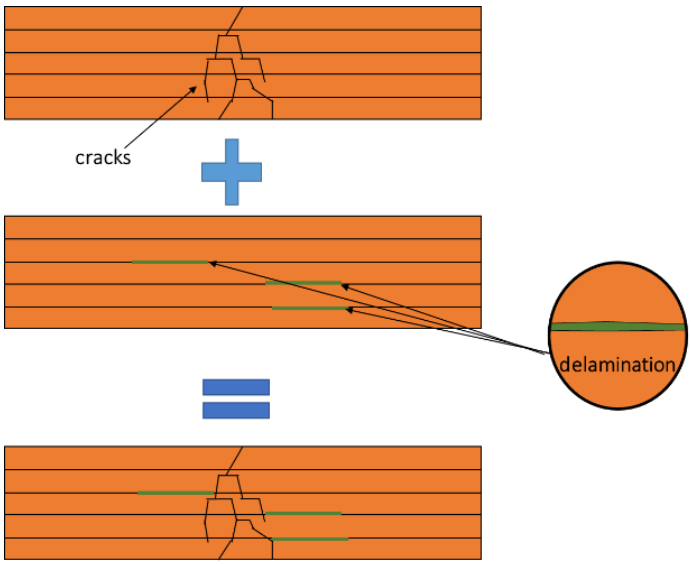

Figure 15-General illustration of internal damage showing cracks (black) propagating through the thickness of the material and delamination (green) propagating along the interface between adjacent layers.

It is still difficult to reconstruct the whole chronological sequence of phenomena that are involved in the process of damage generation. Generally, impact damage is initiated by the creation of matrix cracks (intralaminar) at the interface the between fibre and the resin which then propagate across the laminate's thickness since the interface strength is weaker than matrix and fibre ones. If the laminate is thin (up to around 3 mm), the bending stiffness of the laminate is low and the initial crack, perpendicular to the ply plane, is generated by tensile stresses and localised in the lower portion of the laminate [28]. If the laminate is thick (over 3 mm), the bending stiffness is high, and the crack initiates close to the impact surface and is transversal with respect to the mid-plane of the ply. In addition, these cracks can propagate across the ply thickness and they can generate delamination and intralaminar matrix failure consisting of the separation of two adjacent plies.

It is possible to predict the load energy thresholds for damage initiation using equations [28, 31] based on Fracture Theory [14]. These thresholds correspond to the delamination generation at the first load drop, visible from the force-time curve (equation 29), and to the energy required to generate fibre failure and penetration (equation 30):

$$P_{crit}^2 = \frac{8\pi^2 E h^3 G_{IIc}}{9(1-\nu^2)} \tag{29}$$

$$E_{fibre} = \frac{8\sigma^2 whL}{18E_f}. \tag{30}$$

Where P_{crit} is the load threshold, E is the global stiffness modulus, ν is the Poisson's ratio, G_{IIc} is the fracture energy release rate, h is the thickness of the laminate, L is the unsupported length, E_f is the flexural modulus, w is the width of the composite and σ is the flexural strength of the composite. The value of G_{IIc} varies considerably between laminae at different angles and the higher the angle mismatch, the lower the G_{IIc} value. This is due to the mismatch of bending stiffness that plies at different orientation have between each other. If the angle mismatch is low, bending stiffness is similar, and a lower shear stress is generated at their interface with large energy needed to generate a new surface (delamination). Conversely, if the angle mismatch

is high, the bending stiffness mismatch is high and the shear stress generated between the plies is high, reducing the energy required for generating delamination [32]. It is important to note that there are other parameters that govern the generation of impact damage which can alter the impact behaviour [28, 29] of the material during testing. Such parameters include its mass, thickness, boundary conditions and the typology of projectile [33, 34]. The analysis of the morphology of the impact damage on composite materials can be performed using several techniques including Computed Tomography (CT) scans [35] and microscopy [36] as shown in Figure 16.

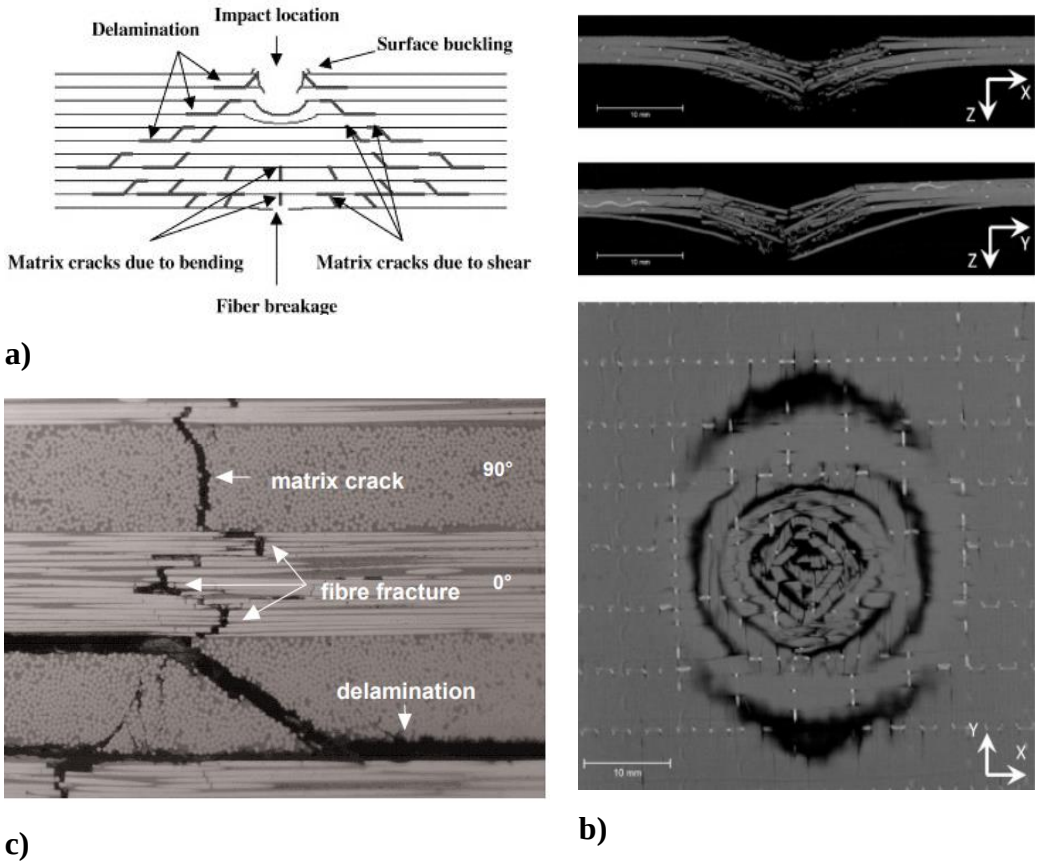

Figure 16-Morphology of impact damage generated within a laminated structure: a) illustration of damage characteristics (images from [36]), b) global view of laminate using CT scans (image from [35]) and c) detail of the impact damage (image from [35]).

As illustrated in this section, it is clear that impact damage is a critical issue for composites, particularly because in most of the cases in which LVIs are involved, visual inspection is ineffective (since the damage is created within the composite

structure with no external evidences of its location). It is therefore fundamental to develop solutions to reduce the entity of the damage itself, thus increasing the tolerance of the material towards an impact event.

2.3.4 Failure Criteria

Damaged areas are generated within the material under certain conditions of stress and strain and it is fundamental to understand these conditions and develop some criteria which allow to predict whether the structure is able to withstand the applied load without failure. These criteria are formulated following the assumptions of homogeneous orthotropic solid ply.

Hashin's fibre failure criterion depends on the laminate strength along the direction of fibres in tension X_T, in compression X_C, the transverse shear strengths S_{12} and S_{13}, as illustrated by Zhang and Abrate [29, 37] in the formula:

$$\left(\frac{\sigma_{11}}{X_T}\right)^2 + \left(\frac{\sigma_{12}}{S_{12}}\right)^2 + \left(\frac{\sigma_{13}}{S_{13}}\right)^2 = 1 \;\; if\ \sigma_{11} > 0 \tag{31}$$

$$|\sigma_{11}| = X_c \qquad if\ \sigma_{11} < 0. \tag{32}$$

where: $\sigma_{11}$is the normal stress along the fibre direction and, σ_{12} and σ_{13} are the shear stresses acting on the laminate. As reported in the equations, it is possible to analyse the stress distribution within the material and if the conditions satisfy the criteria, fibre failure occurs. Similarly, Kim *et al.* [38] used Hashin's criteria to predict matrix failure in tension and compression which depends on the combination of transversal normal stresses σ_{22} and σ_{33} and shear stresses σ_{12} and σ_{13}:

$$\left(\frac{\sigma_{22} + \sigma_{33}}{Y_T}\right)^2 + \frac{{\sigma_{23}}^2 - \sigma_{22}\sigma_{33}}{{S_{23}}^2} + \left(\frac{\sigma_{12}}{S_{12}}\right)^2 + \left(\frac{\sigma_{13}}{S_{13}}\right)^2 = 1 \qquad if\ (\sigma_{22} + \sigma_{33}) > 0 \tag{33}$$

$$\left(\frac{\sigma_{22}+\sigma_{33}}{2\sigma_{12}}\right)^2+\frac{\sigma_{22}+\sigma_{33}}{Y_c}\left[\left(\frac{Y_c}{2S_T}\right)^2-1\right]+\frac{{\sigma_{23}}^2-\sigma_{22}\sigma_{33}}{{S_{23}}^2}+\left(\frac{\sigma_{12}}{S_{12}}\right)^2+\left(\frac{\sigma_{13}}{S_{13}}\right)^2 \geq 1 \quad if\ (\sigma_{22}+\sigma_{33})<0. \tag{34}$$

Where Y_T and Y_C are the transverse strength at tension and compression respectively, S_T is the tension shear strength and S_{23} is the shear strength relative to the stress acting on the plane with normal orientation along the fibre direction.

Three-dimensional Tsai-Hill criterion provides a generalised failure criterion which considers the contribution of the stresses acting along all the directions of the laminate:

$$\left(\frac{\sigma_{11}}{X}\right)^2+\left(\frac{\sigma_{22}}{Y}\right)^2+\left(\frac{\sigma_{33}}{Z}\right)^2+\left(\frac{\sigma_{23}}{S_{23}}\right)^2+\left(\frac{\sigma_{13}}{S_{13}}\right)^2+\left(\frac{\sigma_{12}}{S_{12}}\right)^2-\sigma_{11}\sigma_{22}\left(\frac{1}{X^2}+\frac{1}{Y^2}-\frac{1}{Z^2}\right)-\sigma_{11}\sigma_{33}\left(\frac{1}{X^2}+\frac{1}{Z^2}-\frac{1}{Y^2}\right)-\sigma_{22}\sigma_{33}\left(\frac{1}{Y^2}+\frac{1}{Z^2}-\frac{1}{X^2}\right)=1 \tag{35}$$

Where X, Y and Z are the strength along the fibre, the transverse and the throughout-the-thickness direction respectively. Tension and compression strengths are considered the same. A detailed illustration of damage typologies is reported in Figure 17

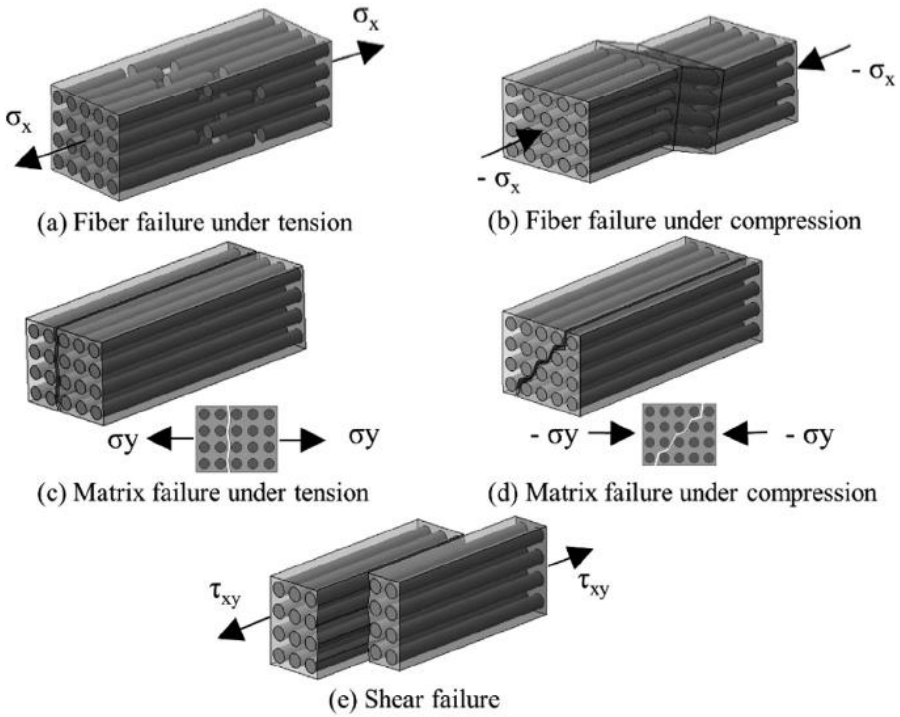

Figure 17- Illustration of intralaminar damage. Image from [34].

Yeh and Kim (tension) [39] and Li (compression) [40] also reported interlaminar failure criteria to predict the stress conditions in which delamination opens.

$$\left(\frac{\sigma_{33}}{Z_T}\right)^2 + \left(\frac{\sigma_{13}}{S_{13}}\right)^2 + \left(\frac{\sigma_{23}}{S_{23}}\right)^2 \geq 1 \qquad if\ \sigma_{33} > 0 \tag{36}$$

$$\left(\frac{\sigma_{13}}{S_{13}}\right)^2 + \left(\frac{\sigma_{23}}{S_{23}}\right)^2 \geq 1 \qquad if\ \sigma_{33} < 0 \tag{37}$$

where: $\sigma_{33}$is the stress along the thickness direction and Z_t is the relative strength. With these equations, it is possible, to estimate the presence of a delaminated area within the laminate by evaluating whether its local stress distribution satisfies the criteria.

3 CHAPTER: Literature review on hybridisation for improvement of mechanical and impact properties

This section will analyse several research works present in the literature relative to each of the papers included in this thesis in order to provide to the reader a clear and accurate report of current hybrid solutions and show the novelty of this research work. As discussed in previous section, impact events, and more specifically the impact damage generated by the interaction between an impacting object and a laminated structure, is a serious and critical problem that spans different industrial sectors including automotive, aerospace and energy. This issue can be associated with the weakening of the structure due to damage generation which increases the risk of catastrophic failure of the component and could compromise the safety of the entire structure. To overcome this issue and increase the appeal of advanced laminated composite systems for the aforementioned sectors, the improvement of the impact behaviour of traditional laminates is required. Several approaches to this improvement have been studied by the research community. The aim of this section is to introduce the concept of hybridisation and to illustrate several works that are already available in literature on this subject to allow the reader to better explain the content of the next chapters. It is important to integrate the introduction and methodologies used in each single chapter with the background reported in this section.

3.1 General solutions for improving impact properties

3.1.1 Matrix Toughening

One of the most popular approaches to enhancing laminates is based on a simple idea; the improvement of a single component of the composite material to increase the performance of the entire structure. Following this approach, the toughening of the polymeric matrix [41] was demonstrated as a valid solution to reducing the matrix cracking and delamination generated by impact loading since the polymer is able to tolerate a higher strain at failure [34].

In his review, Garg [42] compared different characteristics of unmodified and toughened system and considered two typologies of toughened systems: rubber-epoxy and filled epoxy. Rubber-toughened epoxy systems include within the uncured epoxy a percentage of a carboxyl-terminated butadiene-acrylonitrile (CTBN) which can precipitate and react with the epoxy groups of the polymer during the cure. The presence of the rubber allows the system to increase its fracture toughness (up to 30% in composites) in comparison with the untoughened polymer. During the crack propagation, the crack tip displacement is influenced by the cavitation in the rubber or at interface surface, and by the plastic shear stress in the epoxy matrix (Figure 18). However, other properties including stiffness (~-33%), glass transaction temperature T_g (~-20%) and yielding stress (~-22%) are negatively affected by the introduction of rubber.

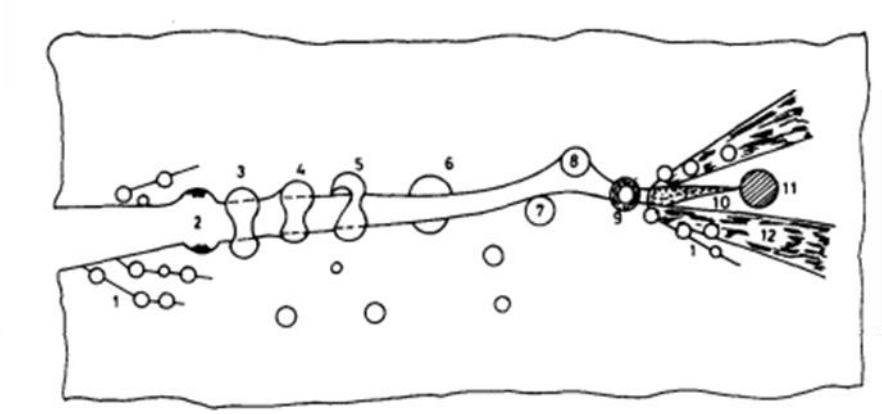

Figure 18-Illustration of the basic mechanics of rubber-based toughened matrix:1) rubber particles inducing shear cracks,2) fracture due to rubber cavitation, 3) stretch of the damage surface, 4) interface separation, 5) fracture of rubber, 6) fracture between rubber elements, 7) interface separation due to tough element, and 8) fracture profile deflection due tough particles, 9) rubber element after cavitation, 10) network of small cracks, 11) onset of the fracture profile showing plastic deformation, 12) yielded area due to shear stress and 13) interaction between crack network. Image from [42].

The use of filler in resin toughening [42] has also proved a popular approach. This process involves mixing particles of inorganic components such as alumina, dolomite and silicon carbide with the resin components. The presence of the filler increases the stiffness, strength, and fracture toughness of the system since the crack is slowed down by the stress alteration in the surrounding area of the particles. This can represent an issue during manufacturing due to the high viscosity of the resin during the manufacturing process and generation of irregular crack propagation after the cure. Another approach to increasing matrix toughness was studied by Tang *et al.[43]* who analysed the use of nanoparticles in enhancing composite interlaminar toughness, thus reducing the generation of delaminated area and increasing the post-impact mechanical properties. The mechanisms behind the effectiveness of nanoparticles are mostly the ones characterised in previous works, [42] however since the particles used are smaller in size, the beneficial effect is amplified [44-46].

3.1.2 Z-stitching and pinning

Another approach that can be exploited to improve laminate resistance is the use of Z-stitching or pinning [47-49]. Z-stitching is a reinforcement along the

through-the-thickness direction of the laminate. Pins or fibres are generally used for this purpose. Several research works investigated the effect of these processes on the interlaminar properties of the laminate. It has been shown that interlaminar damage can be reduced through the presence of Z-reinforcement which increases interlaminar fracture toughness. However, this solution generates an accumulation of defects during manufacturing, for example, resin-concentrated areas that lower the in-plane mechanical properties by 25%. A direct development of this process is the fabrication of 3D reinforcements offering the same advantages of 2D reinforcements with the beneficial effect of the presence of through-the-thickness reinforcement for delamination resistance. This also enables the absorption of more energy due to increased interlaminar shear strength. Selrzer *et al. [50]* observed that composites realised using this type of reinforcement were able to absorb two times the amount of impact energy in comparison to 2D reinforced composites. These results were supported by Bandaru *et al*, who evaluated the improved tensile and impact response of 3D reinforced composites compared to 2D reinforced ones. An illustration of 3D reinforcement is reported in Figure 19. Crucially however, the cost of manufacturing this reinforcement is high and its application is not suitable in all the required applications.

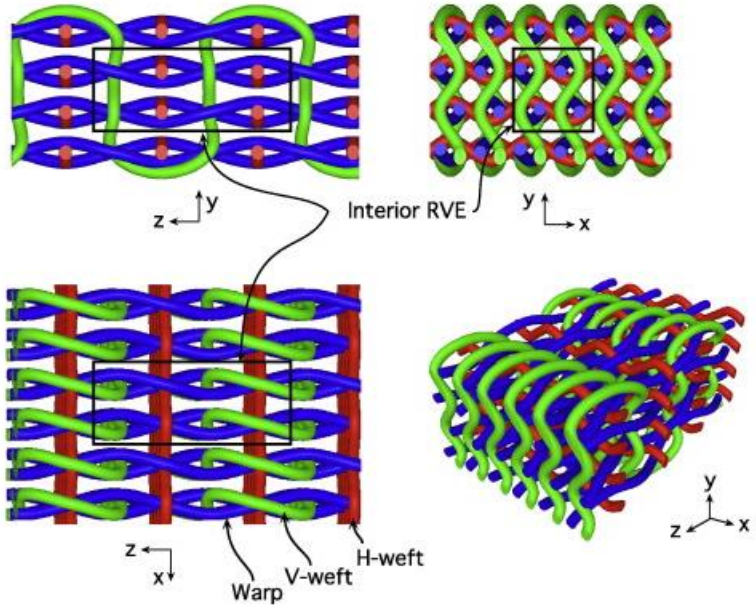

Figure 19-Representation of 3D reinforcement composed of Horizontal weft (H-weft), Vertical weft (V-weft) and warp. The smallest Representative Elementary Volume (RVE) is reported in the black frame. Images from [51].

3.2 Reinforcement hybridisation

3.2.1 General background

Another solution that is widely studied to improve the impact behaviour of composite laminates, is the use of one or more additional reinforcement phases within the composite. This process is termed hybridisation and it can be carried out following several approaches and used to tune the properties of the material towards the application requirements.

Reinforcement hybridisation is a well-known approach within the literature consisting of the introduction of one or more additional fibrous reinforcements into a single polymeric matrix laminate [52, 53]. If the reinforcement is introduced into the material by mixing the new fibres with the ones already reinforcing the material, the hybrid material is defined intraply. If the new reinforcement is introduced as an independent layer within the material, the hybrid material is defined as interply [54]. A schematisation of the two typologies is reported in Figure 20.

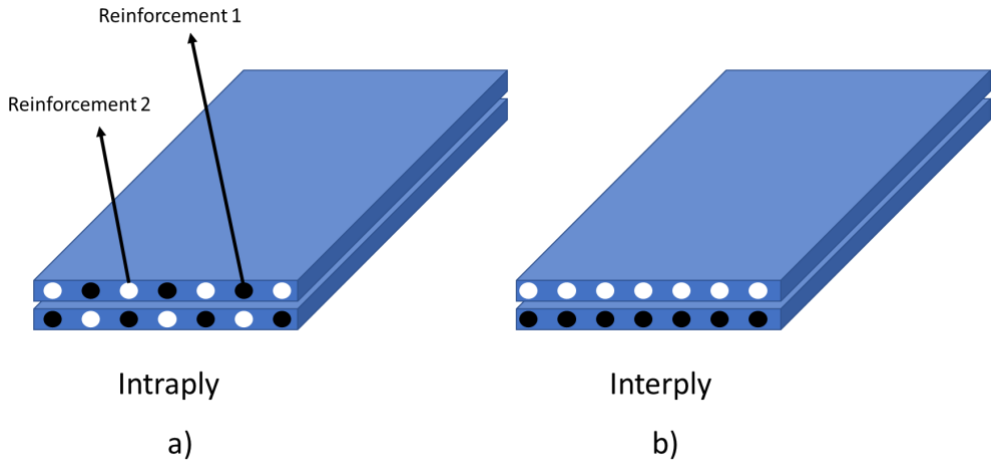

Figure 20-Schematisation of the two different typologies of hybrid reinforcement to manufacture hybrid composites: a) intraply and b) interply.

To explain how the presence of an additional reinforcement affects the mechanical properties and equations seen in Section 2.2, it is necessary to consider the in-plane and the out-of-plane mechanical properties separately.

In-plane properties of intraply hybrid lamina can be studied using micromechanics and macromechanics as shown in Section 2.2 considering that its elastic properties are a combination of the two typologies of fibre reinforcement. Thus, it is possible to obtain this estimation following the equation 38 and 39 derived by the rule of mixture [55]:

$$E_H = E_{f1}V_{f1} + E_{f2}V_{f2} \quad (38)$$

$$\nu_H = \nu_{f1}V_{f1} + \nu_{f2}V_{f2}. \quad (39)$$

Where: E_H is the final modulus of the hybrid reinforcement, E_{f1} and E_{f2} are the elastic moduli of reinforcement 1 (low strain at failure) and reinforcement 2 (high strain at failure) respectively, and, and V_{f1} and V_{f2} are the volume fractions.

It is also possible to estimate the shear modulus and transverse modulus of the final reinforcement by using the inverse rule of mixture [56] as shown equation 40 and 41:

$$G_H = \frac{G_{f1}G_{f2}}{V_{f2}G_{f1} + G_{f2}V_{f1}} \quad (40)$$

$$E_{HT} = \frac{E_{f1}E_{f2}}{V_{f2}E_{f1} + E_{f2}V_{f1}} \tag{41}$$

where G_H and E_{HT} are the shear and transverse moduli of the hybrid reinforcement, G_{f1} and G_{f2} are the elastic moduli of the reinforcement 1 (low strain at failure) and reinforcement 2 (high strain at failure), and, and V_{f1} and V_{f2} are the volume fraction. When the elastic constants are obtained for the fibre reinforcement, it is possible to apply the micromechanics of lamina to obtain the properties of the hybrid composite lamina as shown in Section 2.2. However, it is important to note that some researchers have also found a strong dependency of these properties on the volume fraction [55, 57] of the two reinforcements used showing deviation from the illustrated equations.

When the elastic properties of the intraply hybrid material are known, it is possible to use the macromechanics [58] of lamina illustrated in Section 2.2 to obtain the expression to describe the stress-strain relationship of the lamina:

$$\begin{bmatrix}\sigma_1\\ \sigma_2\\ \tau_{12}\end{bmatrix} = \begin{bmatrix}Q_{11_H} & Q_{11_H} & 0\\ Q_{11_H} & Q_{22_H} & 0\\ 0 & 0 & Q_{66_H}\end{bmatrix}\begin{bmatrix}\varepsilon_1\\ \varepsilon_2\\ \gamma_{12}\end{bmatrix} \tag{42}$$

$$\begin{aligned} Q_{11_H} &= \frac{E_{11H}}{1-\nu_{12}\nu_{21}} & Q_{22_H} &= \frac{E_{22H}}{1-\nu_{12}\nu_{21}}\\ Q_{12_H} &= \frac{\nu_{21}E_{11H}}{1-\nu_{12}\nu_{21}} & Q_{66_H} &= G_{12H} \end{aligned} \tag{43}$$

$$[\sigma] = [Q_f][\varepsilon]. \tag{44}$$

Then, knowing the mechanical behaviour of a single lamina, it is possible to evaluate the mechanic behaviour of the laminate following the same considerations used in Section 2.2:

$$\begin{aligned} A_{ijf} &= \sum_{k=1}^{N} \left(\overline{Q_{ij}}\right)_{fk} (z_k - z_{k-1})\\ B_{ijf} &= \frac{1}{2}\sum_{k=1}^{N} (\overline{Q_{ij}})_{fk} ({z_k}^2 - {z_{k-1}}^2) \end{aligned} \tag{45}$$

$$D_{ijf} = \frac{1}{3}\sum_{k=1}^{N}\left(\overline{Q_{ij}}\right)_{fk}\left({z_k}^3 - {z_{k-1}}^3\right).$$

The subscript f is used indicate the terms in relation to the hybrid laminae.
It is clear that the approach using the macromechanics of laminate is still valid since hybridisation only affects the equivalent stiffness matrixes of the A, B, C and D elements and are still independent from their position along the thickness of the laminate.

Considering the interply hybrid composite, it is possible to apply the micromechanics of lamina as illustrated in Section 2.2 since a single reinforcement is used within the single lamina. Based on the same concept, the macromechanics of lamina can also be applied as previously illustrated. However, when the mechanical behaviour of the laminate is considered, the approach changes since it is necessary to separate the contribute of the reinforcement with low strain at failure and the one with high strain at failure. Consequently, it is possible to use equations 22 to evaluate the contribute on the stiffness matrix of plies with two different reinforcements as separate entities in the sum operator:

$$\begin{aligned} A_{ijf} &= \sum_{k=1}^{N}\left(\overline{Q_{ij}}\right)_{fk}\left(z_k - z_{k-1}\right) \\ &= \sum_{k=1}^{m}\left(\overline{Q_{ij}}\right)_{1k}\left(z_k - z_{k-1}\right) + \sum_{k=m+1}^{p}\left(\overline{Q_{ij}}\right)_{2k}\left(z_k - z_{k-1}\right); \\ B_{ijf} &= \frac{1}{2}\sum_{k=1}^{N}\left(\overline{Q_{ij}}\right)_{fk}\left({z_k}^2 - {z_{k-1}}^2\right) \\ &= \frac{1}{2}\sum_{k=1}^{m}\left(\overline{Q_{ij}}\right)_{1k}\left({z_k}^2 - {z_{k-1}}^2\right) \\ &\quad + \frac{1}{2}\sum_{k=m+1}^{p}\left(\overline{Q_{ij}}\right)_{2k}\left({z_k}^2 - {z_{k-1}}^2\right) \end{aligned} \tag{46}$$

$$D_{ijf} = \frac{1}{3}\sum_{k=1}^{N}\left(\overline{Q_{ij}}\right)_{fk}\left({z_k}^3 - {z_{k-1}}^3\right)$$

$$= \frac{1}{3}\sum_{k=1}^{m}\left(\overline{Q_{ij}}\right)_{1k}\left({z_k}^3 - {z_{k-1}}^3\right)$$

$$+ \frac{1}{3}\sum_{k=m+1}^{p}\left(\overline{Q_{ij}}\right)_{2k}\left({z_k}^3 - {z_{k-1}}^3\right).$$

The subscript m indicates the number of the layers with first reinforcement ply while p the number of layers with the second reinforcement. Following this approach, it is possible to fully characterise the mechanical behaviour of intraply and interply hybrid composites.

When analysing the failure mechanisms of hybrid composites, it is possible to observe that combining fibres with different mechanical properties can enable the activation of particular set of mechanisms, collectively termed the *hybrid effect* [55, 59]. This consist of the apparent increase in strain at failure of the hybrid structure. At the initial stage of failure, this hybrid effect is mainly controlled by the fracture energy of fibres with a low strain at failure (reinforcement 1) while during the damage propagation, the fibres with high strain at failure (reinforcement 2) control the process [57]. Indeed, when a solicitation is applied on the material, the load is initially born by reinforcement 1 since it is stiffer than reinforcement 2. Therefore, when the stiffer fibres reach their strain at failure and start to break, the structure is still able bear the load since reinforcement 2 is still intact. However, since reinforcement 1 has a lower stiffness than reinforcement 1, a load drop in the characteristic curve is observed (Figure 21). Afterwards, the structure is still able to tolerate load until the maximum strain at failure of reinforcement 2 is reached. This allows to observe a higher strain at failure of the structure when compared with a structure using only reinforcement 1 as a fibrous system.

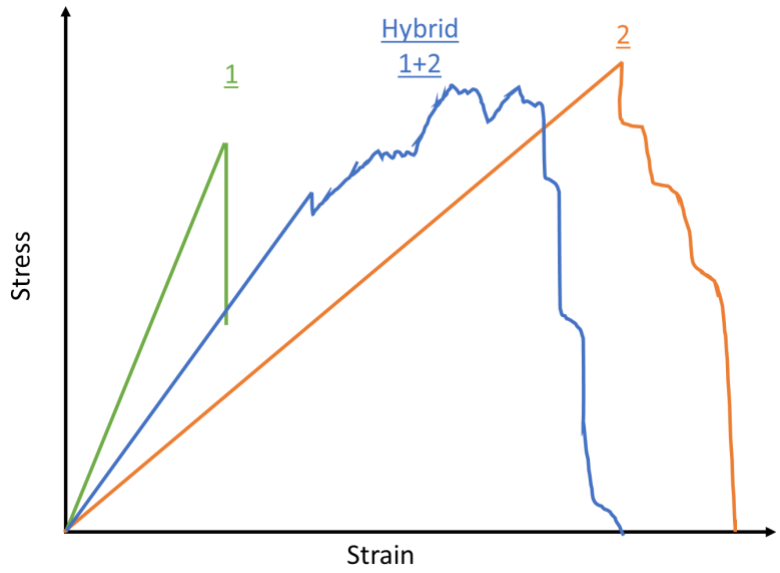

Figure 21-Typical stress-strain curves for composite 1 (low strain) in green, composite 2 (high strain) in orange and their hybrid in blue. Image from [55].

The prevision of maximum strength of the hybrid laminate can be obtained using the formula proposed by Zhang et al. [60] in which it is reported that the hybrid composite reaches failure when either the hybrid laminate or the fibres with higher strain at failure reach the failure condition:

$$\sigma_{Hmax} = max\left[\frac{(E_{f1}t_{f1} + E_{f2}t_{f2})\varepsilon_{f1}}{t_{f1} + t_{f2}}, \frac{E_{f2}t_{f2}\varepsilon_{f2}}{t_{f1} + t_{f2}}\right]. \quad (47)$$

Where σ_{Hmax} is the maximum strength of the hybrid laminate, t_{f1} and t_{f2} are the thickness fractions of the high strain and low-strain reinforcement laminae (1 is the laminate thickness: $t_h=t_{f1}+t_{f2}=1$) and ε_{f1} and ε_{f2} are the strain at failure for the first and second reinforcement fibre.

It is important to observe that hybrid systems are strongly affected by the mechanical characteristics of the fibres. Thus, brittle fibres or plastic fibres have different mechanical behaviours which could substantially change the expected behaviour of the hybrid laminate [52, 53]. Based on this, it is important to analyse the effectiveness of reinforcement hybridisation in improving impact properties by considering several research works which have studied this category of composite materials.

In their extensive review, Safri *et al.* [53] investigated the effect of different typologies of hybrid materials on the impact properties of the structure. Following the description reported in the work, it is possible to identify three categories of hybrid reinforcements based on their origins: synthetic/synthetic (e.g. carbon-glass, Kevlar/glass, Kevlar/carbon), natural/synthetic (e.g. hemp-glass) and natural/natural (e.g. flax-hemp). The work also illustrates that the best performances in terms of impact properties are shown by the synthetic/synthetic hybrid laminates due their higher properties compared to natural fibres.

Following a synthetic/synthetic hybridisation process to obtain the highest mechanical properties, Naik et al. [61] analysed the impact and post-impact properties of glass/carbon hybrid laminates manufactured using different stacking sequences and showed that the mechanical behaviour of the hybrid composites is influenced by the relative position of carbon and glass layers. Specifically, placing the carbon in the outside layers of the laminate resulted in higher mechanical properties, lower notch sensitivity and smaller damaged areas than traditional carbon laminates. This was attributed to the higher mechanical properties of carbon in comparison to glass. Carbon fibres offer a higher stiffness in critical areas such as the top (impact surface) and the bottom (maximum tensile stress) of the laminate while glass fibres promote a higher strain at failure for improved energy absorption [62]. However, the presence of glass increases the total weight of the structure if compared to ones using carbon only.

Synthetic/natural hybridisation has mainly been used to reduce the cost of composite materials whilst preserving high mechanical properties. This typology has been investigated by Sarasini *et al.* [63] who manufactured several configurations of carbon/flax hybrid composites to demonstrate the effectiveness of the hybridisation process in increasing the damage tolerance and, at the same time, increasing the eco-friendliness of this material. It was observed that an improved impact absorption could be obtained by using flax instead of carbon in the external layers of the laminate. This can be attributed to the damping ability of

flax. This can reduce the damage generated into the material by dissipating a higher amount of energy when it is close to the impacted area. However, a limit to the usefulness of natural fibres such as flax is that their presence can cause manufacturing defects in the laminate due to the difficult adhesion between resin and natural fibre surfaces. An additional treatment is, therefore, required to improve the chemical affinity between fibres and resin [64] decreasing the appeal of for these hybrid materials in modern industry.

Natural/natural hybrid composites have shown irregular properties due to the origin and the processing of the fibres' raw materials [53] and have recently have attracted research interest due to their eco-friendly nature and low cost. It is possible to identify many different typologies of natural/natural reinforcements due to the wide availability of local resource necessary to maintain the cost low. Jawaid [65] studied the influence of jute and palm oil fibres in reinforcing epoxy resin and showed a superior mechanical properties when the stronger fibres (jute) are placed on the outer layers of the laminate. However, at this moment, this laminate shows lower mechanical properties than the previous hybrid categories and therefore they have no advanced structural use. However, it is important to underline that the main purpose of this typology of hybrid material is its environmental friendliness and cost reduction. The use of this material could open up the possibility of recycling the structure without any waste or danger to the environment.

To summarise, it is possible to see that these hybridisation approaches offer a valid and effective method for improving impact resistance and energy absorption, however, the drawbacks of weight (synthetic) and inconsistency of properties (synthetic-natural) have, so far, limited their use in advanced applications.

3.2.2 Metal hybridisation

3.2.2.1 General background

Metals can be also used as an additional reinforcement for the design of fibre/metal hybrid laminates and show excellent properties for primary structural

components in advanced applications. However, when coupling metals with fibrous reinforcement and resins it is important to consider the galvanic coupling [66, 67] between the materials. This is critical because corrosion damage can be generated within the structure and it can be a possible cause of catastrophic failure for the entire system. Popular laminated structures have been accepted by aeronautical and aerospace industries including Aramid Reinforced Aluminium Laminate (ARALL) [68, 69] and Glass Laminated Aluminium Reinforced Epoxy (GLARE) [70, 71] (Figure 22). These structures showed remarkable corrosive resistance, fatigue and impact damage tolerance but have higher manufacturing costs than traditional aircraft structures (aluminium only). Another fibre/metal laminated material that is important to mention is Carbon Reinforced Aluminium Laminate (CARALL) which has been studied in several works with promising results [72, 73] however it has limited diffusion due to the aforementioned galvanic coupling between carbon fibres and aluminium [67].

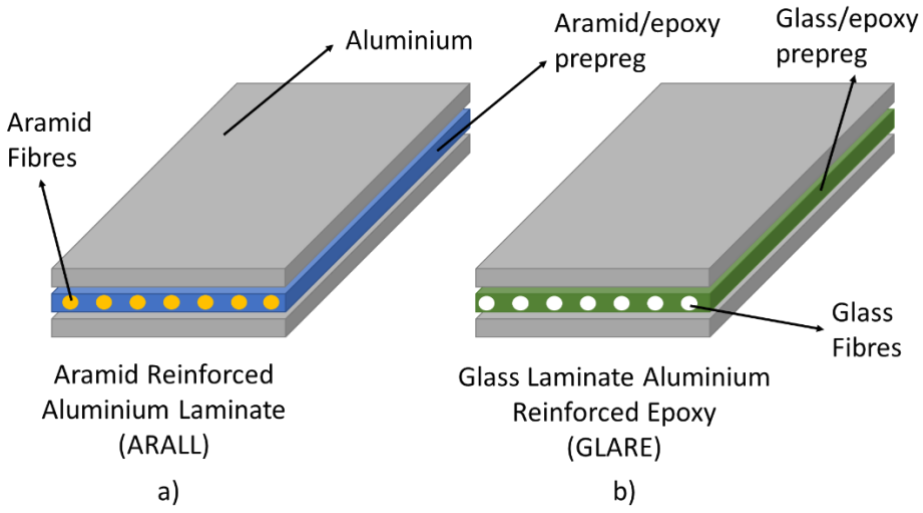

Figure 22- Description of Fibre Metal Laminate (FML) structures.

Another possible metal hybridisation approach to solve the above issues but also promote the activation of additional non-structural features consists of embedding an array of metal wires as secondary reinforcement within a traditional laminate which will be the focus of next paragraph.

3.2.2.2 Analytical description

The descriptions and estimations of mechanical properties of these metal hybrid laminates can be carried out using the same equations and assumptions (equations 41-44, 49) used for interply hybrid composites if the wires are located between the plies, otherwise, the intraply model.

3.2.2.3 Structural benefits: maximum contact force enhancement

One of the first works investigating this hybrid structure was the one published by Bradley *et al.* [74] [75] who studied the modification of mechanical properties to investigate the effective benefits of hybridisation when metal wires are embedded within carbon fibre reinforced laminates. Three configurations of panels were created, wires in the bottom portion of the laminate, wires in the top portion of the laminate and wires in the top and bottom portion of the laminate. Brass-coated steel wires were used. The layout of these samples is reported in Figure 23.

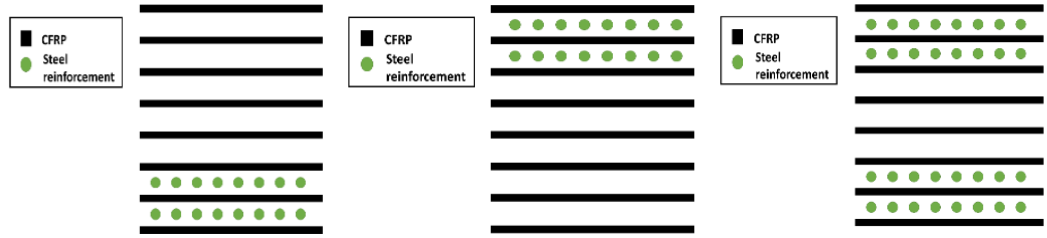

Figure 23-Layout of configuration of the three hybrid samples: a) vf =0.08 (single-surface); b) vf =0.16 (single-surface) and c) vf = 0.25 (double-surface) [74].

Interestingly, results found an improvement in mechanical properties of the hybrid laminate as a function of the positioning of the wires. Interlaminar shear (5-10%), flexural bend strengths (25%) and impact fracture energy (~100%) values all increase when wires were located in the compressive (top) portion of the hybrid laminate. In contrast, when analysing damage propagation using microscopy, samples with the hybrid phase in the tensile (bottom) portion showed a compressive initial failure and complete breakage. No tensile initial failure and no total separation was detected for samples with reinforcement in the compressive part.

Indeed, during impact tests, the introduction of wires in the compressive part of the laminate inhibited or eliminated the compressive mode of failure starting from the contact point. Moreover, other failure processes could take place, including major shear delamination close to the neutral axis or, around the wires' location and ductile failure of the wires themselves. Therefore, an increase of impact proprieties is recorded, and a greater damaged area is identified around the wires' location especially when the wires are placed far from the impact surface. However, even though positive results are obtained using this hybridisation process, the major limitation of this approach is the degradation of the steel wires when coupled with carbon fibres due to galvanic corrosion [76].

Since steel wires are very prone to environmental corrosion when embedded within a laminate, other studies have focussed their attention on the use of Shape Memory Alloys (SMAs) [77] wires as secondary reinforcement due to their corrosion resistance and unique mechanical properties. Such studies analysed their effect on the structural properties when placed on the middle plane of the sample. SMA is an alloy that is characterised by two different phases: a low temperature one with low symmetry termed martensite and a high temperature one with high cell symmetry termed austenite. Thus, a phase-transition temperature T_p can be identified. Martensite can be obtained from austenite through a reversible solid-solid phase transformation induced by temperature, stress and pressure. During this transformation, the properties of the material change significantly with ~75GPa for austenite and ~30GPa for martensite. When stress is applied, the material shows elastic behaviour until a certain value of stress, at which point the stress-induced martensitic transformation is activated producing martensite from austenite.

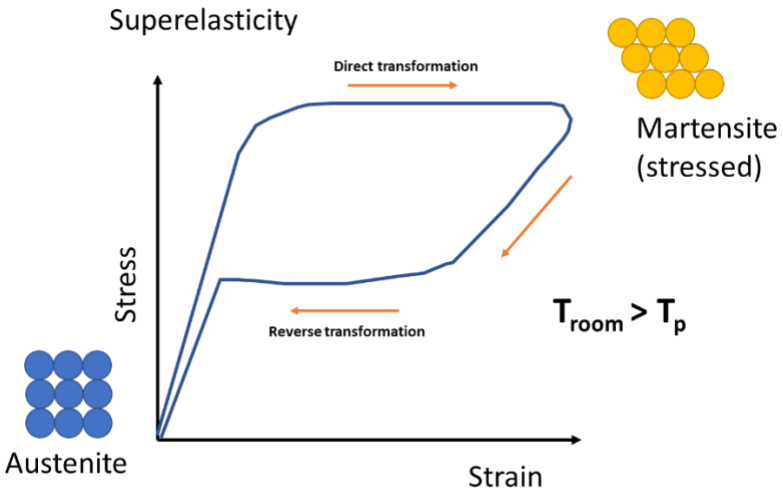

Figure 24-Characteristic curve describing the superelastic behaviour of SMA at room temperature higher than phase-transformation temperature T_p. Orange arrows describes the direction of transformation.

A unique behaviour termed superelasticity is associated with this transformation (Figure 24). Superelasticity involves the production of inelastic strains, the occurrence of a plateau in the stress-strain cure and the occurrence of a plateau in the amount of energy required for the deformation process. Superelasticity [77] is indeed very effective in increasing the impact properties (maximum contact force and absorbed energy) when embedded within a laminate's structure.

Rim et al. [78] investigated the low velocity impact response between Shape Memory Alloy Hybrid Composite (SMAHC) and basalt fibre reinforced polymer, characterising the impact response of hybrid composites and analysing the typology of generated damage. In SMAHC, super-elastic SMA wires were aligned along the centre of the plate, following the schematic layout of manufactured samples is shown in Figure 25:

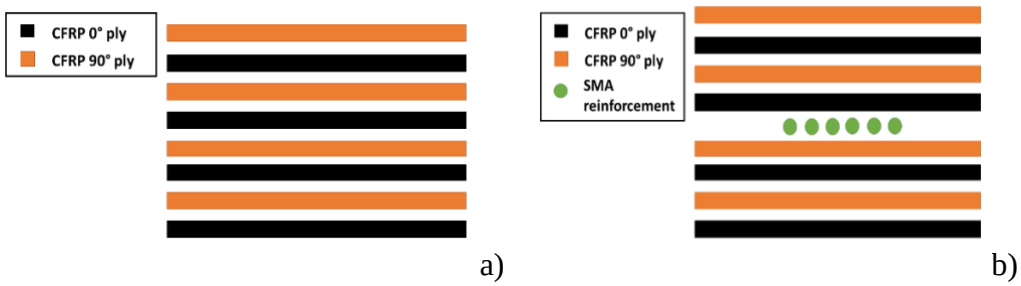

Figure 25-Configurations of samples used by Rim in his experimental campaign; (a) conventional composite plate, (b) SMAHC plate [78].

The results showed that the SMAHC maximum value of contact force was greater than conventional laminates, showing a better behaviour against LVI impacts. This is because SMA wires are able to resist after CFRP fracture and prevent composite plates from damage propagation. Indeed, traditional CFRP clearly shows signs of fracture on the impacted zone while SMAHC presents no signs of fracture. This could be due to the super elastic behaviour of SMA wires, which enables the absorption of larger amounts of impact energy (+7.3%) and avoids severe damage propagation inside the laminates body.

Numerical analyses have been developed to fully understand and optimise the effect of wires on a laminates' mechanical behaviour as reported by Meo et al. [79]. They studied the effect of embedded SMA wires in multi-angle laminates using an LSDYNA code. To develop the FE mesh (Figure 26), solid elements and an orthotropic material with Chang-Chang failure criteria were used.

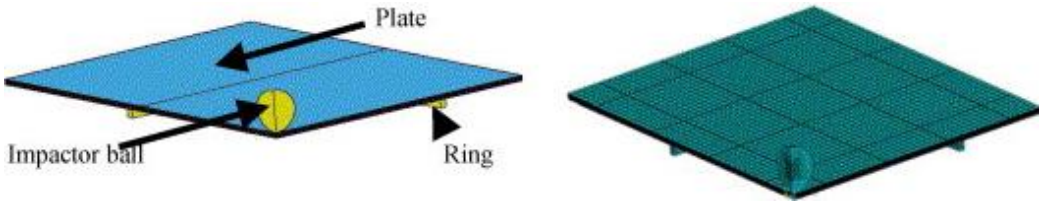

Figure 26-FE model to model impact behaviour of SMCHC [79].

The SMA mechanical properties were simulated implementing the characteristic stress-strain curve of an Ni-Ti alloy (Figure 27) in a special material model available in LSDYNA library that was able to predict the phase transition induced by applied stress [80].

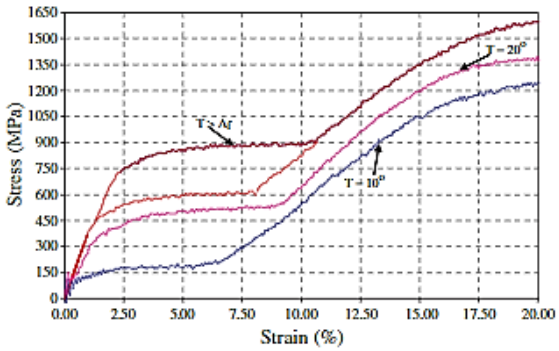

Figure 27-SMA stress-strain curve used to calibrate the material model. The blue curve is obtained at 10°C, the pink one at 20°C and burgundy one at 25°C that is above the temperature (A_f) necessary to guarantee that the structure is all austenitic. The orange curve is the relaxation curve associate with the burgundy one. Image from [79].

Results showed that the presence of SMA was effective in improving the impact response of the laminate, absorbing part of the impact energy during the stress-induced transformation that, otherwise, would be dissipated to create new surfaces (damage). Moreover, it was also observed that the presence of the wires close to the impact surface increased the maximum contact force that the laminate was able to tolerate and significantly reduced the ply failure during the impact event.

3.2.2.4 Non-structural benefits: Structural Health Monitoring, in Situ damage detection and anti-icing

Metal wires enclosed inside the FRP's stacking sequence can not only be used for structural purposes, but also to activate additional non-structural abilities. In particular, the use of the metal reinforcement system can be exploited to set-up a smart network system that enables in-situ Structural Health Monitoring (SHM) for strain sensing [81-83], thermography [84-86], and, anti-icing and de-icing [87]. SHM aims to diagnose the status and the health of the structure and its components throughout its operative life. SHM capabilities can increase the safety of a structure and, using an in-situ smart network avoids the use of external devices during security control and maintenance procedures. A detailed description of each of these additional features is reported in the relative section of Paper A.

Based on this literature review, which has been used as the background of Paper A, the use of metal wires, in particular SMA wires, is an effective solution to improve the impact response of a structure whilst performing SHM and, anti-icing and de-icing procedures with limited use of external devices and tools.

3.2.3 Brick-and-mortar hybridisation

3.2.3.1 General background

Bio-inspired structures also offer an effective solution in improving the impact properties of laminates. More specifically, the toughness of a structure can be greatly improved by mimicking the internal configuration of natural structures as this enables increased energy absorption during an impact event. Indeed, abalone [88], shrimps [89] and mother-of-pearl [90] are just a few examples of biological structures which can be mimicked to create laminates with optimised impact properties. Shells and carapaces, like structural materials, need to be light but at the same time tough to resist predator attacks (or impact events in the case of structural materials). [91]. Generally, a protective shell consists of several layers with different mechanical properties to provide the optimal protection [92]. The outer part of the structure is composed of hardened proteins (mantle) while the inner part is made of a hierarchical structure (nacre). A schematic illustration of the shell structure is reported in Figure 28

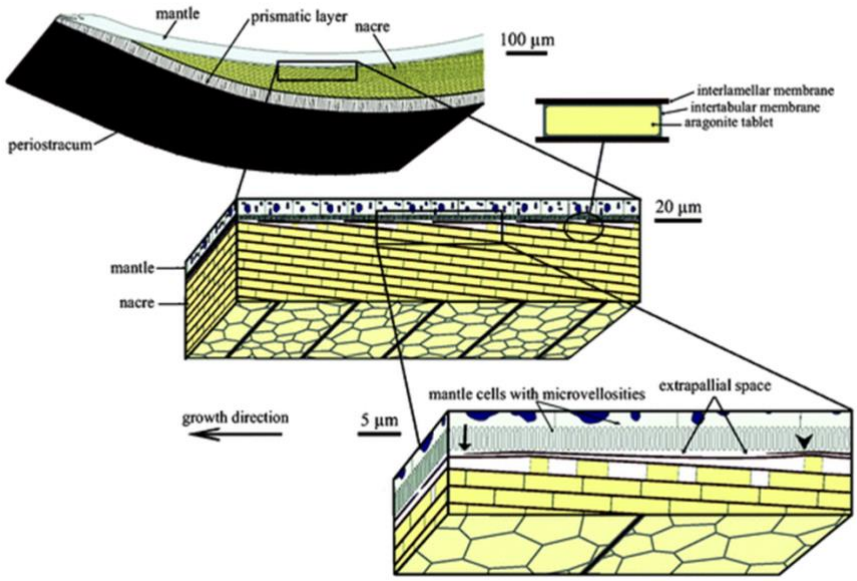

Figure 28-Schematic illustration of the protective shell structure. Image from [92].

The main function of the hard region is to avoid the penetration which occurs as consequence of an impact event whist the nacre functions to provide toughness to the structure, dissipating the impact energy from the interaction via large inelastic strain. The origin of this toughness can be found by analysing the composition of nacre. Nacre is mainly made of brittle aragonite tablets, crystalline forms of calcite $CaCO_3$ (95% of weight) which gives stiffness and stability to the structure and a soft protein-based organic matrix (5% of weight) which holds the aragonite tablets together in a brick-and-mortar structure (from here the hybridisation name). Each aragonite tablet is surrounded by organic matrix which acts as an interface material bonding two adjacent tablets (Figure 29).

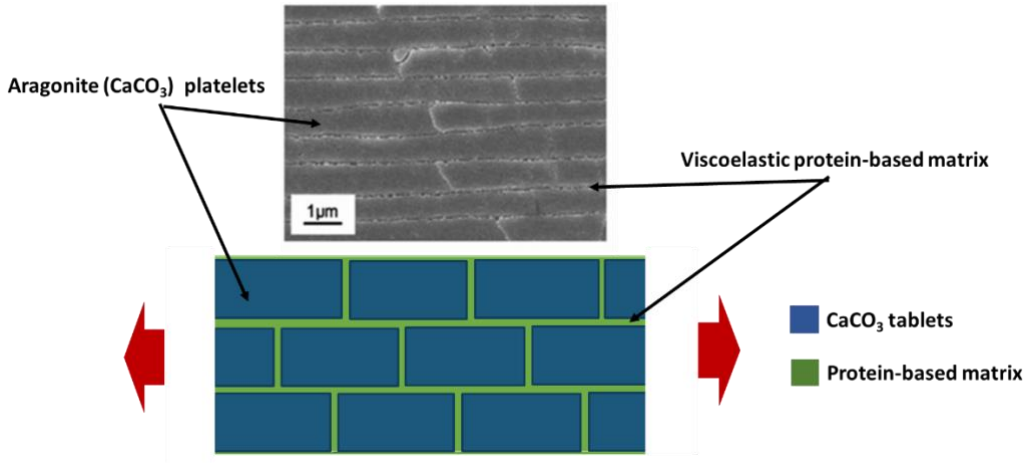

Figure 29- Description of nacre structure: a) image of aragonite tablets glued together by a viscoelastic protein based matrix and b) sketch of the brick-and-mortar configuration of nacre with aragonite table reported in blue and the protein-based matrix reported in green.

This interface plays a very important role during material failure by promoting the activation of several specific mechanisms which increase the strain at failure of the material. Indeed, even if this material is mainly composed of brittle tablets (aragonite) characterised by sudden failure at relatively small strains, it is observed that the structure is able to undergo high deformation, recording a fracture toughness that is nine times bigger than the one of monolithic aragonite [93]. This behaviour is called *pseudoplasticity* and is shown as a plateau in the characteristic stress-strain curve of the biological material. Several research works have studied the toughening mechanisms which are responsible for this pseudoplastic behaviour including tablet pull-out [88], organic matrix bridging [92], plastic deformation at the crack tip [94] and crack deflection [95]. Crack deflection [96] (Figure 30) is the mechanism which is considered to play the critical role in increasing toughness due to the creation of multiple cracks during damage propagation within the structure. When a load is applied, the crack initiates from the soft area between two adjacent plies and starts to propagate along the thickness of the material. The crack has difficulties propagating throughout the aragonite tablet since its fracture toughness is higher than the organic matrix (organic glue). Thus, the crack prefers to propagate by generating surfaces along the interface between the aragonite tablets ($CaCO_3$ bricks) in a zig-zag path (Figure 30).

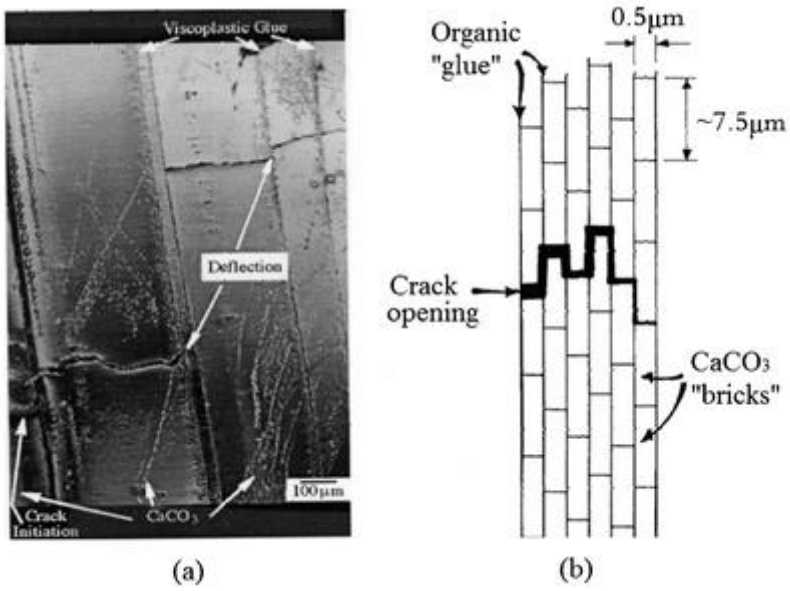

Figure 30-Crack deflection mechanism in nacre: a) micrography of nacre structure during failure and b) schematisation of the failure mechanism. Images from [92].

This phenomenon has been demonstrated by Song et al. [96] who observed no failure of an aragonite tile during a three point bending flexural test, with the propagation of a main crack from the tensile region into the compressive one through the development of branched cracks and secondary small cracks generated along the main crack surface.

Consequently, as reported from the mechanics of fracture [97], the creation of new surfaces requires a certain amount of energy which is proportional to its area. Considering the crack as the profile of this new surface, the longer the crack path, the higher the amount of energy necessary to generate the new areas. Thus, comparing the failure mechanisms of nacre with monolithic aragonite, nacre is able to absorb more energy than monolithic aragonite due to the tortuous path of the main crack propagation and the generation of numerous and small branched secondary cracks shown in Figure 31. In fact, monolithic aragonite does not show multiple cracks but only a single one, as expected for ceramic brittle materials. On the contrary, no brittle failure is shown by the nacre structure.

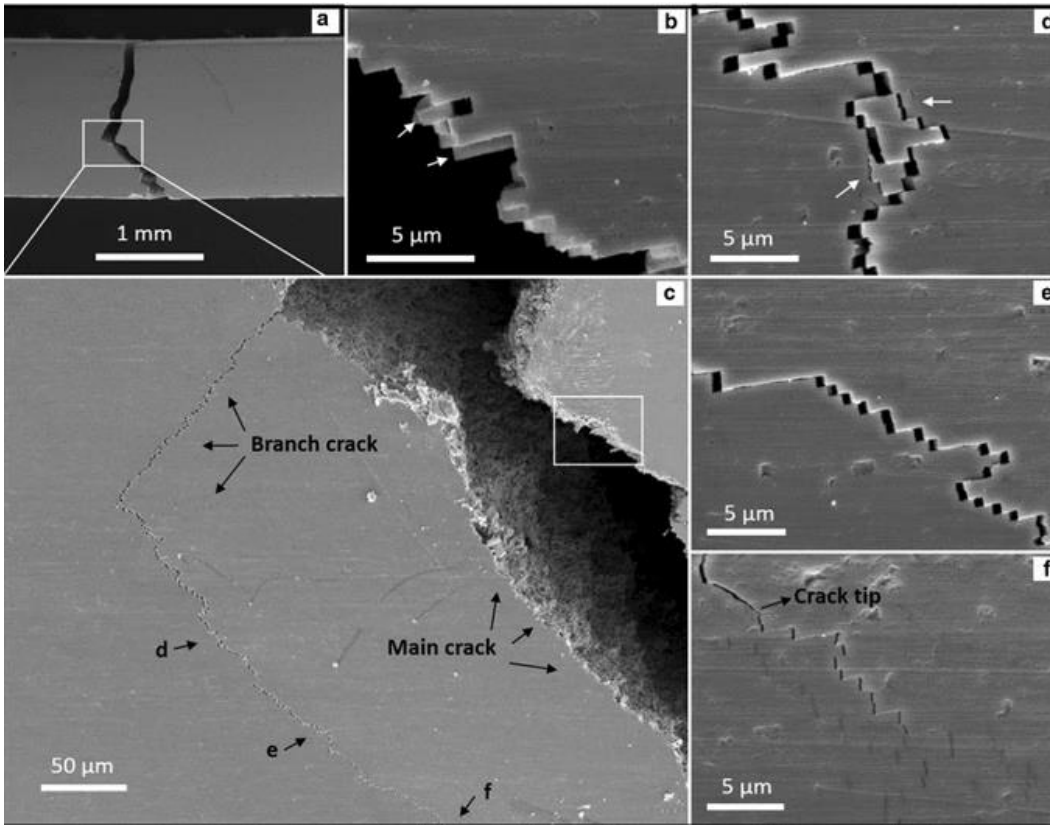

Figure 31-Crack propagation and profile morphology in nacre structure at three different magnitudes: a) an overview of the crack profile, b) the magnitude of the white box showing no fracture of aragonite tablet, c) branch crack investigation along the main crack path. D, e and f) several magnitudes examined at different region along the main crack profile. Images from [96].

Another toughening mechanism which plays an important role during the failure of this biological structure is the *pull-out of the tablets*. This mechanism consists of the relative displacement of adjacent aragonite tablets after the failure of the organic matrix at the interface. The sliding of the tablets between each other aids the system to dissipate a larger amount of energy via the friction generated between the tablets' surface [93]. The higher the number of sliding surfaces, the higher the energy dissipated via friction.

To exploit the advantages of a hierarchical brick-and-mortar structure, researchers have studied several approaches to replicate it using composite materials which mimick the failure mechanisms that promote pseudoplasticity in nacre.

Such approaches have produced laminated composite materials which have shown plasticity and enhanced toughness. It is important to highlight that such a replication process is highly complex since natural structures can adapt during the life of the organism, which is of course, not possible if composite materials are involved. This is a crucial point for bioinspired materials and consequently, only part of the promising potential of the biological structure can be exploited to increase the impact properties of composite materials. Therefore, only specific pseudo-plastic failure mechanisms can be reproduced in hierarchical composite material.

3.2.3.2 Analytical description

The introduction of discontinuities can be considered as reinforcement hybridisation since resin is introduced as a secondary reinforcement aiming not to increase the properties but to activate the pseudoplastic mechanism for the enhancement of toughness with minimal loss of in-plane mechanical properties. In-plane mechanical properties of a single lamina can be estimated using the equations of shear-lag theory [98] reported by Laspalas *et al.* [99] and Zak *et al.* [100] assuming that the discontinuous fibres are aligned (this theory is also reported in Paper B-4 Chapter):

$$E_c' = k_e E_f V_f + E_m V_m$$
$$k_e = 1 - \frac{\tanh(\eta\zeta)}{\eta\zeta} \quad (48)$$

where:

$$\eta = \sqrt{\frac{E_m}{\theta(1+\nu_m)}} \quad (49)$$

$$\theta = E_f \ln\left(0.42\sqrt{V_f}\right) \quad (50)$$

$$\zeta = \frac{l}{d_f}. \quad (51)$$

where k_e and k_s are fibre-length correction coefficients which take into account the discontinuous fibres in function of the unit cell length, l is the length of the fibres and d_f is the fibres average diameter. The other mechanical properties such as E_{22},

G_{12} and ν_{12} can still be estimated using micromechanics equations since the presence of discontinuous fibres is not reported to influence these properties. These properties can then be used in the Classic Lamination Theory to describe the elastic behaviour of lamina and laminate. The traditional approach used in 3 Chapter for conventional lamina and laminate is still valid for these materials. However, their failure model cannot be described using the conventional theory and a theory extension is required.

Following this concept, Narducci *et al*. [101] studied an analytical model for the prediction of the failure behaviour of bioinspired structures replicating nacre configuration within CFRP. A numerical model is also available in this study and is discussed in the next section (Section 3.2.2.3).
The design used to replicate the nacre structure in the CFRP system was obtained by introducing an hourglass-shaped defect within the single ply using a laser cut machine (Figure 32). To create the hierarchical pattern along the thickness of the laminate, the entire pattern was shifted by half a length of the cut along the fibre direction.

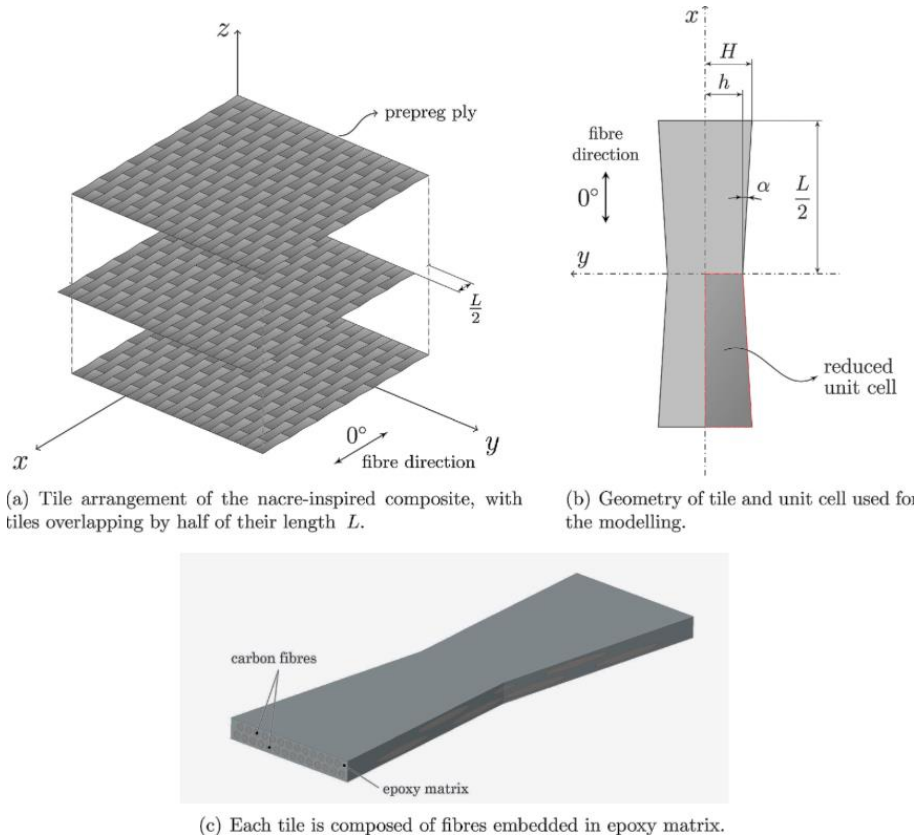

(a) Tile arrangement of the nacre-inspired composite, with tiles overlapping by half of their length L.

(b) Geometry of tile and unit cell used for the modelling.

(c) Each tile is composed of fibres embedded in epoxy matrix.

Figure 32-Design of bioinspired microstructure: a) organisation of tiles, detail of the single tile and c) organisation of fibres and matrix. Image from [101].

The shape and size of the single tablet was designed to avoid failure under the applied load and at the same time to increase the dissipated energy via friction of the tile when pull-out occurs. The dimensional parameters for the tablets design were calculated using the equations reported by Pimenta *et al.* [102] which use a modified Weibull distribution to take into account the probability of failure of the tablet in function of its length (Figure 33):

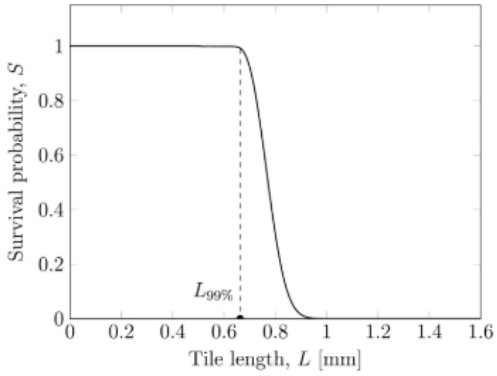

Figure 33-Probability of tile failure in function of the table length. The 99% of survival for the table is marked. Image from [102].

After the resin surrounding the tablets starts to fail, tablets start to move from their position sliding one upon another. Using the equation (52) and considering the frictional shear stress τ_f, frictional coefficient of the tablet μ, its transversal modulus E_y and the stress required for the pull-out σ, it is possible to evaluate the stress-strain relationship during the pull-out σ_P:

$$\sigma_P(\varepsilon) \cong c(\mu, \varepsilon)E_y + \tau_f \frac{L}{2t}(1 - \varepsilon) \quad (52)$$

where t is the thickness of the ply, L is the length of the tile and c is a constant function of friction and the applied strain. Consequently, the energy associated with the pull-out process E_P due to the friction can be calculated using the equation 56:

$$E_P \cong \int_0^{\varepsilon_{max}} \sigma_P(\varepsilon)\, d\varepsilon \quad (53)$$

Where ε_{max} is the maximum strain recorded in the process. A numerical model was developed and validated using these analytical equations. Good correlation was found between numerical and analytical data. Afterwards, the numerical model was used as support tool to design and manufacture different configurations of bioinspired CFRP structures with different tablet lengths, and their performance were evaluated using three-point bending tests. Results confirmed that the presence of the discontinuities promoted the well-known crack deflection mechanisms in the CFRP structure that, together with pull-out and frictional effects, is able to increase the amount of energy absorbed by the structure. Moreover, no catastrophic failure is reported during the tests with no presence of sudden collapse. It is important to

notice that since a unidirectional layup was used to create this bio inspired material, there is no information available to evaluate its performance when applied to multiangle laminated materials. Moreover, this approach involves the use of laser-cut which can damage the material and create zones with irregular properties due to the high temperature reached during the operation. This generates areas partially cured and forms an additional weaker interface with the matrix after curing. This leads to lower fracture properties and a reduction of the resistance of the material when used for advanced structures subjected to impact loading.

3.2.3.3 Structural benefits: toughness enhancement

Experimental studies on the replication of nacre structures within laminates systems such as CFRP was carried out by Malkin et al. [103] who introduced on the single plies of a CFRP laminate a series of discontinuities in order to create a brick -and-mortar structure which used carbon fibres as hard tiles and the resin as organic matrix. These discontinuities were introduced in CFRP beams by cutting the single plies along the width at different positions to layup the structure using different patterns. The design of these structures is reported in Figure 34:

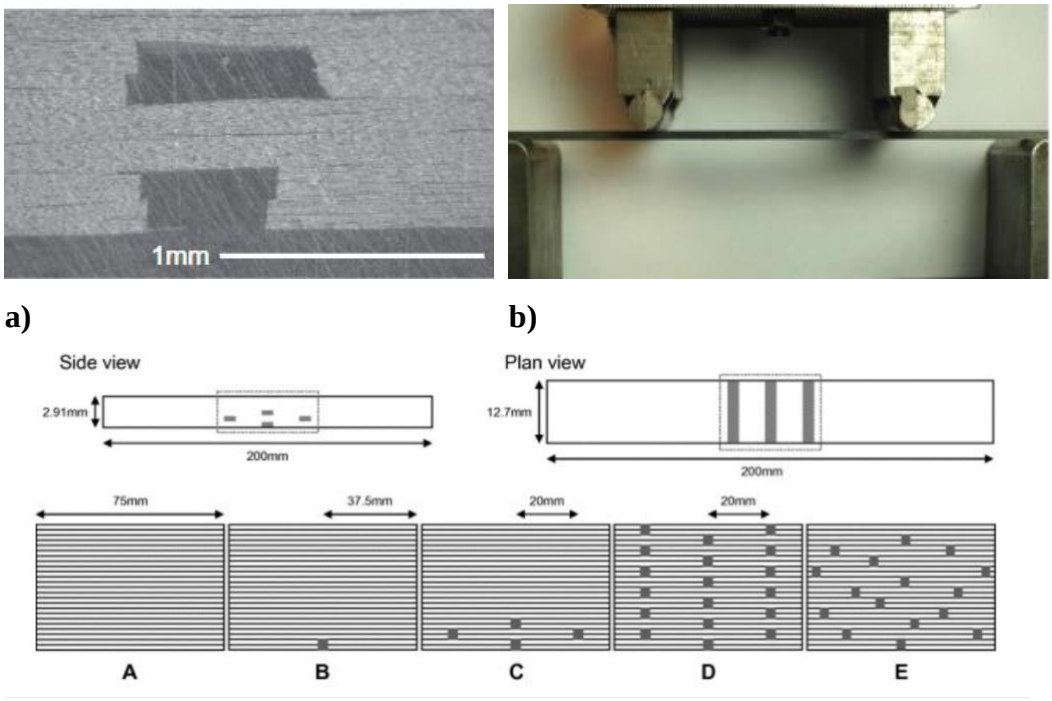

Figure 34-Design of hierarchical CFRP used in the four-point bending testing with five different designs: a) micrograph of surface and internal ply cut, b) CFRP beam during test and c) schematisation of the different configurations. Images from [103].

The effect of these patterns was then evaluated using four-point bending tests and the results showed that the presence of the discontinuities promoted a progressive failure behaviour in CFRP which typically shows a brittle behaviour with a sudden and catastrophic failure. Additionally, they demonstrated that the intensity of stress localisation around the discontinuity was proportional to the spacing between discontinuities with higher stress for smaller spacing. This was also evaluated using a numerical model for a better understanding of the stress distribution. Moreover, they found that the presence of the discontinuity enabled the avoidance of the generation of large delamination across the length of the sample but, instead, the crack propagated across the laminate's thickness via the generation of delamination from one discontinuity to another (see Figure 35.v). This enables the crack to "jump" from one layer to another following the pattern of discontinuities and creating a zig-zag shaped damage (Figure 35.vi) within the laminate. This zig-zag

pattern is not identified in areas where no pattern of discontinuities is introduced, observing an extended delaminated area, typical of traditional laminates.

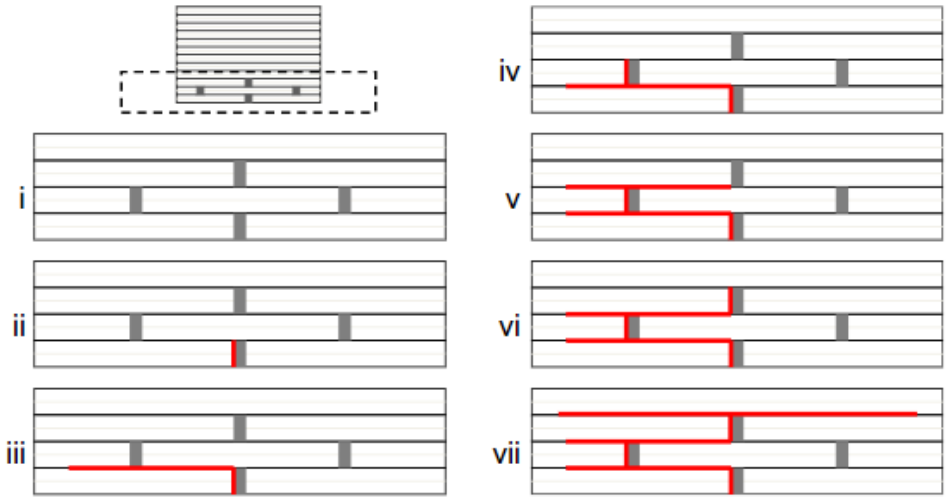

Figure 35-Progressive failure of the hierarchical CFRP structure when an increasing displacement is applied on the sample. Images from [103].

The delamination cannot propagate freely along the length of the sample, but instead, it is forced to follow the predetermined pattern of discontinuities which can be tuned in order to maximise the energy used to generate damage. By increasing the number of discontinuities, the pseudoplastic effect is amplified. Despite these promising results, researchers also found a significant reduction of mechanical properties in comparison to tradition CFRP due to the shortening of the reinforcement.

Based on these experimental results, it is possible to observe the effectiveness of this hybridisation approach in increasing the toughness of the system. Numerical modelling using Finite Element Analysis (FEA) has also been shown to be effective in the prediction of this increase of impact property. In particular, Gu *et al.* [104] designed and manufactured 3D printed laminates using two different photopolymers; a hard one (Stratasys Veromagenta®) to replicate the nacre aragonite tablet and a soft one (Stratasys ® TangoBlackPlus®) for mimicking the

organic interface matrix (Figure 36). These laminates were designed following a cross-ply lamination sequence.

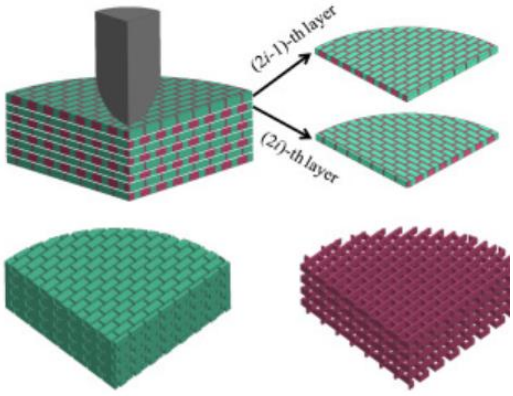

Figure 36-Bioinspired nacre structure design. Hard (green) and soft (magenta) materials are indicated to create the brick-and-mortar structure. Image from [104]

Impact characterisation was carried out using a drop tower impact machine using a weight of 5.5kg and a hemispherical steel head and a numerical model was developed and validated using the experimental impact data to provide information about the stress distribution during the impact event. Comparing the obtained results with those from a monolithic material used as reference, it is evident that the nacre composite can absorb a higher amount of energy (~25%). The monolithic material showed residual velocity after the impact, which meant that the impacting object had perforated the structure. On the contrary, in the case of the nacre structure, the final velocity of the impact object was almost zero, proving that the presence of discontinuities enabled the promotion of all the aforementioned toughening mechanisms typical of nacre systems, which dissipated all the impact energy. Indeed, the crack propagates along the interface between the hard components in a zig-zag path which increases the energy required to generate new surfaces in comparison to a monolithic material. Analysing also the Von Mises stress in the bioinspired structure, crack initialization is localised in the bottom of the sample and propagates towards the surface where the impact takes place. For the monolithic material instead, the failure occurs suddenly reporting the perforation of the structure.

Thus, following the results of these research works, it is possible to increase the strain at failure and toughness of a structure by introducing a regular and organised pattern of discontinuities within the CFRP plies to replicate the brick-and-mortar structure of nacre by enabling its special failure mechanisms.

3.2.3.4 Non-structural benefits: drapability

Besides the structural benefits that hybridisation is able provide to the composite laminated structure, enhanced drapability is an additional benefit activated by this technique. Drapability is the ability of an uncured material to adapt its shape to a mould used during the lamination process. If the mould geometry is complex with small angles and double curvatures, the lay-up procedure can be difficult and not always possible due to the high stiffness of the fibre components. Consequently, it is necessary to increase the drapability of the material to guarantee its forming in advanced shape and profiles used in top-tier industries.

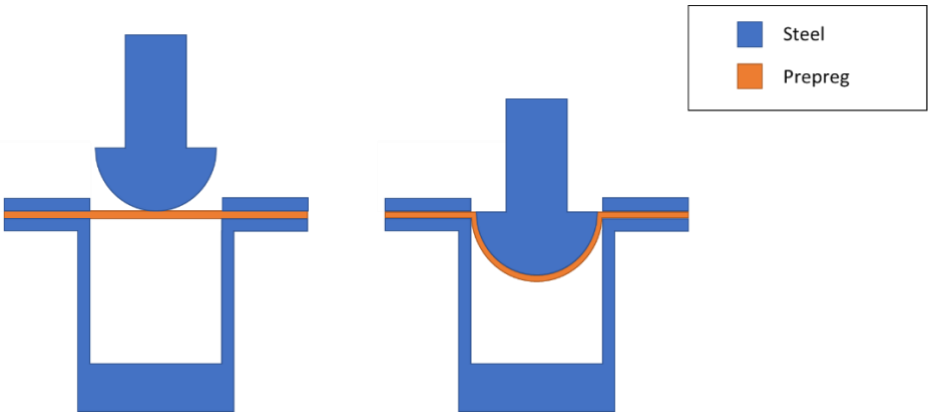

Figure 37- Sketch of prepreg forming using a double-curvature geometry: the steel structure (blue) is used to clamp the prepreg (orange).

Tsuji and Springer [105] showed that the presence of discontinuous fibres increases the potentiality of the uncured material to adapt to complex geometries. They investigated this property by analysing the tip deflection of continuous and discontinuous (uncured) fibre reinforced polymer (Figure 37) and defined the drapability of the discontinuous material as the ratio:

$$\mathfrak{D} = \frac{\delta}{\delta^{\infty}} \tag{54}$$

where δ and δ^{∞} are the deflection for the discontinuous and continuous materials respectively.

Drapability can be influenced by several parameters including fibre length and diameter, fibre alignment, fibre volume fraction and fibre and matrix properties. The deflections of the two typologies of fibre reinforced polymer were experimentally tested using a single cantilever beam test in which the FRP beam was fixed on one end and a displacement was applied on the other. An important parameter considered during this analysis was the ratio between fibre length *l* and fibre diameter *d*.

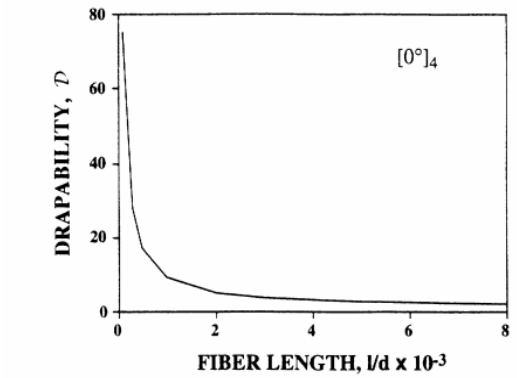

Figure 38-Dependency of drapability on several properties: fibre length, Images from [105].

As it is possible to observe from Figure 38, drapability increases as fibre length is reduced. This can be attributed to the presence of more discontinuities within the laminate for small fibre length, leading to a higher relative displacement between the fibres which allows the structure to adapt its shape to the applied load.

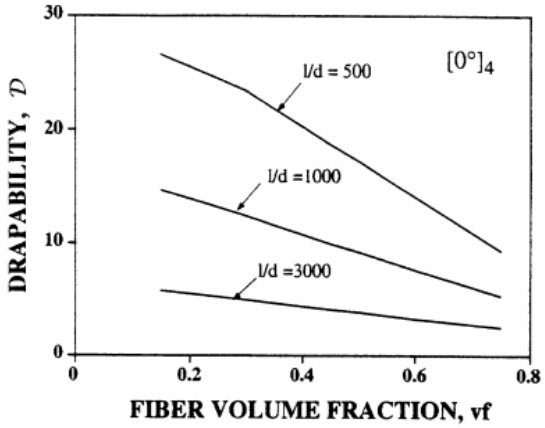

Figure 39-Dependency of drapability on several properties: fibre volume fraction. Images from [105].

Similarly, fibre volume fraction length has a substantial effect on drapability (Figure 39) since its reduction increases the drapability of the material. This is due to the additional space that fibres have available within the matrix, which enables them to adapt more easily to the displacement applied.

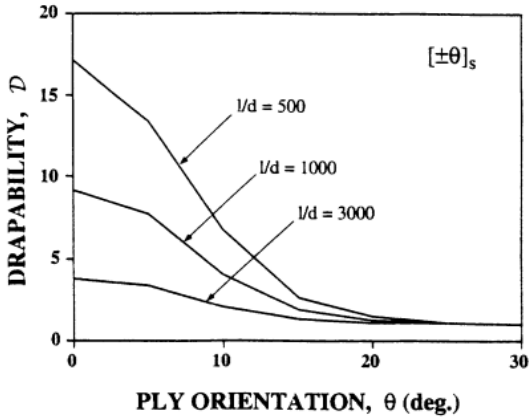

Figure 40-Dependency of drapability on several properties: ply orientation. Images from [105].

It is important to note that this effect is also dependent on the ratio l/d, as an increase of drapability decreases the ratio due to the increasing number of discontinuities.
In Figure 40, it is possible to observe the effect of ply orientation on drapability which decreases with increasing ply orientation with a plateau from ~20° to 30°.

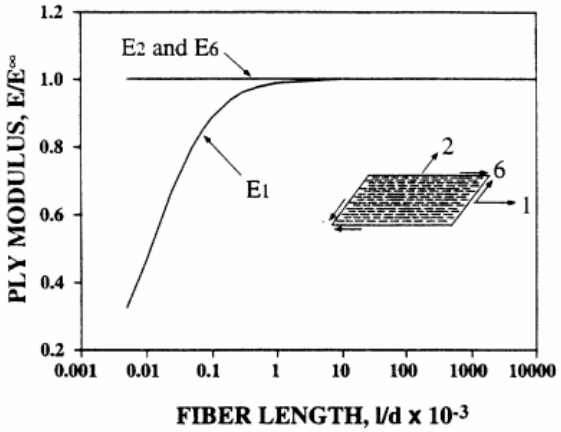

Figure 41- Dependency of elastic modulus from fibre length. Images from [105].

Figure 41 shows how fibre length (or the ration l/d) influences the elastic moduli E_1, E_2 and G_{12} of the ply when discontinuities are introduced using the ratio between the elastic moduli of discontinuous (E) and continuous (E_∞) laminae. E_{22} and G_{12} show a constant trend in function of the fibre length, meaning that these properties are not affected when discontinuous fibres are used to reinforce the lamina. Longitudinal modulus instead shows low modulus when low fibre length is used since the fibre length is too small to bear any load. The modulus increases its value linearly with fibre length until the critical length l_c (see 1 Chapter is reached and a plateau is identified meaning that the reinforcement can totally bear load.

As presented throughout this literature review, the introduction of a pattern of discontinuities within the fibrous reinforcement of the laminated material is an effective method to improve the toughness and drapability of the laminated composite material. This literature review can be fully integrated with the descriptions and methods reported in Paper B in 4 Chapter.

3.2.4 Protective polymeric layer hybridisation

3.2.4.1 General background

Another important impact property to consider is the damage resistance of the laminate, which is fundamental to increasing the reliability and safety of the

material. As shown in 2 Chapter where the failure criteria and damage morphology of laminated composites under impact loading are analysed, the presence of damage greatly affects the mechanical properties. Thus, the reduction of its extent represents an important step-up in the development of composite laminated materials. This can be carried out by hybridising the structure via the introduction of a layer of elastomeric materials within the lamination sequence. This mitigates the impact damage generation within the laminate via the improvement of the damping ability of the material.

In this context, Thermoplastic Polyurethane (TPU) is particularly important. TPU is a multi-block copolymer whose main chains are linked together by urethane bonds. The chains are composed of alternated crystallised hard blocks (di-isocyanate) and amorphous soft ones (polyol). Since the two typologies of blocks are thermodynamically incompatible due to the polarity of hard blocks and the non-polarity of soft ones [106], a microphase separation is observed, despite the fact that the chains are connected by covalent bonds and hydrogen cross-bonds between the lateral group of soft chains. As a consequence of the configuration of these bonds, the polymer is organised into an entangled macromolecular system, as shown in Figure 42 in which the hard blocks are free to move independently from the soft ones.

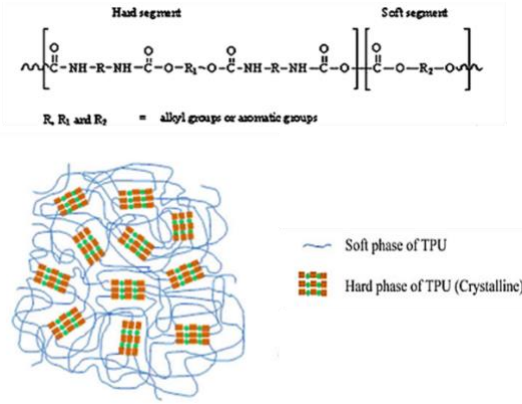

Figure 42-Thermoplastic Polyurethane (TPU) formulation and molecular representation. Images from [107, 108].

The mechanical properties of TPU are strictly related to this organisation and modifying several parameters such as the hard segment content [109], number of NCO (isoctanate) and OH (hydroxil) groups [110], chain extenders [106] and diisocyanate typology [111], it is possible to tune the polymer properties in function of the required applications. In this context, one of the most important mechanical property that characterises TPU is damping [112]. Damping is a material property which quantifies the ability of a system to attenuate, restrict or prevent its oscillations. Generally, this property is evaluated using a Dynamic Mechanical Analysis (DMA) test to measure the complex modulus E* which can be defined as a combination of storage modulus E' and loss modulus E''. Using the loss factor (tanδ) defined as the ratio between the two moduli, it is possible to estimate the ability of the material to dissipate applied oscillations:

$$E^* = E' + iE'' \tag{55}$$

$$tan\delta = \frac{E''}{E'} \tag{56}$$

Microscopically, when a load is applied, the polymer chains tend to organise themselves to adapt towards this new configuration. Since the hard and soft blocks are organised in two separated phases, a relative displacement is involved in the adaptation process with significant friction between the components. Consequently, the higher the movement of the chains, the higher the friction involved, and the energy dissipated via heat generation.

3.2.4.2 Analytical description

The correlation between microstructure and damping was evaluated by Weibo et al [113] who observed that damping of TPU is influenced by the crosslink density of the polymer. Crosslink density is defined as the density of the connections between two different chains in a polymer network and is controlled by the ratio between the NCO and OH groups present within the polymer composition. The higher this ratio, the higher the crosslink density and consequently, the higher the motion resistance of hard segments. Therefore, at high values of crosslink density, a lower damping effect is observed because the relative

displacement between the chains is low. In contrast, for low values of crosslink density, the recorded damping is higher because the hard blocks can move more easily from their initial position leading to a higher relative displacement and a consequent increase of dissipated energy (due to friction). It is important to notice that crosslink density also affects the stiffness and strength of the elastomer and low values can compromise its structural performance (as explained in the following constitutive model). It is possible to describe the mechanical behaviour of the TPU and its associated viscoelastic response due to damping by using the constitutive model used by Qi *et al.* [114]. According to this work, the time-dependent hyperelastic (non-linear elasticity) plastic mechanical behaviour of this material can be separated into two components: the time-independent equilibrium path and the time-dependent out-of-equilibrium path. The first is the main elastic component that thermodynamically considers the decrease of entropy of soft chains as a consequence of their orientation during very slow loading (state of equilibrium). The second, represents the variation in internal energy due to the deformation of the hard blocks and their interaction with soft chains. The viscoelastic effect is also included in these terms mainly generated by frictional effects between the hard and soft components of the polymer. It is possible to represent this in a schematised 1D constitutive model (Figure 43) where the equilibrium behaviour is modelled using a hyperelastic rubbery spring which is able to describe the variation in the entropy of the polymer's chains. In parallel with this element, a series of springs and a viscous dashpots are used to model the viscoelastic-plastic behaviour of the material. The elastic spring characterises the initial elastic contribute related to the internal energy variation while the nonlinear viscoelastic behaviour is modelled using the dashpot which can represent the rate-dependent and temperature-dependent behaviour. Since the hyperplastic spring and the spring-dashpot component are in parallel, they undergo the same displacement.

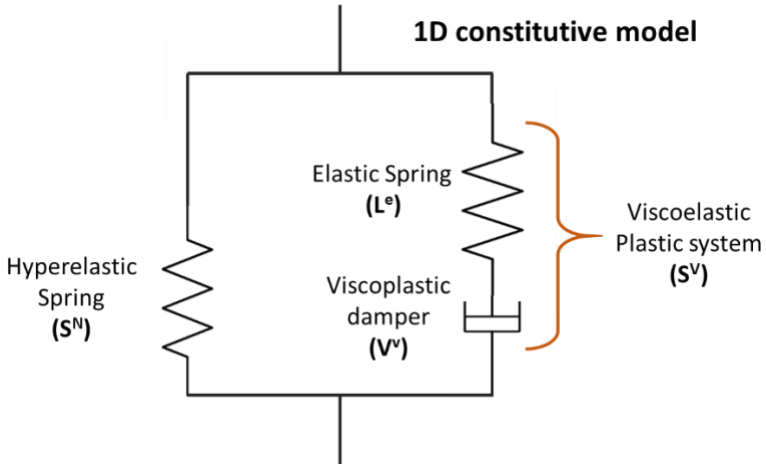

Figure 43-Schematisation of the 1D constitutive model of TPU. Image from [114].

Consequently, it is possible to write equation 57:

$$\boldsymbol{F^N = F^V = F} \tag{57}$$

where $\mathbf{F_N}$ is the deformation gradient of the hyperelastic component, $\mathbf{F_V}$ is the deformation gradient of the viscoelastic-plastic component and **F** is the macroscopic deformation gradient. The total Cauchy stress **S** applied on the material is described by the formula:

$$\boldsymbol{S^N + S^V = S} \tag{58}$$

where $\mathbf{S_N}$ is the stress associated with the hyperelastic component while $\mathbf{S_T}$ is the one associated with the viscoelastic plastic one.

The term $\mathbf{S_N}$ can be expressed using equation 59 and following the Arruda-Boyce eight-chain model [114-116]

$$\boldsymbol{S^N} \propto v_s\sqrt{N}\,\boldsymbol{B} \tag{59}$$

where v_s is the soft chains relative volume, $\boldsymbol{B}$ takes into account the elastic deformation of the elastomer and N is the number of crosslinks

It is possible to characterise the viscoelastic plastic component $\mathbf{S_V}$ following equation 60 [114] considering the elastic $\boldsymbol{V^{Ve}}$ and viscoplastic $\boldsymbol{V^{Vv}}$ components:

$$\boldsymbol{S^V = S^{Ve}S^{Vv}} \propto v_h \boldsymbol{L^e}[ln\boldsymbol{V^V}] \tag{60}$$

where v_h is the effective volumetric fraction of hard domains, $\mathbf{L_e}$ considers the elastic stiffness of the viscoelastic plastic component while $\mathbf{V_V}$ takes into account

the deformation gradient of the visco-plastic component. Boyce *et al.* [117] described this using equation 61 as a function of the visco-plastic shear strain $\dot{\gamma}^v$:

$$\boldsymbol{V}^V \propto \frac{\dot{\gamma}^v}{\sqrt{2\tau_v}}. \tag{61}$$

where τ_v is the equivalent shear stress for the time-independent path. The viscoplastic shear strain of the viscoelastic component is described by the formula:

$$\dot{\gamma}^v = \dot{\gamma_0} e^{\left[-\frac{\Delta G}{k\theta}\left\{1-\left(\frac{\tau_v}{s}\right)\right\}\right]} \tag{62}$$

where $\dot{\gamma_0}$ is a factor proportional to the attempt frequency, ΔG is the energy necessary to activate the process the process at zero stress level, k is the Boltzmann's constant, θ is the absolute temperature and s is the temperature-independent shear strength. Based on this description, it is possible to observe that when a load is applied very slowly, the stress on the material is evaluated by only considering the hyperelastic component. This is because the material has the time to adapt to the deformation following states of equilibrium and is able to reach very high strains. When instead a load is applied at a certain rate, the combination of the hyper elastic and viscoelastic plastic component must be used to describe the stress distribution of the material. It is important to note that in the viscoelastic contribute, the strain rate and thermal dependency are included in the non-equilibrium term described by equation 62. Analysing the dependence of the material on the TPU composition, it is possible to estimate the effect of crosslink density on the equilibrium hyperelastic stress. The higher the density of crosslinks, the higher the stress in the material, meaning a higher stiffness at the same displacement, as is possible to see from equation 59. Similarly, the presence of the hard chains (equation 59) affects the viscoelastic properties of the material, and thus, its damping ability. This is because the higher the volume fraction, the more friction is generated between the hard and soft chains and consequently, the higher the quantity of energy dissipated.

It is clear then that the use of TPU can be beneficial in all applications where impact resistance is important due to the high damping that it is able to provide as seen from the constitutive model. The effect of TPU on impact resistance and the

improvement of the impact behaviour of the laminate when TPU is introduced within the lamination sequence is analysed in detail in the relative manuscript (6 Chapter). The mechanical properties of a hybrid TPU/FRP laminate can be estimated using the micromechanics of the lamina and considering the layer of TPU as a viscoelastic plastic material when it is used as a matrix for the composite material. In contrast, if it is used within the lamination sequence, the layer can be considered isotropic and, the approach described in 2 Chapter can be used.

3.2.4.3 Structural benefits: damage mitigation

The application of TPU to hybridise composite structures can be carried out as suggested by Miller *et al*, [118] who used the TPU polymer as an interleaved component in a cross-ply laminated structure for a fan blade leading edge. The TPU layer was placed at the interface between 0°/90° carbon plies (Figure 44) to maximise the effect of TPU hybridisation within the location of maximum stress. Two different TPU areal weights were used to manufacture the hybrid laminates: 15 g/m2 and 45 g/m2.

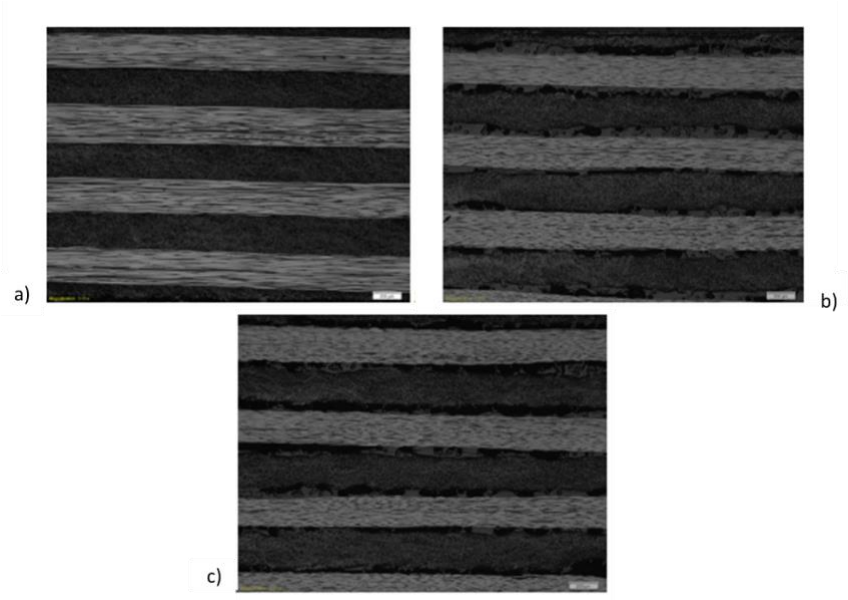

Figure 44-Cross section analysed using optical microscopy: a) traditional laminate and b) 15 g/m2 TPU laminate and c) 45 g/m2 TPU laminate. Images from [118].

From this figure, it is possible to evaluate voids at the interface between the two carbon plies. An increase of interface thickness for the TPU cases of 15 g/m2 and 45 g/m2 is also observed. Static and impact tests were carried out on traditional and hybrid structures to characterise the material and evaluate its performance. Results showed a reduction in compression and tensile properties such as stiffness and strength. This was due to the low stiffness of TPU and the presence of voids within the laminate. However, an increase of interlaminar toughness was found when TPU was introduced within the laminate structure. Impact resistance was also significantly improved as evidenced by the reduction of damaged area for the TPU hybrid laminate in comparison to traditional laminate.

Russo *et al. [119]* used glass fabrics to reinforce TPU and this was used as a matrix for laminated composite materials. The material was then tested under Low Velocity impact conditions to prove the potentiality of this material at different thicknesses (2.1, 3.5, 5.0 mm) for application in low temperatures (20, -25 and -50°C) and harsh environments. Results showed that tests carried out at room temperature and low temperature had comparable impact properties and reported no delamination in any impact. Thus, this material was shown to be effective in the low temperatures used as no increase of damaged area was found when the temperature was reduced. However, no structural applications for this material in a range of temperature between -50/+50°C currently exists.

3.2.4.4 Non-structural benefits: erosion resistance

In addition to the excellent damping ability shown by the TPU material, erosion resistance [122-124] is an outstanding property of TPU. Erosion is mainly due to the impact of small particles at high velocity on the surface of a material. Erosion of ductile materials has been analysed by Tilly [120] who illustrated a two-stage phenomenon. The first stage occurs when the particles that impact the surface generate indentation and material removal while the second stage occurs when the impacting particles split up after the impact and radially spread out from the impact location. It is possible to show the erosion phenomenon considering semi-empirical

models in which the energy that generates the erosion process $Q_{erosion}$ can be calculated using the energy balance:

$$Q_{erosion} = (Q_0^{\frac{1}{2}} - Q_E^{\frac{1}{2}})^2 \quad (63)$$

$$Q_{erosion} = \frac{1}{2} M[V - V_0]^2 \quad (64)$$

where Q_0 is the initial kinetic energy, Q_E is the energy required to generate elastic deformation, V is the particles velocity, M is the particles mass and V_0 is the limit velocity for the particle to impact the structure and generate no damage. To evaluate the primary erosion ε_1(mg/g) it is possible to use equation 65 in function of a general velocity V:

$$\varepsilon_1 = \varepsilon_1^0 \left(\frac{V}{V_r}\right)^2 \left[1 - \left(\frac{d_0}{d}\right)^{\frac{3}{2}} \frac{V_0}{V}\right]^2. \quad (65)$$

Where: ε_1^0 is the maximum erosion at V_r (experimentally evaluated), the velocity used to produce this value; d_0 is the particle diameter below which no damage is created within the structure. The equations used to calibrate the model are produced considering small particles ~5μm and a limit velocity of 243 m/s (experimentally determined) obtaining the equation:

$$\varepsilon_1 = \varepsilon_1^0 \left(\frac{V}{V_r}\right)^2 \left[1 - \frac{9000}{d^{\frac{3}{2}} V}\right]^2 \quad (66)$$

Additional tests are necessary to determine ε_1^0 at V_r and d parameters.

The second stage contribution to this model can be neglected if the particle size is lower than ~30μm in diameter. Otherwise, an additional term is added to equation 67:

$$\varepsilon_1 = \varepsilon_1^0 \left(\frac{V}{V_r}\right)^2 \left[1 - \left(\frac{d_0}{d}\right)^{\frac{3}{2}} \frac{V_0}{V}\right]^2 \quad (67)$$

The application of TPU as a protective layer against erosion on structural materials has been proved successful by Zhang et al, [121] who investigated the wear

behaviour of these hybrid structures. The TPU layer was applied on the surface of the structure and erosion tests were performed using a sand-blasting chamber with boron carbide sand at 8 mm in diameter. The erosion of the material was analysed by weighing the sample before and after the test. A scanning electron microscope was used to evaluate the damage extent and morphology and understand the removal mechanisms. Results showed mass loss (mass after the test divided by the mass before the test) in function of the thickness of the laminate as shown in Figure 45.

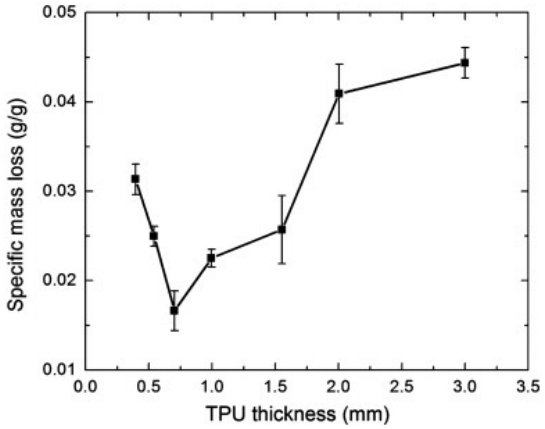

Figure 45-Results of the erosion test performed on TPU protecting the substrate. Image from [121].

As shown by the plot, erosion of TPU at a low TPU thickness is minimal, and erosion tends to decrease with TPU thickness. This behaviour is reversed at around 0.75 mm when TPU erosion begins to increase with increasing TPU thickness. The phenomenology behind this behaviour is still not clear due to the intervention of several thermo-structural mechanisms. The authors' suggested that, generally, during the erosion process, the temperature of the area interested by the erosion locally increases due to friction between the TPU and abrasive particles, decreasing the strength of the material and promoting an augmented erosion of the material in that area. Consequently, the thermal distribution on the eroded area plays an important role in erosion mechanisms, and the ability of a material to resist erosion is based on the thermal conductivity of the material. A high conductivity means that the material can transmit the heat away from the area lowering the temperature; low conductivity instead allows the heat to stack up and increase the temperature. Based

on these considerations, it would seem that at 0.5 mm, the TPU is able to transfer heat to the substrate and limit the detrimental effect of the temperature on the polymer. On the contrary, increasing the thickness of the TPU above 0.5 mm results in a reduction of the ability of the material to transfer thermal energy to the substrate, leading to a build-up of heat in the contact area with a consequent increase in temperature and erosion. This behaviour is evident when analysing the surface topology as reported in Figure 46.

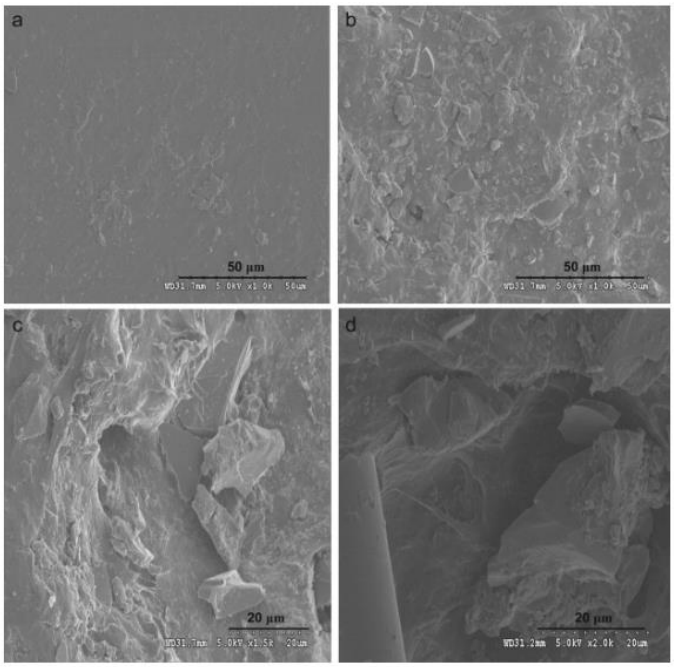

Figure 46-Micrography of TPU: a) before erosion test, b) after the erosion test, c) and d) magnitudes of the eroded area. Images from [121].

As it is possible to see from the images, plastic deformation, cracks and tearing are the effect on the material generated by the thermal effects of weakening under sand blasting leading to the erosion of the TPU material from the substrate. Importantly, only 5% of the materials weight was lost during the test meaning that also in critical conditions, the material offers an adequate protection against wear and erosion and further supports its suitability in advanced applications in harsh environments.

In this literature review, the use of TPU in the hybridisation of laminate structures has been demonstrated as an effective approach to minimising damage from impact due to its excellent damping properties. It also exhibits effectiveness in protecting

materials from harsh environments due to its high erosion resistance. This literature review can be integrated with the descriptions and methods reported in Paper C and Paper D in 5 Chapter and 6 Chapter respectively.

4 CHAPTER: Impact resistance enhancement and enabled SHM features via metal array hybridisation

4.1 Context

Paper A is focused on the design, manufacturing and characterisation of multifunctional composite materials obtained through a hybridisation process involving the introduction of an array of copper and Shape Memory Alloy (SMA) wires within the structure of Carbon Fibre Reinforced Polymer (CFRP). Copper wires were chosen in this research to avoid the corrosion of the metal when exposed to the presence of carbon fibres (as verified for steel wires in Section 3.2.1.3) and to reduce the production cost of the hybrid material since the cost of copper (5.73$/kg) is significantly lower than SMA (150-200$/kg). Also, additionally, the use of copper mesh for lightening protection is already accepted by the aircraft industry [122], thus, regimentations already exist for its use in aerospace structures. Moreover, due to the small wire diameter used in this work, a small weight increase was reported (<1%). Using Low Velocity Impact testing, it was possible to evaluate the improvement of the maximum contact force that the laminate was able to tolerate, demonstrating that the presence the wires changed the impact response of the laminate. In particular, by placing the wires in the top portion of the laminate as described in Bradley's work [74], it was possible to increase the maximum contact force that the material was able to tolerate. In-plane mechanical properties were predicted considering the array of metal wires as hybrid reinforcement and following the equations used to estimate the mechanical properties of interply hybrid laminates (Section 3.2.1.2). Also, as demonstrated by Meo et al [79], it is possible to numerically predict the impact behaviour of this hybrid laminate using

Finite element Modelling (FEM). In addition to the improved impact behaviour, non-structural properties were also enabled by the presence of the wires (smart networks) and these can be used in Structural Health Monitoring (SHM).

Strain sensing was carried out by measuring the resistance of each wire when the laminate was subject to out-of-plane loading. Under loading, the wire deformed following the laminate and since wire geometry is strictly correlated to its resistance value, it changed accordingly. Conversely, when the array of metal wires were inserted within the laminate, it was possible to analyse the magnitude of resistance variation to understand the severity of the applied loading and, simultaneously, locate where the loading took place by identifying the wires that showed greater variation in resistance. It is important to note that for this work, copper wires were not compatible with the provided instrumentation since its resistance variation was too low to be measured. Consequently, since strain sensing ability is independent from the metal typology and only related to the geometrical deformation, SMA wires were used due to their higher resistance variation in function of the load applied. No external sensors were required to detect this information, and this represents a significant benefit for both the versatility and maintenance cost of the structure.

Another non-structural ability that the smart network enables is the possibility for it to be used as an internal heat source for Ir damage detection. When an electrical current was applied to the metal wires, they were heated up via Joule's effect and a heatwave was generated. This heatwave propagated along the laminate material but was slowed down by the presence of damage due to the different thermal conductivity between air (damage) and material (composite) which resulted in higher temperature areas (hot sports) and colder temperature areas (cold spots). No external heat source is required to carry out thermography except an IR camera, which is highly beneficial in certain applications including inspection of narrow or inaccessible locations.

In addition, the use of the metal wires as a heat source can be applied in anti-icing and de-icing procedures, fundamental during off-service and in-service operations. The smart network can be heated up to prevent the formation of the ice layer during the off-service life of the part and to remove an eventual ice layer for the aerodynamic profile that could affect the safety of the entire assembly. Indeed, by tuning the electrical current applied to the system it is possible to generate an adequate temperature on the laminate surface without affecting the mechanical properties of the part.

The original contribution of this paper lies in the use of coppers wires to enhance impact properties whilst also activating non-structural features including SHM abilities and anti-icing systems. In particular, SHM abilities enables reduction of the cost of external sensors (sensing) or heat sources (thermography). Moreover, the system can be used as an anti-icing and de-icing system to protect the surface of the material from ice formation reducing the maintenance operations and guaranteeing the safety of the entire assembly. Also, this work is unique in reporting a systematic analysis of both structural and non-structural properties obtained using copper wires as a smart system.

The Statement of Authorship Form and the paper can be found next.

This declaration concerns the article entitled:	
Development of multifunctional hybrid metal/carbon composite structures	
Publication status (tick one)	
Draft manuscript	
Submitted	
In review	
Accepted	
Published	✓
Candidate's contribution to the paper (detailed, and also given as a percentage)	
The candidate contributed to/ considerably contributed to/predominantly executed the…	
Formulation of ideas:	85% My supervisor proposed the idea to develop the multifunctional system using CFRP and SMA wires. I suggested the use of copper for novelty and cost efficiency and developed the process of testing the material to demonstrate the effectiveness of metal array for SHM purposes.
Design of methodology:	100% I manufactured all the samples used in the experimental campaign and designed all the experimental tests carried out in the work.
Experimental work:	90% I carried out all the impact experimental tests, collected all the data, and analysed all the outputs. My supervisors aided

	me in performing impacts and in the interpretation of the results.
Presentation of data in journal format:	80% I designed the manuscript structure, wrote all the drafts and realised all the figures. Feedback on the draft and help for the paper submission, review and submission was provided by my supervisor

Statement from Candidate			
This paper reports on original research I conducted during the period of my Higher Degree by Research candidature.			
Signed		**Date**	26/05/2020

Development of multifunctional hybrid metal/carbon composite structures

Francesco RIZZO, Fulvio PINTO, Michele MEO*

Mechanical Engineering Department, University of Bath, Bath, United Kingdom

* corresponding author: m.meo@bath.ac.uk

Keywords: Multifunctional, impact, SHM, NDT, de-icing.

ABSTRACT

The aim of this work is to design, manufacture and test a hybrid composite by embedding optimised copper or Shape Memory Alloy (SMA) wires within carbon fibre laminate for improved impact resistance, intrinsic strain sensing and impact detection capability, non-destructive testing and de-icing functionalities. It was demonstrated that with an appropriate optimisation of the wires a reduction of damaged area was experienced. It was shown that the hybrid network can work as a strain sensor by monitoring the variation of its electrical resistance under load and to identify the presence of a localised load such as an impact event. Then, non-destructive capability for assessing defects was shown where, by applying an electrical current to the metal wires, heat was generated and distortion of the thermal field due to a damaged area was measured using a Step Heating Thermography (SHT) process, creating an image of the damage. De-icing operations was presented by exploiting the Joule effect where the local temperature increase was able to melt down an ice layer and hence avoid aerodynamic variation of aircraft surfaces. The results showed that the multifunctionality of this embedded smart material can improve the safety and reliability of aircraft structures and reduce maintenance costs.

1. Introduction

In modern aerospace and automotive industry, Carbon Fibres Reinforced Polymers (CFRP) are largely used for structural applications due to the combination between their specific mechanical properties and low weight. In particular, along the in-plane direction, specific strength and mechanical properties result to be very high, however, because of their intrinsic layered structure, in the through-the-thickness direction, the material shows weak mechanical resistance. As a consequence, composite laminates are susceptible to inter-laminar delamination if subjected to Low-Velocity Impacts (LVIs) that could lead to structure failures. This is widely reported by Abrate [1] in his comprehensive review on composite materials under impact conditions. Over the last two decades, a large amount of research works has been presented and a series of possible solutions have been developed in order to overcome these structural weaknesses. Russel et al. [2-4] modified the matrix toughness in order to achieve global mechanical properties increase, while Tessington and Yaun [5, 6] chose to reinforce carbon fibres-matrix chemical bonding to reach the same properties benefits. The use of design alternatives such as the use of stiches along the thickness direction resulted also to be effective [7-9] as well as the inclusion of +45/-45° woven fabrics [10, 11] within the laminate's stacking. Other researchers followed a different approach embedding together more than a single array of reinforcement leading to a "hybridisation" of the composite material. Bunsell and Naik [12, 13] studied the mechanical behaviour of laminates obtained by laying up both carbon and glass fibres observing an improvement of fracture toughness, impact strength, notch sensitivity and manufacturing costs in respect with a traditional CFRP laminate, but a higher total weight due to higher glass fibres density. Marom et al. [14] suggested a combination of carbon and Kevlar fibres as polymer reinforcement, obtaining an improved fatigue response but reduced stiffness. A very popular solution was the use of Fibre-Metal Laminates (FMLs) such as ARALL [15, 16] and GLARE [17, 18] that showed interesting corrosive resistance, fatigue and impact damage tolerance but higher manufacturing costs. Several researchers focused their attention on the study

of the interaction between metal wires and CFRP: Bradley et al. [19] studied the effective benefits of hybridisation for mechanical properties, verifying the impact properties increase when metal wires are located close to the impacted area. Other works that exploit the unique physical properties of Shape Memory Alloys (SMAs) are focused on the use of SMAs wires as secondary reinforcement. In this context, Paine [20] showed impact resistance increase placing wires in the tensile portion of laminate where martensitic phase transformation generates a plateau region in the stress-strain curve, leading to a hysteresis behaviour where part of energy is dissipated, unlike other metal wires cases. Such behaviour can be exploited to absorb more impact energy during an LVI event. The metal wires enclosed inside the CFRP's stacking sequence, not only may be used for mechanical purposes, but also to activate additional non-structural abilities.

In particular, the use of the metal reinforcement system can be exploited to set-up a smart network system that allows to carry out an in-situ Structural Health Monitoring (SHM) in order to increase the safety level of the structure and avoid the use of external devices during security control and maintenance procedures. Hence, the hybridisation process not only can increase the mechanical resistance improvement, but the same smart material can be exploited to perform a continuous structural integrity monitoring. Hence, a multifunctional composite where both structural (mechanical properties) and non-structural properties (SHM) can be improved by embedding a metallic phase into a polymeric composite material. A real time monitoring of structural health can be achieved by evaluating through electric resistance measurements, the strain distribution over the laminate, and therefore detect a critical load, its exact position, creating an impact detection system. In particular, Abry et al. [21] showed that carbon fibres could act as electric conductors embedded in an insulating matrix. In particular, by performing a resistance measurement during a post-buckling test, they demonstrated the possibility to detect inner defects in the structure but not their exact positions. Schulte et al. [22] reported the possibility to detect the propagation of several typologies of damage inside the CFRP during static or fatigue loading by

monitoring the electrical resistivity of CFRP since fibre breakage decreases the resistivity value. Resistivity dependence from temperature, fibre volume fraction, applied load and stacking sequence is also evaluated and reported in the study. However, several issues were observed using carbon fibres as damage detection material such as difficulties in the connection between the sample and the measuring instrumentation and high fragility of carbon fibres. Other researchers investigated the resistance variation of metal wires embedded within CFRP.

Cui et al. [23] illustrated the mathematical model on the relationship between strain and electrical resistance in a SMA and showed that the relationship is linear and temperature-independent. Nagai et al. [24] presented experimentally the strain sensing ability of SMA wires embedded within CFRP through a tensile test, confirming strain-resistance linear dependence and temperature-independence for martensitic SMA structure. Then the smart reinforcement allowed to analyse the structural integrity of the material once an impact event or damage has occurred. There are different techniques to achieve this objective but over the last decades, among Non-Destructive Techniques (NDTs), Infrared (Ir) thermography resulted reliable in detecting sub-surface damage distribution for both metal and composite parts [25]. The technique is based on monitoring the apparent temperature gradient which is captured on a sample's surface after a heat stimulus is applied. Since the heat diffusion rate of a damaged area differs from an integer one, the heat wave propagation is modified by the presence of cracks or delamination. Traditionally, different external heat sources are used to generate the heat stimulus such as high power photographic flashes [26] or radiators [27] that represent a large limitation of the technique, which results not cost effective and suitable only on large scale applications. Recently, some researchers chose to remove the use of external devices exploiting different solutions to increase the temperature of the laminate from the inside in order to develop what has been called "material enabled" thermography. Suzuki et al. [28] carried out an experimental campaign in which by heating the carbon fibres of an impacted CFRP using an electric current, it was possible to measure the presence of a damaged area due to the increased fibre-fibre

contact points generated by the presence of the indentation. Amhed [29] and Orłowska [30] illustrated the possibility to exploit the presence of an additional embedded component as internal heat source. In [29] a "heat emitting layer" within the laminate stack was embedded, applying an electrical current, a thermal wave was generated, whose propagation through the thickness was used to inspect the sample's integrity. Finite elements simulations were performed to predict the behaviour of the heat wave propagation over damaged areas showing good agreement with the experimental results. However, the insert of these additional layers generates a discontinuity into sample's structure with a local change of mechanical properties. In [30], a 3-D resistive structure was embedded inside the CFRP by drilling the sample. Applying a small current, it was possible to heat the composite along all its directions and to record thermal signals of potential inner defects, even if several manufacturing issues were observed during laminate fabrication because of the drilling tolerance and the presence of holes inside the laminate structure (loss of mechanical properties).

We demonstrate that it is also possible to use the same instrumentation to fulfil another relevant issue in aircraft operations: the de-icing procedure. During the aircraft operative service, the extreme environmental condition (-30/-50 °C) leads to ice growth on wings surfaces. These ice conglomerates can change the geometry of the aerodynamic profile causing a series of potentially critical issues such as unwanted vibrations, loss of aircraft control and in eventually, the total loss of aerodynamic on the wings. In order to avoid this issue, several solutions have been adopted over the years such as mechanical pneumatic systems [31], acoustical systems [32] and electromagnetic pulsing systems [33]. In particular, thermal solutions are largely employed in the modern aircraft industry. The heating of a conductor by Joule effect results very effective in dissolving ice formations, by locally increasing the temperature on the interested part. Different techniques were developed: create short-circuiting condition on conductors [34], apply Eddy-current in AC [35] and use thermoresistive layers which are applied on the top of existing layers [36]. The use of hybrid composite parts may offer another solution to solve

this issue. The embedded SMA wires, if used as a heat source, can dissolve ice on interested surface and consequently, avoid external interventions or the use of complex de-icing mechanisms [37]. Indeed, since the hybrid system is able to generate a large amount of localised heat during damage analysis, it is possible to prevent ice formation on aerodynamics part exploiting the temperature increase on the external surface. In the study of advanced multifunctional materials, a particular mention needs to be made for the use of nanomaterials in fabricating multifunctional composite systems. Chien et al. [38] studied the electrical conductivity and Joule heating of polyacrylonitrile/carbon nanotube composite fibres demonstrating their monitoring and thermo-resistive enhanced features, while Kernin et al. [39] investigated the mechanical, thermal and electrical properties of an epoxy-based nanocomposite when a network of reduced graphene oxide was used as nanofiller. Good electrical conductivity and mechanical properties increase were reported with the possibility to use the material as a strain sensor. Zhang et al. instead [39] studied the use of graphene nano-plates in glass fibre/epoxy composite to obtain an increment in mechanical properties and the possibility to use the same system as monitoring network and Joule heating de-ice system without the necessity of external devices. However, this solution has several issues in transposing the laboratory prototype to the industrial production due to the intrinsic complexity of nanomaterials and their costs.

The aim of this research work is to obtain an optimised embodiment of metal wires within traditional CFRP creating a Multifunctional composites in which the hybrid phase not only works as an additional reinforcement but is also able to enable new additional features by exploiting its thermo-electrical properties [40]. This work presents the design, manufacturing and testing of a hybrid laminate (H-CFRP) in which the hybridisation is obtained by including an array of Shape Memory Alloys or Copper wires within the laminate stacking sequence for multifunctional purposes. In the paper, the manufacturing procedures used to fabricate all the investigated samples are presented in Section 2 while the experimental set-up and testing methods for impact, sensing, Ir damage detection and de-icing tests are

described in Section 3. In Section 4, results and discussions for all the aforementioned testing cases are reported whilst Section 5 includes a results summary and conclusions.

2. Samples Manufacturing

In order to understand the benefits of embedding metal wires inside a CFRP laminates, a series of hybrid samples were manufactured. Using a M21-T800 prepreg system, the samples were cured in autoclave at 180 °C and 100 Psi with a ramp of 0.2°C/min for 2 hours. Two different categories of samples were produced: plates to test hybrid material improvement and complex parts to test the reliability of the hybrid composite concept on proper aeronautical structures. Plates were laminated using different stacking sequences and were cut 150 mm in length, 100 mm in width and around 2 mm in thickness, while the complex parts (leading edge geometry) were manufactured using 12 layer of prepreg obtaining 130 mm of height, 150 mm of length, 120 mm of depth and 2.91 mm of average thickness (Figure 1). Copper wires (0.15 mm diameter) and Shape Memory Alloy (SMA) Nitinol (0.2 mm of diameter) were embedded at different depths within the CFRP with an inter-wires distance of 16.5 mm. In order to obtain an optimal bonding between metal wires and composite matrix (epoxy resin), SMA and copper wires were treated using two different methods. SMA surface was treated using a 10% NaOH anodic oxidation to modify the surface and increase the bonding strength between SMA and resin [41, 42]. Copper wires, instead, were treated using sand paper to increase the roughness of the metal surface and then its bonding strength with epoxy matrix [43]. Bottom W (Figure 1.a) and Top W (Figure1.b) configurations were fabricated inserting copper wires (global weight increase of ~1%) respectively between the first and the second ply (9 layers in total) from the bottom of the laminate and between the eighth and ninth ply, in order to evaluate the increase of impact properties in reference with a traditional CFRP (Figure 1.c) (Ref). Sens Cu (Figure 1.d) and Sens SMA (Figure 1.e) samples were produced by

inserting copper and SMA wires respectively between the third and fourth ply (7 layers in total) in order to test the impact localisation and sensing ability of the smart embedded system. Characterised by the presence of a Polytetrafluoroethylene (PTFE) patch inserted between the sixth and seventh ply, Therm PTFE (Figure 1.f) was fabricated using the same stacking sequence of previous samples in order to simulate a damaged area and to validate the feasibility of the Ir technique. In the Leading Edge PTFE (Figure 1.g), together with an array of SMA wires (fifth and sixth ply), a PTFE patch was inserted between the ninth and tenth ply to simulate a delaminated area in a real aerodynamic part. Leading Edge SMA (Figure 1.h), instead, was produced using a double array of SMA wires between the fourth-fifth plies and ninth-tenth plies in order to evaluate the possibility to detect real defective areas inside a complex structure using the same Ir technique. A detailed description of samples denomination and layup is reported in Table 1.

Table 1-Manufactured samples specs. (w: wires; p: PTFE patch)

Label	Number of samples	N° Plies	Aim	Wires	Lamination sequence
Bottom W	3	9	Impact/Damage detection	Copper	[0/w/90/0/90/0/90/0/90/0]
Top W	3	9	Impact/Damage detection	Copper	[0/90/0/90/0/90/0/90/w/0]
Ref	3	9	Impact	No Wires	[0/90/0/90/0/90/0/90/0]
Sens Cu	1	7	Sensing	Copper	[0/90/0/w/90/0/90/0]
Sens SMA	1	7	Sensing	SMA	[0/90/0/w/90/0/90/0]
Therm PTFE	1	7	Damage detection	SMA + PTFE	[0/90/0/w/90/0/90/p/0]
Leading Edge PTFE	1	12	Damage detection	SMA+ PTFE	[0/0/0/0/0/w/0/0/0/0/p/0/0/0]
Leading Edge SMA	1	12	Impact/ Damage detection	SMA	[0/0/0/0/0/w/0/0/0/0/w/0/0/0]

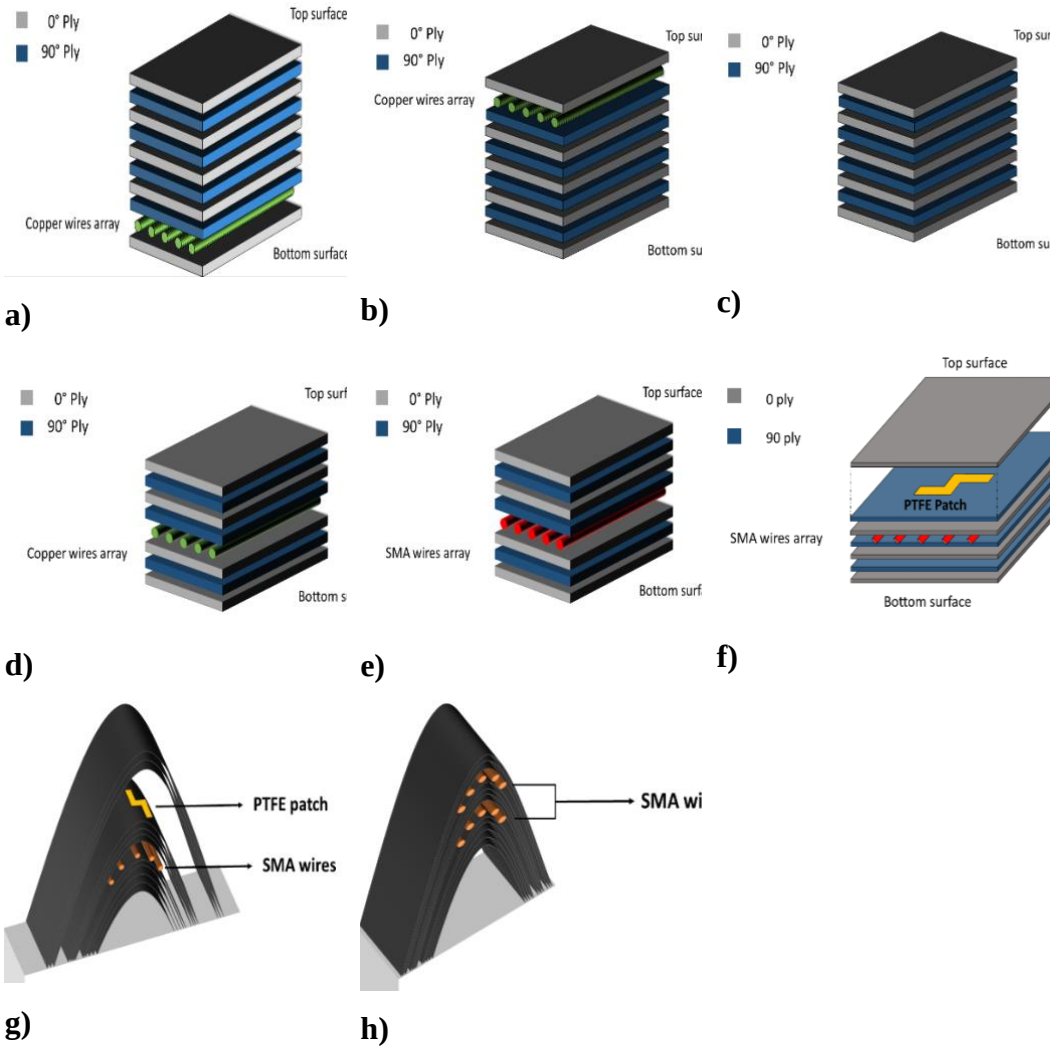

Figure 1-Stratification layout of manufactured samples: a) Bottom W (Copper wires far from impacted surface); b) Top W (Copper wires close to impacted surface); c) Ref (no wires); d) Sens Cu (copper wires-sensing); e) Sens SMA (SMA wires-sensing); f) Therm PTFE (SMA wires + PTFE patch-thermography; g) Leading Edge PTFE (leading edge-SMA wires+ PTFE patch-thermography); h) Leading Edge SMA (Leading edge -Double SMA wires-Thermography).

3. Experimental set-up

3.1 Impact Campaign

A drop tower machine was used to perform Low-Velocity Impact (LVI) tests on the samples. The impact load is applied using a hemispherical tip (20 mm of diameter) of hardened steel dropped from a height of 0.20 m with a total impactor mass of 12.864 Kg. The applied impact energy was 25J. A laser triggered system

was used to collect the experimental data and a MATLAB code was used to elaborate the output data. The tests were performed following the BS EN ISO6603-2:2000 standard evaluating the impact behaviour of two different wires configurations: Bottom W configuration was tested with wires on the opposite side of impacted surface, while Top W configuration with copper wires close to loaded area. Samples were compared with a traditional CFRP laminate (Ref) obtained with the same stacking sequence but without any metal reinforcement.

3.2 Sensing feature

Both tests were performed using an Instron Universal Tester (3369) to apply the displacements on Sens Cu and Sens SMA while a 6 ½ digit multimeter (VOM) Agilent 34401A monitored the electrical resistance during the tests. Three-point bending tests were performed on each sample placing them on two supporting pins at a set distance apart while a third loading support was lowered from above at a constant rate of 0.2 mm/min until sample failure. The applied load generates tensile stress in the convex side of the specimen and compression stress in the concave side. Insulating tape (PTFE) was used to avoid any interferences that could affect the resistance measurements. Punch tests were conducted using a spherical tip of hardened-steel and applying the load to an exact point on the sample. The sample was constrained on a hollow support using four G-clamps on its four corners and the punching support was lowered at a constant rate of 0.2 mm/min. Hence, it was possible to partially extend the results taken from the static case (punch test) to the dynamic case (impact load) as reported in literature [44] [45] since in both cases, an external displacement is applied on a single point of the sample. Damage detection

3.3 Damage detection

To test the feasibility of this approach two different configurations were investigated. For single wire configuration, the test was performed generating heat from each of the different wires within the laminate structure; the current applied

in this case was of 3 A. For multiple excitation of the wires, a multiplex system managed by an Arduino module was designed and manufactured in order to generate heat by applying a current in a sequence on all the wires. Since it is possible to scan with a specific frequency even large samples, by using this approach it is possible to reduce the total amount of power required. In addition, when the system is used together with the strain detection method, only specific portions of the sample (i.e. the critical parts in complex structures) can be scanned diverting more power on smaller areas, thus increasing the resolution of the inspection while keeping the required power to the minimum. In this case, the current applied was of 1.5 A. Since the position of the wires will determine the relative distance between the potential damaged area and the portion of the samples accessible for the thermal analysis, different typologies of hybrid samples were tested and subjected to different damage conditions:

- **SMA/CFRP (Therm-PTFE, LeadingEdge-PTFE and LeadingEdge-SMA):** Therm-PTFE and LeadingEdge-PTFE samples were manufactured with an embedded Polytetrafluoroethylene (PTFE) patch to simulate the presence of a damaged area at a certain depth within the laminate structure. The samples were analysed with both the single wire configuration and the multiplex system. Leading Edge SMA instead was manufactured with no PTFE patch and subjected to a LVI to generate a real internal defect.

- **CU/CFRP (Bottom-W and Top-W):** The copper hybrid samples were manufactured with no patches and subjected to a Low-velocity Impact (LVI) using a weight drop tower in order to generate barely visible impact damage (BVID). The used energies were 20J and 25J. The samples were investigated using only single wire configuration and a comparison between the different damaged areas was reported.

A power supply provided for the continuous electrical current (3 A for single wire configuration and 1.5A for multiplex one) and an electrically cooled Ir camera

(CEDIP) was used to collect thermal data with a resolution of 320x240 pixels (weight x height), maximum frame rate of 150 Hz and temperature sensitivity of 30 mK. Digital units (apparent temperature) are the camera units used to evaluate the intensity of the thermal radiation (emissivity) recorded in a certain interval of time. In order to obtain an estimation of the real temperature of the body, can be related to the camera temperature sensitivity [37]. However, since the real temperature measurement can be affected by several conditioning parameters including material thermal properties, environmental conditions and camera focus, all the thermal images are reported using digital units instead of °C in order to present thermal results with the best resolution, free from external conditioning. All measurements are recorded at room temperature (25°C). Because of the presence of the internal heat source, it is possible to use different typologies of thermographic inspection such as Pulsed Thermography (PT), Pulsed Phase Thermography (PPT), Lock-In Thermography (LIT) and Step Heating Thermography (SHT) without the need of additional equipment or specific setup. In this case a SHT method was used in order to detect damaged areas also at deeper locations inside the laminate, and the camera was used to monitor the magnitude of the apparent temperature variation on the sample surface during both cooling and heating processes. A background subtraction was executed on the measurements selecting 100 frames before the heating process and calculating the data average for each images' pixel. The total observation time was 5 s for the single wire configuration and 9 s for the multiplex configuration with 0.01 s of interval for wires switching.

3.4 De-icing feature

A thick layer of ice was built up on sample surface using a freezing spray agent and thermal scanning of 30 s was conducted heating up the wires. Using electricity passing through the wires (0.55 A and 3.04 V), heat can be generated to locally increase the surface temperature of the sample and melt the ice on its surface. In order to increase the temperature of a large area by using a single power supply, to keep the power consumption low and to route the heat only the most

sensitive zone of the part (leading edge), the multiplex configuration was chosen. Thermal data were collected using the same camera configuration used for the previous tests. Results were reported at three different time steps (0 s, 15 s and 30 s) to illustrate the effective ice dissolution. All the tests were performed at room temperature (25°C). Mechanical properties detriment is a well-known issue for commercial de-icing systems already used on structural components and mainly depends on two factors: the time of actuation and the temperature intensity. It was demonstrated that when a CFRP component is exposed at temperatures of 100-150°C for 45 min, a detriment of the mechanical properties occurs with a loss of ~6% -14% [46] and that a severe degradation of the material occurs when exposed to a temperature over 180°C [47]. Analysing the typical temperatures involved during the heating of the metal reinforcement and the time of actuation of the heating system, it is possible to identify a range of temperature of 50-80°C [37, 48] for a time of 9-30 s. Consequently, comparing the used temperature and time of activation of the hybrid system with the critical ones, it is clear that the mechanical properties detriment due to heat transfer can be assumed very small and localized around the metal area with no influence on the general properties of the laminate.

4. Results and discussion

4.1 Impact Campaign

The impact campaign was conducted in order to understand the real improvements in terms of mechanical properties when metal wires are embedded within the CFRP during the manufacturing process as additional reinforcement. Although previous results in literature indicated that the best location along the thickness for metal wires is close to the impact surface [19], it is necessary to confirm this on the manufactured H-CFRP in order to understand the best position of the embedded network along the laminate's thickness in order to maximise the efficiency of the non-structural functionalities. In fact, as described in this work, the position of hybrid network through the thickness is important for accurate

damage detection and strain sensing functionalities. Based on this consideration, it is important to consider how the metal network location changes affect the impact resistance of the proposed hybrid material. During an impact the hybrid laminate is also loaded in the out-of-plane direction, and the impact energy will be absorbed by damage, and plastic deformation of the wires. In this work, a comparison between two different hybrid composite configurations under impact loading is presented. The two tested configurations, as previously reported, are structured in function of the relative position of wires and impacted surface. For thin walled structures, during the impact event, the laminate portion below the neutral plane is subjected to tensile stress while the other part, is interested by compressive one. For brittle materials [49], this tensile stress should be minimised, hence, the array of metal wires has the function of absorbing as much impact energy. Moreover, as illustrated by Bradley [19], the structure failure modes are different in function of the presence of wires: if the wires are close to impacted area, the sample's stiffness is locally increased and the failure mode is no more by buckling compression, but shear failure is the main cause of composite breakage. Analysing the failure mechanism of the two wires configurations, it is possible to identify two opposite behaviours. When metal arrays are located far from the impacted area (tensile portion of laminate), the impact energy propagates across the sample's thickness, generating, in the compressive zone, moderate damaged zones (buckling compression). However, across the middle plane, the stress typology switches from compression to tension, leading to a different and more dangerous situation. Along the wires, the crack extension is intensified by two different mechanisms: weak matrix-metal interface (that creates a preferential zone for cracks' nucleation and propagation), and stresses accentuation around discontinuities edges. These mechanisms coupled with the tensile stress (that accelerates the defect propagation), lead to a catastrophic and sudden failure of composite with massive damaged area in the lower part of laminate. On the other hand, when the hybrid component is localised on the compressive zone of laminate (in the proximity of the impacted area), the impact energy generates a damaged area on the portion around the length of wires where no weak zones are present. Dissipating a large amount of energy both to plastically

deform the wires and to propagate the cracks, reduced delamination area can be observed. Based on this consideration, the best eligible configuration to increase the mechanical properties of laminate is expected to be the one with wires in the compressive portion of plate, as close as possible to the impacted zone, in order to dissipate as much energy as possible in the less sensitive part of composite [19, 50]. The experimental data confirms the validity of the previous concepts as shown in Figure 2.

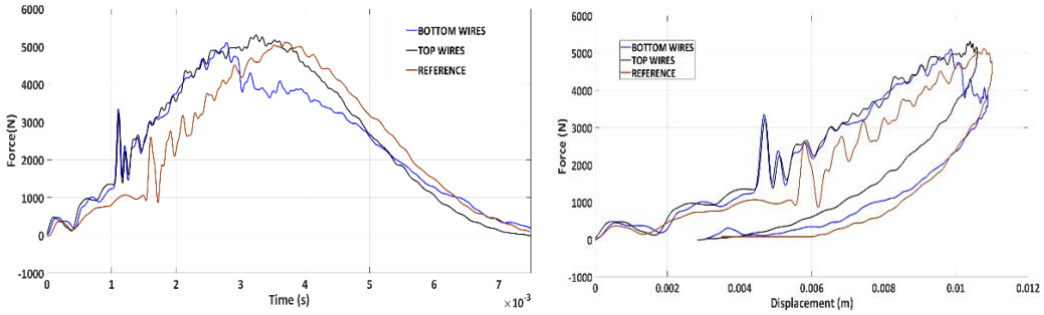

a) **b)**

Figure 2-Force-Displacement curve of different wires configurations: a) Time – Force plot and b) Displacement-Force plot.

The best behaviour is shown from the Top W configuration, which has wires close to the impacted surface and the maximum contact load recorded during the tests (5281 N). On the contrary, Bottom W shows an evident load drop in the impact curve, suggesting structural collapse in progress inside the sample. Comparing the Top W and Ref (reference), it shows that the Top W has a slightly improved impact behaviour than traditional CFRP at relative maximum displacement value. On the other hand, the hybrid component has a negative effect on Bottom W since the load drop is more pronounced than the reference, indicating a worse structural breakage during the impact event. An improved impact response for the sample with top wires was confirmed by ultrasonic phased array inspections. A 5 MHz Phased Array Transducer with 128 Channels (National Instrument) was used for this purpose. The difference in terms of delaminated area is reported in Figure 3 where amplitude colour map is shown for each plate. The extent of the delaminated area was calculated using an image processing software and the measurements are reported

in Table 2. The smallest delaminated area is found in the Top W -4% smaller than the Ref one, while the Bottom W damaged area is +18% greater. Absorbed energy and maximum tolerated load are also reported in Table 2 together with delaminated areas extension.

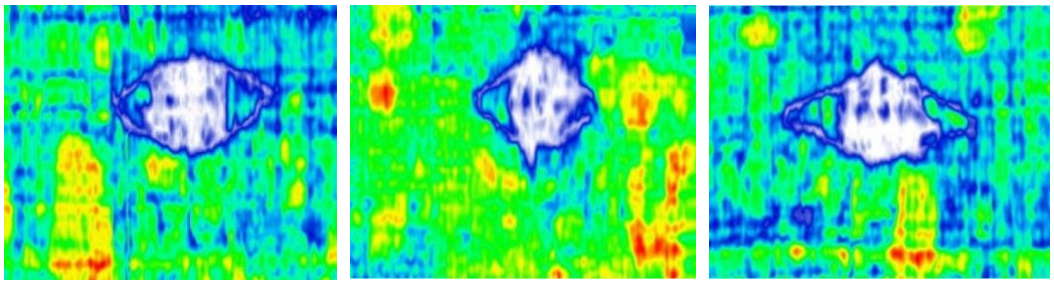

BOTTOM TOP REFERENCE

Figure 3-Ultrasonic Phased Array ultrasonic scan with wires positioned at different locations within the samples thickness and traditional unreinforced laminate.

Table 2-Impact energy absorbed, maximum load, maximum displacement and damaged area for Bottom W, Top W and Ref configurations with statistical variation (3 samples for each configuration).

Samples	**Typology**	**Absorbed Energy [J]**	**Maximum Load [N]**	**Maximum Displacement [mm]**	**Damaged Area [mm2]**
1	Bottom Wires	14.85±1.48	5235±151	7.64±0.43	1128±136
2	Top Wires	14.51±0.23	5281±57	7.53±0.07	884±54
3	Reference	14.46±0.18	5077±151	7.54±0.17	919±24

4.2 Sensing Features

The hybrid phase can be also exploited as strain sensor to detect the position and the magnitude of the external stimulus, monitoring the change of its electrical resistance. Two typologies of tests were conducted: 1) three-point bending to investigate the correlation between resistance variation and displacement when a distributed load is applied and 2) punch test to test the reliability of the method to detect impact-like events.

In order to evaluate the electrical resistance variation avoiding differences given by the wires length and measurement fluctuations, a normalised electrical resistance $\bar{R}$ is calculated using as reference the electrical resistance of the wire when no displacement is applied. According to the equation (1), the normalised resistance is calculated:

$$\bar{R} = \frac{R_n - R_0}{R_0} s \tag{1}$$

Where: R_n: measured resistance [Ω] and R_0:reference resistance [Ω].

Equation (2) is used to calculate the electrical resistance of a metal wire:

$$R = \rho \frac{L}{S} \tag{2}$$

where, ρ: the resistivity of the material [Ω·m], L: length of the wire [m] and S is cross section of the wire assumed constant [m2].

Assuming that a uniform load is applied along the midspan of the sample, it is possible to consider each laminate-wire system as a 1D beam under bending loading (Figure 4) and the beam theory can be applied. It is assumed that the plate and the wires are well-bonded and have no relative displacement when a load is applied uniformly along the span of the plate. Consequently, the flexural solicitation of wire and laminate has the same value.

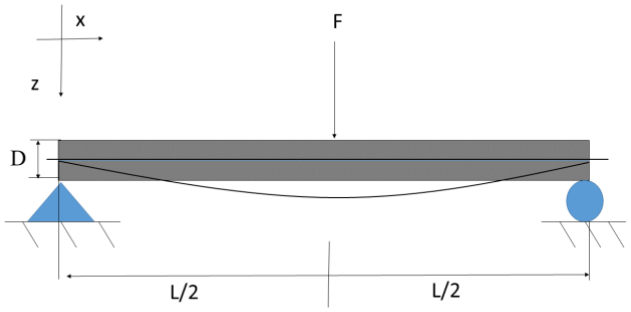

Figure 4-Scheme of 1D beam simply-supported.

In order to calculate the deflection of the beam, the Euler -Bernoulli beam theory can be used:

$$\frac{d^2}{dx^2}\left(EI\frac{d^2w(x)}{dx^2}\right) = q(x) \tag{3}$$

where, w (x): deflection of the beam in the z direction at some positions x [m]; q: applied force for unit of length [N]; E: Elastic modulus [GPa]; I: Second moment of area [m4]. In order to obtain the maximum deflection in the centre of the beam, the hypothesis of small deformations, linear elasticity and normal neutral surface are assumed. Solving the equation for this supported beam configuration, the deflection of the beam, the slope ϑ(x) and the bending moment M(x) in function of the x-position along the beam can be written using the Macaulay's notation [51]:

$$M(x) = \frac{1}{EI}\left(\frac{F}{2}\langle x\rangle^1 - \frac{F}{2}\langle x - \frac{L_0}{2}\rangle^2\right) \tag{4}$$

$$\vartheta(x) = \int M dx = \frac{1}{EI}\left(\frac{F}{4}\langle x\rangle^2 - \frac{F}{2}\langle x - \frac{L_0}{2}\rangle^2 - \frac{F{L_0}^2}{16}\langle x\rangle^0\right) \tag{5}$$

$$w(x) = \int\int M(x)dx = \frac{1}{EI}\left(\frac{F}{12}\langle x\rangle^3 - \frac{F}{6}\langle x - \frac{L_0}{2}\rangle^3 - \frac{F{L_0}^2}{16}\langle x\rangle^1\right) \tag{6}$$

where x is the position along the x-axis [m]; F the force applied on the sample [N]; and $L_0$the initial length of the beam [m]. The subscript *c* is used to reference the laminate parameters while with the subscript *w*, the wire's ones. The maximum deflection evaluated in the centre of the beam at $L_0/2$ is:

$$w_{max} = \frac{F{L_0}^3}{48E_cI_c}. \tag{7}$$

This value represents the flexure extension applied by the test machine on the sample.

The relation between bending moment and longitudinal stress is expressed using the equation:

$$\frac{M(x)}{I_c} = \frac{\sigma(x)}{z} \tag{8}$$

where z is the distance in respect to the neutral plane of laminate along the z-direction that corresponds to the wire location [m] and $\sigma(x)$ is the longitudinal stress [Pa] defined using the elastic constitutive law ($\sigma(x)=E\varepsilon(x)$). Since the displacement of wire and laminate is the same under bending conditions, the longitudinal strain of the laminate at the z-distance from neutral plane corresponds to the longitudinal

strain of the wire placed at same distance from the neutral plane. Moreover, considering the relative position between wires and middle plane of the laminate (Figure 5), it is possible to observe that the wire is very close the outer surface of the sample, therefore the term z in the equation above can be assumed as equal to half the thickness of the sample (D/2).

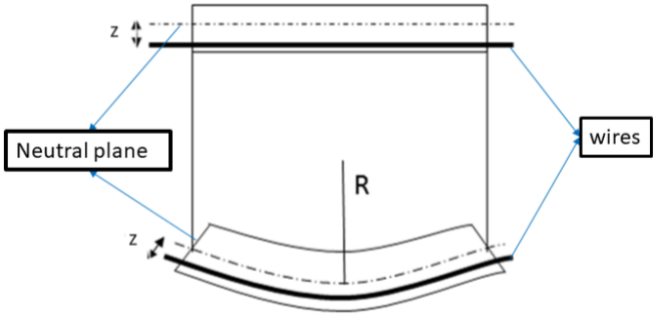

Figure 5 -Configuration of wires within the laminate

According to the equation 8, the longitudinal strain *ε(x)* can be written as:

$$\varepsilon(x) = \frac{z}{EI} M(x) \tag{9}$$

In order to estimate the longitudinal strain ε_c at positon z along half of the laminate length (symmetrical view), an integral view is used considering:

$$\varepsilon_c = \int_0^{\frac{L_0}{2}} \varepsilon(x)\, dx = \frac{z}{E_c I_c} \int_0^{\frac{L_0}{2}} M(x) dx. \tag{10}$$

Using equation (6) for the bending moment equation and considering the first portion of beam, the total longitudinal strain is calculated:

$$\varepsilon_c = \frac{{L_0}^2 z}{16 E_c I_c} F. \tag{11}$$

Under the aforementioned hypothesis, the bending moment applied on the laminate (M_c) is equal to the bending moment applied on the wire (M_w):

$$M_c = M_w \tag{12}$$

Using equation (9) in (12), it is possible to calculate the longitudinal strain applied on the wire (assumed as a cylinder) during bending:

$$\varepsilon_w = \alpha \varepsilon_c \tag{13}$$

$$\alpha = E_c I_c / E_w I_w \tag{14}$$

It is important to notice that the differences in terms of mechanical and geometrical properties between composite and wire are considered into the coefficient α. Due to the two different strains of composite and wire, shear stress is generated along the resin interface between the two components. This interface is assumed totally elastic under the hypothesis of perfect bonding.

By considering the expression of ε for the wire's strain calculation:

$$\varepsilon_w = \frac{L - L_0}{L_0} \tag{15}$$

It is possible to write the final length L using (11) and (12) as:

$$L = \alpha \frac{{L_0}^3 z}{16 E_c I_c} F + L_0 \tag{16}$$

This equation represents the length in function of the applied load.

From (2) and (13):

$$R = \frac{\rho}{S}\left(\alpha \frac{{L_0}^3 z}{16 E_c I_c} F + L_0\right) \rightarrow R = \Delta R + R_0. \tag{14}$$

Based on equation (14), it appears clear that by analytically evaluating the resistance variation of the embedded wires, it is possible to detect the intensity of an applied flexure load on the sample. It is possible to notice the linear trend of the equation with a slope equal to the first term of the expression (ΔR) and with second term as intercept (R_0). The intercept represents the value of the resistance for the unloaded wire, while the slope represents the variation in resistance generated by the flexure loading.

It is possible to rewrite equation (14) in function of the flexure extension, by using the deflection definition equation (6):

$$R = \frac{\rho}{\mathrm{S}}(3 z \alpha w_{max} + L_0). \tag{15}$$

This equation allows to calculate the theoretical behaviour of the resistance in function of the flexure extension applied during the three-point test. In this case, the first term is the slope of the line while the second remains the intercept.

In order to validate the analytical model illustrated above, samples were tested on both sides in order to generate respectively elongation and compression on the wire

under test. The two behaviours have to follow the equation (16) where the z-value is positive in the positive direction of z-axis if the wires are in the lower part of the composite, while negative when the wires are in the upper part of the laminate. During the test campaign, Sens-Cu and Sens-SMA samples were tested, however only for Sens-SMA samples it was possible to correlate the resistance variation with the applied displacement. Sens-Cu samples, in fact, showed no correlation due to the low resistivity of copper (1.68·10-8 Ω·m) which generated a very small resistance variation. The multimeter used was characterised by limited number of digits and the measured resistance was below the instrument sensitivity. Consequently, the resistance variation recorded during the test was not the real one but the result of a truncation error that affected the measurement. On the other hand, Sens SMA showed good correlation between the two parameters since the SMA resistivity (1.08·10-6 Ω·m) is considerably higher than copper one leading to higher resistance variation. The experimental results for three-point bending test are shown in the figures below. Figure 6.a represents the mechanical data collected during the flexural test where the flexural load follows a linear trend with the flexural extension, in accordance with [52]. In Figure 6.b, the theoretical behaviour of the resistance variation and the experimental curves show a comparable linear trend for low values of flexure extension that tends to slightly diverge for higher values of the flexural extension since the hypothesis of small displacement is not valid due to a large deformation of the wires (26%) that can lead to a mismatch with the theoretical prevision for high values of flexure extension. From Figure 6.b and the Figure 6.c, the resistance variation with increasing flexural extension follows a linear trend hence, it is possible to monitor the strain distribution by measuring the behaviour of electrical resistance. In order to verify the same trend of resistance variation when the wires are compressed, a second test was performed. In this case, the sample was set in the test machine with the wires facing the loading support in order to apply compressive stress on the SMA wires (Figure 6.c). By analysing the behaviour of the same wire in both compression and tension, it is possible to estimate the trend of the two configurations and observe the same modulus for each experimental point as shown in Figure 6.d.

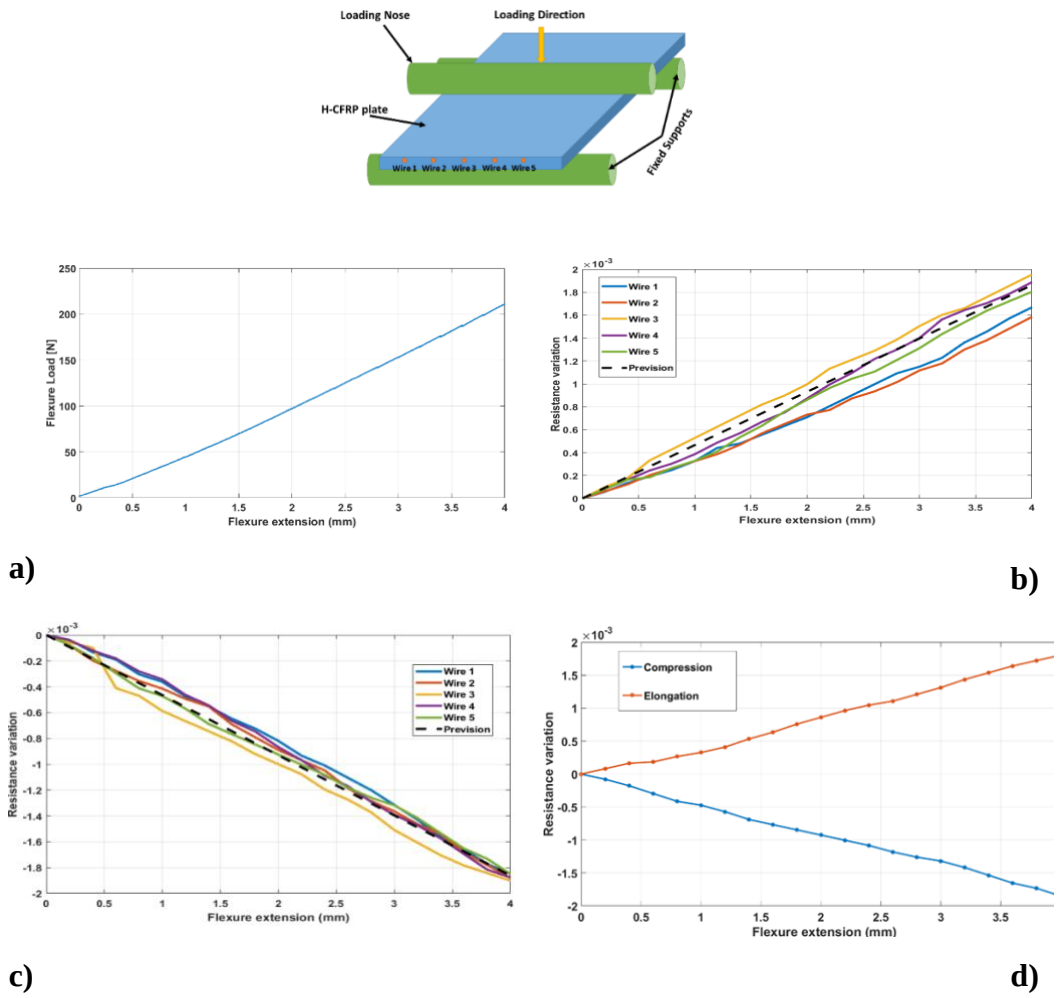

Figure 6-Experimental data for three-point bending test: a) Flexure Load vs. Flexure extension curve. b) Electrical resistance variation curves with stretched wires. c) Electrical resistance variation curves with compressed wires. The theoretical prevision is reported.

Since, the good correlation between theoretical and experimental data confirmed the correlation between the applied load and the variation of the electrical resistance of the wires, a punch test was performed to investigate the possibility to detect the exact position of an impact event applying a concentrated deformation in a single point rather than over the entire width of the sample. This model was realised considering a static case where SOLID45 (eight nodes and orthotropic material properties) elements were used. The displacement of 4 mm (maximum applied displacement measured during the tests) was applied at the centre of the top surface in correspondence with Wire 3. The sample was constrained on its four corners,

fixing all the degrees of freedom. The plate's dimensions were 150 mm x100 mm x1.3 mm.

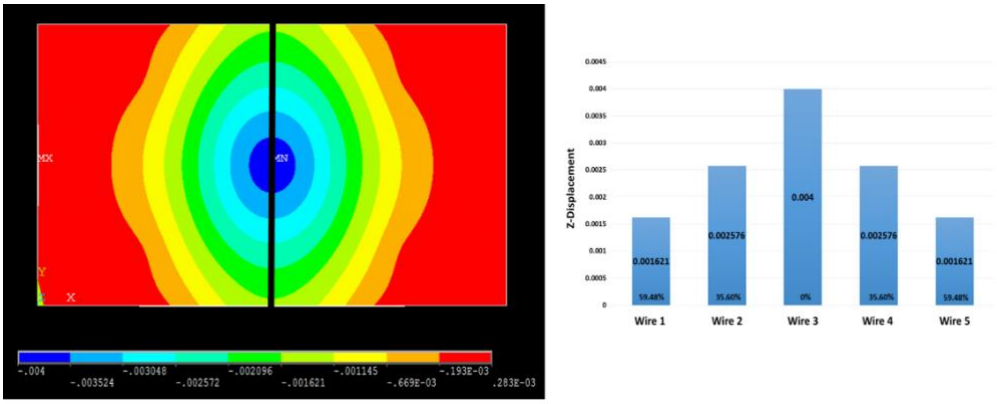

Figure 7-FEM model of the CFRP sample (frontal view). Z -displacement is shown using the colour-map to estimate the magnitude. The maximum deflection values are indicated by the black line. Displacement values are evaluated for each wire considering their maximum deflection and percentage reduction respect to the experimental displacement applied.

From Figure 7, the maximum displacement corresponds to the location where the tip applies the load and the external rounded zones are progressively less interested by the deformation. Along the black line, the maximum deflection can be linked to the previous test where the maximum deflection was applied by the moving pin. Considering that on that line, the conditions of maximum deflection, mandatory for the theoretical model, are still valid, it is possible to extend the theoretical model developed for the three-point bending test to the punch test. In Figure 7, displacement and wires position are reported and qualitatively, it is possible to determine the magnitude of the resistance variation for each wire. As mentioned previously, the Wire 3 location is where the maximum displacement is observed and where z-displacement is equal to the punching deformation. Wire 2 and Wire 4, symmetric respect to Wire 3, are characterized by a lower elongation since, the z-displacement magnitude is reduced by 35.6% in the area surrounding the punch location Wire 1 and Wire 5 instead, are located in an area on which the z-displacement is reduced by 59.47% than the central one. Consequently, the values of resistance variation measured on the external wires will be less relevant than the ones measured for the internal wires. These results show that by monitoring the

resistance variation of the embedded wires network it is possible to localise the presence of an impact event in real time on the surface of the sample. In Figure 8.a, the flexure load follows an exponential trend with the flexure extension which it is congruent with the other experimental data in literature for compressive test on CFRP [53]. In addition, in Figure8.a, the resistance variation in function of the flexure displacement is illustrated, reporting a different response of the metal wires when the flexural displacement is applied on the centre of the sample. The greater resistance variation is shown by the Wire 3 trend while the other wires exhibit lower values. The displacement is applied directly on the Wire 3 position which reports a behaviour similar with what observed during the three-point bending test (Figure 6). Indeed, as shown from the FEM model, the maximum deflection is located in that point and consequently, the theoretical model used for the correlation of the three-point bending tests can be extended to associate the experimental data of Wire 3 during the punch tests. On the contrary, the other wires respond with a very low fluctuation of resistance because their displacement values are lower than the central wire ones, hence the theoretical model is not applicable in these locations. The comparison between the experimental data collected of Wire 3 and the theoretical model for three point bending test matches for low-middle values of displacement while for higher values there is a slight mismatch due to the small displacement assumption. However, the experimental data proved a good correlation between displacement and resistance variation for the Wire 3 and the ability to identify the presence of an applied load caused by an impact event.

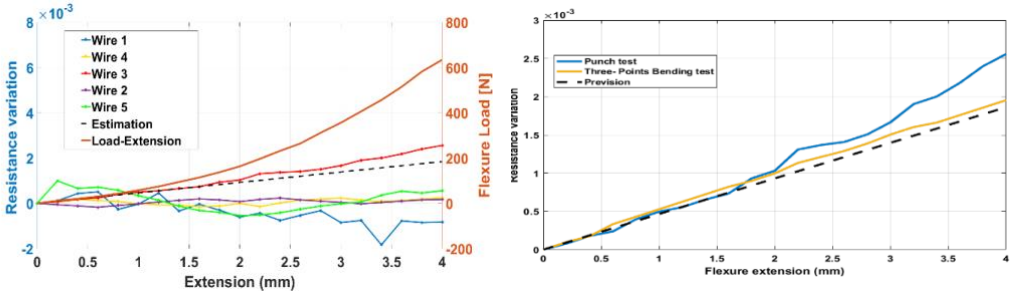

a) ***b)***

Figure 8-Experimental data for punch test: a) Flexure Load vs. Flexure extension curve and Electrical resistance variation curves with theoretical estimation for Wire 3; b) Comparison between Wire 3 results for the different tests. The prevision is reported.

4.3 Damage detection

Exploiting the thermo-resistivity of embedded metal wires, it is possible to scan composite structures and identify the delaminated areas. By applying an electrical current to the wires, a thermal wave via Joule effect are generated and propagates towards the surface and monitored using an Ir thermal camera.

- ***SMA/CFRP with PTFE patch***

Unlike metals whose thermal properties are isotropic, for composite materials along the fibre direction, the thermal conductibility is higher than in the transverse one because the resin reduces the thermal conductibility. Hence, the heat diffuses not uniformly along the principal directions of the material. This allows identifying a zone where thermal diffusivity is different from the rest of the part, as in the case of a delaminated area. The rate at which this wave propagates in the sample for a given current generated at a given depth depends on physical properties of the entire sample (as thermal conductivity) and it is strongly affected by any discontinuities within the laminate thickness. Hence, the presence of an internal damage would interact with the wave propagating from the embedded wire towards the top surface, leading to a localised variation of the apparent temperature in an area on the surface perpendicular to the damaged point.

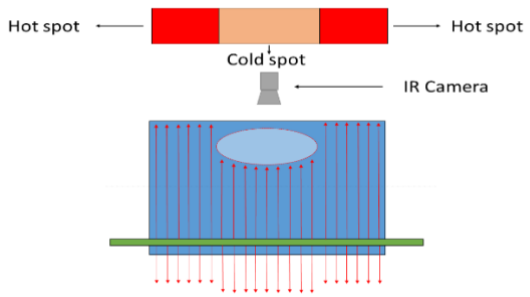

Figure 9–Layout heatwave propagation inside hybrid CFRP composite interacting with a delaminated zone (PTFE patch), far from the delaminated area.

This is illustrated in Figure 9 where the camera is able to identify hot spot zones that correspond to areas in which the heat is not influenced by the internal discontinuity and cold spot zones where instead the heat is unable to propagate due to the presence of structural discontinuities (PTFE patch). Therm-PTFE was analysed by placing the Ir camera in front of the sample, facing the PTFE patch. Figure10 shows the results captured from two different points laying on different portions on the same wire. In particular, the orange curve corresponds to an undamaged area, while the blue curve represents the variation of the superficial apparent temperature in a spot placed perpendicularly to the PTFE patch. The graphs show a thermal wave propagating in the sample's thickness towards the top surface, leading to an increase in the apparent temperature. In facts, the heatwave is slowed down due to a lower thermal conductibility of discontinuity and, due to the non-homogenous thermal properties of CFRP, the heatwave is unable to go around the damaged area, spread in the transverse direction and mask the delaminated area. The sign of the apparent temperature variation (whether positive or negative) depends on the relative positions of the damage, the heat source and the Ir Camera.

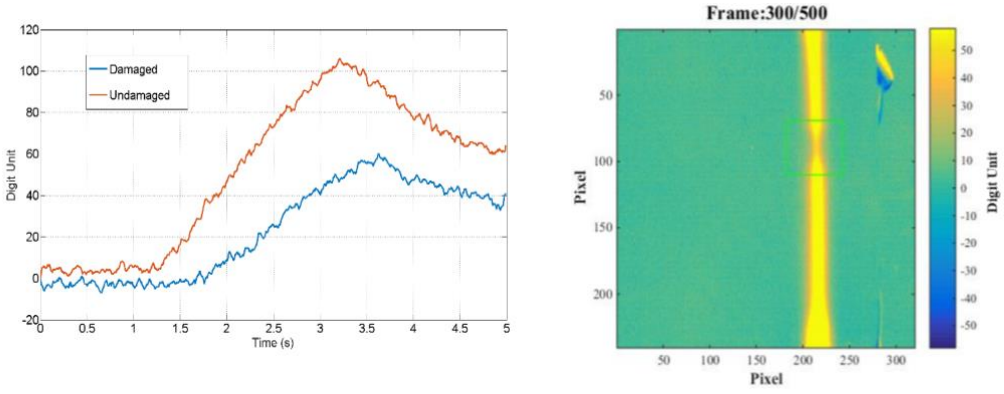

Figure 10-Images acquired during the test after the background subtraction operation for Therm SMA, together with the curves recorded from two areas corresponding to a damaged and undamaged spots on the sample's surface.

The presence of the discontinuity affects both the amplitude and the slope of the curve relative to the damaged area allowing a rapid localisation of the internal damage from the heating and cooling portions of the curve. One of the drawbacks

of the single-wire configuration is the necessity to connect each wire to a different power source to generate a heat gradient large enough to scan the entire surface of the part under examination. This requires a large consumption of power since each wire needs to be fed separately. In addition, the connections and electric circuits on each wire can locally affect the generated gradient in different areas of the samples, leading to reading uncertainties and detection issues (i.e. false positives). To overcome this limitation, a multiplex system was designed and built able to scan the sample by automatically switching between the different wires, synchronising the length of the excitation for each wire and regulating the current; this reduces the power requirements since the multiplex system requires only a single power supply channel to be connected. The curves captured with the multiplex system are presented in Figure 11 and show a trend similar to the one observed in the single wire configuration. In this case, however, due to the scanning system, the heating is limited at a defined time interval. The interval between the excitation of each wire plays a fundamental role in the output of the results. In particular, it was found that when the interval time τ is too small (in the interval between 5-500 ms) the generated heat wave at first is not able to reach the surface and it slowly diffuses into the laminate bulk. This slow propagation is able to "mask" the presence of the internal damaged area since the heat front has enough time to go around the PTFE patch and reach the top surface. For this reason the scanning time was chosen with an interval τ of 1s.

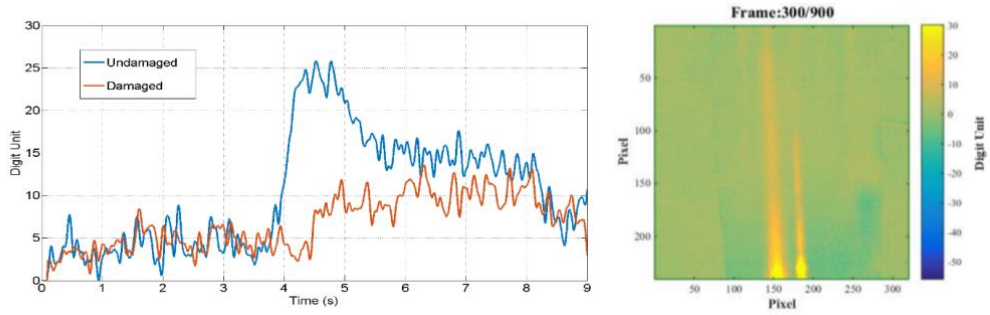

Figure 11-Apparent temperature variation and thermogram captured for Therm SMA in the multiplex configuration

Two monitoring configurations were tested: Configuration 1 shows wires and camera placed on the same side (the heat crosses only few layers before being recorded by Ir Camera) while Configuration 2 has wires and camera located on the opposite side (the heat crosses the entire sample thickness before being recorded by Ir Camera).

- ***Bottom W: Configuration 1***

Bottom W samples (impacted on the surface far from wires) were analysed by placing the infrared camera on the opposite side to the impact surface using and energy 20J and 25J. The relative position of the wires, impact surface and camera are illustrated in Figure 12:

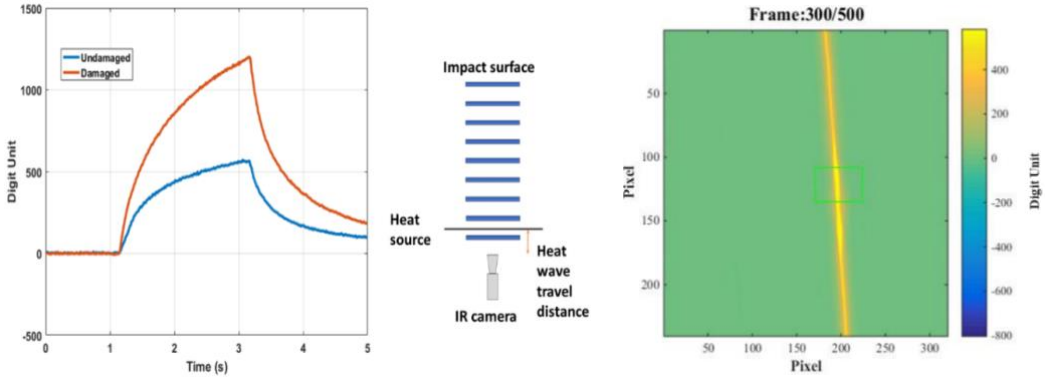

Figure 12-Thermogram and thermal behaviour after background subtraction for Bottom W (configuration 1 -20J) with relative position of wires, heat source, Ir camera and impacted area.

It shows the variation of the apparent temperature on two spots selected along the same wire: the blue curve represents an undamaged area, while the orange curve is the surface spot correspondent to the 20 J impact point. The colours-scaled image represents the location of the impact damage.

The results show an increase in the apparent temperature change in the damaged area, unlike the previous case. This can be explained by the fact that the delamination caused by the impact is located mostly above the wires (see Figure 13.a), consequently, when the wire is heated, the heatwave cannot propagate through the delamination and heat builds in the opposite direction towards the

surface monitored with the Ir camera. As a consequence, the damaged zone shows an increased apparent temperature variation in respect with the undamaged areas.

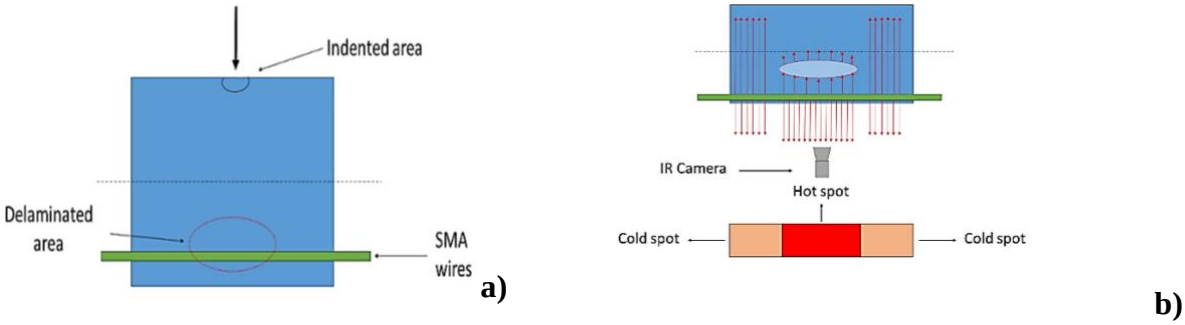

Figure 13-Bottom W layout after LVI event: a) Relative positions of wires, delamination, impacted area and camera; b) heatwave propagation (red arrows) and heat distribution scheme inside laminate interacting with the delaminated area near the wires. The camera was located close to the wires.

As shown in Figure 13.b, the heatwave is unable to propagate through the delamination due to different thermal properties and, consequently, temperature heat increases in the area free from structural discontinuity that is closer to the camera position. In other zones, the heat can flow without accumulation since no discontinuity is found. The camera, close to the wire position identifies a hot zone where the heat is accumulated (delaminated area) and several cold zones where the heat is free to propagate. Thermal results for Bottom W impacted with 25 J, are reported in Figure 14.

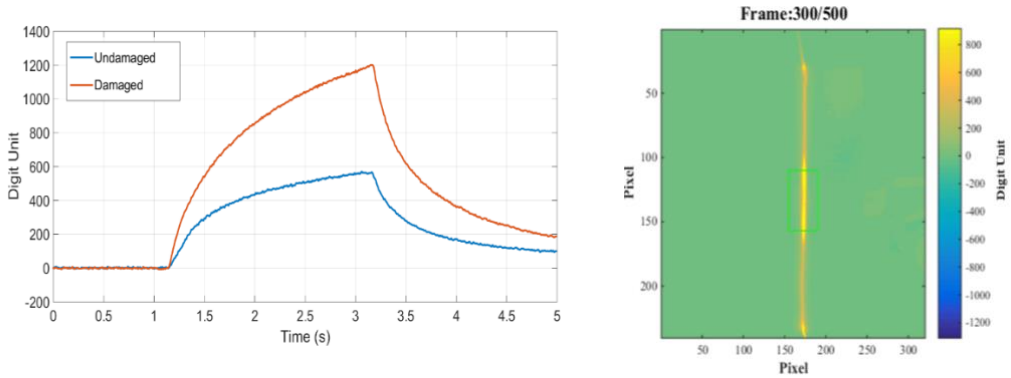

Figure 14-Thermal behaviour and thermography after background subtraction for Bottom W (Configuration 1-25J)

Impact data at 25 J is comparable to 20J, showing an increase in the apparent temperature variation on the damaged area. To investigate the effect of the impact

energy on the thermal response of the two impacted samples, the contrast was calculated with a linear subtraction between the damaged curve and the undamaged curve signals for each set of data using Equation (19).

$$C_{A_i} = \left\| A_{und_i} - A_{dam_i} \right\| \quad (19)$$

Where A_{undi} represent the signal recorded for an undamaged part on the *i*th wire, while A_{dami} is the signal recorder for a damaged point on the same *i*th wire. Figure 15.a shows that the difference between the two signals affects both the portions of the curves (heating and cooling). The contrast curve of 20J sample is characterised by a lower amplitude in the first heating portion than 25J one, and by an opposite behaviour in the cooling portion. The curve maximum point is higher for the 20 J Bottom W, even though the two peaks are not correspondent due to different turning off times. To quantify the difference between the curves, the maximum peaks difference was calculated for the undamaged curves and the damaged ones using the formula below:

$$\Delta_{peaks} = max_{S7} - max_{S1} \quad (20)$$

Where:

max_{S7} is the Maximum digit unit value of 25 J Bottom W;

max_{S1} is the Maximum digit unit value of Sample 20J Bottom W contrast.

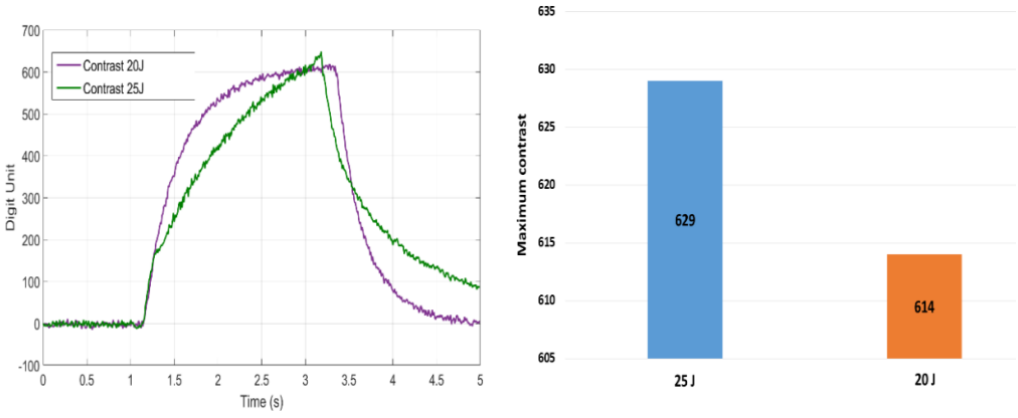

a) **b)**

Figure 15-Thermal contrast analysis for Configuration 1: a) Comparison between 25J and 20J Bottom W curves and b) comparison between maximum peaks differences of damaged and undamaged curves of 25J and 20J Bottom W.

As shown in Figure15.b, results clearly indicate the higher amplitude value of 25 J Bottom W in respect with 20J one. As illustrated previously, this difference in the contrast amplitude can be attributed to the effect of the higher extension of the delamination zone for the 25J impacted sample. A larger delaminated area (as a result of an impact at a higher energy level) affects the propagation of the heat wave in a way which is proportional with the energy level. These results show that there is a correlation between impact energy and amplitude of the contrast signal and can be used to evaluate the severity of the damaged area.

Bottom W: Configuration 2

For Configuration 2, data were collected on the same samples by placing the camera on the same face where the impact occurred (Figure 16.a). Figure16.b shows how the heatwave generated from the wire propagates towards the thermal camera. The temperature is slowed down by the delamination while in the other areas, it is free to spread out. The camera, located far from the heat generation wires, records a higher amplitude (hot spot) in the zone where the heat is free to propagate while where the delamination is present, consequently, the amplitude results to be lower, differently from the previous test.

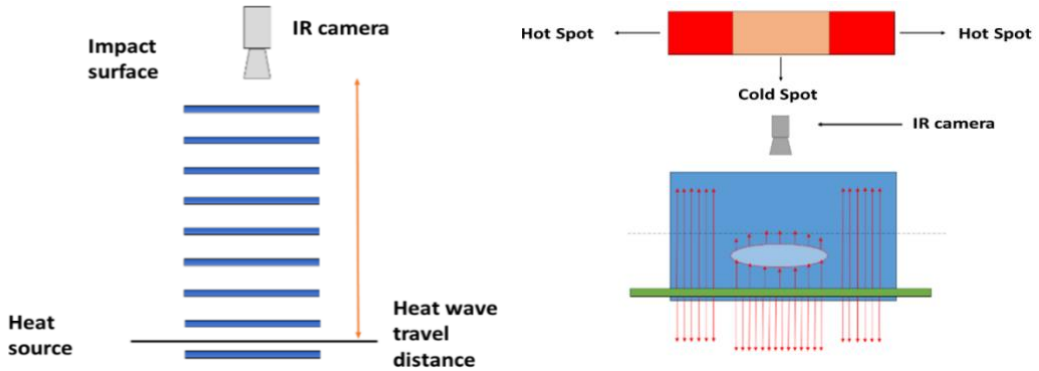

Figure 16-Layout of thermography set-up for Bottom W (Configuration 2): a) Relative position of Ir-Camera, heat source and impact location; b) heatwave propagation and heat distribution scheme inside laminate interacting with the delaminated area near the wires. The camera is located far from wires.

The relative difference between the readings collected from the damaged and undamaged areas (20J) is clear allowing identification of the presence of the damage in correspondence with the impact location as shown in Figure 17.

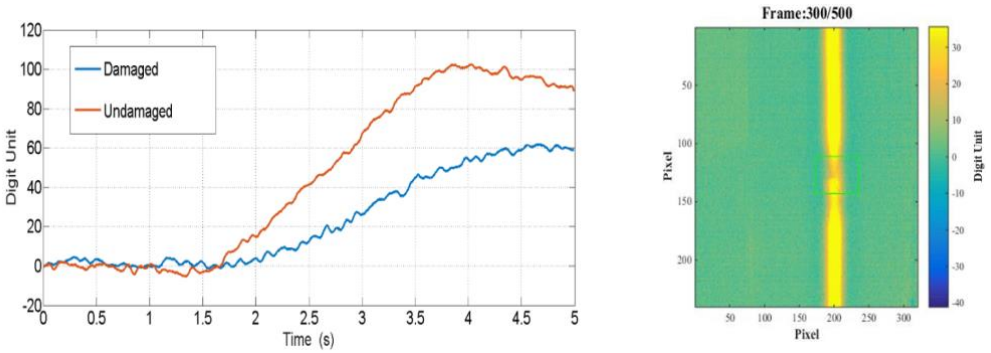

Figure 17-Thermal behaviour and thermography after background subtraction for Bottom W (Configuration 2-20J).

The presence of the impact damage but also the indentation was clearly identified. The compression of composite layers in correspondence of the contact point between penetrator tip and sample surface facilitates the diffusion of heatwave through the laminate that leads to an increase of apparent temperature in that area.

Figure 18 shows the results captured from 25J Bottom W. The image shows clearly where the damage is located as the thermogram shows different amplitude values between the undamaged and damaged zones to indicate the presence of a damaged area. Several bright spots in the central portion of the sample show the zone where the impact took place (indentation), while darker zones indicate the delaminated areas. Comparing thermograms at different level of energy (20J and 25J), it is possible to observe that on the top surface the cold area of 25J sample is larger than 20J one suggesting a more extended internal delamination generated by the higher impact energy applied. As reported for Configuration 1, the comparison between 20J and 25J Bottom W was investigated by a contrast analysis between damaged and undamaged areas.

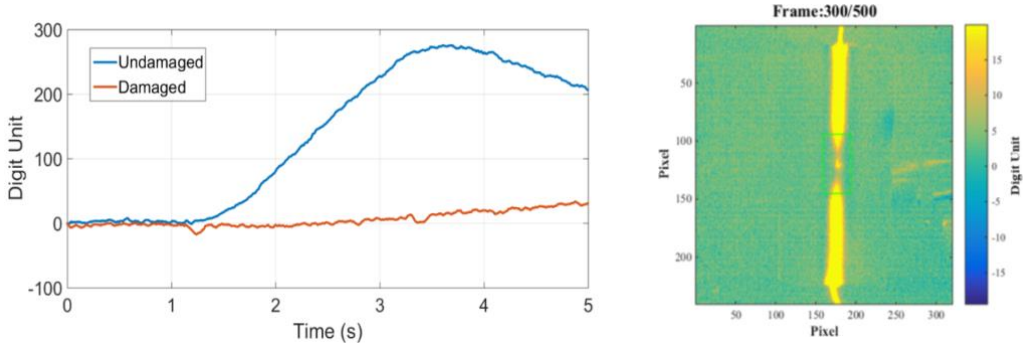

Figure 18-Thermal behaviour and thermography after background subtraction for Bottom W (Configuration 2-25J)

Figure 19.a shows that the difference between the two impact events is even more evident in this case than in the results obtained from Configuration 1. In particular, the contrast signals for the 25J appear to influence both heating and cooling portions of the signals, indicating a more extended internal damage. To quantify this difference, maximum peaks difference is done following the same approach of Configuration 1. Figure 19.b clearly indicates that 25J sample shows a higher amplitude value than 20J sample. As illustrated previously (see Figure 14) also in this case, the delamination zone is more extended in 25J Bottom W because of the higher impact energy. This case is similar to Configuration 1 results.

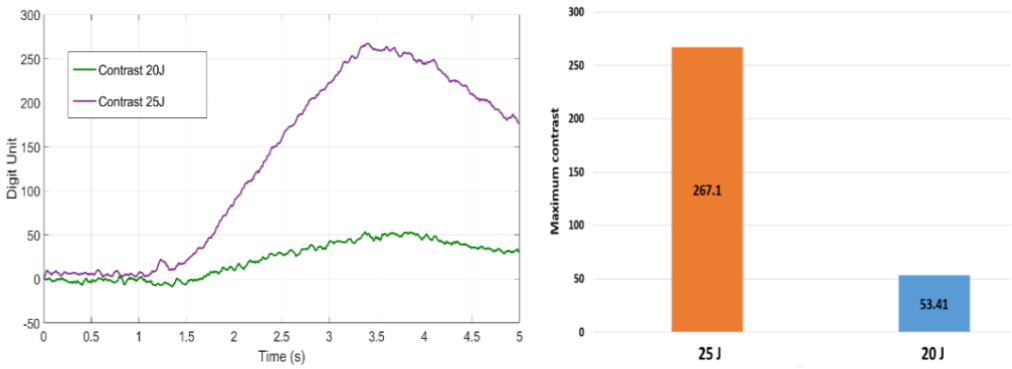

a) **b)**

Figure 19-Thermal contrast analysis for Configuration 2: a) Comparison between 25J and 20J Bottom W curves and b) comparison between maximum peaks differences of damaged and undamaged curves of 25J and 20J Bottom W.

- ***Top W: Configuration 2***

It is important to notice that Top W samples were tested by setting up the camera using Configuration 2, since this potentially is a situation more critical than Configuration 1. Since damaged area, wires and impacted area are far from the observation point, the heatwave may spread out without showing the presence of a defected area. In the case of Configuration 1 instead, the situation is similar to the Configuration 1 of Bottom W where the camera is located in proximity of the wires position, impacted area and damaged area that allow to detect easily the discontinuity inside the laminate's body. Top W samples (impacted on the surface close to wires) were analysed by placing the infrared camera on side opposite to the impact location and using energies of 20J and 25J. The results collected from Top W impacted at 20J are reported in Figure 20:

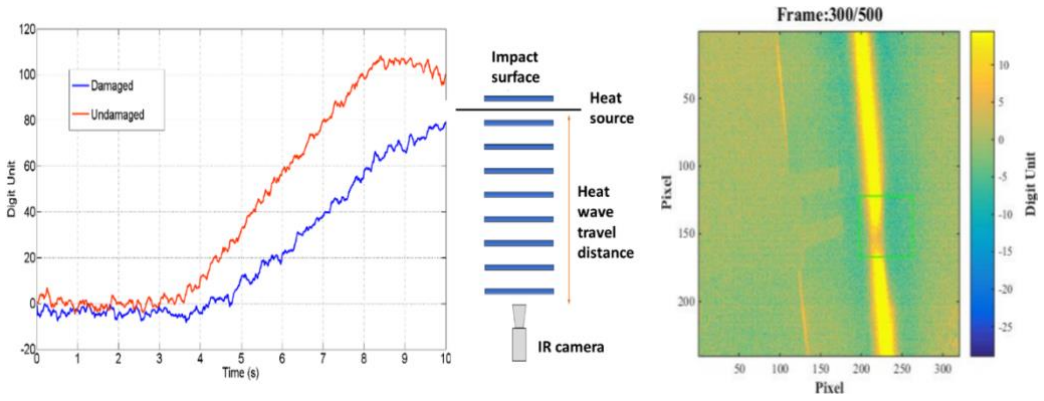

Figure 20-Thermogram and thermal behaviour after background subtraction for Top W (configuration 2 -20J) with relative position of wires, heat source, Ir camera and impacted area.

Analysing the colour map, the delamination does not cross entirely the area correspondent with the embedded wire but seems more concentrated on the right side of the image. This effect is explained with the position of the wire along the xy plane of the laminate. While in the previous case the wire chosen for the analysis was the one passing directly through the middle of the sample, in this case the wire used as heat source was placed on the side of the sample. Considering that the sample was impacted in the centre, it is expected that the damaged areas are more concentrated around the central portion of the sample rather than the sides, which were held in the sample's holder during the impact test. It is important to notice that

even though the heat source is not directly positioned on the delamination, the superficial apparent temperature gradient not only allows the identification the damaged areas, but it also gives information regarding the correct position and extent of the delamination along the xy plane of the laminate. The schematic layout is reported in Figure 21.

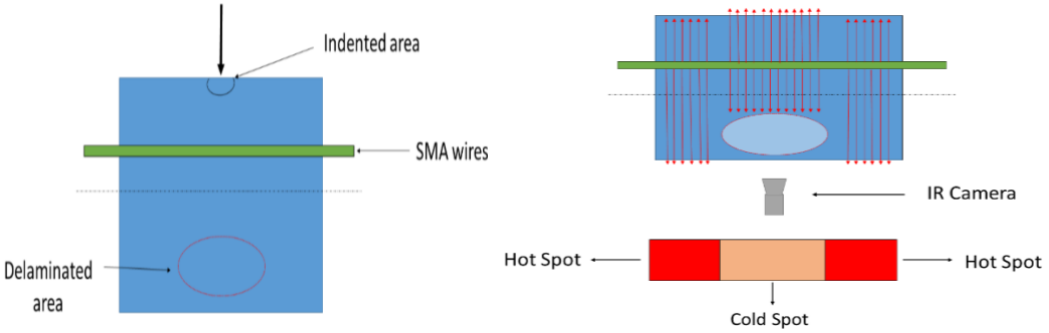

Figure 21-Top W layout after LVI event: a) relative position of wires, delamination, impacted area and camera position; b) heatwave propagation (red arrows) and heat distribution scheme inside laminate interacting with the delaminated area far from the wires. The camera is located far from wires.

Data recorded for 25 J Top W is illustrated in Figure 22 identifying damaged and undamaged areas. In this case, the delamination is far from the wires and the camera is located near to the discontinuity. The heatwave spreads out in the sample but, it slows down (cold spot) near the delamination, while, far from that zone, it is free to flows outside to be recorded from the camera (hot spot).

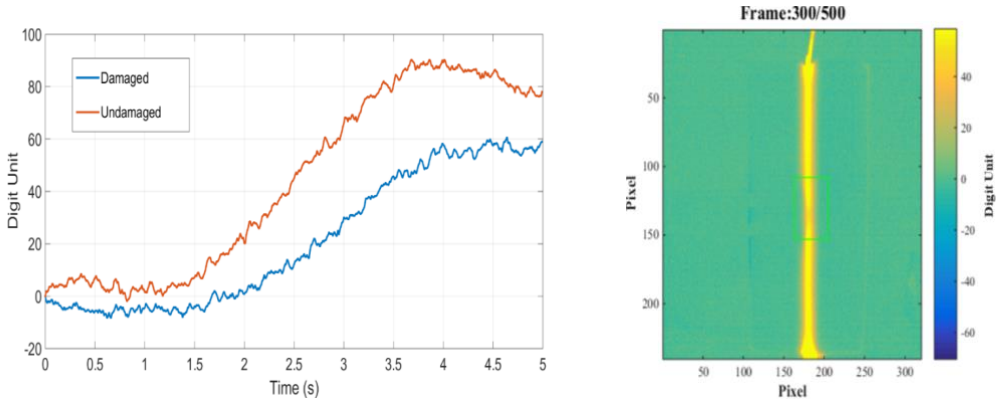

Figure 22-Thermal behaviour and thermography after background subtraction for Top W (configuration 2-25J)

The damage in the 25 J appears less evident than 20J one, but it is visible in the thermogram after the background subtraction. The thermogram shows a marked difference from the hot (undamaged areas) and cold (damaged areas) spots. To determine the entity of the difference in the damage detection, the comparison between contrast and the maximum peaks difference were calculated. From Figure 23, the contrast results similar between the two samples and it is not possible to estimate the biggest damage, even though different impact energy were used, 25J and 20J.

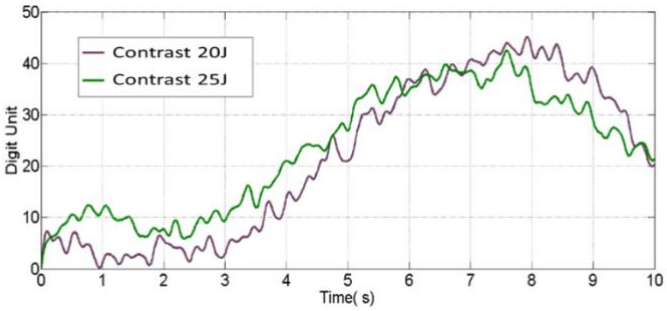

Figure 23-Thermal contrast comparison between 20J and 25J Top W (configuration 2).

This irregularity is caused by the rough thermal data in which, the data fluctuation influences the correct data trend.

- **SMA/CFRP Leading Edge with PTFE**

A Leading Edge-PTFE sample was analysed to evaluate the damaged zone in a complex structure obtaining the same quality and resolution of the analyses on plate-like structures. The PTFE patch was designed using an asymmetrical shape to confirm the validity of the technique even with complex geometry damage. Ir Camera, PTFE patch size and position, and heatwave propagation are reported in Figure 24.

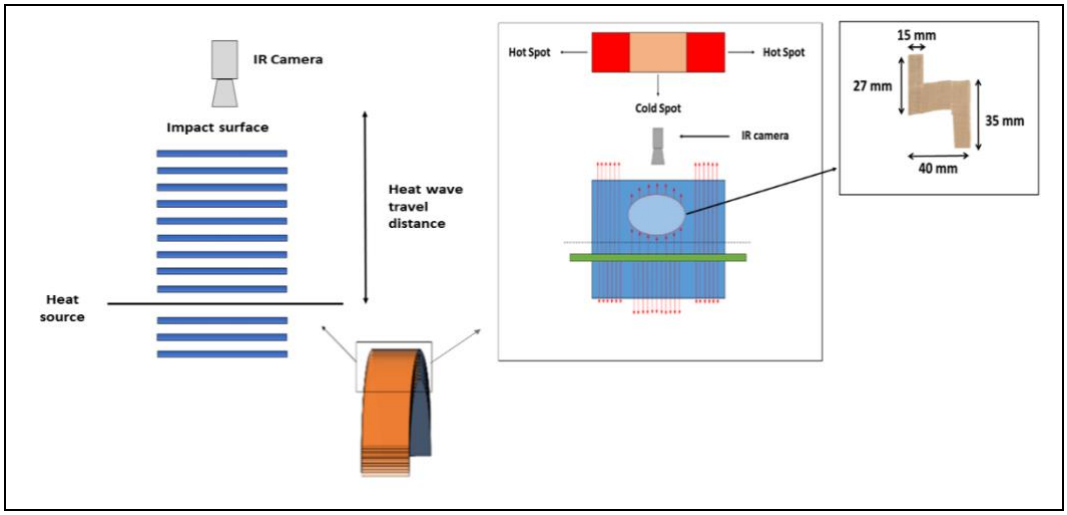

Figure 24-Leading edge PTFE layout and heatwave propagation inside hybrid CFRP composite interacting with a delaminated zone (PTFE patch geometry)

In order to test the effectiveness of the thermography, multiplex configuration was performed. The thermal data recorded by the thermal camera are reported in Figure 25

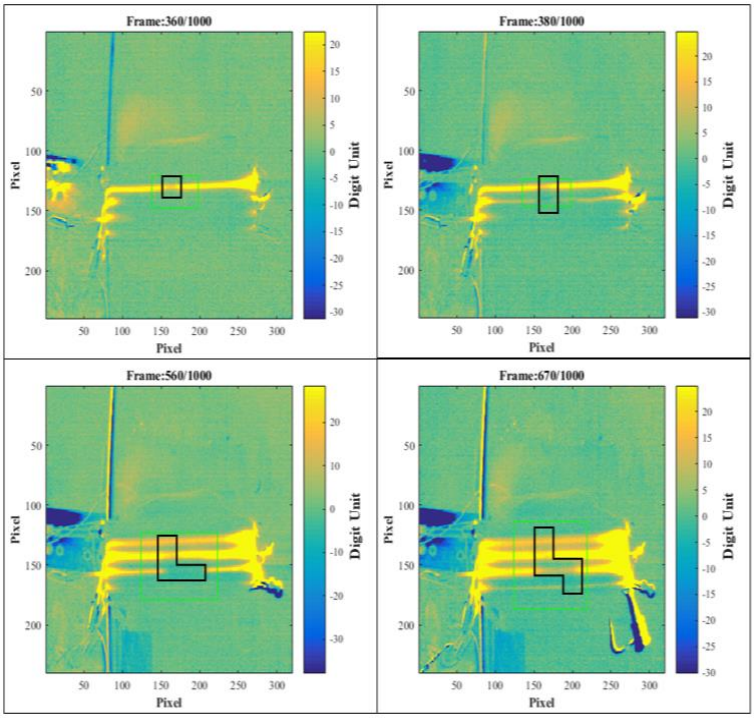

Figure 25-Thermal images evaluated after the background subtraction procedure for Leading Edge PTFE (multiplex configuration).

It is clear that the heatwave is unable to flow uniformly in the sample because of the thermal properties differences between damaged areas (PTFE patch) and CFRP and, consequently, the generation of hot spots (undamaged CFRP) and cold spots (damaged area) occurs. This behaviour is shown between different wires and it is congruent with a typical heating-cooling curve. Analysing the images, it is possible to localise different damaged areas with a similar extent for the wires 2, 3 and 5 where it is evident a small discontinuity along the wire path from which it is possible to recognise a specific pattern. In fact, it is possible to detect the damage size and position with a good precision to confirm the damage detection ability of H-CFRP laminates. The damage, in fact, results to have an asymmetrical shape, matching the original PTFE patch shape.

- **SMA/CFRP leading edge LVI**

A real internal damaged area generated by a low velocity impact was studied. Leading Edge-SMA sample was manufactured with a double layer of SMA wires to improve the impact properties and to allow a damage detection using the in-situ thermal technique after impact. The impact energy used to test this sample was set to 15 J.

In order to understand the extension of damage and the distribution inside the structure, the multiplex configuration was performed. The thermal data collected by the thermal camera are reported in Figure 26 where the apparent temperature variation of laminate surface is shown. Wire 3 shows cold spots all along its path to represent the presence of damage on all its length; while other wires were used as reference since they are free from any discontinuities. In this case, the heatwave slows down due to delamination area where air is present. The different thermal properties affect that zone, changing the thermal diffusion in that specific area. In the other sample part, instead, the heatwave is free to spread uniformly in the sample: the difference between these two areas gives an indication about the structural integrity of the hybrid laminate.

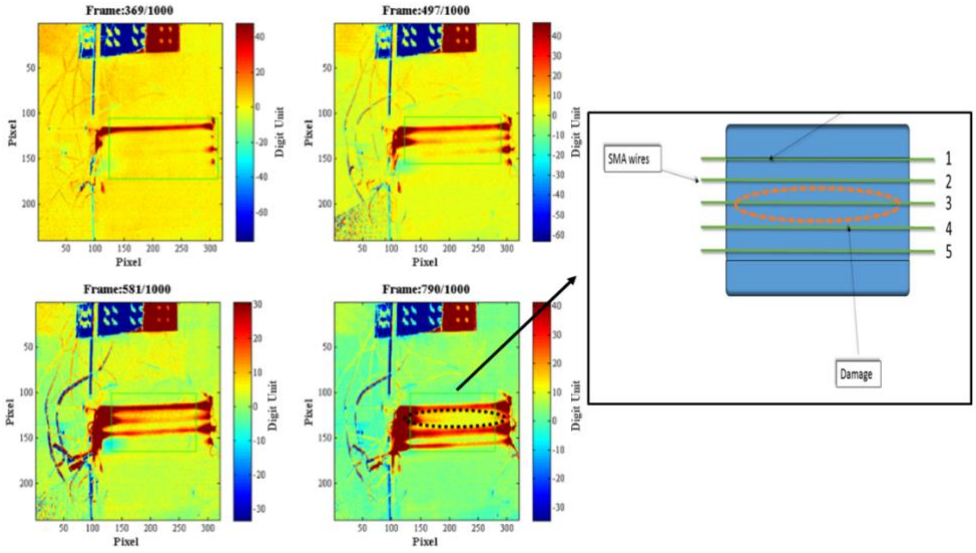

Figure 26–Thermal images of Leading Edge SMA evaluated after the background subtraction procedure (multiplex configuration) with schematic layout of damaged area position.

In fact, the delaminated area is clearly detected in the central portion of the sample, where wire 3 is located.

4.4 De-Icing system

The proposed material concept de-icing capability was investigated exploiting the thermos-resistive properties of the embedded hybrid layer. In aeronautic, ice formation on the wing surface is a common problem and requires the use of external systems to defrost the concerned surface in order to avoid incidents or crashes [54]. In fact, if ice is allowed to build up to a significant thickness, it can change the shape of aerofoil and flight control surfaces, degrading the performance, control or handling characteristics of the aircraft as reported by Bragg and al. [55]. De-icing tests were conducted on a Leading edge SMA sample. The aim of this test is to carry out a feasibility investigation to understand the potentiality of the hybrid embedded system to be employed in de-icing applications. In Figure 27.a, the thermogram was reported in reference on a central spot of the sample where each curve was evaluated in a different instant of time.

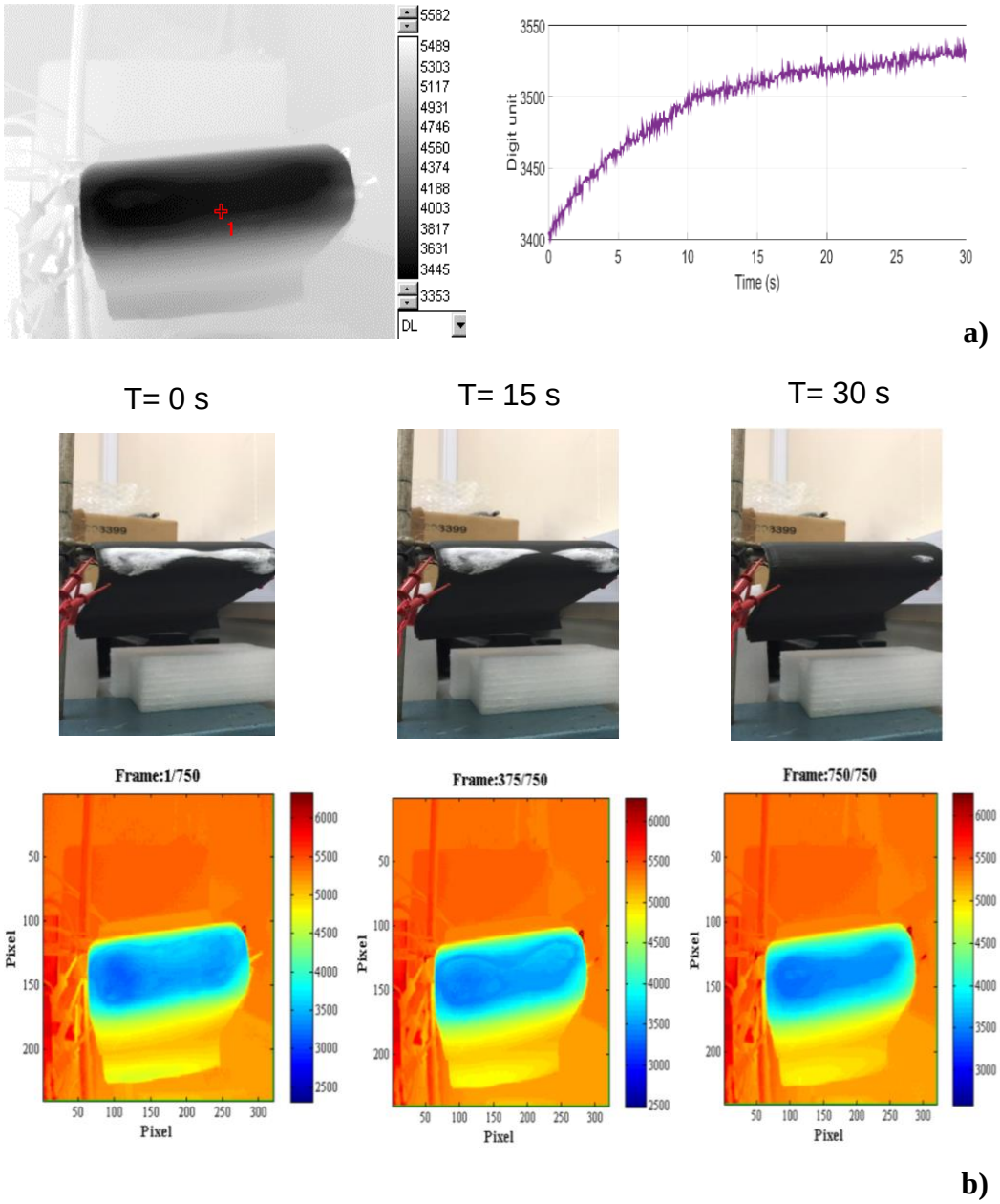

Figure 27-De -icing process on Leading Edge PTFE at different time steps: a) Thermogram of apparent temperature and b) relative thermal images reporting the ice dissolution.

It is evident the validity of the procedure to melt down the ice on the sample surface as shown in Figure 27.b. During the scanning, wires generate heat that spreads out towards the surface. This process requires a certain time to be efficient, but it is still possible to see that the ice disappears efficiently even at 15 s from the beginning of the excitation. Afterwards, the single reference point chosen for the thermogram, due to ice melting, shows no further information regarding to the condition of the

entire surface. In order to clarify the thermal distribution on whole sample surface, the apparent temperature was evaluated along two different lines: a horizontal and vertical one that crossed the reference points used in the previous tests. As shown in Figure 28, the apparent temperature results at minimum in both cases, at T=0 s, when the ice is present on the composite surface (blue curve). At T=15 s (yellow curve), the temperature increases due to wires heating. Along x-axis, its distribution remains congruent with the previous curve even if at higher temperature; while along the y-axis, apparent temperature increases more on the ends the sample than on the centre. At T= 30 s the ice is mostly dissolved on the entire sample. Along the x-axis the apparent temperature remains the same on the centre, but changes on the ends where sensibly increases. Along y-axis, instead, apparent temperature appears mostly the same even if increase slightly on the borders. The data shows an optimal behaviour in de-icing ability as ice is completely disappeared from sample surface in 30s of thermal excitation. Consequently, it is free from any defects that may cause interferences on the aerodynamic design. It is important to underline that the generated heat is directly proportional to the applied electrical current (temperature) and the time of activation. For instance, considering the experimental parameters used for a single wire, a voltage of 3.04 V and 0.55 A is applied in order to generate 1.67 W of thermal power P (Joule's effect). A preliminary estimation of the required deicing energy is calculated using the formula:

$$Q_{tot} = Q_{lh} + Q_f = m_{ice}(C_{lh} + C_f(T_0 - T_f)) \qquad (21)$$

where C_{lh} and C_f are ice the specific heat of fusion (333.55 kJ/kg) and specific heat capacity (4.18 kJ/(kg·K)) respectively, m_{ice} is the mass of the ice layer, T_0 is the initial temperature measured on the sample surface (-30°C) and Tf is the final temperature acceptable for deice requirements (+6°C) [56]. The mass of ice is calculated considering leading edge area extension of 0.015 m^2, thickness of 3 mm (volume of 4.5E-5 m^3) and ice density (0.92 kg/m3). Using these values in equation 21, the resultant energy for deicing is estimated around 20 J/(kg·K). Considering the available thermal power and the required thermal energy for the deicing, the minimum time of activation tact can be estimated using the formula:

$$t_{act} = \frac{Q_{tot}}{P}. \quad (22)$$

The time of activation of the system is then calculated and around 12 s are required for each wire to allow the leading edge surface to reach the optimal temperature and minimize the adhesion of the ice layer on sample surface allowing aerodynamic interactions to remove it [56]. According to this preliminary estimation, it is clear that the system can be tuned to generate the right amount of heat to deice the leading edge surface in function of the ambient conditions. Indeed, it is important to notice that for extremely cold environments (temperature lower than -30°C) in order to reach the optimal surface temperature and melt down the ice layer, the deicing system has to be activated for a longer interval of time with an optimized current feed since mechanical properties could be locally affected by the temperature increase as already discussed previously. It is also important to underline that some operative parameters can influence this calculation including the distance between external surface of the component and the metal wires, since a shorter time interval is required to reach the melt-down temperature on the part. Following a different approach and applying a lower current for a longer time period, instead, it is possible to obtain a uniform temperature over all the surface that is potentially suitable during off-service schedule to avoid the ice formation on critical surfaces. In addition, the heating system also can be used to maintain an optimal constant temperature during in-service operations to prevent mechanical properties detriment due to low temperature [57-59]. Therefore, by carefully tuning the length of the excitation and the intensity of the current it is possible to generate an internal heatwave strong enough to melt ice formation while providing for a safety device to avoid the mechanical properties reduction in extremely cold environments.

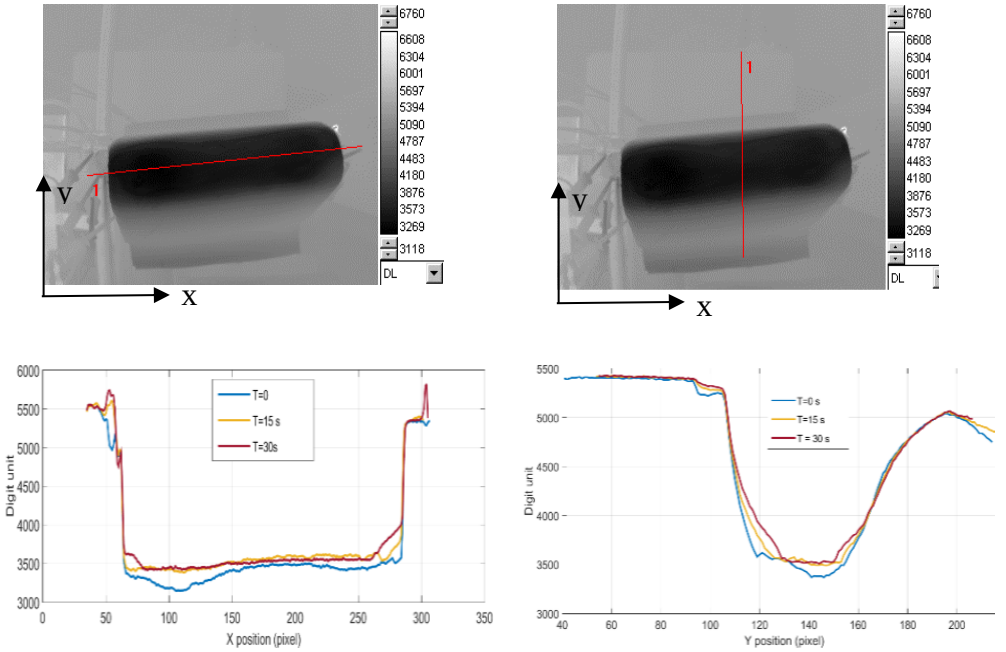

Figure 28 –Thermogram of apparent temperature along sample x-axis and y-axis.

5. Conclusions

This study proposes a smart multifunctional composite material where a hybrid phase (metal wires and carbon fibres) allows impact resistance enhancement, strain monitoring, damage detection and de-icing. Several typologies of samples were experimentally tested investigating the advantages of the smart network embedded within the CFRP. The effect of the hybridisation on the impact properties was investigated locating the metal array at different positions along the laminate's thickness and subjecting the samples to low-velocity impacts. A smaller delaminated area (-4%) were recorded with respect to a traditional CFRP when the hybrid phase was placed into the compressive portion of laminate with global weight increase only of 1%. The strain sensing ability was evaluated by measuring the electrical resistance variation of the array in presence of a distributed and a concentrated load. Both cases reported a congruent correlation with the theoretical model and, in particular, in the concentrated case, it was possible to identify the specific point where the load was applied. Furthermore, once that the system records the evidence of an impact event, the presence of a damaged area can be

identified within the laminate's body using Ir damage detection technique. The hybrid phase can be used as a heat source exploiting its thermo-resistivity via Joule effect by applying an electrical current on the wires, while an Ir camera records thermal data. The proposed approach allows scanning composite structures to detect delaminated areas, cracks or other BVIDs, while optimising power consumption and inspection time. Both simulated (PTFE patch) and real damage were successfully identified on both flat panels and leading edge geometries. Finally, de-icing capability was demonstrated. The results showed that it was possible to remove an ice layer from the leading edge surface by performing a thermal scanning of 30s and focusing the power only on the wires that surround the very edge of the sample using the multiplex system. The proposed smart material concept could improve the safety and reliability of aircraft structures and reduce maintenance costs.

Acknowledgements

This paper has been funded by the EXTREME project of the European Union's Horizon 2020 research and innovation programme under grant agreement No. 636549.

REFERENCES

[1] Abrate S. Impact on laminated composite materials. Appl Mech Rev. 1991;44:155-90.

[2] CHEN G, BIDINGER G, LOU M. IMPACT DEMAGE TOLERANCE OF THIN WALL COMPOSITE STRUTS. 34th Structures, Structural Dynamics and Materials Conference1993. p. 1398.

[3] Recker H. Highly damage tolerant carbon fiber epoxy composites for primary aircraft structural applications. 34 INTERNATIONAL SAMPE SYMPOSIUM AND EXHIBITION, 19891989. p. 747-58.

[4] Russell AJ, Street KN. The effect of matrix toughness on delamination: static and fatigue fracture under mode II shear loading of graphite fiber composites. Toughened composites: ASTM International; 1987.

[5] Tissington B, Pollard G, Ward I. A study of the impact behaviour of ultra-high-modulus polyethylene fibre composites. Composites Science and Technology. 1992;44:197-208.

[6] Yuan Q, Wu D, Gotama J, Bateman S. Wood fiber reinforced polyethylene and polypropylene composites with high modulus and impact strength. Journal of Thermoplastic Composite Materials. 2008;21:195-208.

[7] Ko FK, Hartman D. Impact behavior of 2-D and 3-D glass/epoxy composites. Materials Science for the Future: 31 st International SAMPE Symposium and Exhibition1986. p. 1272-84.

[8] Liu D. Delamination resistance in stitched and unstitched composite plates subjected to impact loading. Journal of Reinforced Plastics and Composites. 1990;9:59-69.

[9] Lopresto V, Melito V, Leone C, Caprino G. Effect of stitches on the impact behaviour of graphite/epoxy composites. Composites Science and Technology. 2006;66:206-14.

[10] Kim J-K, Sham M-L. Impact and delamination failure of woven-fabric composites. Composites Science and Technology. 2000;60:745-61.

[11] Ishai O, Shragai A. Effect of impact loading on damage and residual compressive strength of CFRP laminated beams. Composite Structures. 1990;14:319-37.

[12] Bunsell A, Harris B. Hybrid carbon and glass fibre composites. Composites. 1974;5:157-64.

[13] Naik N, Ramasimha R, Arya H, Prabhu S, ShamaRao N. Impact response and damage tolerance characteristics of glass–carbon/epoxy hybrid composite plates. Composites Part B: Engineering. 2001;32:565-74.

[14] Marom G, Drukker E, Weinberg A, Banbaji J. Impact behaviour of carbon/Kevlar hybrid composites. Composites. 1986;17:150-3.

[15] Vogelesang L, Marissen R, Schijve J. A new fatigue resistant material: Aramide Reinforced Aluminium Laminate (ARALL). 1981.

[16] Gunnink J, Vogelesang L, Schijve J. Application of a new hybrid material (ARALL) in aircraft structures. Proceedings of the 13th Congress of the International Council of the Aeronautical Sciences (ICAS), Washington1982. p. 990-1000.

[17] Vlot A. Glare: history of the development of a new aircraft material: Springer Science & Business Media, 2001.

[18] Vlot A, Gunnink J, Alderliesten R, Van der Hoeven W, de Boer A, Hart W, et al. Towards technology readiness of fibre metal laminates- Glare Technology Development(GTO) 1997-2000. ACUN- 3 International Composites Conference, Proceedings, Sydney, Australia, Feb 5-9, 2001, Sydney 2052, Australia, University of New South Wales, 20012001. p. 243-56.

[19] Bradley P, Harris S. Strategic reinforcement of hybrid carbon fibre-reinforced polymer composites. Journal of Materials Science. 1977;12:2401-10.

[20] Paine JS, Rogers CA. The response of SMA hybrid composite materials to low velocity impact. Journal of Intelligent Material Systems and Structures. 1994;5:530-5.

[21] Abry J, Bochard S, Chateauminois A, Salvia M, Giraud G. In situ detection of damage in CFRP laminates by electrical resistance measurements. Composites Science and Technology. 1999;59:925-35.

[22] Schulte K, Baron C. Load and failure analyses of CFRP laminates by means of electrical resistivity measurements. Composites Science and Technology. 1989;36:63-76.

[23] Cui D, Song G, Li H. Modeling of the electrical resistance of shape memory alloy wires. Smart Materials and Structures. 2010;19:055019.

[24] Nagai H, Oishi R. Shape memory alloys as strain sensors in composites. Smart Materials and Structures. 2006;15:493.

[25] Meola C, Carlomagno GM. Recent advances in the use of infrared thermography. Measurement science and technology. 2004;15:R27.

[26] Sakagami T, Kubo S. Applications of pulse heating thermography and lock-in thermography to quantitative nondestructive evaluations. Infrared Physics & Technology. 2002;43:211-8.

[27] Maierhofer C, Brink A, Röllig M, Wiggenhauser H. Transient thermography for structural investigation of concrete and composites in the near surface region. Infrared Physics & Technology. 2002;43:271-8.

[28] Suzuki Y, Todoroki A, Mizutani Y. Diagnosis for CFRP aircraft by Joule heating using lightning protection system. Proceedings of 12th Japan International SAMPE Symposium & Exhibition: Japan SAMPE; 2011.

[29] Ahmed T, Nino G, Bersee H, Beukers A. Heat emitting layers for enhancing NDE of composite structures. Composites Part A: Applied Science and Manufacturing. 2008;39:1025-36.

[30] Orłowska A, Kołakowski P, Holnicki-Szulc J. Detecting delamination zones in composites by embedded electrical grid and thermographic methods. Smart Materials and Structures. 2011;20:105009.

[31] Martin CA, Putt JC. Advanced pneumatic impulse ice protection system (PIIP) for aircraft. Journal of Aircraft. 1992;29:714-6.

[32] Graber DJ, Mack GJ. Acoustical anti-icing system. Google Patents; 1991.

[33] BOND T, Shin J. Results of Low Power Deicer tests on a swept inlet component in the NASA Lewis Icing Research Tunnel. 31st Aerospace Sciences Meeting1993. p. 32.

[34] Hydro M. Ice Storm Management of Overhead Lines. CEA Workshop, Ier1993.

[35] Yasui M, Maekawa K, Naganuma Y, Suzuki K, Kojima Y, Ando H. Removal of icy snow accumulation on the transmission line by applying LC-spiral rod. Fujikura Technical Review. 1987;16:26-33.

[36] Giamati MJ. Electrothermal de-icing system. Google Patents; 1997.

[37] Pinto F, Ciampa F, Meo M, Polimeno U. Multifunctional SMArt composite material for in situ NDT/SHM and de-icing. Smart Materials and Structures. 2012;21:105010.

[38] Chien A-T, Cho S, Joshi Y, Kumar S. Electrical conductivity and Joule heating of polyacrylonitrile/carbon nanotube composite fibers. Polymer. 2014;55:6896-905.

[39] Kernin A, Wan K, Liu Y, Shi X, Kong J, Bilotti E, et al. The effect of graphene network formation on the electrical, mechanical, and multifunctional properties of graphene/epoxy nanocomposites. Composites Science and Technology. 2019;169:224-31.

[40] Pinto F, Maroun F, Meo M. Material enabled thermography. NDT & E International. 2014;67:1-9.

[41] Ogisu T, Ando N, Takaki J, Okabe T, Takeda N. Improved Surface Treatment of SMA Foils and Damage Suppression of SMA-Foil Embedded CFRP Laminates. Journal of Intelligent Material Systems and Structures. 2001;12:265-70.

[42] Angioni SL, Meo M, Foreman A. Impact damage resistance and damage suppression properties of shape memory alloys in hybrid composites—a review. Smart Materials and Structures. 2011;20:013001.

[43] Yang R, Xu XS, Li KZ. The Influence of Metal Surface Roughness on Bonding Strength of Metal and Composite Material. Advanced Materials Research. 2015;1095:879-82.

[44] Kwon YS, Sankar BV. Indentation-flexure and low-velocity impact damage in graphite epoxy laminates. Journal of Composites, Technology and Research. 1993;15:101-11.

[45] Nettles AT, Douglas MJ. A comparison of quasi-static indentation to low-velocity impact. 2000.

[46] Hawileh RA, Abu-Obeidah A, Abdalla JA, Al-Tamimi A. Temperature effect on the mechanical properties of carbon, glass and carbon–glass FRP laminates. Construction and Building Materials. 2015;75:342-8.

[47] Wolfrum J, Eibl S, Lietch L. Rapid evaluation of long-term thermal degradation of carbon fibre epoxy composites. Composites Science and Technology. 2009;69:523-30.

[48] De Giorgi M, Nobile R. A possible use of SMArt thermography for the control of GFRP composite laminate. Procedia Structural Integrity. 2018;12:239-48.

[49] Wilson CD. Linear elastic fracture mechanics primer. 1992.

[50] Khalili S, Shokuhfar A, Ashenai Ghasemi F, Malekzadeh K. Dynamic response of smart hybrid composite plate subjected to low-velocity impact. Journal of composite materials. 2007;41:2347-70.

[51] Macaulay W. Note on the deflection of beams. The Messenger of Mathematics. 1919;48:129-30.

[52] Gibson RF. Principles of composite material mechanics: CRC press, 2016.

[53] Botelho EC, Silva RA, Pardini LC, Rezende MC. A review on the development and properties of continuous fiber/epoxy/aluminum hybrid composites for aircraft structures. Materials Research. 2006;9:247-56.

[54] COLE J, SAND W. Statistical study of aircraft icing accidents. 29th Aerospace Sciences Meeting1991. p. 558.

[55] Bragg M. Aircraft aerodynamic effects due to large droplet ice accretions. 34th Aerospace Sciences Meeting and Exhibit1996. p. 932.

[56] Meier O, Scholz D. A handbook method for the estimation of power requirements for electrical de-icing systems. DLRK, Hamburg. 2010;31.

[57] Sánchez-Sáez S, Gómez-del Rıo T, Barbero E, Zaera R, Navarro C. Static behavior of CFRPs at low temperatures. Composites Part B: Engineering. 2002;33:383-90.

[58] Nettles A, J. Biss E. Low Temperature Mechanical Testing of Carbon-Fiber/Epoxy-Resin Composite Materials1996.

[59] Zaoutsos S, Zilidou M. Influence of extreme low temperature conditions on the dynamic mechanical properties of carbon fiber reinforced polymers. IOP Conference Series: Materials Science and Engineering: IOP Publishing; 2017. p. 012024.

.

5 CHAPTER: Toughness improvement via the introduction of a 3D discontinuity pattern

5.1 Context

Paper B illustrates the design, manufacturing and characterisation of a bioinspired discontinuous laminated material which showed enhanced toughness with a relatively small loss of mechanical properties. The aim of this work was to hybridise the structure by introducing resin discontinuities along the fibres length following a 3D hierarchical pattern inspired by the brick-and-mortar inner structure of nacre (as shown in Section 3.2.2.3), obtaining a hybrid structure showing enhanced toughness and drapability compared to traditional structures. The mechanical properties of this structure can be estimated using modified micromechanics of lamina theory (Section 3.2.2.2) for the single hybrid layer and standard macromechanics of laminate theory for the laminate's properties (Section 2.2.5). The enhancement of toughness is due to the presence of the pattern of resin pockets which mimics the nacre structure. This pattern changes the failure mechanisms of the structure during out-of-plane loading and enables the generation of a higher amount of crack surfaces with a consequent increase of absorbed energy. This work analysed the influence of the manufacturing parameters (distance between in-plane discontinuities) on the mechanical and impact proprieties obtaining a hybrid material which was able to absorb high impact energy and exhibited high drapability. This enhanced property was experimentally tested under Low-Velocity impact conditions and the data was used to validate a numerical model developed to predict the impact behaviour of the material and analyse its

stress distribution during the dynamic event, not possible during experimental testing. Damage extent was also evaluated both experimentally and numerically.

The use of hybridisation for enhancing impact properties by introducing discontinuities into the laminate reinforcement not only enables the improvement of the toughness of the material but also enables an important non-structural benefit: the enhancement of drapability (see Section 3.2.2.4). This is due to the intrinsic nature of a laminate structure with discontinuous reinforcement which is able to locally adapt to a shape without residual stress or wrinkles as reported in the literature review.

The original contribution of this research lies in the uniqueness of the manufacturing techniques used to introduce nacre' structure within multiangle laminates, the synergic static and impact characterisation of the mechanical properties, and the development of a numerical model used to predict and describe the flexural and impact response of the material.

The Statement of Authorship Form and the paper can be found next.

This declaration concerns the article entitled:	
3D bio-inspired hierarchical discontinuous CFRP with enhanced ductility	
Publication status (tick one)	
Draft manuscript	
Submitted	
In review	
Accepted	

Published	✓
Candidate's contribution to the paper (detailed, and also given as a percentage)	
The candidate contributed to/ considerably contributed to/predominantly executed the…	
Formulation of ideas:	80% The idea was formulated together with my supervisor. I ideated the process to introduce the 3D discontinuity pattern in flexural and impact samples. My supervisor suggested how to aid several technical issues during the development.
Design of methodology:	100% I manufactured all the samples using in the experimental campaign and developed the numerical model used to predict the structures mechanical response and failure mechanisms.
Experimental work:	100% I carried out the flexural and impact experimental campaigns, collected the data, processed the outputs and sorted the results.
Presentation of data in journal format:	90% I designed the manuscript structure, wrote all the drafts and realised all the figures. Feedback on the draft and help for the paper submission and review were provided by my supervisors.
Statement from Candidate	
This paper reports on original research I conducted during the period of my Higher Degree by Research candidature.	

Signed		**Date**	26/05/2020

3D bio-inspired hierarchical discontinuous CFRP with enhanced ductility

Francesco RIZZO, Fulvio PINTO, Michele MEO*

Mechanical Engineering Department, University of Bath, Bath, United Kingdom

* corresponding author: m.meo@bath.ac.uk

Keywords: Ductility, impact, discontinuous fibre;

ABSTRACT

Impact Discontinuous Carbon Fibre Reinforced Polymers (DCFRPs), due to their increased drapability, allow manufacturing of complex components that continuous CFRPs are unable to replicate. However, these materials might have reduced mechanical properties given by the loss of reinforcement continuity. This paper proposes a new bio-inspired pattern configuration of DCFRPs for the improvement of the mechanical properties (e.g. strain to failure and toughness) by exploiting failure mechanisms such as crack deflection and fibres pull-out, while preserving the high formability of DCFRPs. Resin pockets are introduced and arranged in specific three-dimensional patterns to mimic the hierarchical distribution of hard and soft phases typical of several biological systems. Finite Element models for three-point bending and Low-velocity impact tests were developed to optimise patterns and understand failure mechanisms experienced during static and dynamic tests. Experimental tests were carried out on the 3D hierarchical structures to prove its effectiveness in unidirectional and cross-ply CFRP stacking sequences. Good agreement was obtained between the numerical and experimental results especially in the prediction of the absorbed impact energy. The results demonstrated the effectiveness of the bio-inspired solution in improving the absorbed impact energy of CFRP while increasing drapability of existing prepreg materials.

1. Introduction

Over the last ten years, Carbon Fibre Reinforced Polymers (CFRPs) structures have become common in a wide variety of structural applications including aerospace, automotive and railways in which materials with high strength-to-weight ratio are necessary to improve performance and to reduce energy consumption [1]. However, a key limitation of the extensive use of these materials is their limited drapability especially in reproducing complex geometries. Drapability or formability [2] is the ability of the uncured material to adapt its shape on a complex mould during its lamination procedure. This is, in fact, a critical parameter for the use of fibres in complex manufacturing procedures since, due to their high stiffness, they are difficult to deform and adapt on a surface parallel to their orientation. In order to overcome this drawback and increase the appeal from advanced industry for this material, several studies proposed the introduction of discontinuities along the fibres length in order to improve the material drapability [3-5]. Indeed, shortening the continuous long fibres, fibres have an increased mobility in the location of the discontinuities [4, 6] that allows to the material to follow more extreme curvatures and profiles, and, thus, to be employed for a wider number of applications where high formability is required. However, discontinuous CFRP structures show lower in-plane mechanical properties in comparison with continuous one [7] due to their "softer" zones (discontinuities) and consequent stress intensification (notch sensitivity factor) in their location [8]. This behaviour, the intrinsic layered nature and the low impact resistance along the out-of-plane direction leads this material to be very sensitive against Barely Visible Impact Damage (BVID) under Low velocity Impact (LVI) conditions. Based on these considerations, the overdesign of the composite primary structure with a high safety factor [9] is then required and consequently, the benefits of using composite structures are partially lost.

A possible approach to overcome this limitation is the systematic design and optimisation of the discontinuities position in order to minimise the in-plane

mechanical properties detriment of CFRP and guarantee its high formability during the manufacturing operations. Furthermore, discontinuities can be organised in patterns whose location and distribution can be studied and optimised to promote the introduction of a non-linear failure behaviour i.e. pseudo-plasticity [10] that similarly to plasticity into metals, it is able to create a plateau into the characteristic stress-strain curve of laminated material. This new mechanical feature can, not only, increase strain at failure, toughness and impact response of the material but also to provide for a visible warning of the structural damage allowing a prompt intervention before the sudden and catastrophic collapse of the structure.

The maximum expression of discontinuities pattern optimisation can be found in nature where several bio-composite materials can be identified in biological systems including bones [11], wood [12], molluscs exoskeleton including shrimps and abalone [13], and in the inner shell layer of mother–of pearl (nacre) of bivalve molluscs. The main function of the nacre and cuticle exoskeleton is the protection of the inner organs from external menaces. Nacre [14-16] consists of a brick-and-mortar composite structure with short aragonite (made of CaCO3 agglomerates) tablets acting as rigid reinforcement embedded within organic viscoelastic matrix in which, the discontinuities between two adjacent rigid components are organised in a hierarchical architecture. This hierarchical organisation [17] spans multiple length scales from nanoscale to macroscale [18-20] and is the main reason for the interesting properties that characterise the excellent mechanical behaviour of the structure. Indeed, even if the main brittle components (aragonite rigid tablets), the nacre is able to reach high deformations [21] and in terms of ultimate strength intensity factor, it has been proven to be between 30 and 40 times tougher than monolithic aragonite. This improved toughness is due to several additional mechanisms including strain hardening, tablets pull-out, damage diffusion and crack deflection contribute to improve the toughness of the material, dissipating a higher amount of energy during the failure of the hierarchical structure. Strain hardening [22, 23] is due to the sliding of the different aragonite tablets ahead and around the open crack where both interlock and matrix friction provide a further

friction factor which increases the energy dissipation. Tablets pull-out [24] is the consequence of tablets sliding that results in the bridging of crack surfaces with a limited effect on energy dissipation via friction. The most effective mechanism of energy dissipation is the crack deflection [25, 26] due to the hierarchical arrangement of the bio-composite structure. This structure provides an efficient load transfer between the different aragonite tablets and throughout the pattern of discontinuities located between two adjacent tiles and along the thickness direction. This leads to matrix shear failure with crack surfaces that propagate around the reinforcement showing no failure during this process. Consequently, a longer crack path is generated within the structure with relative creation of a higher number of new surfaces dissipating a larger amount of energy [8] via plasticity (non-linear mechanics). Following this concept, several works have been focused on the adaptation of nacre microstructure with the development of bio-inspired hybrid composite materials using traditional ones such as CFRP [27] and GFRP [28]. Using nacre structure as inspiration and considering that the main source of its unique failure behaviour is the well-designed hierarchical structure, an adaptation process is performed by mimicking the organisation of its short reinforcement into the laminated composite. Indeed, by organising the fibrous reinforcement as the rigid component of nacre and considering the polymeric matrix as soft components, it is possible to create a discontinuities pattern inside the laminate structure. This leads to the activation of several pseudo-plastic mechanisms, typical of nacre mechanical behaviour that can increase the toughness and strain at failure of the brittle composite structure improving the impact response of the material. Attempts [27, 29] in creating a hierarchical discontinuous structure within a unidirectional CFRP laminate consists in inserting of several discontinuities as resin pattern into the CFRP structure by cutting every single ply along its width and aligning the two ends at a certain variable distance. The procedure was periodically repeated with an offset along the samples thickness by overlapping the different discontinuous layers to create a zig-zag pattern. In-plane and flexural mechanical properties of this structure were tested using uniaxial tensile and a three-points bending tests. From these, it was clear that the crack could propagate with no damage on reinforcement

fibres leading to an increase of the global toughness of the material. Different configurations were tested in function of the offset distance and gap length, and good results were obtained analysing the strain at failure after tensile tests. Even though, a reduction of maximum strength was observed due to the notch sensitivity generated by the discontinuities presence.

Even though the observed results are remarkable, several manufacturing issues were evaluated during production procedure including accurate locating of discontinuities and optimal distribution of their pattern that represent a limit of the industrial application. The development of novel manufacturing procedures, including high precision laser-cut and 3D printing, in fact, can offer a solution to this production issue since they allow controlling position and finishing of resin patterns with a higher accuracy and higher freedom in the geometrical shapes than traditional manufacturing. In particular, 3D printing technologies allows the grown control of the structure during the manufacturing process adapting its architecture alongside the material fabrication. X.Gu et al. [30] studied an emerging manufacturing process based on the use of 3D printing technologies to obtain a hierarchical microstructure of nacre within a laminated material. During the manufacturing procedure, two different typologies of thermoplastic resins at high and low moduli were used to simulate the reinforcement and the matrix component respectively. Each ply was then manufactured, stacking up the different layers using a cross-ply lamination sequence and the impact properties were evaluated using an impact rig. Comparing the results with a monolithic configuration, the superior impact properties of hierarchical structure were shown and used to validate a numerical model. However, CFRP has no immediate applications in 3D printing technologies since the use of structural thermoplastic polymers is still under development. Narducci et al. [31] used laser cut technology to create a complex and optimised pattern of CFRP tiles in order to maximise strain hardening and damage deflection phenomena. An hourglass tiles shape was optimised to add a friction component during failure via tiles-interlocking when sliding and pull-out mechanisms occur. Moreover, in order to include a crack deflection component, a

pattern of discontinuities was introduced along the thickness direction by overlapping the tiles by half of their length. Three-point bending tests results were shown reporting an absence of brittle failure under out-of-plane loading conditions.

Based on literature and developing an innovative manufacturing procedure to introduce the resin pattern in cross-ply CFRP structures, this work is focused on the design and characterisation of a discontinuous bio-inspired laminated composite material showing improved impact response. By introducing and replicating the discontinuities pattern (resin pockets) along the in-plane and through-the-thickness directions of a unidirectional and cross-ply ($[0/90]_n$) CFRP structures, a 3-Dimensional (3D) hierarchical CFRP structure was realised. Different manufacturing solutions were proposed in order to optimise the introduction of the discontinuities pattern while the optimum elemental cell length was found out via trade-off between pseudo-plasticity and flexural strength and modulus. Their effectiveness was evaluated analytically via a modified composite micromechanics model and experimentally via three-point bending tests. Output data were used to validate the numerical model and tune its mechanical properties including flexural stiffness and flexural strength. Finally, an experimental impact campaign was carried out on the hierarchical impact samples in order to characterise the impact response of the bio-inspired CFRP structure and verify the mechanical properties variation. A numerical model was then developed and validated for theoretical support for pseudo-plastic behaviour improvement. In this work, the description of 3D hierarchical bio-inspired structure design and the manufacturing processes used to obtain hierarchical CFRP laminates are presented in Section 2 while Section 3 illustrates experimental set-up, numerical modelling, results and discussion of three-point bending tests. Section 4 reports experimental set-up, numerical modelling, results and discussion of impact tests. Conclusions are reported in Section 5.

2. 3D hierarchical bio-inspired structure

The nacre exoskeleton structure has been used as inspiration source to design a unique discontinuities pattern to increase the amount of energy absorbed by the laminate structure during quasi-static and LVI loading. In this work, pseudo-plasticity was obtained by inserting a pattern of discontinuities into the laminate body by interrupting the long fibre continuity of the uncured CFRP material along its in-plane direction. Design parameters and the layout of the 3D hierarchical pattern for an elemental cell are reported in Figure 1a (side view) and Figure 1b (top view), where H (mm) is the length of the discontinuity, W (mm) is its width and D_X (mm) and D_Y (mm) are the width and length of the elemental cell respectively.

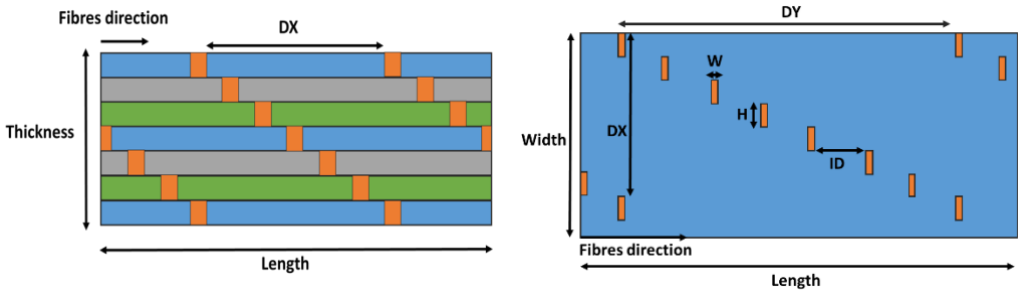

a) b)

Figure 1- Schematisation of the discontinuity pattern considered during the experimental campaign: a) side view and b) top view

Considering H and the number of plies of the structure (P_n), D_X can be defined according to Equation 1:

$$D_X = P_n H. \quad (1)$$

The length between two consecutive resin pockets is defined as Inter-discontinuity Distance ID (mm) and evaluated using the Equation 2:

$$ID = \frac{D_Y}{P_{n-1}} \quad (2)$$

Based on this in-plane pattern and imitating the out-of-plane distribution of the hierarchical bio-structure of the nacre [32], the final bio-inspired structure was created by reproducing the same distribution of resin pockets along the stacking

sequence and, shifting and overlapping two consecutive layers by an offset distance ID along DY direction.

A representation of the patterns shifting procedure is illustrated in Figure 2 for the first three layers.

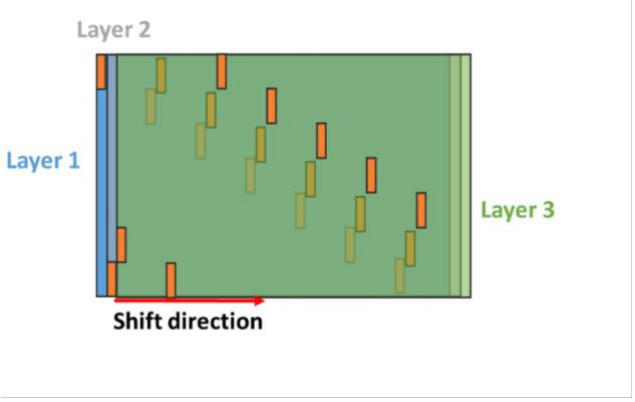

Figure 2-Layout of pattern shift along the thickness of the laminate. The pattern shift distance is ID.

Composite micro mechanic of the lamina [33] is able to predict with a certain accuracy the mechanical properties of a unidirectional laminated composite under several constitutive hypotheses including uniform average stress distribution within the fibres, roughly hexagonal fibres packing; isotropic, homogenous, void-free and linearly-elastic matrix; and homogenous, regularly-spaced, linearly-elastic fibres, following the equations below:

$$E_c = E_f V_f + E_m V_m \quad (3)$$

$$\sigma_c = \sigma_{fu} V_f + \sigma_{mu} V_m. \quad (4)$$

Where: V_f, E_f and σ_{fu} are the fibre volume fraction (0.6), the Young's modulus (~260-290 GPa) and the maximum tensile stress (~2500-2900 MPa) of the fibres, respectively; V_m, E_m and σ_{mu} are matrix volume fraction, elastic modulus (~1-5 GPa) and tensile matrix strength (~70-120MPa) respectively.

The creation of the resin pattern within the laminated structure changes the nature of the material since the continuity of the fibres is lost and a discontinuous structure is obtained leading to the loss of validity for Equation 3 and 4. Consequently, in order to predict the average mechanical properties (elastic modulus and strength) of this system, an alternative analytical model is proposed.

Using the definition of critical fibre length (l_c), it is possible to define the minimum length for fibres to transfer efficiently load and be effective in the reinforcement process [34]:

$$l_c = \sigma_{fu} d_f \backslash 2\tau_i \tag{5}$$

where τ_i is the interface shear strength (~10-40MPa) and d_f is the fibres diameter (~1-50 μm), resulting in a critical length of 1 mm. When the reinforcement fibres are continued and well-distributed along the single lamina, the fibre length (l) is $l > l_c$, and the fibres are an active component in transferring and tolerating load, while if $l < l_c$, the fibres are short and dispersed and therefore unable to transfer efficiently the load making the matrix properties dominant over the fibres ones.

Based on this premise, in order to allow the fibres to act as an effective reinforcement within the structure, all the used elemental cell lengths (8, 10, 20 and 50 mm) were set up to largely exceed this critical length. To evaluate the modulus and strength of such short fibrous reinforced system, a modified shear-lag theory for composite material [35, 36] is used taking into account the aspect ratio of the carbon fibres with the following equation:

$$E_c{}' = k_e E_f V_f + E_m V_m \tag{6}$$

$$\sigma_c{}' = k_s \sigma_{fu} V_f + \sigma_{mu} V_m \tag{7}$$

where k_e and k_s are fibre-length correction coefficients to take into account the discontinuous fibres in function of the unit cell length. The expression to define κ_e is given by Equation 8:

$$k_e = 1 - \frac{\tanh(\eta\zeta)}{\eta\zeta} \tag{8}$$

where:

$$\eta = \sqrt{\frac{E_m}{\theta(1+\nu_m)}} \tag{9}$$

$$\theta = E_f \ln\left(0.42\sqrt{V_f}\right) \tag{10}$$

$$\zeta = \frac{l}{d_f}. \tag{11}$$

Under the same hypothesis, the fracture-based correction coefficient κ_s [37] is defined as:

$$\kappa_s = 1 - \frac{\varphi}{2\zeta} - \frac{12.5}{\zeta\varphi} + \frac{5\sigma_{mu}}{\zeta\sigma_{fu}} \tag{12}$$

$$\varphi = \frac{\sigma_{fu}}{2\tau_i}. \tag{13}$$

It is important to notice that for high values of ζ (aspect ratio), both coefficients tend to 0, leading to obtain the properties of a traditional laminate material with a continuous reinforcement (no presence of resin pattern). On the contrary, for low values of ζ, k_e and κ_s tends to 1 leading to an unreinforced laminate material since fibres are too short to tolerate and transfer load. Thus, E_c and σ_c are two functions with a lower limit corresponding to $E_m V_m$ and σ_{mu}respectively, and an upper limit corresponding to the values described by Equation 3 and Equation 4 (elastic modulus and strength respectively). Analytical data are reported in Figure 3 in which an explorative analysis is reported comparing the analytical modulus and strength trends with the flexural results obtained in this work for different fibre lengths ($l=D_Y$) (see Section 3). It is important to notice that no direct correlation is possible since analytical model reports tensile properties while the experimental results are obtained from flexural tests, but it is still possible to compare their trend since flexural properties are related to tensile ones. Indeed, under the conditions of isotropic and homogenous material, tensile and flexural properties correspond, but in this case, due to the orthotropic nature of the material and different measurement conditions, there is a difference between their values [38]. However, the mechanical properties variation due to unit cell length is independent from the material nature and their trend correlation still holds qualitatively.

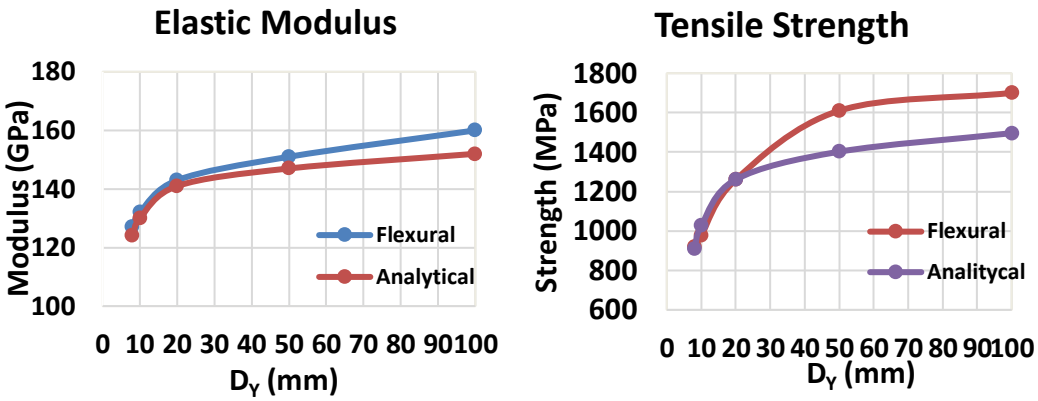

Figure 3- Variation of flexural modulus and flexural strength with D_Y alongside the analytical prediction of elastic modulus and tensile strength results

It is evident from this data that the analytical model is able to predict the trend of the mechanical properties variation (elastic modulus and strength). In particular, both these properties trends are upper asymptotic towards the reference material properties (without the presence of resin pockets pattern) for the experimental tests and E_c and σ_c (traditional composite micromechanical equations) for the analytic model. This represents an interesting data for material optimisation since the D_Y=50 mm values are close to the composite elastic modulus and strength without resin patterns (~150 GPa and 1500MPa respectively) and able to show a pseudo-plastic behaviour. However, due to the limitations of initial hypotheses, the values obtained from analytical model are overestimated but still useful to be employed as a reference for mechanical performance optimisation at different unit cell length (D_Y) and an initial condition for the validation of the numerical model developed to predict the pseudo-plastic behaviour of the hierarchical composite material. Indeed, the pseudo-plastic behaviour derived from the presence of the resin pattern introduction, is difficult to predict using an analytical model due to several complex non-linear mechanics including crack propagation, pull-out and fragmentation. However, several analytical models have been developed to predict pseudo-plastic behaviour in nacre-like structures [39, 40] but the Representative Volume Element (RVE) method for symmetrical columnar structures considered in these works is incompatible with the 3D resin pattern investigated in this work since no periodic boundary conditions can be identified for this case. Based on these considerations,

in this work a numerical model was preferred to be used as reference for the design and experimental characterisation of the pseudoplastic laminates.

The introduction of the pattern of discontinuities into the laminate was carried out by following two different manufacturing procedures. In the first, named Direct Approach (DA), a specific mask was designed and manufactured with a laser cutter and used to create every single discontinuity of the in-plane pattern by cutting with a high-precision sharp blade, the CFRP fibres of the uncured material. Afterwards, during the stacking up sequence, the 3D-hierachcial design was obtained by overlapping and offsetting the in-plane structure along the out-of-plane direction. Disadvantages of DA are the formation of some defects, caused by fibre loss and non-uniform pressure during the cutting that could affect the mechanical properties. Moreover, structure configuration characterised by small D_Y values were more affected by these defects than configurations with higher D_Y values. Nevertheless, good experimental results and good correlation with numerical simulations were found for D_Y values of 50 mm that showed no influence of manufacturing defects on mechanical properties. Following DA approach, unidirectional samples were created by cutting eight unidirectional layers 120 mm x 17.5 mm in size. Due to the geometrical parameters of the pattern, the same distribution is repeated every seven plies, therefore Ply 1 and Ply 8 are equal. In contrast, the alternative design approach, named Indirect Approach (IA), consists in the creation of the patterns by cutting a CFRP prepreg with the length equal to the distance between two discontinuities and, afterwards, assembly of these multiple bands following a correct sequence in order to create the hierarchical structure. Following this solution, it was possible to generate the discontinuities pattern with an increased accuracy in comparison to the previous approach; however, an increase of discontinuities size was reported due to the operator limit in cutting small width for CFRP stripes. Following the IA procedure, another set of unidirectional samples were manufactured cutting 50mm x 5mm stripes of unidirectional CFRP prepreg and, organizing the single parts in function of the design parameters during the layup procedure, the same discontinuities pattern illustrated previously is obtained

as a CFRP plate of 500mm x 35mm. This plate was then cut after the cure process using an abrasive blade and several samples 100mm x 17.5mm in size were obtained as reported in Figure 4.

a)

Figure 4-Images of unidirectional CFRP samples using IA procedure.

Based on the results obtained with unidirectional specimen, Cross-Ply (CP) CFRP samples were realised by extending the hierarchical structure concept in cross-ply CFRP laminates in order to investigate the effect of pseudo-plasticity in multidirectional composite structures. Following this premise, a cross-ply lamination sequence ($[0/90]_{nS}$) with a size of 120mm x 20mm was used to manufacture cross-ply CFRP samples. Using the DA procedure, an angular rotation of the pattern was applied on the plies with a different fibres ordination during the discontinuities pattern creation. In particular, a rotation of 90° was applied to the pattern for 90° orientated plies to generate a consistent design of discontinuous fibres inside the laminate's pattern. The rotation of the pattern had no influence on the planar shifting.

A schematisation of pattern rotation and through-the-thickness shift is illustrated in Figure 5 where the procedure is shown for the first three plies.

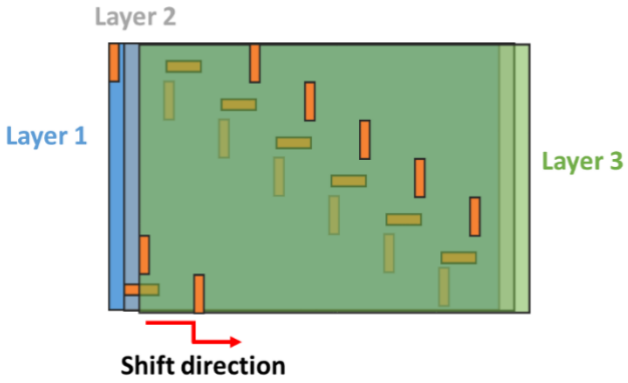

Figure 5-Layout of pattern shift along the cross-ply laminate thickness. The pattern shift distance is ID while the rotation angle is 90°.

Similarly, to samples CP, impact samples were manufactured using DA manufacturing procedure with a cross-ply configuration and cut 150mm x 100mm in size as suggested by the BS EN ISO6603-1:2000 and BS EN ISO6603-2:2001 impact standards. Average thickness of the impacted samples was around 1.36 mm. Traditional CFRP laminates (with no discontinuity pattern) for each samples set were manufactured as baseline. Unidirectional CFRP prepreg (Tenax® IMS65 filament yarn with CYTEK 977-2 resin system) with a depth of 0.18 mm was used to manufacture all the samples. In order to remove air between the plies and increase the inter-ply compaction, vacuum was applied on all the uncured samples for 30 minutes and then, using an autoclave assisted curing procedure, they were processed with a pressure of 100 Psi, a temperature of 180°C with a ramp of 3 °C/min for 3 hours under vacuum. At the end of the process, an assisted cooling operation was carried out. Table 1 reports all the sample specifications involved in the experimental campaign.

Table 1-Manufactured samples specs

Sample typology	Stacking sequence	Manufacturing approach	Number of plies (L_n)	H (mm)	D_Y (mm)	D_X (mm)	Length (mm)	Width (mm)	Average thickness (mm)
Unidirectional	$[0]_8$	DA	8	2.5	8, 10, 20 ,50	17.5	120	17.5	1.23
Unidirectional	$[0]_8$	IA	8	5	50	17.5	100	17.5	1.24
Cross-ply	$[(0/90)_4/0]$	DA	9	2.5	50	20	120	20	1.38
Unidirectional reference	$[0]_8$	-	8	/	/	/	120	17.5	1.2
Cross-ply reference	$[(0/90)_4/0]$	-	9	/	/	/	120	20	1.34
Impact	$[(0/90)_4/0]$	DA	9	2.5	50	20	150	100	1.38
Impact reference	$[(0/90)_4/0]$	-	9	/	/	/	150	100	1.38

3. Three-point bending tests

3.1. Experimental set-up

In order to characterise the 3D hierarchical CFRP structure, three-points bending tests were carried out using an Instron universal tester (3369) machine and following the standard ASTM D790. A cylindrical loading nose and steel cylindrical supports with a radius of 2.5 mm were used while supports span was set at 69 mm. A cross-head speed of 6.9 mm/min was used. Several values of D_Y were tested to identify its optimal value using a load cell of 50 kN. In Figure 6, images of experimental setup are reported.

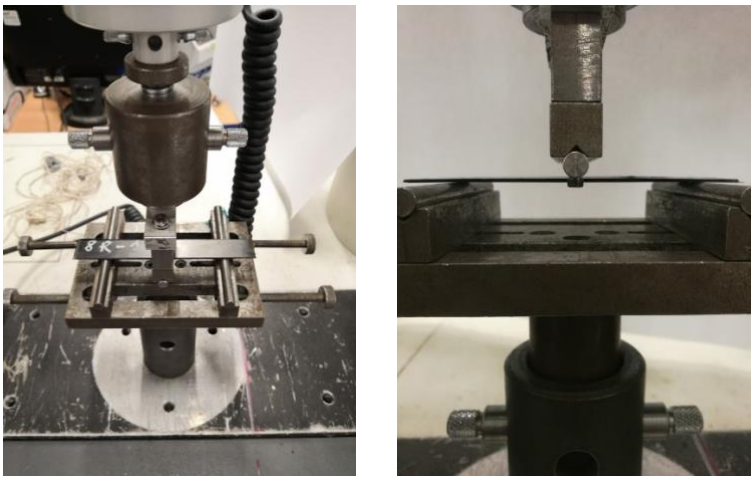

a) b)

Figure 6- Three-points bending machine set-up:a) frontal view and b) lateral view.

3.2. Numerical model set-up

In order to offer a theoretical support during the manufacturing process and to allow provision of further experimental results after its validation, a Finite Element Analysis (FEA) code was developed. Using a commercial code LS-DYNA, a non-linear implicit numerical model was developed to simulate the mechanical behaviour of laminated material. Using full-integrated solid elements and orthotropic material MAT_022 (COMPOSITE_DAMAGE), 120 mm x 20 mm x 1.26 mm CFRP laminates were modelled. Similarly, resin pockets of 3D hierarchical structure were simulated using an isotropic material model MAT_024 (PIECEWISE_LINEAR_PLASTICITY) with a full-integrated solid element formulation. Erosion control was activated to remove the resin elements after failure. RIGIDWALL_CYLINDER cards were used to model the steel supports while MAT_001 (ELASTIC) with full-integrated solid element formulation was used to model the loading cylindrical nose. Materials properties are reported in Table 2 and Table 3 where E11 and X1t are obtained via analytical model (Equation 6 and Equation 7).

Table 2- Material properties of CFRP used for FEA model. RO: density, modulus of elasticity (E11, E22, E33), poisson's ratios (PR12 ,PR31, PR32), shear modulus (G12, G23, G31), normal and transverse strength under traction and compression (X1t, X1c, X2t, X2c), shear strength (S12, S23, S31).

MATERIAL	RO (Kg/m3)	E11 (GPa)	E22 (GPa)	E33 (GPa)	PR21	PR31	PR32	G12 (GPa)	G23 (GPa)	G31 (GPa)	X1t (MPa)	X1c (MPa)
CFRP	1560	152.6	8.9	8.9	0.0535	0.0535	0.449	4.6	3.7	3.7	1500	950

PART	X2t (MPa)	X2c (MPa)	S12 (MPa)	S23 (MPa)	S31 (MPa)
CFRP	70	250	105	89	105

Table 3- Material properties of steel and resin used for FEA model. RO: density, modulus of elasticity (E11), poisson's ratios (PR12), yeild strength (UY), tangent modulus (ETAN), effective plastic strain at failure(FAIL).

MATERIAL	RO (Kg/m3)	E (GPa)	PR	UY (MPa)	ETAN (GPa)	FAIL
Steel	7830	210	0.3	/	/	/
Resin	1160	2	0.35	82.4	0.005	0.04

Using a penalty-based contact typology to define the interaction between the laminate and the loading nose, key parameters including friction, contact stiffness and penalty equation were defined in function of the properties of steel and CFRP and the loading nose was located in contact with the surface of the laminate. A total displacement of 13 mm was applied during the three-point bending test. Output data were collected evaluating the reaction force between CFRP surface and loading nose, and post-processed using a MATLAB code. The same numerical setup was used to develop FEA code for unidirectional samples (for DA and IA approaches). Images of the model are shown in Figure 7

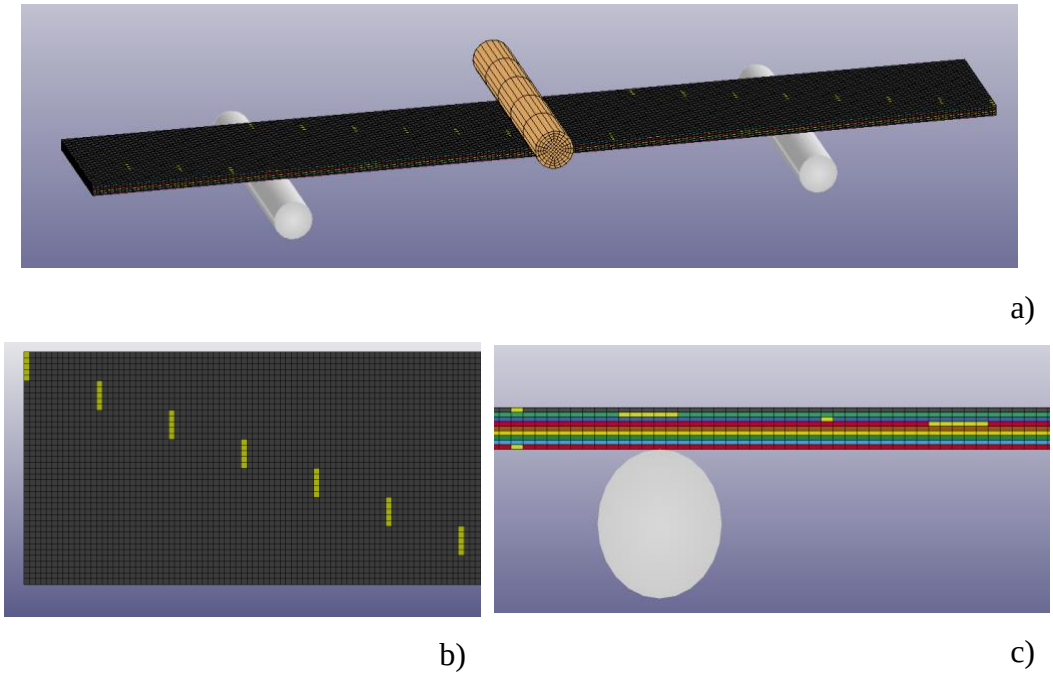

Figure 7- FEA model layout for three-points bending: a) isometric view, b) top view and c) lateral view.

3.3. Results and discussion

The discontinuity pattern was developed to introduce a pseudo-plastic behaviour in the CFRP structure's failure mode. The causes of this behaviour are explained by the presence of stress intensification points due to the different mechanical properties between the discontinuities (resin pockets) and the surrounding areas (CFRP), and the onset of fibre pull-out and crack deflection

during crack propagation. All these pseudo-plastic mechanisms are able to increase the global strain at failure and then the toughness of the structure.
Stress intensification (or notch sensitivity), as studied in fracture mechanics [41], is a mechanical phenomenon generated when a discontinuity is introduced within a uniform body. The discontinuity locally creates an area where stresses are intensified, and its effect is amplified when a regular pattern of discontinuities is introduced into the laminate [42]. When cracks are generated in correspondence with one of these discontinuities, they start to propagate through the thickness of the laminate with a convoluted path (crack deflection), following the 3D hierarchical pattern. This leads to a fragmentation of the CFRP structure and a higher amount of dissipated energy since multiple and convoluted cracks require more energy to propagate and generate new surfaces than a single crack [43]. During the CFRP fragmentation, fibre pull-out occurs due to matrix failure leading to a gradual and smooth failure behaviour that prevents a catastrophic collapse of the structure. Even though these series of mechanisms increase the toughness and strain at failure of the structure alongside reliability and safety, however, due to the presence of the discontinuities, negative effects in mechanical properties of the laminate can be observed and, therefore, a careful design of the geometrical features of the hierarchical design is necessary.

Based on these considerations and analysing the effect of several configurations of discontinuity patterns at different D_Y values (8, 10, 20 and 50 mm), a trade-off between the flexural modulus and flexural strength, and pseudo-plasticity was carried out, supported by the analytical results of the elastic modulus and tensile strength obtained considering the modified micromechanical equations (Equation 6 and Equation 7). Indeed, analysing the curves in in Figure 8.a., the effectiveness of the introduction of the discontinuity pattern in enabling pseudo-plasticity is demonstrated by the presence of a stress plateau for all the samples configurations with no signs of brittle behaviour during failure. Increasing the size of D_Y, flexural strength and flexural modulus of the laminate increase while a decrease in extension of pseudo-plastic plateau is recorded. This is due to the dependency of these

properties from the number of discontinuities introduced within the structure. Consequently, the increase of the D_Y value reduces the number of discontinuities within the structure, increasing the flexural modulus and strength of the structure. Flexural modulus and flexural strength variations with D_Y are reported in Figure 8.b. As it is possible to analyse from the curves, in fact, a value of D_Y equal to 50mm shows the highest mechanical properties and a good pseudo-plastic behaviour with a good potential for trade-off between the two variables. Flexural results of continuous CFRP sample (100 mm) are reported in Figure 8 as reference.

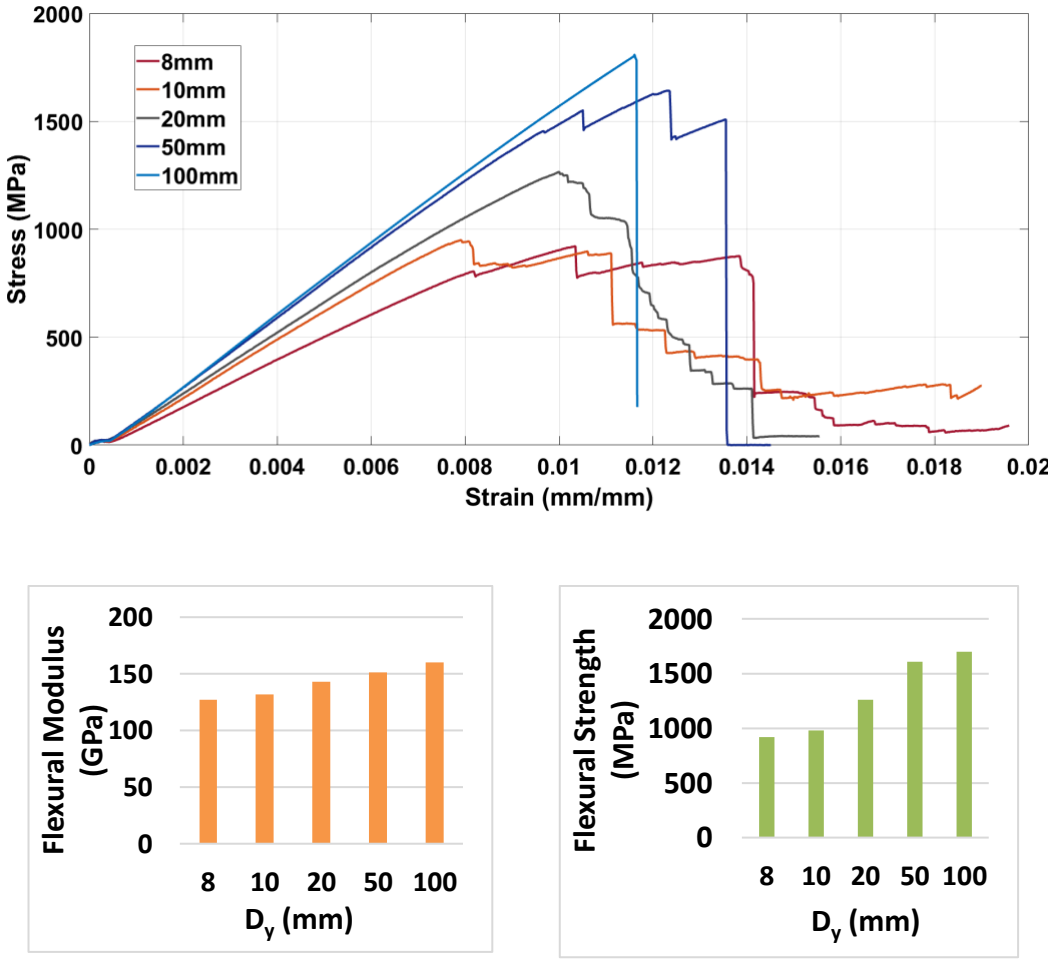

Figure 8-Experimental flexural results for unidirectional configuration (DA procedure) configuration at different D_Y values reporting flexural modulus and strength.

In order to validate the effect of the discontinuities patterns in contrast with a traditional laminate Computed Tomography (CT) scan analyses were carried out

analysing the crack propagation mode in different samples. Results are shown in Figure 9.

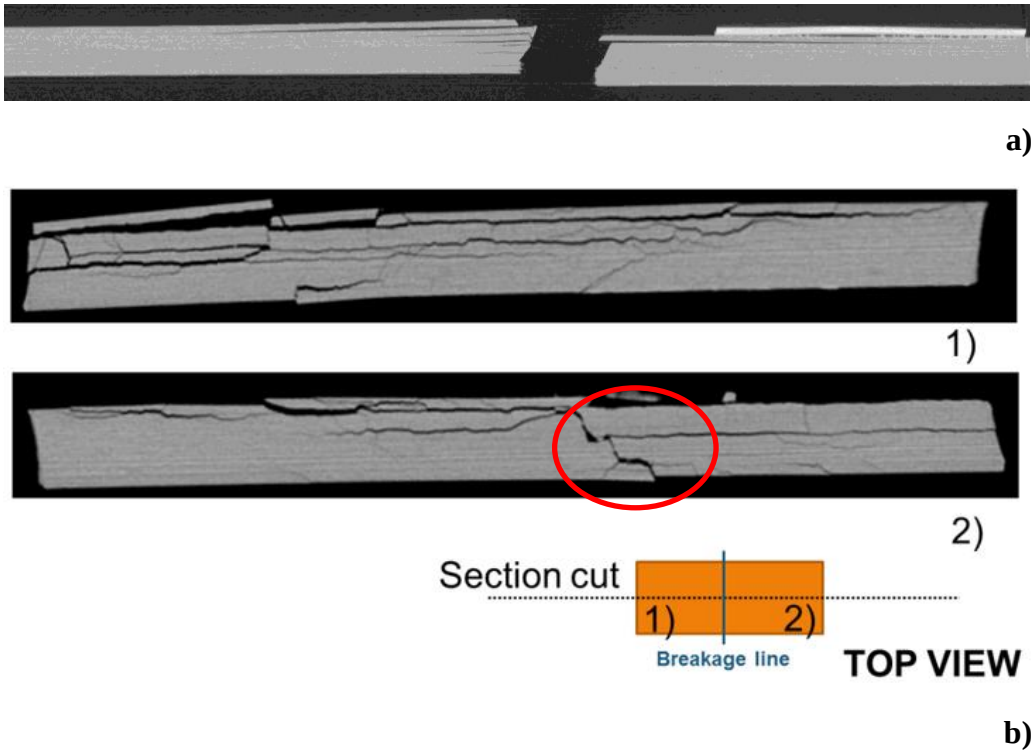

Figure 9 – CT scan images of tested samples: a) traditional CFRP reference and b) U sample where is possible to observe the crack propagation along the discontinuity pattern (red circle).

Analysing the images, it is clear that they propagate through the thickness of the sample following the 3D hierarchical pattern of discontinuities (Figure 9.b). Indeed, a crack deflection mechanism with a convoluted crack path is identified since regularly spaced resin pockets allow a sort of "zig-zag" pattern, in contrast with an unprocessed material where the crack propagation is transversal to the loading section (Figure 9.a) [44]. As a consequence, a higher amount of energy is absorbed by the hierarchical CFRP since the energy required by the crack to propagate is proportional to its length [8]. Moreover, strain hardening is reported by the output data with an increase of strain at failure in comparison with a traditional CFRP structure.

Based on the experimental data, damage topology and analytical model prevision, a value of D_Y equal to 50 mm was selected for the rest of the experimental campaign as the best compromise between strength, modulus and pseudo-plasticity.
The output data of the flexural experimental campaign on 3D hierarchical structure are reported in Figure 10. FEA model is reported in the same graph.

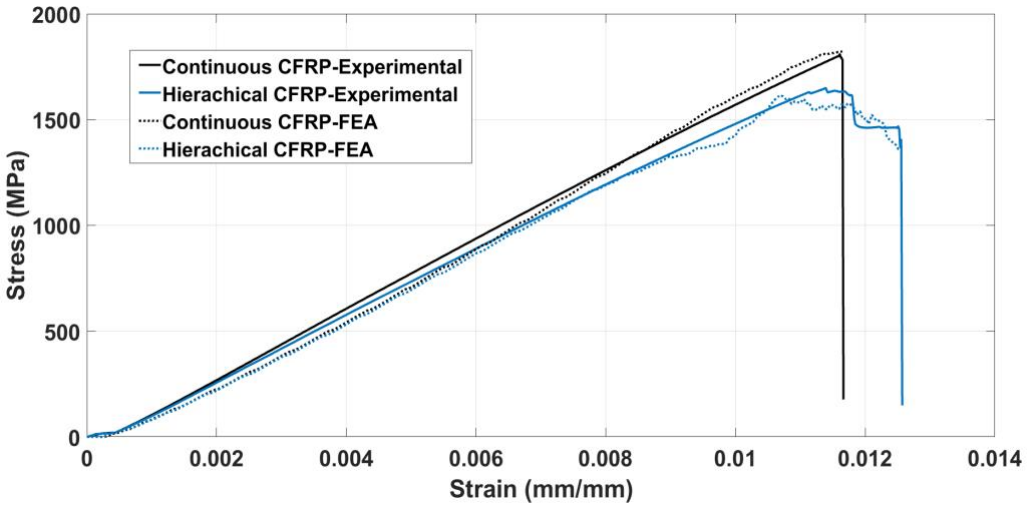

Figure 10- Experimental stress-strain curves of unidirectional configuration obtained via DA procedure. FEA stress-strain curves are reported.

Table 4 reports the statistical data from the evaluation of flexural modulus, flexural strength (first peak in the curve), flexural strain (when flexural strength is reached) and strain at failure (last peak before failure). Average and standard deviation are reported for each output parameter.

Table 4- Experimental data report for unidirectional configuration obtained via DA procedure. Mean and standard deviation for each parameter are reported.

Sample	Number of species	Energy [J]		Flexural modulus [GPa]		Flexural strength [MPa]		Flexural strain [mm/mm]		Strain at failure [mm/mm]	
		Mean	Standard dev.	Mean	Standard dev.	Mean	Standard dev.	Mean	Standard dev.	Mean	Standard dev.
Unidirectional- DA	3	10.43	0.71	157	0.0106	1640	35	0.0114	0.0002	0.0122	0.0003
U reference	3	10.31	0.3	160	0.0387	1720	67	0.0117	0.0001	/	/
Unidirectional- DA (Numerical)	/	10.40	/	155	/	1643	/	0.0114	/	0.0126	/
Unidirectional reference (Numerical)	/	10.34	/	162	/	1820	/	0.0107	/	/	/

Analysing the results, a minimal variation in comparison with traditional references of -5% for flexural strength is reported since, as illustrated previously, the presence of the discontinuity pattern compromises the structural continuity of hierarchical samples. On the contrary, a small increase of the strain at failure (+4.1%) is recorded in the comparison between 3D hierarchical structures and baselines. This is due to crack deflection and pull-out mechanism that allow the stable failure generating the stress plateau in the experimental curves. Using these experimental data, a validation of the FEA model was carried out and a good agreement between numerical and experimental results was found in mechanical response prevision.
Unidirectional samples obtained following the IA procedure are tested using the same test conditions and the output results are reported in Figure 11.

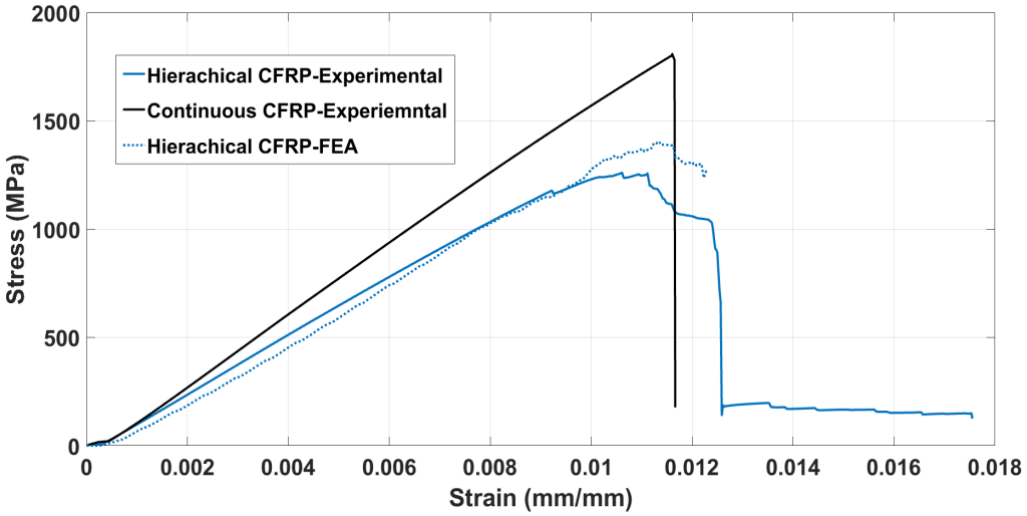

Figure 11-Experimental stress-strain curves of unidirectional configuration obtained via IA procedure. FEA stress-strain curve is reported.

The details of the output results are reported in Table 5

Table 5- Experimental data report for of unidirectional configuration obtained following IA procedure. Mean and standard deviation for each parameter are reported.

Samples	Number of species	Energy [J]		Flexural modulus [GPa]		Flexural strength [MPa]		Flexural strain [mm/mm]		Strain at failure [mm/mm]	
		Mean	Standard dev.	Mean	Standard dev.	Mean	Standard dev.	Mean	Standard dev.	Mean	Standard dev.
Unidirectional-IA	4	9.68	0.59	143	2.9	1198	77.84	0.01	0.00011	0.0127	0.00046
Unidirectional reference	3	10.31	0.3	160	3.87	1720	67	0.0117	0.0001	/	/
Unidirectional- IA (Numerical)	/	10.60	/	138	/	1234	/	0.0102	/	0.0123	/

In this case, the decrease of mechanical properties of this configuration in comparison with a traditional CFRP are more significant especially in terms of flexural modulus (-10%) and flexural strength (-30%) due to the increase of the notch sensitivity for discontinuities size (H=0.5 mm). The bigger size of the resin pockets allows having a higher strain at failure than in the hierarchical samples (+3.93%) with an increase of +7.9% on the traditional references. Hence, the pseudo-plastic behaviour is more evident for the IA unidirectional configuration.

Also, in this case, FEA model is able to predict the experimental behaviour showing a good agreement with experimental data even though an overestimation of flexural stress is reported due to numerical instabilities. Flexural modulus and strain at failure have a good correspondence with experimental data. Cross ply samples were tested using the same experimental setup. Output results are reported in Figure 12

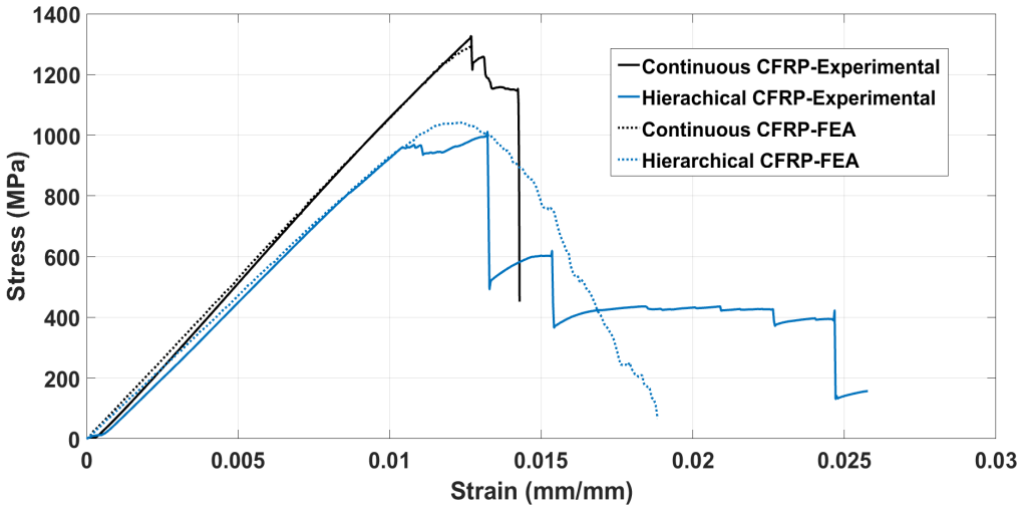

Figure 12-Experimental stress-strain curves of cross-ply configuration. FEA stress-strain curve is reported

Output details of the characteristic mechanical properties of cross-ply CFRP samples are reported in Table 6.

Table 6- Experimental data report for cross-ply configuration. Mean and standard deviation (SD) for each parameter are reported.

Sample	Number of species	Energy [J]		Flexural modulus [GPa]		Flexural strength [MPa]		Flexural strain [mm/mm]		Strain at failure [mm/mm]	
		Mean	SD	Mean	SD	Mean	SD	Mean	SD	Mean	SD.
CP samples	3	12.6	2.15	98	4.8	1023	42	0.0127	0.00094	0.0248	0.0012
CP references	3	9.53	1.43	107	2.9	1284	179	0.0127	0.0017	0.0138	0.00089
CP samples (simulated)	/	11.45	/	100	/	1041	/	0.0122	/	0.0172	/
CP references (simulated)	/	8.97.	/	108	/	1291	/	0.0126	/	/	/

As shown in the data analysis, also in case of the cross-ply samples, the mechanical properties are inevitably reduced if compared with the pristine material in terms of flexural modulus and flexural strength by -8.4% and -20% respectively. However, the toughness (+24%) and the strain at failure (+44.35 %) show a remarkable increase in comparison with a cross-ply traditional CFRP. Indeed, in this case, crack deflection mechanism is able to absorb more energy since the angle component is added to the discontinuity pattern leading to a longer and convoluted crack path. Unlike in the previous cases, the leading failure phenomenon is the delamination between plies with different orientations [45] that helps the crack propagating through the sample. In fact, due to the larger scale of the delamination phenomenon, a higher number of resin pockets are involved in the process and a higher number of cracks starts to propagate along different positions of the discontinuities pattern. In other words, delamination becomes a catalyst for crack deflection mechanism.
The trade-off between the pseudo-plastic behaviour and mechanical performance is analysed for unidirectional (DA and IA) and cross-ply configurations. The trade-off results are illustrated in Figure 13, where the effectiveness of the 3D hierarchical approach is demonstrated to have the best effects on cross-ply stacking sequence.

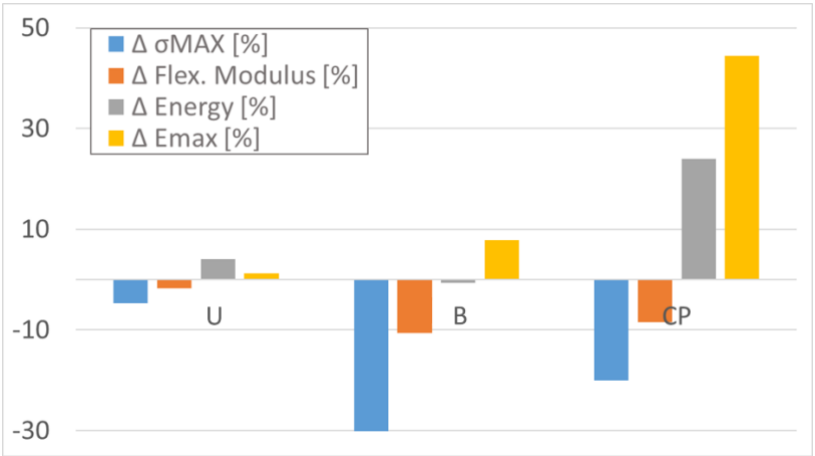

Figure 13-Trade-off between pseudo-plastic behaviour and mechanical properties of all the samples tested during the experimental campaign. The results indicate that the discontinuity pattern gives best results for complex stacking sequences rather than for unidirectional samples. U=Unidirectional with DA procedure, B=Unidirectional with IA procedure and CP=cross-ply

The FEA model is able to simulate this experimental test and have a good agreement with values of flexural modulus and maximum strength even if part of the pseudo-plastic effect is underestimated.

4. Low velocity impact tests

4.1. Experimental set-up

A drop tower machine (2.66 kg of impacting weight) was used to perform LVIs on the 3D hierarchical samples. A hemispherical tip of 20 mm of diameter was used to apply the impact load on the samples surface using different level of: 4J, 8J and 12J with an impact velocity of 1.73 m/s, 2.45 m/s and 3.03 m/s respectively. Samples were placed into the impact machine using a clamping support in which the samples were fully constrained in order to avoid undesired vibrations.

Using a USB-PICOSCOPE Oscilloscope and a Kistler Load cell, impact data were obtained and raw load signals (Time-Volt) were collected from the oscilloscope and converted into Force-Displacement curves [46]. BS EN ISO6603-1:2000 and BS EN ISO6603-2:2001 standards were used as guidelines for impact set-up and results interpretation. Impact machine scheme and apparatus are illustrated in Figure 14.

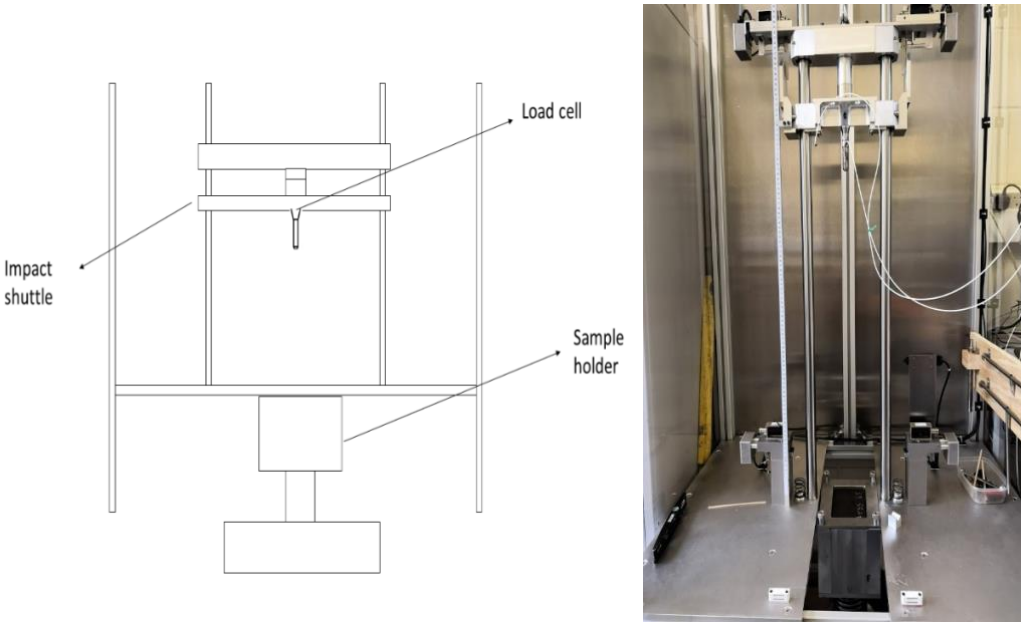

Figure 14-Impact machine used during the impact campaign: a) scheme and b) apparatus

4.2. Numerical model set-up

Once the model was validated for the three-point bending test, an explicit non-linear FEA model was developed based on a cross-ply configuration of an aeronautic laminate in order to have a prevision of the experimental data of a Low Velocity Impact (LVI) test. The size of the CFRP plate was 150 mm x 100 mm x 1.39 mm and the hemispherical impacting mass was modelled as a semi-sphere of 20 mm in diameter. A traditional CFRP plate model was developed as baseline for the impact behaviour evaluation of numerical 3D hierarchical structure. Default LS-DYNA element formulation was used for the solid elements while a Flanagan-Belytschko stiffness form formulation for hourglass control was used to control the energetic degeneration of the solid elements. LS-DYNA theory manuals [47, 48] were used for support during the model development.

Images of the model are shown in Figure 15:

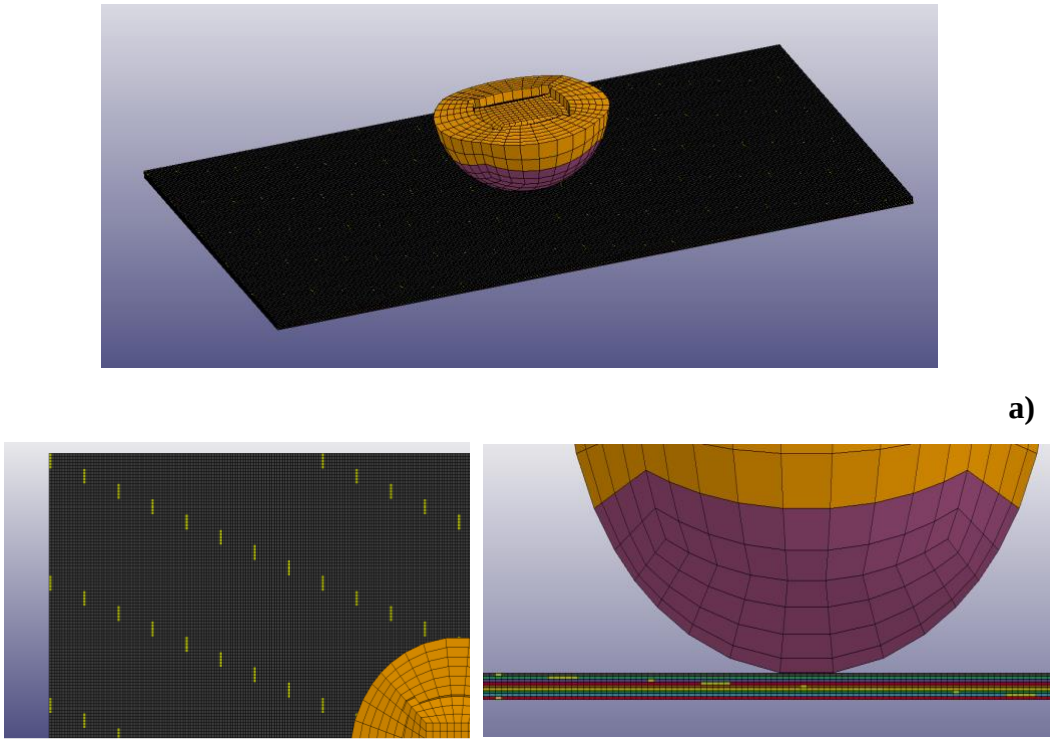

a)

b) **c)**

Figure 15- FEA model layout for LVI test:a) isometric view, b) top view and c) lateral view.

In order to model the discontinuity pattern inside the material using MAT_024 (PIECEWISE_LINEAR_PLASTICITY) material model, mesh sizing was chosen ad-hoc to have a consistent dimension along the in-plane and out-of-plane directions with each element 0.5mm x0.5 mm x0.17 mm in size. The reason for the mesh refinements is due to the small dimensions of the discontinuities pattern (H=2.5 mm, W=0.5 mm, D_Y = 50 mm, DX=20 mm) that constrain the global mesh size of the model forcing the use of a uniform refined mesh (565100 elements in total). It is possible to see in Figure 15.c how the discontinuities pattern changes in function of the orientation of the relative layer, as the case for the CP samples. Contact between the impacting object and CFRP plate was modelled using a PENALTY-BASED contact algorithm in which the erosion of negative volume elements was activated, while plate boundaries conditions were modelled as simple supported. To take into account the damage mode in CFRP plates, MAT_261 orthotropic material [49-51] was used to simulate the single plies of the CFRP material.

Damage prediction of fibre and matrix is defined for each element using tensile, shear and compressive strengths as activation criteria for damage initiation while, the relative toughness parameters are used as the complete failure of the single elements.

Delamination was modelled using a TIEBREAK_CONTACT model [47]. This contact is considered a tied contact before the failure criteria is satisfied. Afterwards, the contact switches its formulation into a penalty-based one. The failure criteria used in this work was a stress-based criterion with linear damage development.

MAT_261 parameters are reported in Table 7:

Table 7-MAT_261 orthotropic material card paramters:RO: density, modulus of elasticity (E11, E22, E33), poisson's ratios (PR12 ,PR31, PR32), shear modulus (G12, G23, G31), normal and transverse strength under traction and compression (X1t, X1c, X2t, X2c), shear strength (S12, S23, S31), compresisve fibre failure energy (ENKINK), tensile fibre failure energy (ENA), Intralaminar matrix tensile energy failure (ENB), Intralaminar matrix trasnverse shear energy failure (ENT) and Intralaminar matrix longitudinal shear energy failure (ENL).

MAT	RO (Kg/m3)	E11 (GPa)	E22 (GPa)	E33 (GPa)	PR21	PR31	PR32	G12 (GPa)	G23 (GPa)	G31 (GPa)	X1t (MPa)	X1c (MPa)
CFRP	1530	152	8.9	8.9	0.0535	0.0535	0.449	4.6	3.7	3.7	1500	950

MAT	X2t (MPa)	X2c (MPa)	S12 (MPa)	S23 (MPa)	S31 (MPa)	ENKINK (J/m2)	ENA (J/m2)	ENB (J/m2)	ENT (J/m2)	ENL (J/m2)
CFRP	70	200	80	80	80	75100	50100	478	900	900

Resin pocket (MAT_024) parameters are reported in Table 3.

Contact force and plate deflection were collected from the reaction force between the impacting mass and the plate, and from displacement of the impacting mass, respectively. Using these output data, the force–displacement curves were obtained via MATLAB elaboration.

4.3. Results and discussion

Force-displacement curves for experimental tests are reported in Figure 16.

HIERACHICAL-4J

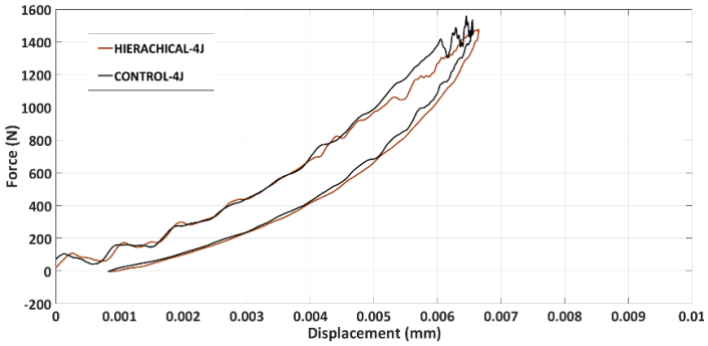

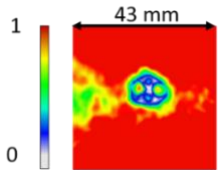

CONTROL-4J

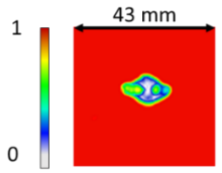

HIERACHICAL-8J

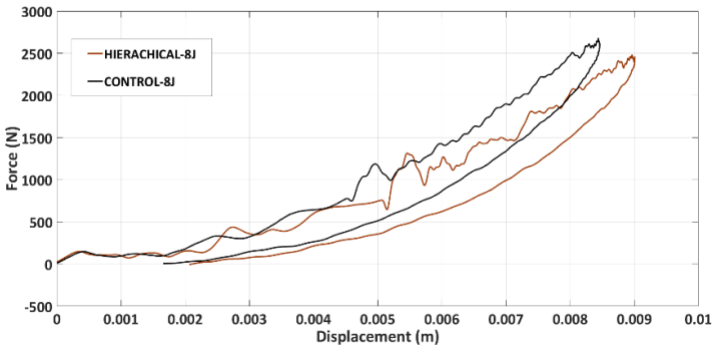

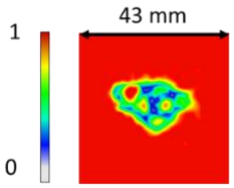

CONTROL-8J

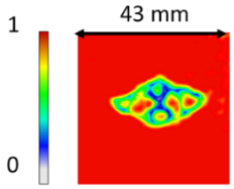

HIERACHICAL-12J

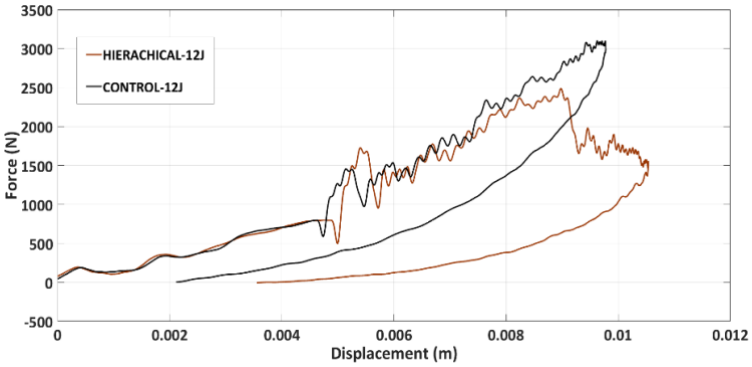

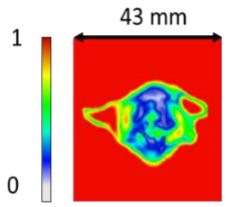

CONTROL-12J

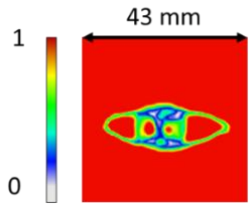

Figure 16-Force-Displacement curves and relative C-scan for experimental tests where the label HIERACHICAL corresponds to the 3D hierarchical CFRP samples and CONTROL to the traditional CFRP. The relative energy is reported for each curve.

To investigate the inner damage generated during the impact, an Ultrasonic Non-Destructive Technique (NDT) was used to evaluate the damaged area extension. C-scan images were obtained using a 5 MHz Phased Array Transducer with 128 Elements (National Instrument). The difference in terms of normalised amplitude in 16-bit colour scale is reported Figure 16 where the C-scan results are reported for each plate. In order to evaluate the damage topology, pseudo-plasticity effectiveness and crack distribution along the 3D hierarchical CFRP samples, a Computed Tomography (CT) scan was performed on all the impacted samples (bio-inspired and control). The output images are reported in Figure 17. All the images were collected using the same view, analysing a portion of the impacted area of the laminate.

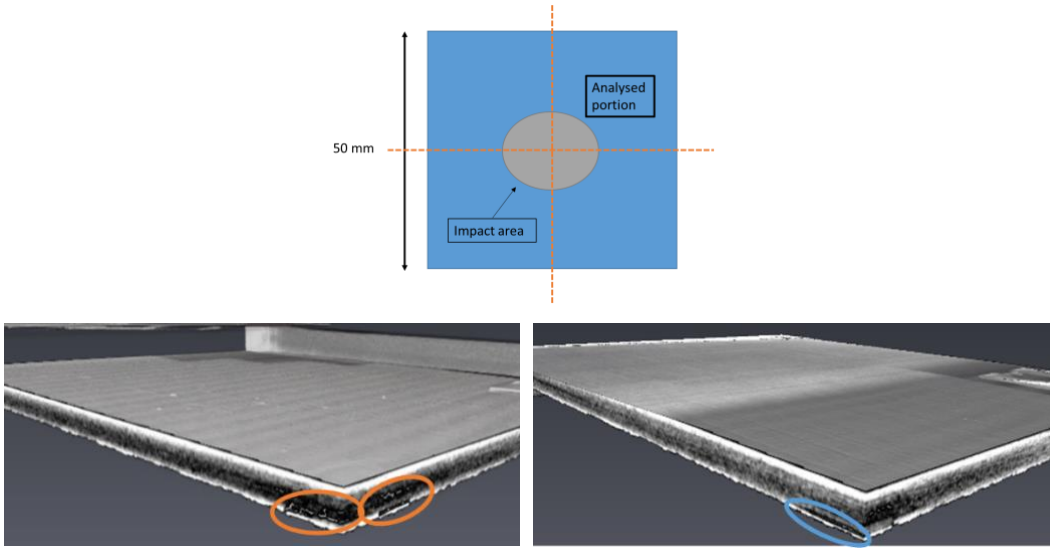

a) **HIERACHICAL-4 J**

b) **CONTROL-4 J**

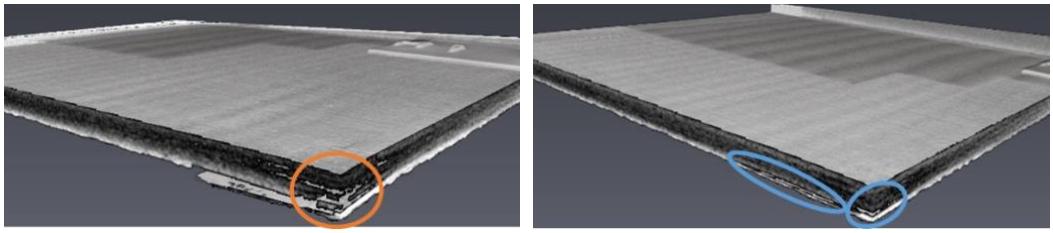

c) d)

HIERACHICAL-8 J **CONTROL-8 J**

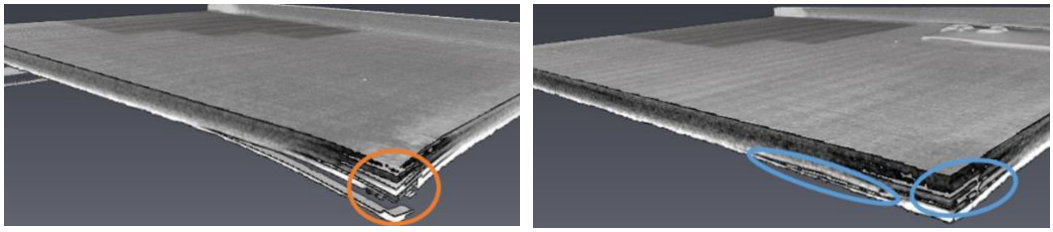

e) f)

HIERACHICAL-12 J **CONTROL-12 J**

Figure 17- CT scan damage detection technique of the impacted samples: (a, c, e) 3D hierarchical samples impacted at 4J, 8J and 12 J respectively and (b, d, f) traditional CFRP samples impacted at 4J, 8J and 12J respectively Scanned area of the samples (50mm x 50mm) and the analysed portion are indicated in the reported scheme.

Statistical data for the impacted samples is reported in Table 8.

Table 8-Statistical data from impact campaign. 4J, 8J and 12J are the impact energies and the impact parameters of Peak Force, Maximum Displacement, Absorbed Energy and Delaminated area are reported.

REFERENCE				
Energy (J)	**Peak Force (N)**	**Max Displacement (mm)**	**Absorbed Energy (J)**	**Delaminated Area (mm^2)**
4	***1670***	***0.00661***	***1.3176***	***95.63***
8	***2805***	***0.00824***	***2.8857***	***225.76***
12	***3271***	***0.00962***	***5.6752***	***275.63***
HIERACHICAL				
Energy (J)	**Peak Force (N)**	**Max Displacement (mm)**	**Absorbed Energy (J)**	**Delaminated Area (mm^2)**
4	***1479***	***0.00661***	***1.3339***	***125.73***
8	***2610***	***0.00883***	***3.1581***	***238.59***
12	***2613***	***0.0105***	***9.4788***	***450.82***

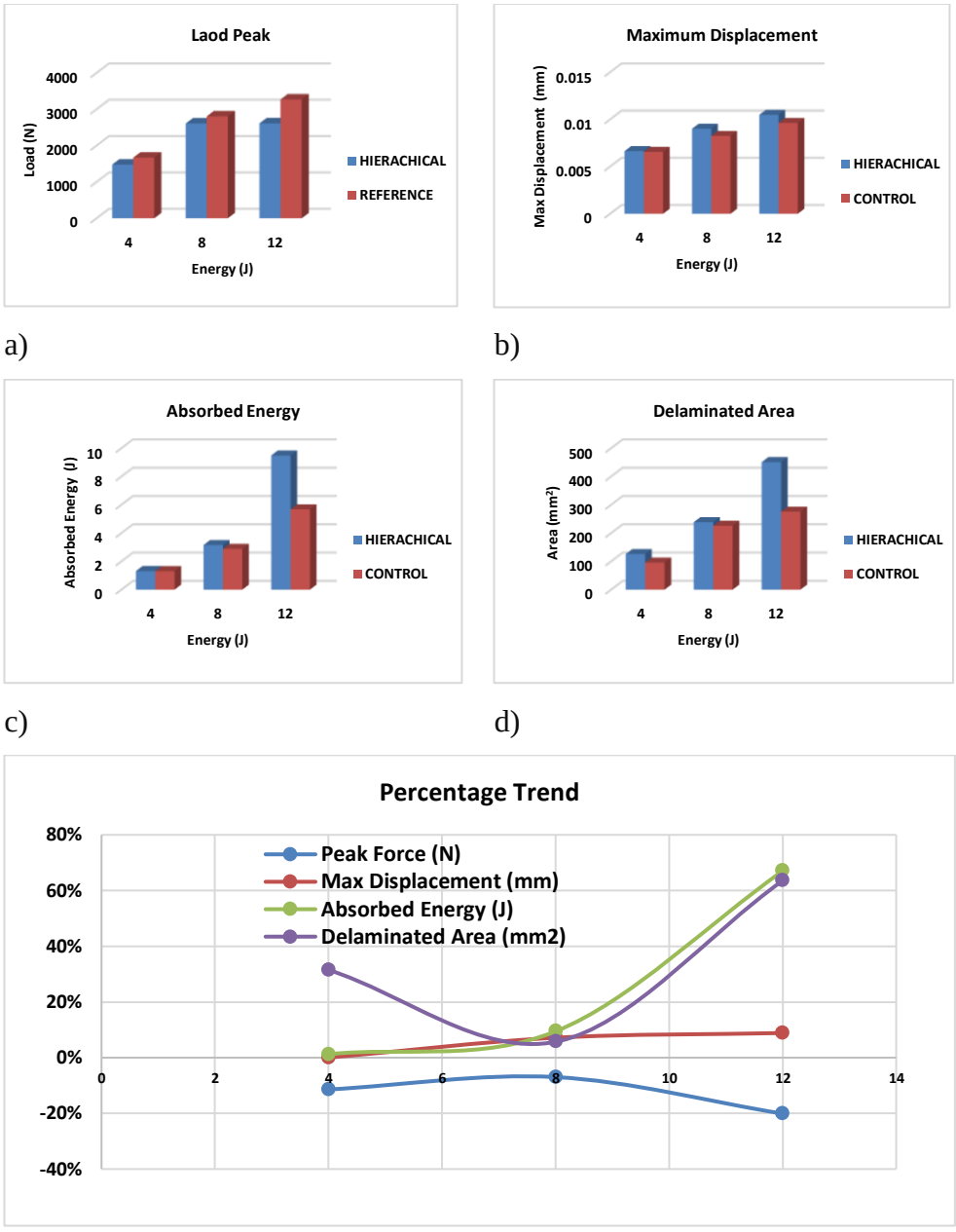

Figure 18- Statistical data charts on impacted data for 4J, 8J and 12J impacts for control and 3D hierarchical CFRP sets: a) maximum contact force, b) maximum displacement, c) absorbed energy, d) damaged area extension and f) percentage variation of each statistical parameter.

From Figure 18, it is clear that at different impact energies, the impact behaviour and the relative pseudo-plastic effect exhibited by the bio-inspired samples is significantly different to the control samples. Considering the impacts at 4J, no

difference in terms of impact response is reported for maximum displacement (+0.006%) and absorbed energy (+1%) reported in Figure 18.b and Figure 18.c. This is because pseudo-plastic features activation is restricted by the small impact energy amount introduced into the sample. However, it is still possible to notice differences in terms of peak force and delaminated area (Figure 18.a and Figure 18.d), with a percentage variation of -11% and +31% respectively due to the presence of the pattern of discontinuities that decreases mechanical properties, generating wider damaged area as shown in C-scan images (see Figure 16). CT-scanning (Figure 17a and Figure 17.b) confirms this trend showing a wider damaged area for the hierarchical samples with signs of zig-zag crack propagation throughout the discontinuities pattern in a non-uniform damage propagation (orange circles). On the contrary, traditional CFRP show a classical reversed cone damage failure mode [28] with a symmetrical distribution of the damaged area, mainly constituted by delamination (blue circles). For results for the impact at 8J, the activation of pseudo-plastic abilities such as crack deflection and fibres pull-out, and the consequent enhanced toughness and strain at failure lead to a higher amount of energy absorbed during the LVI event. Even though the load peak is reduced by -7%, the effects of these mechanism are clear on the maximum displacement, absorbed energy and delaminated area that show a variation in comparison with unprocessed CFRP of +7%, +9% and +6% respectively. As for the internal defects, the C-scan images show a wide damaged area inside the sample with a circular shape around the impact area while, for the control samples, the damage is displayed as a delamination areas in cross-ply configuration [53]. By comparing CT-scan images between the two configurations, it is possible to identify the crack deflection mechanism following the resin pattern which lead to a fragmentation of the inner portion of the laminate. This different behaviour explains the increased absorbed energy and larger damage extension in the bioinspired samples compared to the controls ones. In control samples, delamination is clearly identified in the laminate's body and for this reason, no signs of damage are visible on the impacted surface of the sample. It is important to underline that the 3D hierarchical CFRP structures impacted at 8J show evident signs of damage in

correspondence to the indentation point. This is an important warning sign that the structure is able to provide that allows an immediate identification of the damaged portion without the use of NDT.

These results and evaluations are also verified in the 3D hierarchical samples impacted at 12J, where the higher impact energy amplifies the effects of pseudo-plasticity. Reporting a load peak reduction of -20% and an increase in maximum displacement of +9%, this typology is able to absorb high amounts of impact energy (+67%). This value is consistent with the energy absorption data found for static tests and is confirmed by the C-scan images that report increased damaged areas inside the laminate (+64%) but limiting the damaged area in a circular portion surrounding the indentation. Analysing CT scan images, it is clear that pseudo-plastic effects were activated and exploited to generate numerous cracks that follow the resin patterns. Several fragmented areas are observed in the inner structure with a consistent presence of indentation and structure failure, visible from the external surfaces of the samples. In contrast, control samples, show a traditional BVID that is not visible without the use of NDT analyses. The introduction of 3D hierarchical patterns into CFRP structures demonstrates its effectiveness in increasing toughness and strain at failure, generating a wider and fragmented damaged area in comparison with traditional laminates when undergoing LVI event. Moreover, the activation of crack deflection along the samples thickness, in addition to the pull-out of carbon fibres from the crack surfaces increases the absorbed energy of the bio-inspired structure. Numerical modelling confirms these energy absorption improvements, reporting a good correlation with experimental results as observed in Figure 19 and Figure 20.

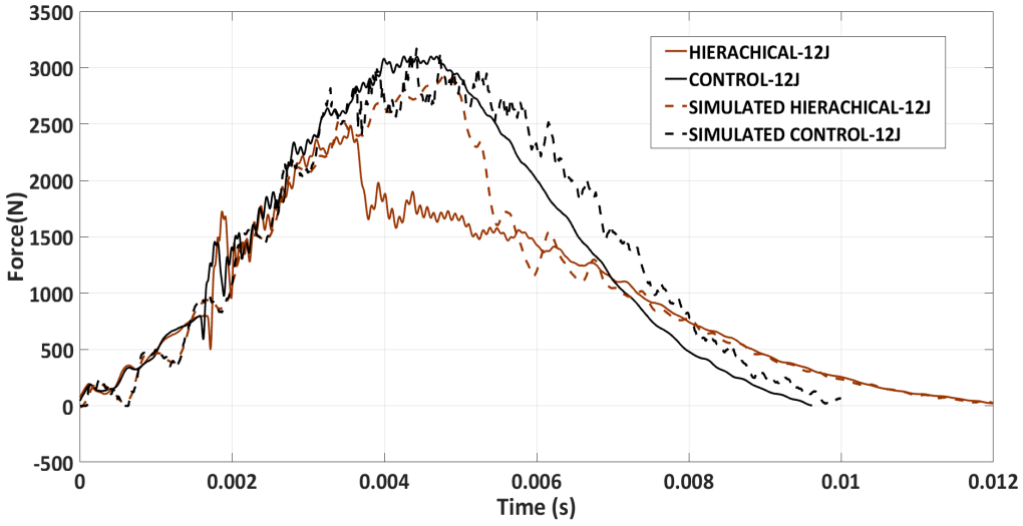

Figure 19-Force-time plot for 12J impacts results reporting numerical FEM results for the same impact event.

Numerical model is reported only for 12 J case since it is the case at higher energy and the most critical conditions in terms of pseudo-plastic behaviour and failure mechanism involved. A similar impact behaviour is observed in terms of stiffness and strength between numerical and experimental results for hierarchical CFRP even if an overestimation of maximum force (+20%) is reported due to the complex fracture mechanism involved during pseudo-plastic behaviour simulation. The comparison between numerical and experimental data of traditional laminated composite shows an excellent match of stiffness and maximum contact force (+2%). In order to analyse the performance of the hierarchical material in impact energy absorption and the maximum displacement reached during the impact event, force-displacement comparison plot between experimental and numerical impact tests is reported in Figure 20.

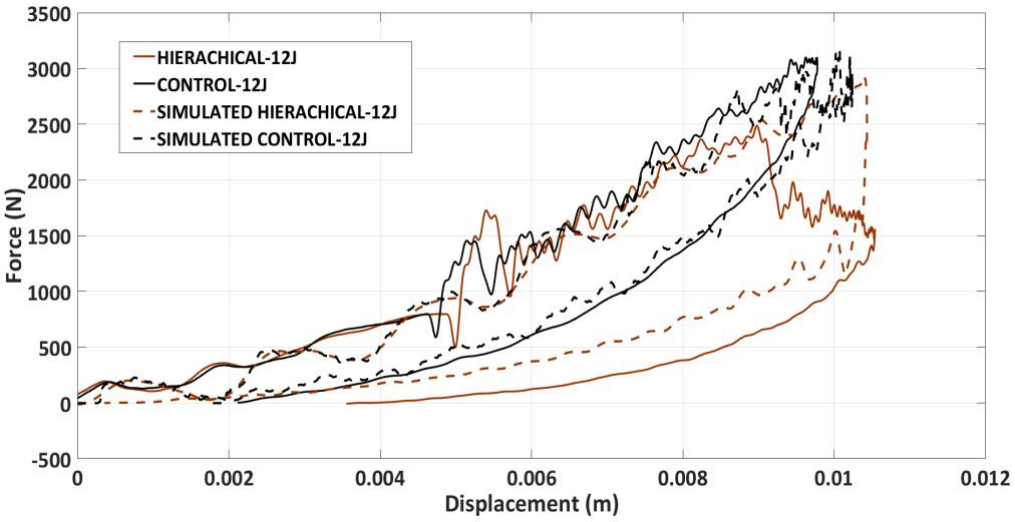

Figure 20- Force-displacement plot for 12J impacts results reporting numerical FEM results for the same impact event

As it is possible to observe from the graph, the pseudo-plasticity is completely taken into account from the numerical model reporting matching maximum displacement between numerical and experimental response of hierarchical composite structure with a difference of -1%. Similarly, impact responses of traditional laminates are similar in terms of maximum displacement with a variation of +6% for numerical data over experimental. Analysing the absorbed energy, the traditional laminate shows similar values between the numerical and experimental (-8% of variation), while absorbed energy prediction for the hierarchical material shows differences in terms of damage evolution that affects the curves fitting due to the complex nature of failure mechanisms involved (crack propagation, pull-out and fragmentation). Nevertheless, the numerical model is able to predict the global impact energy absorption of the hierarchical material with a difference of -4% in comparison with experimental.

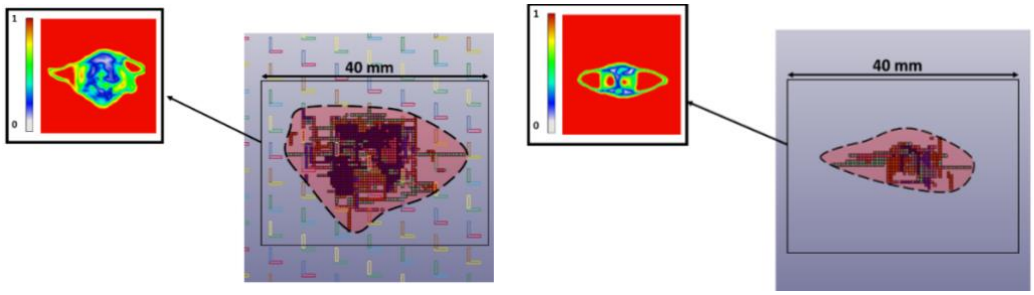

a) **b)**

Figure 21- Damage comparison between eroded elements of numerical model and C-scan damage images of impacted samples: a) hierarchical and b) control.

In order to confirm the numerical model reliability in damage mode prediction, eroded elements evaluation is used to compare damage within the numerical hierarchical and traditional laminates with damaged areas detected within the real structures using C-scan. Their comparison is reported in Figure 21 where it is possible to observe damaged areas with similar shape and extension for both experimental and numerical cases, demonstrating the reliability of the numerical model in predicting impact response, damaged area extent and severity, and impact energy absorption ability of the 3D bio-inspired hierarchical CFRP.

5. Conclusions

This paper presents new and optimised of Discontinuous Carbon Fibre Reinforced Polymers (DCFRPs) by mimicking biological hierarchical structures in order to improve impact response while preserving high-formability of composite laminates. Indeed, while it is well known that simple discontinuous fibres lead to a detriment of in-plane mechanical properties, by arranging these discontinuities in specific three-dimensional patterns it is possible to improve the toughness and strain at failure by enabling additional pseudo-plastic dissipative mechanisms such as crack deflection and fibres pull-out, thus preventing the typical brittle failure of composite laminates.

Experimental and numerical results are reported under static (three-point bending tests) and dynamic (Low Velocity Impacts) loading conditions. The effectiveness

of several manufacturing alternatives for the introduction of discontinuities patterns and their main design parameters were evaluated. A Direct A Direct Approach manufacturing procedure with a 50 mm long elemental cell was chosen over an Indirect Approach (IA) for the discontinuities pattern design since IA showed significant loss in mechanical properties (at least 20%) when compared to traditional CFRP due to the increase of notch sensitivity for larger discontinuities size, required from the manual nature of the approach. Three-points bending tests were carried out on the bio-inspired and traditional unidirectional CFRP samples to evaluate the difference in terms of mechanical response. Small variations of around +4%,-4%, -1.2% and +1.2% for strain at failure, maximum strength, flexural modulus and toughness respectively were found between the two configuration. The bioinspired structures displayed an effective pseudo-plastic behaviour with no signs of brittle failure in the laminate. Based on these results, the hierarchical concept was extended to a more complex CFRP laminate configuration (cross-ply stacking sequence) and the mechanical response investigated using a three-point bending methodology. Significant increases in toughness and strain at failure of +24% and +44% alongside a reduction in terms of maximum strength and flexural modulus of -20% and -8.4% was reported, confirming the effectiveness of the discontinuities pattern in increasing the CFRP toughness. A good correlation between experimental and simulated results was found, with excellent accuracy in strength and modulus prevision. In addition, in order to demonstrate the efficiency of pseudo-plasticity in dynamic loading conditions, a LVI impact campaign at several impact energies was carried out. Impact results showed an increase of +67% and +9% for absorbed energy and maximum displacement respectively. Good agreement was shown with numerical impact results with a variation in terms of -4% in the prevision of the absorbed energy of the 3D hierarchical structure allowing the use of this material in crashworthiness application when high energy dissipation is required.

In conclusion, this discontinuous bio-inspired material can be used in advanced applications and complex manufacturing process where impact toughness and high-performance are the main objective during the operative life of the structure.

REFERENCES

[1] Feraboli P, Masini A, Taraborrelli L, Pivetti A. Integrated development of CFRP structures for a topless high performance vehicle. Composite Structures. 2007;78:495-506.

[2] Neoh E-T. Drape properties of thermostetting prepregs: Massachusetts Institute of Technology, 1992.

[3] Pinto F, White A, Meo M. Characterisation of ductile prepregs. Applied Composite Materials. 2013;20:195-211.

[4] Tsuji N, Springer GS, Hegedus I. The drapability of aligned discontinuous fiber composites. Journal of composite materials. 1997;31:428-65.

[5] Chang IY, Pratte JF. LDF™ thermoplastic composites technology. Journal of Thermoplastic Composite Materials. 1991;4:227-52.

[6] Gutowski T, Hoult D, Dillon G, Gonzalez-Zugasti J. Differential geometry and the forming of aligned fibre composites. Composites Manufacturing. 1991;2:147-52.

[7] Simmons A. An analysis of the properties of carbon fibre aligned discontinuous prepreg tape. SAMPE, Baltimore (USA). 2012.

[8] Anderson TL. Fracture mechanics: fundamentals and applications: CRC press, 2017.

[9] Ilcewicz L, Murphy B. Safety & certification initiatives for composite airframe structure. 46th AIAA/ASME/ASCE/AHS/ASC Structures, Structural Dynamics and Materials Conference2005. p. 1877.

[10] Li VC, Wu H-C. Conditions for pseudo strain-hardening in fiber reinforced brittle matrix composites. Applied Mechanics Reviews. 1992;45:390-8.

[11] Rho J-Y, Kuhn-Spearing L, Zioupos P. Mechanical properties and the hierarchical structure of bone. Medical engineering & physics. 1998;20:92-102.

[12] Meyers MA, Chen P-Y, Lin AY-M, Seki Y. Biological materials: structure and mechanical properties. Progress in Materials Science. 2008;53:1-206.

[13] Li X, Wang J, Du J, Cao M, Liu K, Li Q, et al. Spear and shield: survival war between Mantis Shrimps and Abalones. Advanced Materials Interfaces. 2015;2.

[14] Chen P-Y, McKittrick J, Meyers MA. Biological materials: functional adaptations and bioinspired designs. Progress in Materials Science. 2012;57:1492-704.

[15] Barthelat F. Nacre from mollusk shells: a model for high-performance structural materials. Bioinspiration & biomimetics. 2010;5:035001.

[16] Barthelat F, Tang H, Zavattieri P, Li C-M, Espinosa H. On the mechanics of mother-of-pearl: a key feature in the material hierarchical structure. Journal of the Mechanics and Physics of Solids. 2007;55:306-37.

[17] Sun J, Bhushan B. Hierarchical structure and mechanical properties of nacre: a review. Rsc Advances. 2012;2:7617-32.

[18] Yourdkhani M, Pasini D, Barthelat F. Multiscale mechanics and optimization of gastropod shells. Journal of Bionic Engineering. 2011;8:357-68.

[19] Katti KS, Katti DR, Mohanty B. Biomimetic lessons learnt from nacre. Biomimetics Learning from Nature: InTech; 2010.

[20] Meyers MA, Lin AY-M, Chen P-Y, Muyco J. Mechanical strength of abalone nacre: role of the soft organic layer. Journal of the mechanical behavior of biomedical materials. 2008;1:76-85.

[21] Wang R, Suo Z, Evans A, Yao N, Aksay I. Deformation mechanisms in nacre. Journal of Materials Research. 2001;16:2485-93.

[22] Evans A, Suo Z, Wang R, Aksay I, He M, Hutchinson J. Model for the robust mechanical behavior of nacre. Journal of Materials Research. 2001;16:2475-84.

[23] Jackson A, Vincent JF, Turner R. The mechanical design of nacre. Proc R Soc Lond B. 1988;234:415-40.

[24] Lin AY-M, Meyers MA. Interfacial shear strength in abalone nacre. Journal of the mechanical behavior of biomedical materials. 2009;2:607-12.

[25] Barthelat F, Rabiei R. Toughness amplification in natural composites. Journal of the Mechanics and Physics of Solids. 2011;59:829-40.

[26] Faber KT, Evans AG. Crack deflection processes—I. Theory. Acta metallurgica. 1983;31:565-76.

[27] Czél G, Pimenta S, Wisnom MR, Robinson P. Demonstration of pseudo-ductility in unidirectional discontinuous carbon fibre/epoxy prepreg composites. Composites Science and Technology. 2015;106:110-9.

[28] Czél G, Jalalvand M, Wisnom MR. Demonstration of pseudo-ductility in unidirectional hybrid composites made of discontinuous carbon/epoxy and continuous glass/epoxy plies. Composites Part A: Applied Science and Manufacturing. 2015;72:75-84.

[29] Malkin R, Yasaee M, Trask RS, Bond IP. Bio-inspired laminate design exhibiting pseudo-ductile (graceful) failure during flexural loading. Composites Part A: Applied Science and Manufacturing. 2013;54:107-16.

[30] Gu GX, Takaffoli M, Hsieh AJ, Buehler MJ. Biomimetic additive manufactured polymer composites for improved impact resistance. Extreme Mechanics Letters. 2016;9:317-23.

[31] Narducci F, Pinho S. Exploiting nacre-inspired crack deflection mechanisms in CFRP via micro-structural design. Composites Science and Technology. 2017;153:178-89.

[32] Römer L, Scheibel T. The elaborate structure of spider silk. Prion. 2008.

[33] Jones RM. Mechanics of composite materials: CRC press, 2014.

[34] Petersen R. Discontinuous fiber-reinforced composites above critical length. Journal of dental research. 2005;84:365-70.

[35] Laspalas M, Crespo C, Jiménez M, García B, Pelegay J. Application of micromechanical models for elasticity and failure to short fibre reinforced composites. Numerical implementation and experimental validation. Computers & Structures. 2008;86:977-87.

[36] Zak G, Haberer M, Park C, Benhabib B. Mechanical properties of short-fibre layered composites: prediction and experiment. Rapid Prototyping Journal. 2000;6:107-18.

[37] Piggott MR. Short fibre polymer composites: a fracture-based theory of fibre reinforcement. Journal of composite materials. 1994;28:588-606.

[38] Otani LB, Pereira AHA, Melo JDD, Amico SC. Elastic Moduli characterization of composites using the Impulse Excitation. 2014.

[39] Begley MR, Philips NR, Compton BG, Wilbrink DV, Ritchie RO, Utz M. Micromechanical models to guide the development of synthetic 'brick and mortar'composites. Journal of the Mechanics and Physics of Solids. 2012;60:1545-60.

[40] Barthelat F. Designing nacre-like materials for simultaneous stiffness, strength and toughness: Optimum materials, composition, microstructure and size. Journal of the Mechanics and Physics of Solids. 2014;73:22-37.

[41] Wilson CD. Linear elastic fracture mechanics primer. 1992.

[42] He K, Hoa S, Ganesan R. The study of tapered laminated composite structures: a review. Composites Science and Technology. 2000;60:2643-57.

[43] Friedrich K. Application of fracture mechanics to composite materials: Elsevier, 2012.

[44] Nakanishi Y, Hana K, Hamada H. Fractography of fracture in CFRP under compressive load. Composites Science and Technology. 1997;57:1139-47.

[45] Tao J, Sun C. Influence of ply orientation on delamination in composite

laminates. Journal of composite materials. 1998;32:1933-47.

[46] Ginzburg D, Pinto F, Iervolino O, Meo M. Damage tolerance of bio-inspired helicoidal composites under low velocity impact. Composite Structures. 2017;161:187-203.

[47] Hallquist JO. LS-DYNA theory manual. Livermore software Technology corporation. 2006;3:25-31.

[48] Hallquist JO. LS-DYNA keyword user's manual. Livermore software Technology corporation. 2007;970:299-800.

[49] Manual L-DKUs. vol. II. Livermore Software Technology Corporation (LSTC). 2013.

[50] Pinho ST, Robinson P, Iannucci L. Fracture toughness of the tensile and compressive fibre failure modes in laminated composites. Composites Science and Technology. 2006;66:2069-79.

[51] Pinho S, Iannucci L, Robinson P. Physically based failure models and criteria for laminated fibre-reinforced composites with emphasis on fibre kinking. Part II: FE implementation. Composites Part A: Applied Science and Manufacturing. 2006;37:766-77.

[52] Abrate S. Impact on laminated composite materials. Appl Mech Rev. 1991;44:155-90.

[53] Wisnom M. The role of delamination in failure of fibre-reinforced composites. Phil Trans R Soc A. 2012;370:1850-70.

1. .

6 CHAPTER: Damage mitigation for Hybrid CFRP composites under Low Velocity Impact Loading

6.1 Context

Paper C illustrates the manufacturing and impact characterisation (experimental and numerical) of a hybrid laminate obtained by introducing a layer of Thermoplastic Polyurethane (TPU) within the lamination sequence of the material. This polymer was chosen for this study over others (silicone, SBR and neoprene) due to flexibility in terms of the manufacturing process and tailorability of mechanical and thermal properties. High deformation at failure and high abrasion resistance of this material were also important characteristics considered for its selection. The main objectives of this paper were to investigate the impact mitigation ability that TPU provides due to its excellent damping ability (Section 3.2.3.1) and to confirm the possibility of realising the hybrid laminate using one-step manufacturing, enabling the reduction of the cost of additional operations after the production of the component. The decision to position the TPU on the surface of the material where the impact occurs was taken due to previous works which used the polymer as an interleaved layer between plies and found this compromised the performance of the structure (see Section 3.2.3.3). The use of TPU material as a coating for laminated materials was considered as the optimal protective polymer layer, not only due to damage mitigation ability, but also due to its non-structural features of erosion reduction (see Section 3.2.3.4). Such features protect the substrate from the abrasive action of particles in harsh environments, for example on aircraft wings and blades of wind turbines. Temperature is an important factor

to consider in the use of TPU since its properties are strictly related to this parameter. The use of TPU at low temperatures is currently acceptable since low temperature has no influence on the damaged area extent generated during the impact event (see Section 3.2.3.3). The suitability of TPU at high temperatures however, is questionable, and, in this work, thermal and thermo-mechanical characterisation was carried out on the material demonstrating its suitability for temperatures above ~50°C. However, an incompatibility between the cure temperature of the prepreg (180°C) used in this study and the TPU (~150°C) tolerated temperature was identified. Consequently, a custom cure process was designed and carried out to confirm the potentiality of the creation of this material using a one-step manufacturing process. This one-step manufacturing process is fundamental to increasing the industrial appeal of laminated materials in advanced sectors. The impact characterisation was carried out using a drop tower and the data was used to validate a numerical model developed using a Lsdyna code to predict the impact response of the hybrid structure and the extent of the damaged area generated during this dynamic event. Both experimental and numerical analyses showed an excellent potentiality in the damage mitigation of the hybrid material reporting in certain cases the reduction of 100% of the damaged area compared to traditional laminates.

The original contribution of this study lies in the design of the custom one-step manufacturing process, thermo-mechanic characterisation of the TPU used as coating and the experimental and numerical characterisation of the hybrid material obtained by introducing the polymer into the lamination sequence of the structure prior to the cure process.

The Statement of Authorship Form and the paper can be found next.

This declaration concerns the article entitled:	
Thermoplastic polyurethane composites for railways applications: experimental and numerical study of hybrid laminates with improved impact resistance	
Publication status (tick one)	
Draft manuscript	
Submitted	
In review	
Accepted	
Published	✓
Candidate's contribution to the paper (detailed, and also given as a percentage)	
The candidate contributed to/ considerably contributed to/predominantly executed the…	
Formulation of ideas:	60% I developed the idea jointly with my supervisors.
Design of methodology:	70% I collaborated in the design and manufacturing of the samples during the experimental campaign. I designed and developed the FEM model used for data correlation and the global data correlation
Experimental work:	90% I collaborated in performing impact testing and relative data collection. I collected the results form numerical model and correlated the experimental with numerical results. I carried out the post-impact testing and I collected the relative data. I interpreted all the experimental and numerical data.

Presentation of data in journal format:	70% I designed the manuscript structure, wrote in collaboration all the drafts and realised all figures. Feedback on the draft and help for the paper submission, review and submission were provided by my supervisors.

Statement from Candidate			
This paper reports on original research I conducted during the period of my Higher Degree by Research candidature.			
Signed		**Date**	26/05/2020

Thermoplastic polyurethane composites for railways applications: experimental and numerical study of hybrid laminates with improved impact resistance

Francesco RIZZO[1], Stefano CUOMO[1], Fulvio PINTO[1], Gianpio Pucillo[2], Michele MEO*[1]

[1] Department of Mechanical Engineering, University of Bath, Bath, United Kingdom

[2] Department of Industrial Engineering University of Naples "Federico II", Italy

* corresponding author: m.meo@bath.ac.uk

Keywords: composite laminate, hybrids, CFRP, TPU, flying ballast, impact energy.

ABSTRACT

Due to the introduction of highly restrictive safety and pollution legislations in the railways industry, weight reduction has become an increasingly important topic over the last decade. Carbon Fibre Reinforced Polymer (CFRP) constitute an excellent alternative to traditional materials, due to their high specific in-plane mechanical properties. Their use in railways industry, however, is currently hindered by their weak out-of-plane properties. Bogies and under-frames are often subjected to impact loadings caused by objects and debris surrounding the tracks (i.e. ice, ballast) that become airborne during the train transit and impact lower part of the carriage. While metal structures absorb impact energy via plastic deformation, in CFRP Barely Visible Impact Damage (BVID) can occur, weakening the component, and often lead to catastrophic failures.

This work proposes a method for improvement of impact absorption performance of railways composite structures via the addition of a Thermoplastic Polyurethane (TPU) coating to CFRP laminates. The thermo-mechanical behaviour of the

thermoplastic layer was investigated Differential Scanning Calorimetry (DSC) and Dynamic Mechanical Analysis (DMA) analyses to optimise the manufacturing process, while damping tests were carried out to demonstrate its unaltered energy absorption ability in the final manufactured structure. TPU/CFRP plates (150 mm x 100 mm of in-plane size) were subjected to 2, 3 and 5J impacts and the results were compared with traditional CFRP laminates. Non-Destructive (i.e. C-Scan, Phased Array) and Compression-After-Impact tests were carried out on the impacted samples to assess the damaged area and residual in-plane mechanical properties. Results show that the TPU layer modifies the energy absorption mechanism, preventing the propagation of damage within the CFRP and resulting in undamaged samples even at the highest energy. In order to predict the TPU/CFRP impact behaviour and identify the best process parameters to optimise impact energy absorption, a Finite Element model was developed and validated using experimental data. The comparison showed good correlation, and a fine approximation of the different impact mechanisms was observed with a maximum error of 5% between experimental and simulated output values. The experimental and numerical results show that the TPU/CFRP laminates constitute a novel solution for the manufacturing of lighter and safer railways composite structures.

1. Introduction

Over the last twenty years, the mass of rail vehicles has increased by more than 35% due to the technological improvements of structures, subsystems and apparatus necessary to comply with market demands and higher safety requirements (CEN-EN 12663, EN 15227) Indeed, increased comfort requirements pushed manufacturers to install on rail vehicles more complex facilities, such as air conditioning systems, noise and vibration insulations and media devices, in order to improve the quality of the journey. At the same time, as consequence of safety legislation strengthening, railways vehicles became more complex and several mechanical systems, such as brakes and crash boxes, increased their size and weight to satisfy higher performance demands. Heavier trains require greater drive power

and therefore railways industry developed larger and heavier motors (electric or diesel) which, in turn, need stiffer and more resistant bogies to withstand stresses caused by larger dynamic solicitations. In addition, higher velocity demanded structural changes in structures such as windows, doors and front cabs, causing an additional weight component for the entire rolling stock due to higher stiffness and more complex geometries necessary to comply with the standards.

All these additional systems and the increased mass of structural component negatively affected the economy of railways industry, leading to a rise in production costs, higher energy consumption, larger amount of CO_2 emissions and greater track wear.

In this context, railway systems require a new technological approach to fabricate light-weight structures for train vehicles, also considering that several railways track providers, such as UK Network Rail, set up their network usage contract charges on the mass of the vehicles to reduce the track consumption and renewal costs [3]

In order to meet the low mass requirement, the use of composites materials in railways structures and components can represent an excellent solution to reduce the global weight of the train structure while keeping the same mechanical properties in terms of stiffness and strength.

In general, major mass distribution in rail vehicles, as stated by Euro Transport Consult [4], is located in motor bogies, motors and drives (22%), car-body (21%), interiors (17%) and trailer bogies (15%). Therefore it is clear that by using composites materials in primary structures, not only it is possible to reduce weight by 20-40% [5] but also lower maintenance costs also due to the higher corrosion resistance typical of composite materials [6,7]. Lighter car bodies would also need less power and braking equipment, leading to a reduction of the rotating masses, with an overall mass reduction considering that a traditional high-speed train brake disc weighs around 100 kg [8].

Composite materials in railways have been already used for interiors applications (seats, panels and secondary structures) but only in recent times, some structural applications have been proposed such as a the Glass Fibre Reinforced Polymer (GFRP) bogie realized and tested by Goo et al. under different loading conditions [9], and the front cab sandwich shock absorber designed and simulated numerically by Grasso et al. [10]. By applying fibre-reinforced polymers in the primary structures Siemens developed a light-weight train, reducing the mass per seat value by 34% (357 kg) compared to the previous generation trains [4]. Heller et al. manufactured a hybrid body railway vehicle using GFRP sandwich composites for both sidewall and ceiling panels, achieving a mass reduction of almost 20% in comparison with a traditional stainless steel body [11]. Similarly, CG Rail recently produced a rail vehicle made in large part (around 70%) of composite components, developing a manufacturing process capable of producing large CFRP profiles with wall thickness up to 25 mm. The total mass reduction in comparison with an aluminium car body vehicle is almost 30%, due to a 90% CFRP content in main large structures such as front cab and under-floor panelling [12].

Although the studies mentioned above prove that composite structures are making some headway in the railways industry, one question that still needs to be asked, however, is whether composite components would be able to fully substitute traditional metal structures despite their weak resistance to loads in the out of plane direction. Indeed, it is well known from the aerospace sector that mechanical properties detriment caused by impact events [13] is the principal critical limitation to the implementation of the composites in primary load-bearing structures. Referring to the specific case of railways industry, Onder et al. [14] assessed the damage caused by impact loadings on E-glass/polyester laminate structures and pointed out the effects of impacts at four velocity levels (40 m/s, 70 m/s, 100 m/s, 130 m/s). Goo et al. [9] evaluated the structural integrity of a bogie frame, made of glass/fibre epoxy 4-harness laminate subjected to impacts at three different energy levels (5, 10 and 20 J), showing a detriment of residual properties by almost 18%,

with increased damage area at higher energy levels and for sharper edges of the impacting object.

The issue of impact resistance is of fundamental importance for railways components due to flying ballast projections [14], a phenomenon for which general objects such as debris, leaves and ice become airborne due to aerodynamic and mechanical causes, and impact the bottom portion of the vehicle in transit causing damage. These impacts, generally characterised by a minimum energy level of around 5 J [9], can generate Barely Visible Impact Damage (BVID) into composite components, leading to a detriment of mechanical properties in terms of strength and stiffness [15-17] that can result in unexpected failure of the component, exposing the entire structure and passengers to serious dangers.

Hence, to fully exploit the intrinsic lightness of composite materials within the railways sector, new approaches are constantly investigated to enhance their out-of-plane properties without losing the desired in-plane characteristics. Riccio et al. demonstrated the effectiveness of optimising the laminate layup and skin thickness in order to minimise the delaminated area during composite failure and improve its resistance against out-of-plane dynamic loading [18]. In addition, the same authors investigated impact resistance improvement of composite panels via the use of selective stitching to prevent skin-stringer debonding showing superior mechanical properties in comparison with reference [19]. Rechack et al. inserted adhesive layers between cross-ply graphite/epoxy laminates and found that the polyamide-epoxy adhesives are able to toughen the interfaces between laminae increasing absorbed energy due to increased contact area (+40%) and reducing matrix cracking [20]. Siegfried et al. studied the effect of carbon nanotubes on woven carbonfiber/epoxy composites and evaluated that CNT improved Mode II interlaminar fracture energy (+22% compared with the reference material) and damage tolerance of composite but they also increased their sensitivity to the onset of matrix cracks with a larger delamination area after impact [21]. Ruggeri et al. demonstrated a significant increase of impact damage tolerance for composite fan

blades applying thermoplastic poluyrethane (TPU) interleave layers, observing no delamination in the interleaved region [22]. Following a similar approach, Martone et al. developed a damping behaviour model for thermoplastic polyurethane interleaved composite and reported an improvement in terms of dynamic reponse towards LVI events when the interleave layers are inserted symmetrically within the laminate's stacking sequence [23]. Russo et al. instead, proposed a woven glass fibre/thermoplastic polyurethane composite that showed no delamination after impact (even at low temperatures and for thick plates) however, increasing the thickness of the laminates, the effect of the interleaved layers loses its efficiency as an increased crack initiations tendency was recorded [24].

Altough these research works proved the efficiency of the TPU as a energy absorption media for composite materials, the presence of an interleaved layer tends to generate interfacial delamination and debonding issues, with an unacceptable decrement of the in-plane performances. Furthermore, manufacturing processes become more complex with the consequences of extended lamination process time and the necessity of specifically trained operators. In order to overcome these issues, a possible alternative approach is to develop a coating layer that can be laminated on the structure's surface and act as a shielding layer, protecting the laminate thanks to its viscoelastic damping mechanism and high strain at failure [25] without affecting the in-plane composites properties, while also guaranteeing manufacturing time saving. Similar solutions are already used in the aerospace industry, where polyurethane coatings are sprayed on the lower areas of aircraft fuselages or used as a protective layer on the landing gear panel against scratches and impact damage caused by landing strip debris [26]. Another sprayed coating solution (epoxy resin reinforced with synthetic fibres) is already used in railways in order to protect bogie axles from any debris or objects and any corrosion phenomena [27]. However, all these applications require skilled operators to carry out the coating operations, giving restrictive limits in terms of manufacturing and increasing the cost of the final product.

In this work, a TPU layer was introduced as a superficial layer on the impact surface of CFRP laminates to improve impact performances. A “one-step” manufacturing solution is proposed to carry out the coating operation at the same time of the consolidation of the CFRP laminae in autoclave without any added complexity to the manufacturing process. Prior to the experimental campaign, an extensive material charachterization for TPU material was carried out in order to verify its compatibility with the autoclave curing process and in particular to avoid any degradation or reaction with the composite’s matrix at high temperatures. Differential Scanning Calorimetry (DSC) and Dynamic Mechanical Analysis (DMA) were carried out to determine the variation of the TPU’s mechanical behaviour and its suitability for autoclave uses during both cooling and heating processes and under mechanical loads at different frequencies. Once the TPU compatibility for autoclave process was verified, the effectiveness of the coating as protective layer was investigated, via extimating the damping ability of the TPU by measuring the vibrations suppression characteristics of the coated and uncoated laminates. In order to measure the improvement in the out-of-plane properties, an experimental campaign was carried by subjecting TPU-coated CFRP panels to Low Velocity Impacts (LVIs) and comparing the results with traditional CFRP laminates. Three different energy levels, 2 J, 3 J and 5 J to simulate the BVID inflicted by flying ballast and damaged areas were analyzed using non-destructive damage detection techniques (C Scan – Phased Array and CT-Scan). In order to have a deeper understanding of the phenomena involved during the impact event and to offer a cost-effective support for the future design of commercial products using TPU/CFRP composite as structural material, a 3D Finite Element Analysis (FEA) model was developed using an explicit LS-DYNA software (R10) and validated using impact data. Furthemore, using a Compression-After-Impact (CAI) test, residual mechanical properties of the impacted samples were investigated and correlated with the damaged area evaluation.

1.1 Thermoplastic Polyurethane

TPU is a polymer formed by linear segmented block copolymers having soft amorphous segments and hard crystalline segments [28]. Soft segments are made of long flexible polyether or polyester chains while hard segments are made of diisocynate with the addition of a chain extender (low molecular weight diol). In the polymer meso-structure, each soft segment is linked to two hard ones which are interconnected by hydrogen bonds and act as multifunctional tie points, creating a physical crosslink and reinforcing fillers. On the other hand, soft segments generate an elastomers matrix, which is responsible for the TPU elastic properties. This polymeric blend is used in several engineering applications due to its mechanical strength, low-temperature high performance and impact energy absorption and therefore it was selected as protective layer for this experimental work.

2. Material Characterisation

In order to evaluate the physical and chemical properties of the TPU and its manufacturing behaviour when used as a coating on a CFRP structure, an extensive characterization campaign was carried out. In this experimental part, the thermo-mechanical behaviour of TPU was analysed using DSC and DMA in order to evaluate the TPU suitability of autoclave assisted cure procedures. DSC was used to evaluate the thermal parameters of the thermoplastic polymer such as Glass Transition (Tg) and Melting point (Tm), fundamental for composite-TPU cure process optimisation. DMA, instead, was carried out to confirm the invariance of the TPU mechanical behaviour at different temperatures (-50 / +180 °C) and frequencies to verify compliance with the typical railways operative conditions.

2.1 DSC-Differential Scanning Calorimetry

A DC Q20 (TA Instruments, New Castle,USA) was used to operate the thermal tests. Four tests were carried out on samples weighting 6-8 mg and following the same temperature programme cycle: 1) heating – 2) cooling – 3) heating. Three tests reached the maximum temperature of 170 °C while the last test

was heated up to 200 °C, to investigate the presence of any melting process also at temperatures above the traditional curing temperature of carbon laminates.

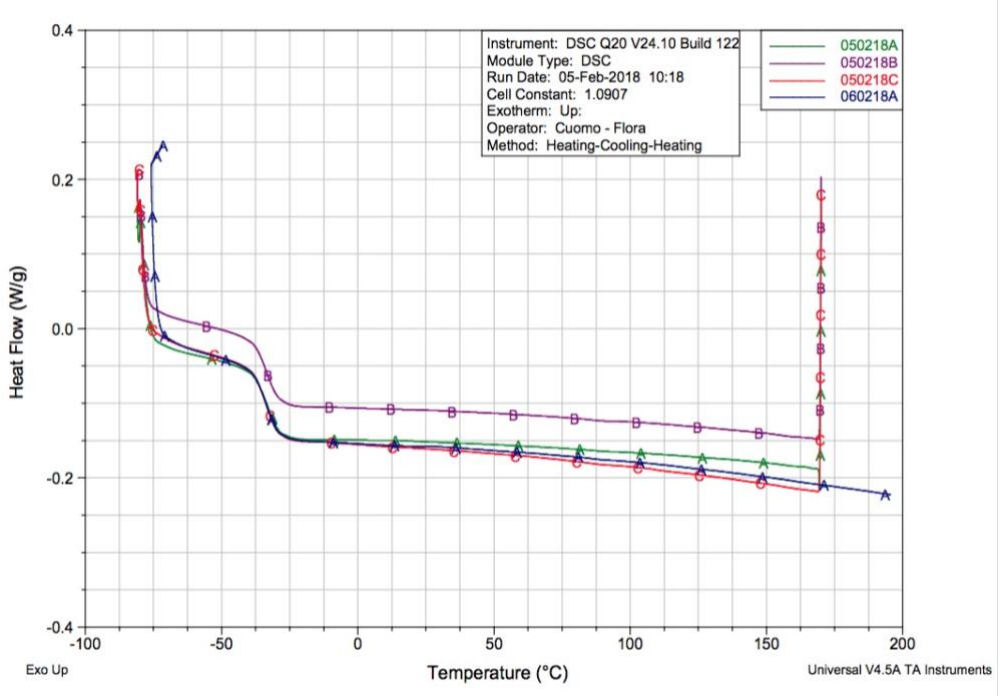

Figure 1-Temperature vs Heat Flow curves obtained for the different TPU samples

In Figure 1, DSC curves clearly show an average glass transition at -33.35°C, demonstrating that TPU is suitable for railways applications also in climatic areas where extreme temperatures conditions are reached during winter, without any risk of transition from the rubbery to the glassy state, hence without damping performances detriment.

In addition, no melting process (absence of endothermic peak) is highlighted, even in the last run (060218A curve in Figure 1) at 200°C. Considering that melting is a typical phenomenon of the crystalline domains, this behaviour suggested that the TPU selected for this experimental campaign was completely amorphous and suitable for its use at high temperature.

2.2 DMA – Dynamical Mechanical Analysis

To evaluate material response variation toward load frequency and temperature, a Tritec 2000 DMA (Tryton Technology Ltd., Leicester, UK) was used to perform Tensile/Temperature and Tensile/Temperature/Frequency scans, following the ISO 6721-11:2012 standard [29]. Both these tests are necessary since in a complex system like a rail vehicle, sudden temperature changes can affect the mechanical response of specific components and possible defects in the primary structures can generate vibrations in a frequency range usually between 1 and 50 Hz. Indeed, it is worth noting that a damaged wheel running at 250 km/h with a radius of 0.5 meters, is able to generate an excitation with a frequency of 22 Hz that directly affects the railway car body. In Temperature-scan the specimen was subjected to an oscillating stress, varying the temperature from -60 to 180 °C, with two frequencies (1-10 Hz) and a heat rate of 2 °C/min. In Frequency-scan, the max temperature was set at 100 °C, the heat rate at 2 °C/min and the frequency varied between 1 and 80 Hz. Liquid nitrogen was used as cooling medium during both tests. It is important to underline that the setup parameters were chosen considering the operative limits of railways defined by legislation (1-50 Hz in frequency and -25 /+45 °C as third climatic class temperature range –EN 50125.2008), able to verify the suitability of TPU in this application.

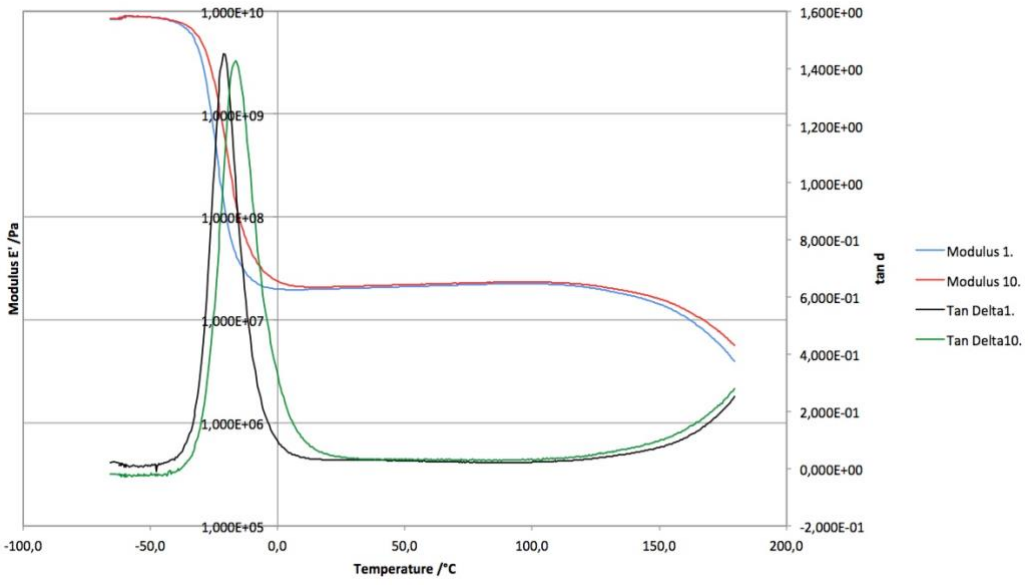

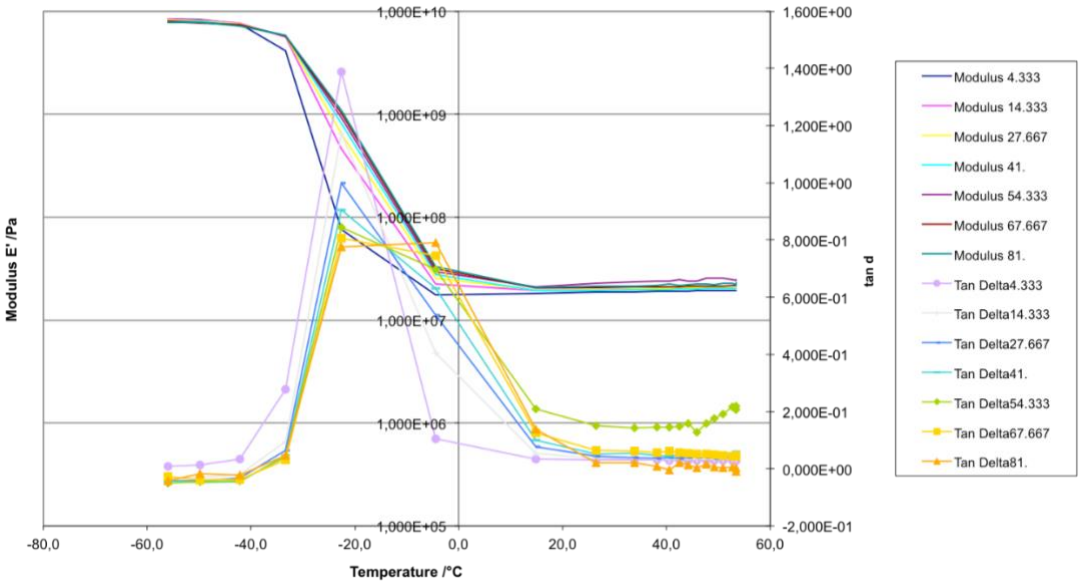

Figure 2-Temperature Scan (top) Frequency Scan (bottom).

Figure 2 shows the characteristic trend of the storage modulus E' and the damping tan δ varying with temperature and frequency. For very low temperatures, since molecular chains are tight and fixed, no responses are allowed to the applied stress and there is no resonance with the sinusoidal load, due to high stiffness (glass state). As heating increases, glass transition occurs and the chains in the amorphous region start a large-scale motion, resonating with the applied load. In this phase, the storage modulus decreases by one order of magnitude and the molecular motion associated with the glass transition is time dependent. Therefore, Tg increases when heating rate increases or test frequency increases; hence, output data showed above are consistent since in the glass transition range, both tan δ peak and storage modulus variation, are shifted to higher temperatures as the frequency is increased from 1 to 10 Hz Figure 2 top) and from 1 to 80 Hz (Figure 2 bottom). After glass transition, it is possible to evaluate a rubbery plateau due to the slippage of the molecular chains. When the temperature reaches the onset melting, free volume increases, and the material is able to flow since the molecular chains can slide on each other. Analysing the results, it is also clear that after 150 °C the material starts showing signs of degradation of mechanical properties, compromising the dynamical response of the material, which becomes frequency dependent. From the Frequency

scan (Figure 2 bottom) it is pointed out that, at different railways operative frequencies, TPU undergoes a variation of Tg from -30 °C to -20 °C, but considering that this value is still way below operative conditions, this means that even in harsh winter environments TPU will show no changes in terms of damping ability and elastic properties.

Based on these results, it is possible to conclude that the use of TPU is suitable for railways applications where a broad range of different frequencies excitations affect the vehicle and its structures. However, considering that the molecular structure of the TPU will start to degrade at 150°C and that the cure temperature for epoxy systems used in this study is 180°C, it would not be possible to include the TPU layer with the uncured CFRP layers in a "one-step" manufacturing procedure. To address this, a reduction of curing temperature, with a consequent increase of curing time, is necessary to guarantee the correct and complete cure of the CFRP laminate and the stability of the TPU polymeric system. The new cure time was obtained using a numerical linear interpolation (Figure 3) considering the starting temperature (180°C) and time (3h) parameters and fixing the final temperature (120°C).

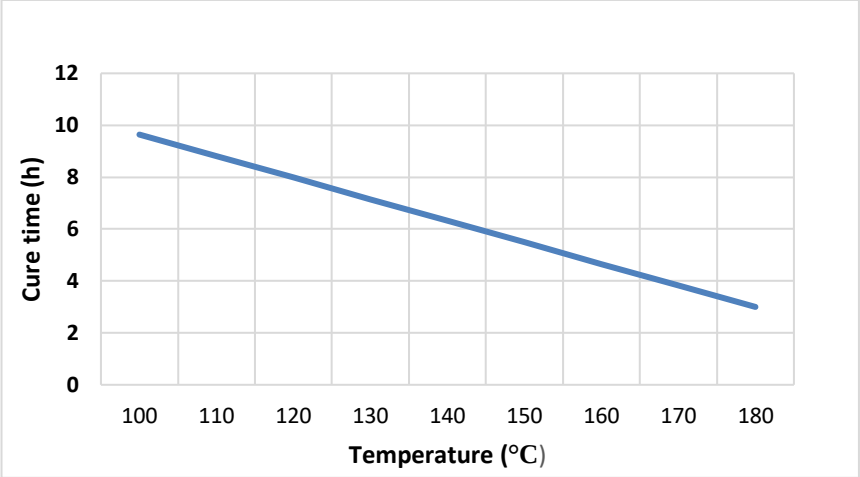

Figure 3-Interpolation curve used to estimate the cure time of the TPU-coated samples.

2.3 Damping Test

To evaluate the energy absorption properties of TPU/CFRP samples, damping tests were carried out. The test configuration (Figure 4) was a single cantilever beam (80 mm x 10 mm; w/l=1/8), excited with an impulsive load on the free end and the oscillations were measured by a laser transducer (μ ε optoNCD T2300).

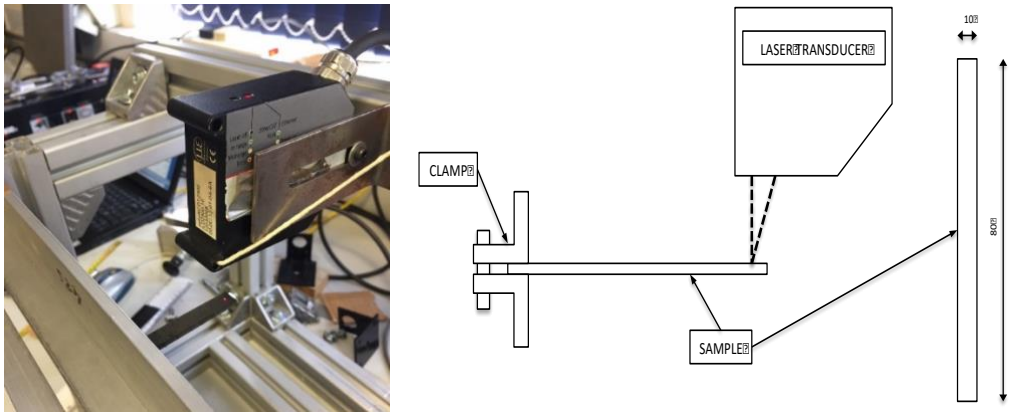

Figure 4-Damping test setup (left) and scheme (right).

The capability of the TPU/CFRP samples to attenuate the impulsive load was evaluated with the logarithmic decrement δ_{av}, which can be defined as:

$$\delta_{av} = \frac{1}{n} \ln \left(\frac{U_{n-1}}{U_n} \right) \quad (1)$$

where U_n is the amplitude of the oscillation.

In order to evaluate the optimal damping performances, different configurations of TPU/CFRP samples were tested. The main configuration was obtained following the one-step manufacturing process, with TPU applied simultaneously with uncured CFRP (TPU Autoclave Cured) and the results were compared with an uncoated laminate (Autoclave Cured). Moreover, in order to analyse the effectiveness of the proposed manufacturing process, damping tests were performed also on another configuration where the TPU layer was applied on the surface of an already cured laminate using a traditional epoxy adhesive (TPU Glued).

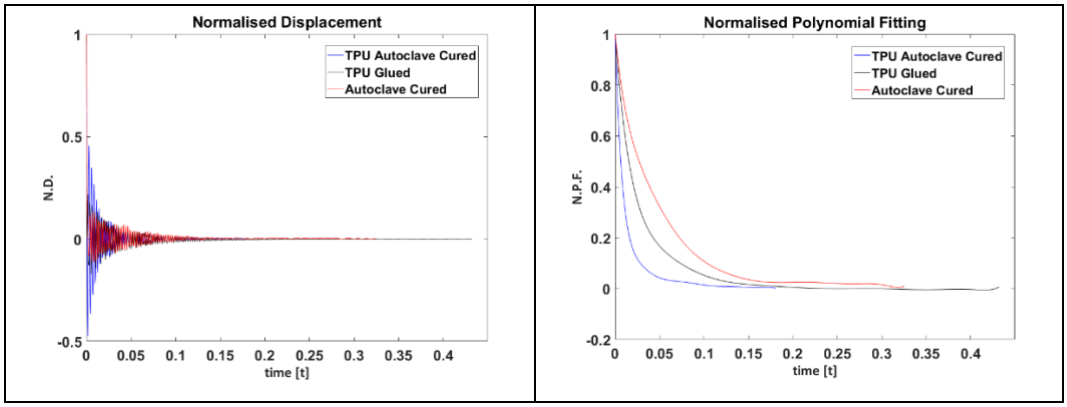

Figure 5- Damping test results: Displacement (left) and Damping (right) Curves

Table 1- Logarithmic decrement (δ_{av}) and weight variations for TPU Autoclave Cured and TPU Glued configurations compared to Autoclave Cured (control).

% variation compared to the reference (N_x)						
Type	**δ_av**	**Variation**	**Weight [g]**	**Variation**	**δ per unit of**	**Variation**
Autoclave Cured	0,0557	/	2.505	/	0.0222	/
TPU Glued	0,1014	182%	3.43	+36.9%	0.0300	135%
TPU Autoclave Cured	0,2160	387%	3.378	+34.8%	0.0629	283%

Analysing the logarithmic decrement evaluated for the different configurations (Figure 5), the TPU in the CFRP laminate leads to an increase of damping properties in both one-step and glued manufacturing procedures, showing an increase of 387% and 182% respectively, in comparison with traditional CFRP laminates. It is important to underline, however, that the presence of the TPU layer affects the weight of the laminate, therefore these results were rescaled evaluating the values of δ per unit weight (see Table 1), leading to a variation of +283% and +135% for the two configurations. In conclusion, considering the significant increment in damping properties for the "one-step" manufacturing procedure, this configuration was selected for the impact test sample manufacturing.

2.4 Samples Manufacturing

The material used to fabricate the CFRP samples was a carbon fibres pre-preg (CYCOM 977-2 thermoset epoxy system). A cross ply staking sequence of 11 plies ($[0/90/0/90/0/\overline{90}]_s$) was used during the layup procedure where each ply was cut at 150 mm x 100 mm in size. Prior to the autoclave process, the uncured CFRP was coated via direct application of the TPU layer and a metal plate was used as mould to obtain a good adhesion between the two materials. Images of the manufactured samples are reported in Figure 6.

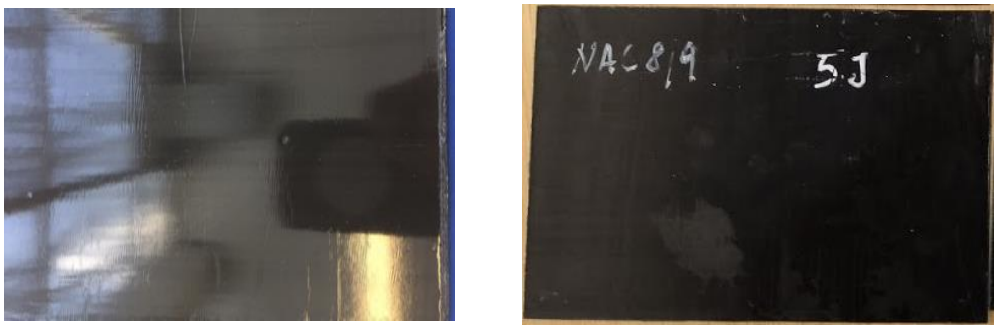

a) **b)**

Figure 6-Standard impact plates used during experimental campaign: a) TPU-coated CFRP and b) traditional CFRP

The average thickness of the laminates was 2.00 mm (CFRP) and 2.8 mm (TPU/CFRP). A sketch of the sample layup is reported in Figure 7.

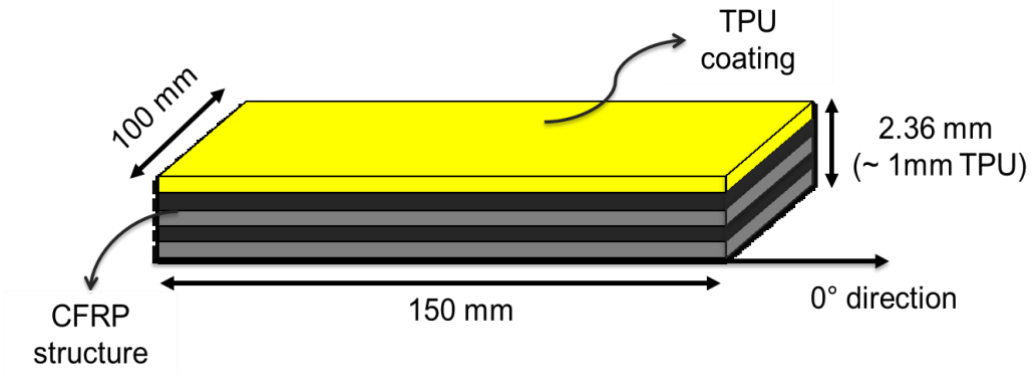

Figure 7- Sketch of TPU-coated CFRP plates used during impact campaign

3 Low Velocity Impact Test

3.1 Experimental setup – LVI tests

Impact tests were carried out on TPU/CFRP samples and compared with traditional laminates to investigate the effects of the TPU layer on the impact properties of the composite structure. Three different energy levels (2J, 3J and 5J) were used to simulate the minimum conditions to generate a flying ballast BVID in a CFRP structure as specified by the European Regulatory Framework. The samples were placed into the impact machine (2.66 kg shuttle weight) using a dedicated clamping support to apply the appropriate boundary conditions in order to avoid undesired vibrations. Impact data were collected using a Kistler Accelerometer and raw signals (Time-Volt) were converted into Force-Displacement curves following BS EN ISO6603-1:2000 and BS EN ISO6603-2:2001 standards. The impactor rig scheme and apparatus are illustrated in Figure 8. All the samples were impacted following the same procedure with TPU samples being impacted with the polymer layer facing the impactor tip.

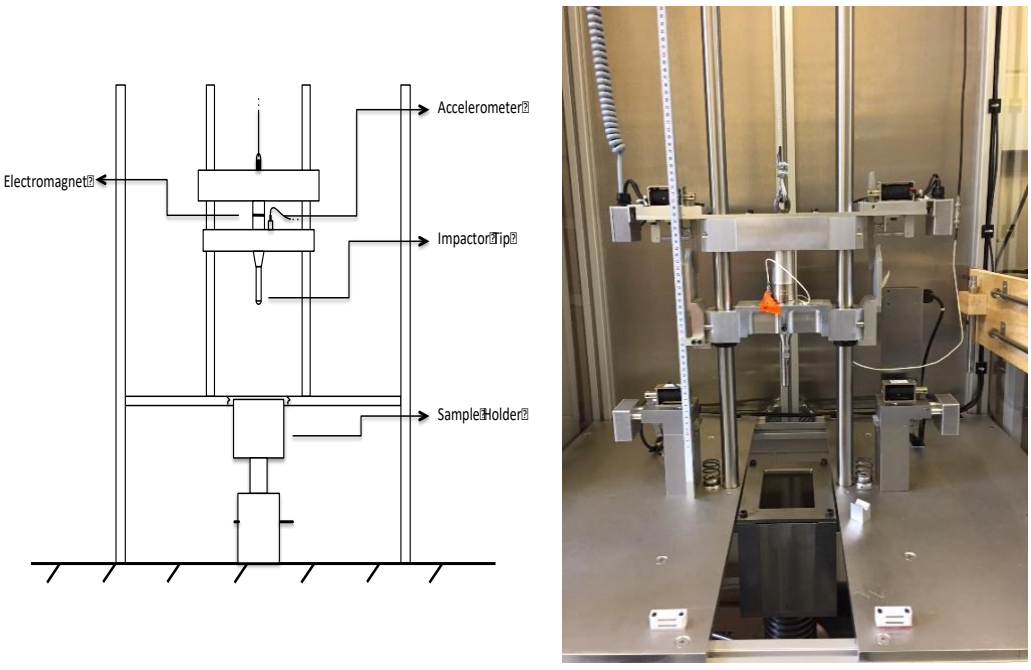

Figure 8-Impactor Rig scheme and detail

3.2 Experimental setup – Phased-Array scan and CT scan

The planar extension (2D) of the internal damage was investigated using a 5MHz Phased-Array Transducer at 128 Channels (National Instrument, Austin, CA). The beam length of each transducer corresponds to 0.58 mm in the real scale of the sample and the images were collected with a fixed width size of 225 pixels. A digital-real scale conversion was, then, possible through direct correlation between the full length of 128 transducers (real dimension) and the relative pixels collected (digital). Images displayed the in-plane amplitude variation in a 16-bit colour-map scale from which damaged areas can be identified. The colour scale used was between 0 and 40 V where the colour red was the maximum value and the colour white the minimum.

Volumetric (3D) images of internal damaged areas were collected using a Computed Tomography (CT) Scan (Nikon XT H 225, Tokyo, Japan) to confirm the results obtained with the Phased-Array and to further analyse the impact damage typology in three dimensions. Images were collected for the entire volume of the samples and then elaborated to show the fit view of the damaged areas.

3.3 Numerical Model Set-up

The testing required for the validation of a specific design in terms of safety and reliability is both expensive and time consuming due to the entity and complexity of the process also due to the wide range of design parameters that need to be taken into account during the development of new material solutions to manufacture primary structural components.

Finite Element (FE) modelling is one of the most powerful tools used by modern industry to reduce the number of experimental tests that are required to validate a certain design, leading to a consequent reduction in costs and process time. Indeed, after its validation, the use of numerical model allows to optimise critical design parameters (weight, size and geometry) that advanced sectors demand for the application of TPU/CFRP. Based on this premise and on the necessity to develop an accurate design and an optimisation tool for a future use of TPU/CFRP laminates

in real commercial parts, a three dimensional (3D) explicit Finite Element Model (FEM) was implemented using LS-DYNA. The computational FE mesh is reported in Figure 9 where in the side view, it is possible to see the presence of TPU (top layer) as coating for the CFRP laminate.

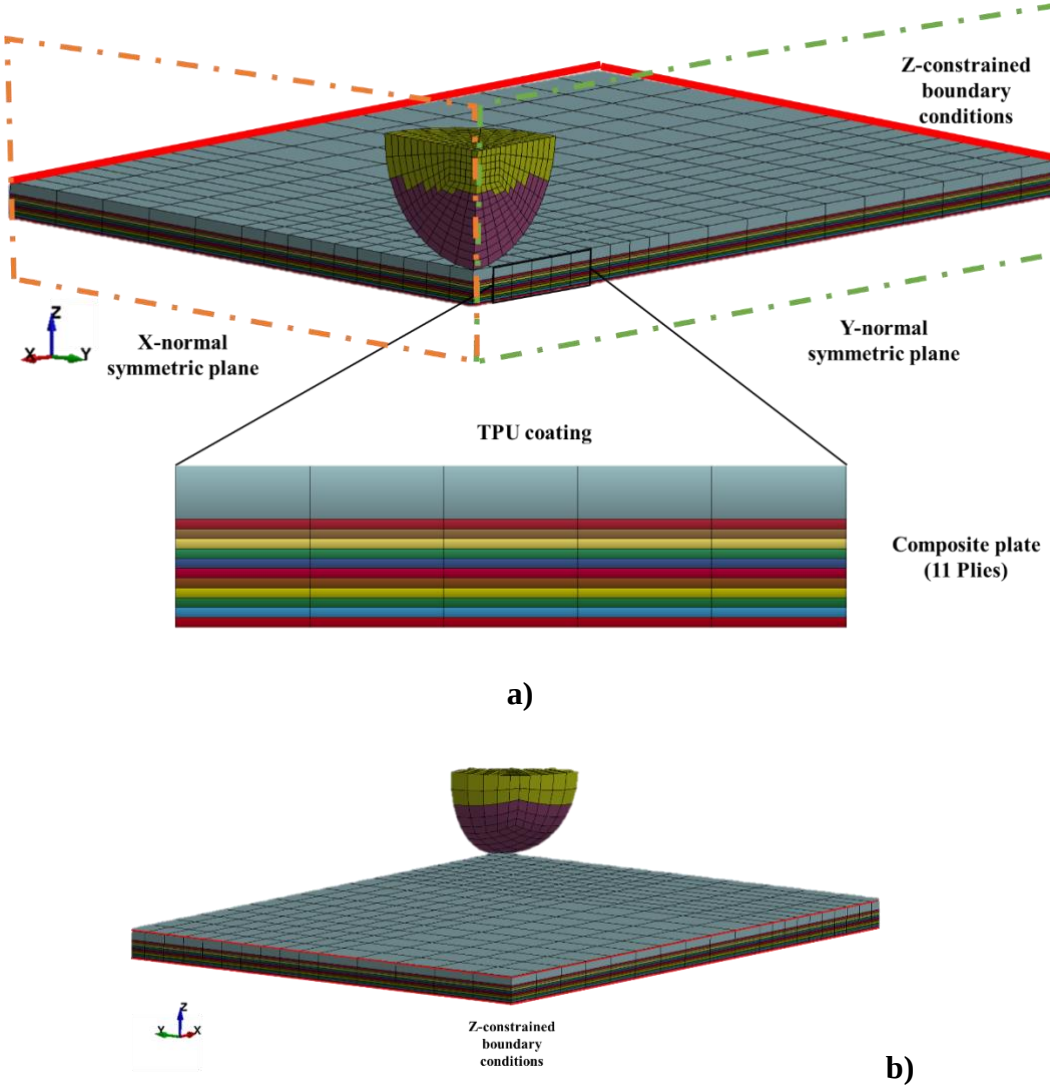

Figure 9-FE mesh used in the simulated LVI: a) front-isometric and lateral view with detail of the TPU coating and CFRP plate where symmetric planes and boundary conditions are reported and b) back-isometric view of the boundary conditions of the plate

The impactor body was simulated as a hemispherical body of 20 mm diameter, a mass of 2.66 kg and 3D brick elements using an ELASTIC isotropic material card (E=210 GPa and ν=0.3). The material was assumed elastic (no plastic deformation)

since impact velocity is very low (1.93m/s for 5J case) and no plastic deformation was observed on the impacting tip during the experimental case. Parameters used during the analyses are reported in Table 2.

Table 2-MAT_261 orthotropic material card paramters:RO: density, modulus of elasticity (E11, E22, E33), poisson's ratios (PR12 ,PR31, PR32), shear modulus (G12, G23, G31), normal and transverse strenght under traction and compression (X1t, X1c, X2t, X2c), shear strenght (S12, S23, S31), compresisve fibre failure energy (ENKINK), tensile fibre failure energy (ENA), Intralaminar matrix tensile energy failure (ENB), Intralaminar matrix trasnverse shear energy failure (ENT) and Intralaminar matrix longitudinal shear energy failure (ENL).

MAT	RO (Kg/m^3)	E11 (GPa)	E22 (GPa)	E33 (GPa)	PR21	PR31	PR32	G12 (GPa)	G23 (GPa)	G31 (GPa)	X1t (MPa)	X1c (MPa)
CFRP	1530	110	4.9	4.9	0.0535	0.0535	0.449	4	4	4	1500	950
MAT	X2t (MPa)	X2c (MPa)	S12 (MPa)	S23 (MPa)	S31 (MPa)	ENKINK (J/m^2)	ENA (J/m^2)	ENB (J/m^2)	ENT (J/m^2)	ENL (J/m^2)		
CFRP	70	200	80	80	80	75100	50100	478	900	900		

A constant stress element formulation was used to model the 3D brick elements with an average in-plane size of 2.5mm. Each ply was modelled using a single 0.18mm thick element layer. The material characteristics of the composite plate (150 mm x100 mm x 3 mm in size) was defined using a MAT_261 (LAMINATED_FRACTURE_DAIMLER_PINHO) orthotropic material implementing a progressive damage model considering non-linear in-plane shear behaviour [32]. The definition of angles and stresses in fracture plane are reported in Figure 10

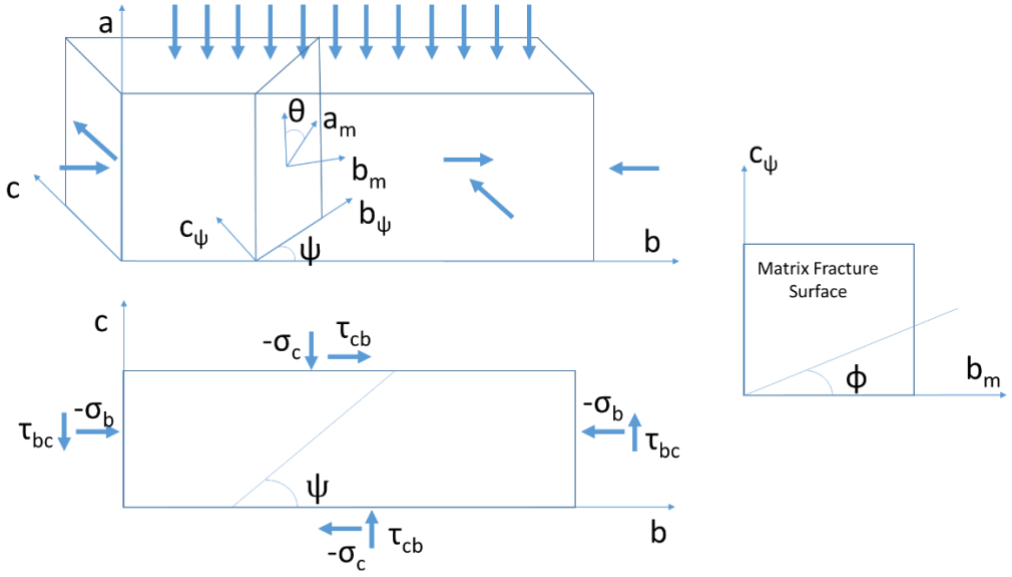

Figure 10- In fracture plane stresses and angles definition (29).

The damage initiation for longitudinal and intralaminar failure was calculated using the stress state for each time step and the relative material strength parameters. Failure criteria are defined as:

Logitudinal (fiber) tension

$$\frac{\sigma_a}{X_{1t}} = 1 \tag{2}$$

Longitudinal (matrix) failure:transverse tension (if σ_n>0)

$$\left(\frac{\sigma_n}{X_{2t}}\right)^2 + \left(\frac{\tau_T}{S_T}\right)^2 + \left(\frac{\tau_L}{S_{12}}\right)^2 = 1 \tag{3}$$

Longitudinal (matrix) failure:transverse compression/shear (if σ_n<0)

$$\left(\frac{\tau_T}{S_T - \mu_T \sigma_n}\right)^2 + \left(\frac{\tau_L}{S_L - \mu_L \sigma_n}\right)^2 = 1 \tag{4}$$

With

$$\begin{aligned} \sigma_n &= \frac{\sigma_b + \sigma_c}{2} + \frac{\sigma_b - \sigma_c}{2}\cos(2\Phi) + \tau_{bc}\sin(2\Phi) \\ \tau_T &= -\frac{\sigma_b - \sigma_c}{2}\sin(2\Phi) + \tau_{bc}\cos(2\Phi) \\ \tau_L &= \tau_{ab}\cos(\Phi) + \tau_{ca}\sin(\Phi) \\ S_T &= \frac{X_{2c}}{2\tan(\Phi_0)} \end{aligned} \tag{5}$$

$$\mu_T = -\frac{1}{\tan(2\Phi_0)}$$

$$\mu_L = -S_{12}\frac{\mu_T}{S_T}$$

$$\mu_L = -S_{12}\frac{\mu_T}{S_T}$$

considering Φ_0 as the fracture angle (53°). Longitudinal compression failure criterion definition can be found in literature (29). In Figure 11, the damage evolution law for MAT_261 is reported for each failure criterion.

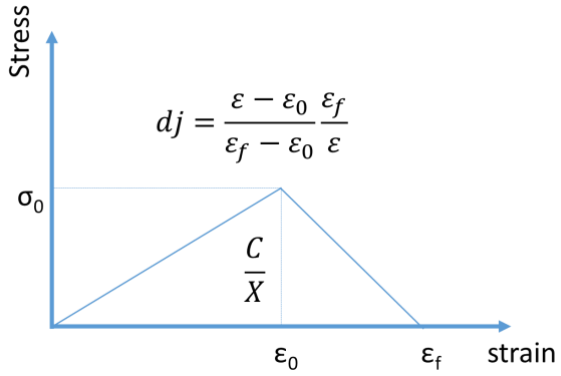

Figure 11-Damage evolution law for MAT_261 (29)

When the stress state is within the criteria values, the material behaves as elastic orthotropic. When, instead, one of the criteria is met, the stress is reduced by a coefficient of *(1-d_j)* where d_j is one of the damage function of the different failure modes, showing a fracture-based linear damage evolution with fracture toughness (one for each failure criterion) as critical value C. Each damage function is normalised for the element characteristic length X (see Figure 11) to have consistency between different element sizes. Element erosion was, then, evaluated for each element that satisfies one of these fracture criteria. All the equations on damage initiation and fracture criteria were reported in the MAT_261 card section of the material manual [33]. In order to predict the delamination component during the dynamic event and take into account the interlaminar properties of laminated material, a TIEBREAK_CONTACT (OPTION 6) was implemented between each layer of the hybrid structure. This particular contact [34] couples together the nodes of two adjacent plies until failure initiation, defined by interlaminar interface

toughness G_{IC} (230 J/m2) and G_{IIC} (650 J/m2) and the relative normal ($\sigma_f = 4.6MPa$) and shear ($\tau_f = 13MPa$) stresses. The tiebreak failure criterion is defined using the normal and shear components of the stress state at a certain time step:

$$\left(\frac{|\sigma_n|}{\sigma_f}\right)^2 + \left(\frac{|\tau_n|}{\tau_f}\right)^2 \geq 1 \quad (6)$$

(Where σ_n and τ_n are the normal and shear stress."

Afterward the damage was scaled in function of the inter-laminar distance until complete interface separation that occurs when the distance between the plies reaches its critical value (0.1mm).

Then, the contact is converted into a traditional PENALTY_BASED contact. The. TPU coating material was simulated using an isotropic VISCOELASTIC material card [35,36] and all the used elastic parameters were defined considering the results obtained from DMA tests and data fitting with experimental results. The viscoelastic material properties are defined by the equation 7:

$$G(t) = G_\infty + (G_0 - G_\infty)e^{-\beta t} \quad (7)$$

where G_0 represents the short-time shear modulus (~6.4GPa), G_∞ the long-time shear modulus (4.4GPa), β the decay constant (~1) and t the time of observation. This material was chosen since no relevant permanent deformation are found on the real TPU layer after the impact event and therefore the viscoelastic behaviour for the involved impact energies can be assumed without plastic effects. Boundary conditions of mesh model are applied by constraining all displacements along the z-direction of the external lateral edges of the plate. Interaction between impactor body and TPU/CFRP surfaces is modelled using PENALTY_BASED contact for which the erosion of elements with negative volume is allowed to avoid numerical issues. All the materials parameters used in the numerical model are reported in Table 2.

4 Results and Discussion

Output data obtained from the impact campaign are reported in Figure 12 in which Force-Time and Force-Displacement curves and their comparison are illustrated.

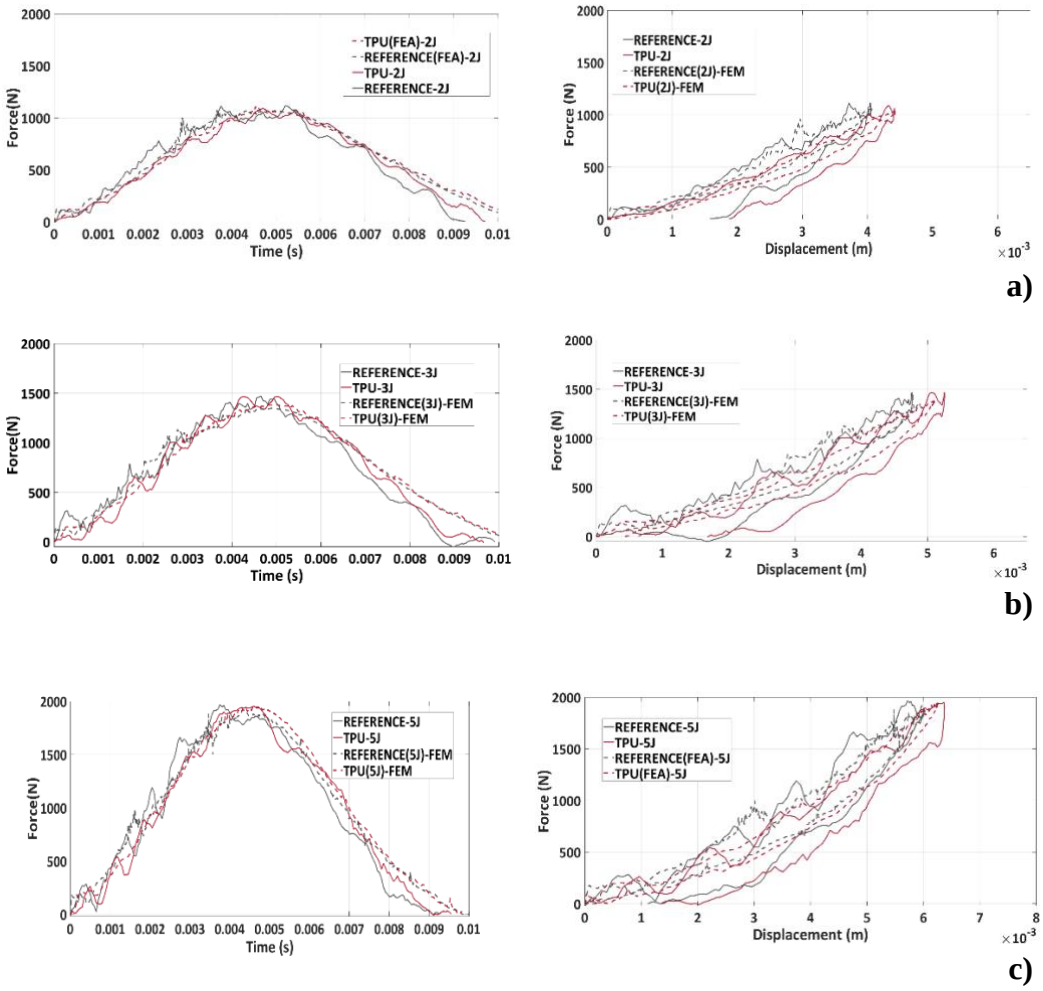

Figure 12-Impact results curves obtained from impact tests on Control and TPU samples for different levels of energy: a) 2J, b) 3J and c) 5J). Force-time and Force-Displacement curves reported.

The extent of the internal damage was evaluated using Phased array scans (Figure 13) from which a statistical analysis was carried out to demonstrate the consistency of damage extension results. Similarly, to understand the typology and topology of the damage inside the laminate's structure and to assist Phased-Array results, CT-scan images were examined. (Figures 13 and 14)

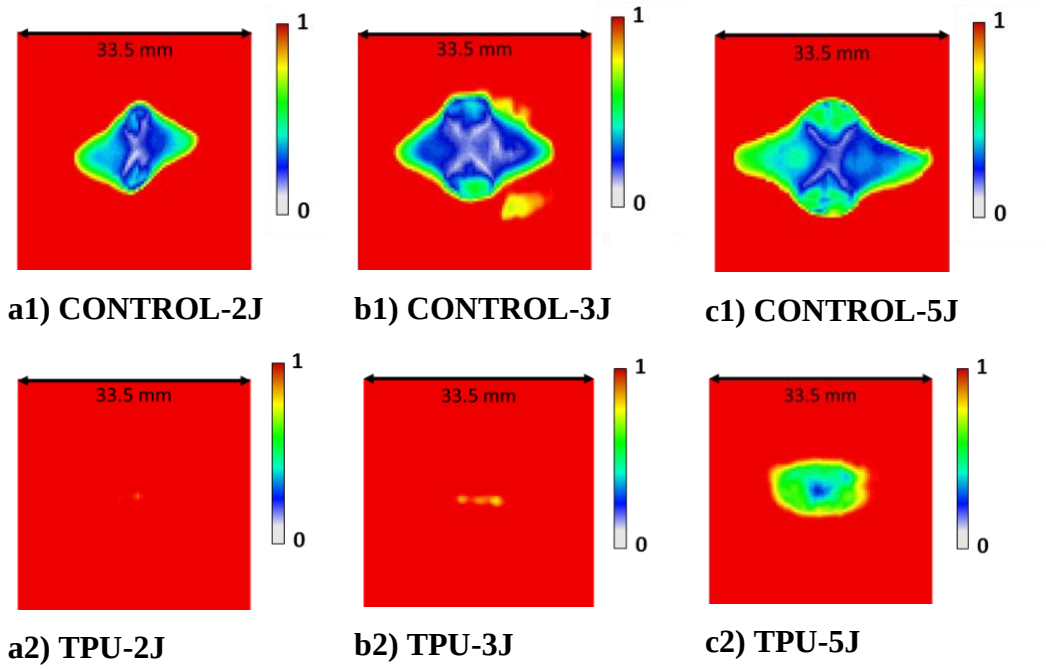

Figure 13-Phased-Array scans from the impacted samples: a1,b1,c1) control samples impacted at 2J,3J and 5J, , b1,b2,c2) TPU-coated samples impacted at 2J,3J and 5J. Images are collected from the external surface, far from the impacted one. The colour scale represents the normalised amplitude.

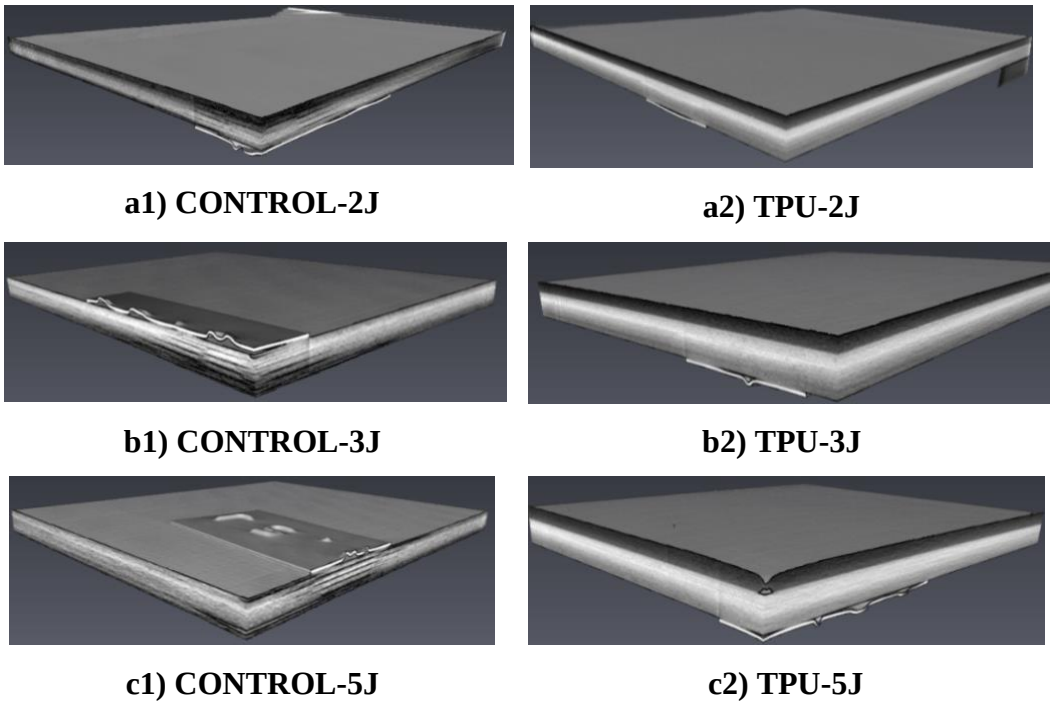

Figure 14-CT scan damage detection technique from the impacted samples: a1,b1,c1) control samples impacted at 2J,3J and 5J, , b1,b2,c2) TPU-coated samples impacted at 2J,3J and 5J.

Statistical data with mean values and standard deviations for each energy level and configuration are reported and compared in Table 3 and Figure 15.

Table 3-Statistical data from impact campaign. 2J, 3J and 5J are the impact energies and the impact parameters of Time of Contact, Peak Force, Maximum Displacement, Absorbed Energy and Delaminated area are reported.

REFERENCE					
Energy (J)	**Time of Contact (ms)**	**Peak Force (N)**	**Max Displacement (mm)**	**Absorbed Energy (J)**	**Delaminated Area (mm2)**
2	*9.34 ± 0.188*	*1083 ± 18*	*4.05 ± 0.10*	*0.95 ± 0.02*	*234.2 ± 24.1*
3	*9.07 ± 0.33*	*1420 ± 20*	*4.78 ± 0.26*	*1.32 ± 0.06*	*350.9 ± 2.6*
5	*8.78 ± 0.33*	*1895 ± 57*	*5.93 ± 0.26*	*2.21 ± 0.20*	*485.5 ± 67.9*
TPU					
Energy (J)	**Time of Contact (ms)**	**Peak Force (N)**	**Max Displacement (mm)**	**Absorbed Energy (J)**	**Delaminated Area (mm2)**
2	*10.12 ± 0.22*	*1103 ± 42*	*4.56 ± 0.21*	*0.88 ± 0.07*	*0*
3	*9.58± 0.06*	*1421 ± 13*	*5.04 ± 0.32*	*1.33 ± 0.09*	*0*
5	*9.14 ± 0.20*	*1976 ± 43*	*6.22 ± 0.29*	*2.19 ± 0.09*	*157.4 ± 20.5*

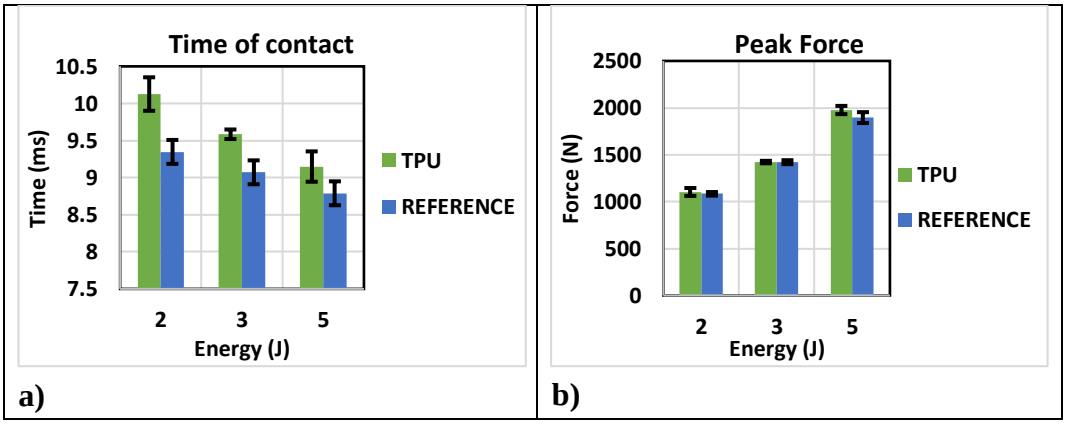

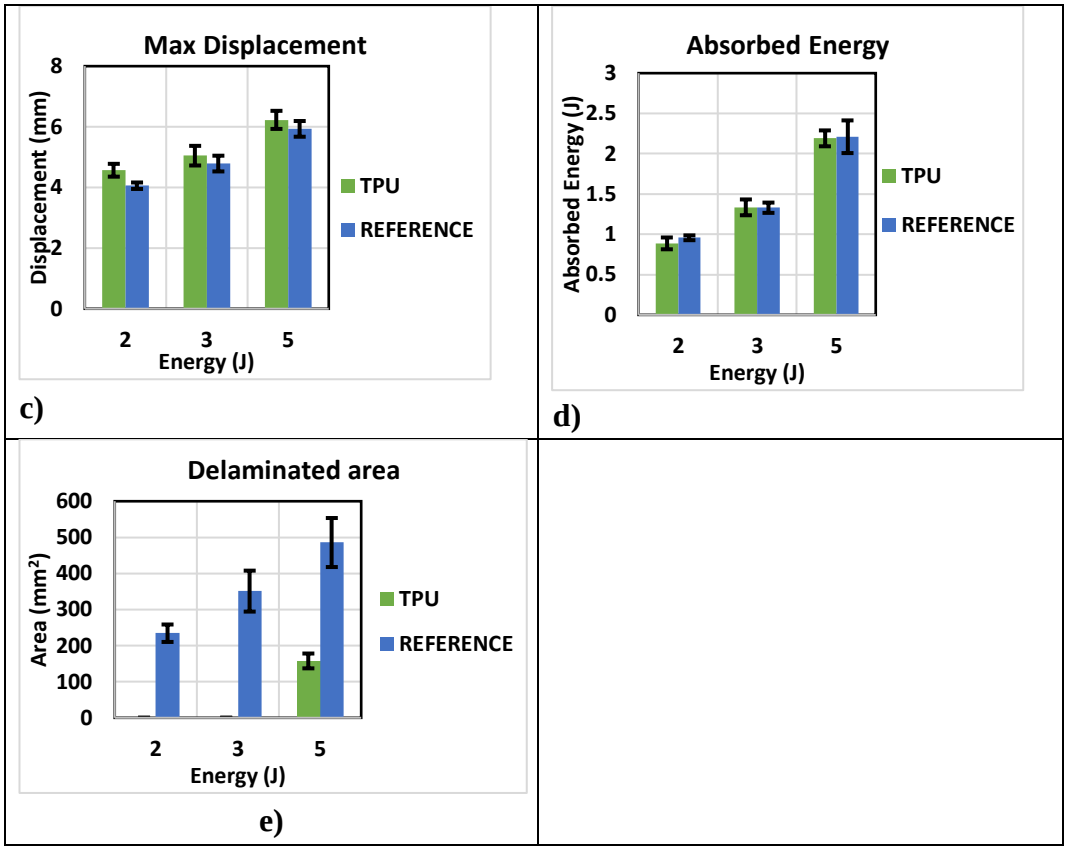

Figure 15-Statistical data charts on impacted data for 2J, 3J and 5J impacts. Mean values for each impact parameters and respective standard deviations are reported in the column chart for control and TPU sets: a) time of contact, b) maximum contact force, c) maximum displacement, d) absorbed energy and e) damaged area extension measured from C-scan images. TPU samples have no structural damage within the CFRP portion and the reported values correspond to the TPU-CFRP interface separation.

As predicted in literature [37], the impact behaviour of both configurations changes according to the impact energy. In particular, for TPU/CFRP samples, maximum displacement and time of contact (in comparison with uncoated samples) increase by +8.34% and +12.58% for 2J, +5.66% and +5.44% for 3J and, +4.10% and 5.01% for 5J, (see Figure 15.c and Figure 15.a), reporting that the increase in displacement between TPU coated and control samples tends to decrease for higher energetic impacts due to the viscoelastic effect of TPU layer [38]. The presence of TPU has reduced influence on force peak values (Figure 15.b) with minimal variations in terms of impact response for the different energy levels (see Figure 15). The percentage variation in comparison with the reference is +1.85% for 2J, +0.08% for 3J and +4.26% for 5J.

Another important result is shown from Figure 15.d, where a similar absorbed energy is reported for both tested configurations (see Figure 15.e), suggesting that the presence of the TPU coating enables different energy absorption mechanisms. As a consequence, it is important to correlate the information obtained with the LVIs tests with the internal integrity status of post-impact samples. Phased-Array images of control samples (Figure 13) indicate widespread damaged areas with damage extension increasing with impact energy. In contrast, TPU/CFRP samples show no signs of defects within the laminate, with the exception of the samples impacted at 5J, where a small damage can be seen in correspondence with the indentation point area. The variations in terms of damaged areas between TPU-coated and traditional CFRP samples are -100% for 2J (undamaged), -100% for 3J (undamaged) and -67.5% for 5J. CT scan images of the control samples (Figure 14) show wide damaged areas that can be clearly identified as a typical reversed pine-tree propagation shape characteristic of matrix failure, whose severity and extension increase with the increase of impact energy, confirming the results shown for Phased-array images. On the contrary, CT scan images of TPU-coated samples show no signs of damage in the entire body of laminate for all impact energies, in apparent contrast with what observed with the Phased-Array scans for the 5J samples (Figure 14.c2). The difference between the outputs of the two tests was found to be due to the presence of a small area within the TPU layer showing signs of interface separation between TPU and CFRP that was indistinguishable from a structural damage from the Phased-Array images. Consequently, TPU coated samples impacted at 5J do not present any sign of structural damage in the CFRP portion since the damaged area detected in the Phased-Array images corresponds to the TPU interface separation.

By comparing the experimental results with the output of the numerical model, it is possible to observe that the model is able to predict the damage-suppression ability of the TPU coating, as reported in the comparison graphs in Figure 10. In particular, the numerical curves for traditional CFRP laminate show load drops similar to the

ones observed experimentally (around 3ms for 2 and 3 J, and around 3ms and 4.5ms for 5J), while numerical simulation of the TPU-coated samples show no damage, also confirming the experimental results. An error of +2% and -0.7% for 2J for uncoated laminates and +8% and +3% for the TPU/CFRP is found in terms of maximum contact force and maximum displacement between experimental and numerical results, showing a good accuracy in predicting the impact output data for both traditional and TPU/CFRP. Similarly, considering 3J impacts, the overall for maximum contact force and maximum displacement is around the same values detected for the 2J impact case with +5% and -0.2% respectively for the reference samples and +2% and -0.1% for the TPU/CFRP ones. 5J impact case, as well, shows differences in the terms of maximum force and maximum displacement similar to the two previous cases, reporting -1% and -4% for the reference configuration and +1% and +0.3% for the hybrid case. Thus, the results show a good correlation between experimental data and the numerical model for values of stiffness, maximum displacement and maximum contact force, even if the force-displacement descendent curve portion presents a slight mismatch. These small variations can be the result of the formation of defects during the cure process that affect the numerical data for mechanical properties and the elastic energy release during the unloading phase of the impact event.

In order to explain the different behaviour of the TPU-coated CFRP, it is important to analyse the different mechanisms utilised to store or absorb energy by estimating the energy transfer from the impacting mass to the sample during the impact event (34,35,36). In general, for LVI impacts where no visible damage is reported, a total kinetic energy transfer (E_{total}) takes place from the impactor's tip to the sample in correspondence with the contact point, and the energy is distributed into the laminate with different forms. One such form is the elastic energy contribution ($E_{elastic}$), which represents the ability of the material to store energy via non-permanent geometrical deformation. This energy is transferred back to the penetrator after maximum displacement of the plate is reached. Another form is the

energy absorbed ($E_{absorbed}$) by the impacted object [39,41,42]. Therefore, for the energy conservation balance it is possible to write:

$$E_{total} = E_{elastic} + E_{absorbed} \quad (8)$$

$E_{absorbed}$ can be further divided into three different contributions: E_{damage}, representing the energy required to generate damage inside the structure (e.g. fibre failure, matrix failure and delamination), $E_{viscous}$ that is the energy absorbed via viscoelastic mechanisms [43] and $E_{dissipation}$ which encompasses all other dissipation modes including heat, inelastic behaviour of components and all non-linear behaviours. Thus, the equation can be written as:

$$E_{total} = E_{elastic} + E_{damage} + E_{viscous} + E_{dissipation} \quad (9)$$

Considering the layered nature of CFRP, [44], in traditional laminates damage generation is the main cause of energy dissipation, due to the creation of new surfaces between two adjacent plies at different fibre orientations (i.e. delamination). For this reason, a notable amount of energy is absorbed in a laminated system and the E_{damage} term represents the highest contribution in equation (9).

In contrast, using a TPU layer, an additional damage suppression ability is introduced into the CFRP system due to the high strain at failure and damping ability of the polymer [45].

Indeed, since TPU is characterised by a lower stiffness and higher strain at failure, it is able to increase the global elastic energy threshold that the material can tolerate before damage is generated. As a consequence, a lower amount of energy is found into the E_{damage} term and consequently, less impact energy is dissipated via the creations of defects. In addition, the hybrid system is able to absorb a larger amount of impact energy via viscoelastic losses of TPU layer. This allows to take into account more energy into the $E_{viscous}$ term and lower the weight of the E_{damage} term, meaning smaller damaged areas generated into the sample.

Therefore, it is possible to conclude that the coupled effects of increased elastic properties and improved damping given by the TPU layer, allow the absorption of

all the impact energy via these two components, generating no damaged areas within the laminate's body.

5 Compression-after-Impact (CAI)

In order to confirm the results obtained with the LVIs and the NDT analyses, post-impact samples were subjected to a Compression-After-Impact (CAI) campaign to analyse the residual compressive strength and prove the damage suppression ability of the TPU layer.

5.1. Experimental setup

CAI tests were performed using an Instron Universal Machine 5585 in compressive mode following the standard ISO 19352:2009. A rig of 150mm x 100 mm was used to constrain the sample and guarantee a pure compressive load applied on the sample section. A schematisation of the used rig is reported in Figure 16:

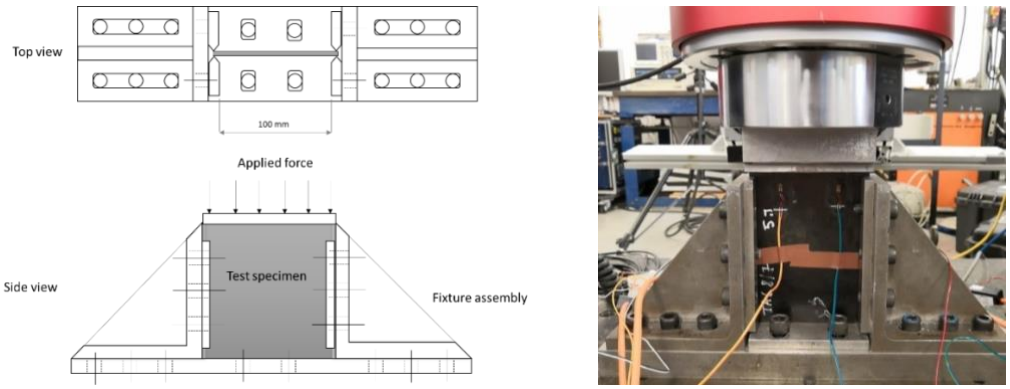

Figure 16-Schematisation of CAI rig assembly

Samples were stabilised at the edges by the fixture without constraining the in-plane transverse deformation. For all tested samples, four strain gauges were used in order to record the applied strain and ensure the parallelism to the lateral supports, flatness and exact positioning of the sample in the rig. During the tests, the force was recorded and elaborated using equation 10 to evaluate the residual compressive strength of each sample. Considering this equation, F_{CAI} is the peak force reached

during the compression test while S is the cross-section area as stated in the standard test method.

$$\sigma_{CAI} = \frac{F_{CAI}}{S}. \tag{10}$$

5.2. Results and discussion

CAI results are reported in Figure 17, where output values correspond to the residual compressive strength evaluated considering 100% as an undamaged CFRP structure.

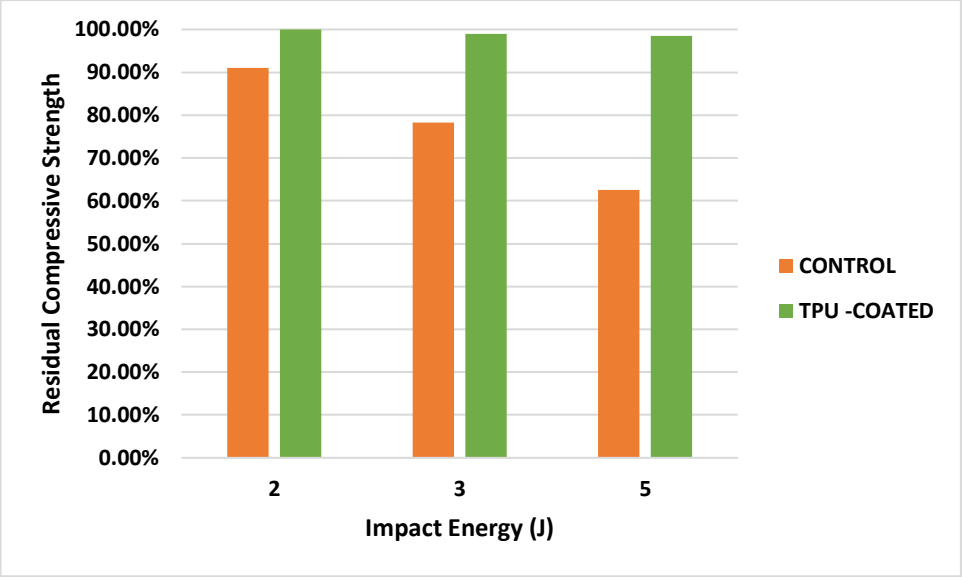

Figure 17- CAI results obtained from the test of samples impacted at 2J, 3J and 5J

Since TPU coated samples showed an asymmetrical geometry (TPU layer on one surface) during CAI failure, a small bending component was observed affecting the recorded compressive strength. This led to an oscillation in the residual compression strength for TPU-coated samples at different impact energies. In order to overcome this issue, TPU layer was carefully removed from the samples prior to the tests ensuring that no damage was created within the laminate during the operation using c-scan analyses.

As it is possible to see from the results, traditional CFRP samples show a significant reduction in terms of residual compressive strength that becomes more dramatic as the impact energy increases (90.96% for 2J, 78.19% for 3J and 62.54% for 5J). TPU

samples instead, show higher in-plane residual compressive properties due to the absence of damaged areas in the laminate body, confirming what observed from the previous tests.

6 Conclusions

The principal aim of this work was to investigate the improvement of the impact properties derived from the application of a layer of Thermoplastic Polyurethane blend as coating layer on the impact surface of CFRP laminates. This superficial layer was applied on the samples' surface during the lamination sequence prior to the curing process, using a "one-step" manufacturing process aimed at reducing costs and time in comparison with conventional coating procedures. An extensive study was carried out using Differential Scanning Calorimetry (DSC) and Dynamic Mechanical Analysis (DMA) to determine the optimal cure parameters for autoclave curing in function of the thermal properties of the polymer and the operative conditions in railways. Results showed TPU glass transaction at -33°C and mechanical properties degradation at 150°C in range of frequency between 1 and 80Hz that overestimates the real operative conditions of the material in railways. Damping tests were performed showing an increment of 113% and 387% in logarithm decrement for the TPU/CFRP manufactured with the "one-step" process in comparison with TPU glued on CFRP and traditional uncoated CFRP. An impact campaign was then carried out and the results indicated that traditional CFRP laminates show large internal damaged areas that become larger for higher impacts, while no sign of damage was found in the TPU coated laminates. This is attributed to the presence of TPU capable of storing elastic energy and dissipate higher amount of impact energy via viscoelastic losses, with no measurable damage (i.e. cracks and delamination). This result was confirmed by analysing the residual compressive strength of traditional and TPU-coated laminates, showing no variation in residual mechanical properties for TPU-coated CFRP since no damage was generated during LVI event. In contrast, traditional

CFRP laminates showed a significant variation in residual strength (90% for 2J, 78% for 3J and 62% for 5J) in function of impact energy due to delamination. A numerical model was then developed to support the optimisation process of the TPU-coated CFRP for designing future advanced structural components where this material will be used. A good correlation between experimental and numerical results was found with a maximum error of 8% between experimental and numerical data, demonstrating that the developed numerical model is an excellent tool to predict the mechanical response of TPU/CFRP laminates.

In conclusion, the introduction of TPU as an additional reinforcement layer for damage suppression makes hybrid TPU/CFRP laminates a promising candidate for the development of a new generation of lightweight railways vehicles, able to withstand flying ballast-like events without the generation of BVIDs, enhancing safety and reliability of the entire rolling stock.

Funding

The author(s) disclosed receipt of the following financial support for the research, authorship, and/or publication of this article: This paper has been funded by the EXTREME project of the European Union's Horizon 2020 research and innovation programme under Grant Agreement No. 636549.

References

1. UNI EN 12663. 2010;
2. Standard E. EUROPÄISCHE NORM Railway applications - Crashworthiness requirements for railway vehicle bodies. 2005;
3. Group RD. Rail Delivery Group Charges and Incentives User Guide June 2014. 2014;(June).

4. Tech EE. Energy Efficiency Strategies for Rolling Stock and Train Operation. Technical Report; 2005.

5. Mair RI. Fibre Reinforced Polymers-From Aerospace to Infrastructure. Society of Manufacturing Engineers; 2000.

6. Vlot A. Glare: history of the development of a new aircraft material. Vol. 1, Kluwer Academic Publishers. 2001. 222 p.

7. Gunnink JW, Vlot A, De Vries TJ, Van Der Hoeven W. Glare technology development 1997-2000. Appl Compos Mater. 2002;9(4):201–19.

8. Koenig J, Friedrich IH. Integral consideration of the lightweight design for railway vehicles. InYoung researchers seminar 2011.

9. Goo JS, Kim JS, Shin KB. Evaluation of structural integrity after ballast-flying impact damage of a GFRP lightweight bogie frame for railway vehicles. J Mech Sci Technol. 2015;29(6):2349–56.

10. Grasso M, Gallone A, Genovese A, Macera L, Penta F, Pucillo G, Strano S. Composite Material Design for Rail Vehicle Innovative Lightweight Components. InProceedings of the World Congress on Engineering 2015 ;2: 1-3.

11. Heller P, Korinek J, Triska L. HYBRID BODY OF UNDERGROUND RAILWAY CAR: PATH TOWARDS REDUCED WEIGHT OF RAIL VEHICLES. MM Sci J [Internet]. 2015;665–9. Available from: http://www.mmscience.eu/content/MM_Science_201516.pdf

12. SiebelT. C, G Rail unveils world's first CFRP rail vehicle, [Internet] ,USA, Composite World, [2018/9/19; 2019/5/31]. Available from:https://www.compositesworld.com/news/cg-rail-unveils-worlds-first-cfrp-rail-vehicle

13. Abrate S. Impact on Laminated Composite Materials. Appl Mech Rev [Internet]. 1991;44(4):155. Available from: http://appliedmechanicsreviews.asmedigitalcollection.asme.org/article.aspx?articleid=1394347

14. Onder A, Oneill C, Robinson M. Flying Ballast Resistance for Composite Materials in Railway Vehicle Carbody Shells. In: Transportation Research Procedia. 2016. p. 595–604.

15. Cantwell WJ, Morton J. Impact resistance of composite materials. A review. Composites [Internet]. 1991;22(5):347–62. Available from: http://dx.doi.org/10.1016/0010-4361(91)90549-V

16. Cartié DDR, Irving PE. Effect of resin and fibre properties on impact and compression after impact performance of CFRP. Compos - Part A Appl Sci Manuf. 2002;33(4):483–93.

17. Wang S-X, Wu L-Z, Ma L. Low-velocity impact and residual tensile strength analysis to carbon fiber composite laminates. Mater Des [Internet]. 2010;31(1):118–25. Available from: http://linkinghub.elsevier.com/retrieve/pii/S0261306909003446

18. Riccio A, Russo A, Sellitto A, Raimondo A. Development and application of a numerical procedure for the simulation of the "Fibre Bridging" phenomenon in composite structures. Compos Struct. 2017;

19. Riccio A, Linde P, Raimondo A, Buompane A, Sellitto A. On the use of selective stitching in stiffened composite panels to prevent skin-stringer debonding. Compos Part B Eng. 2017;

20. Rechak S, Sun CT. Optimal Use of Adhesive Layers in Reducing Impact Damage in Composite Laminates. Compos Struct 4 [Internet]. 1987;9(6):18–31. Available from: http://www.springerlink.com/index/10.1007/978-94-009-3457-3_2

21. Siegfried M, Tola C, Claes M, Lomov S V., Verpoest I, Gorbatikh L. Impact and residual after impact properties of carbon fiber/epoxy composites modified with carbon nanotubes. Compos Struct. 2014;111(1):488–96.

22. RuggeriR, Martin RE, and Mccorkle LS. Impact behavior of composite fan blade leading edge subcomponent with thermoplastic polyurethane interleave. NASA, 2015, pp. 19–24. In: 20th International Conference on Composite Materials; 19-24 Jul. 2015; Copenhagen; Denmark.

23. Martone A, Antonucci V, Zarrelli M, Giordano M. A simplified approach to model damping behaviour of interleaved carbon fibre laminates. Compos Part B Eng. 2016;97:103–10.

24. Russo P, Langella A, Papa I, Simeoli G, Lopresto V. Low-velocity Impact and Flexural Properties of Thermoplastic Polyurethane/Woven Glass Fabric Composite Laminates. In: Procedia Engineering. 2016. p. 190–6.

25. Pichaiyut S, Nakason C, Vennemann N. Thermoplastic elastomers-based natural rubber and thermoplastic polyurethane blends. Iran Polym J (English Ed. 2012;21(1):65–79.

26. Rathod VT, Kumar JS, Jain A. Polymer and ceramic nanocomposites for aerospace applications. Appl Nanosci. 2017;

27. Lucchini UK, Axle Surface Coatings, [Internet], UK, Institution of Mechanical Engineers, [2018/4; 2019/5/31]. Available from: http://files.imeche.org/events/downloads/S1486/Axle%20Coatings.%20Sean%20Barson.pdf;

28. Frick A, Rochman A. Characterization of TPU-elastomers by thermal analysis (DSC). Polym Test. 2004;23(4):413–7.

29. ISO 6721-11:2012 Plastics — Determination of dynamic mechanical properties —.

30. EN 50125 -. 2008;

31. REFRESCO, Damages scenarios, Deliverable 7.2, [Internet] ,EU, UNIFE, [2014/12; 2019/5/31]. Available from: http://www.refresco-project.eu/wp-content/uploads/2015/02/D7.2_Damage_Scenarios.pdf

32. Pinho ST, Iannucci L, Robinson P. Physically based failure models and criteria for laminated fibre-reinforced composites with emphasis on fibre kinking. Part II: FE implementation. Compos Part A Appl Sci Manuf. 2006;

33. Manual, LS-DYNA Keyword User'S. "vol. II." Livermore Software Technology Corporation (LSTC) (2013);

34. Hallquist JO. LS-DYNA keyword user's manual. Livermore Softw Technol Corp. 2007;970:299–800.

35. Thota NM, Epaarachchi JA, Lau KT. Evaluation of the blunt thoracic trauma due to baseball impacts–review of the Blunt Criterion. 2014;

36. Smith L, Nevins D, Dat NT, Fua P. Measuring the accuracy of softball impact simulations. Sport Eng. 2016 Dec;19(4):265–72.

37. Abrate S. Impact on Composite Structures. 2005. 304 p.

38. Qi HJ, Boyce MC. Stress-strain behavior of thermoplastic polyurethanes. Mech Mater. 2005;

39. Delfosse D, Poursartip A. Energy-based approach to impact damage in CFRP laminates. Compos Part A Appl Sci Manuf. 1997;28(7):647–55.

40. Shyr TW, Pan YH. Impact resistance and damage characteristics of composite laminates. Compos Struct. 2003;62(2):193–203.

41. Williams K V., Vaziri R. Application of a damage mechanics model for predicting the impact response of composite materials. Comput Struct [Internet]. 2001;79(10):997–1011. Available from: http://ac.els-cdn.com/S0045794900002005/1-s2.0-S0045794900002005-main.pdf?_tid=dbd0ea4a-42cc-11e5-aa7b-00000aacb362&acdnat=1439588513_b6c79eda6172dc2053acb31fc1cc79de

42. Shyr T-W, Pan Y-H. Impact resistance and damage characteristics of composite laminates. Compos Struct [Internet]. 2003;62(2):193–203. Available from: http://linkinghub.elsevier.com/retrieve/pii/S0263822303001144

43. Jones DIG. Handbook of Viscoelastic Vibration Damping. John Wiley & Sons Ltd, editor. 2001.

44. Wisnom MR. The role of delamination in failure of fibre-reinforced composites. Philos Trans R Soc A Math Phys Eng Sci [Internet]. 2012;370(1965):1850–70. Available from: http://rsta.royalsocietypublishing.org/cgi/doi/10.1098/rsta.2011.0441

45. Nakamura M, Aoki Y, Enna G, Oguro K, Wada H. Polyurethane damping material. J Elastomers Plast. 2015;47(6):515–22.

7 CHAPTER: Damage mitigation for CFRP structures against High Velocity Impact events

7.1 Context

As shown in Paper C, it is possible to fabricate a hybrid laminated material by introducing a layer of protective polymer within the lamination sequence of the laminate. In particular, a layer of TPU was used as coating for the CFRP laminate obtained using a one-step manufacturing process by applying the polymer on the material surface before the cure process. This allowed to obtain a hybrid laminated structure with enhanced damage mitigation abilities and excellent erosion resistance due to the additional damping and the intrinsic abrasion resistance offered by the polymer located on the structure's surface. In this work (Paper D), this concept was pushed forward, and the same hybrid material was applied to a more complex structure currently used in many aircraft applications: a T-stiffened panel. T-stiffened panel (realised using traditional CFRP) response under in-service operative conditions was evaluated using an experimental and numerical high-velocity impact characterisation campaign. Experimental data was collected using a single stage pressure gun and a high-speed camera and was used to validate the numerical model in predicting the impact response and the extent of damage generated within the structure. Similarly, an additional impact campaign was carried out on TPU/CFRP plates to experimentally and numerically characterise the behaviour of the hybrid material under high velocity impact conditions. This numerical model was developed starting from the one illustrated in Paper C using high velocity impact conditions instead of low velocity ones. Afterwards, since the

numerical models were both validate for the T-stiffened panel and the hybrid material, a further numerical model was developed to analyse the behaviour of the T-stiffened panel realised using the hybrid material. An additional study on the optimal thickness of TPU was then carried out to maximise the damage mitigation potential of the TPU/CFRP material. It is important to note that in this study the same considerations as Paper C on suitable temperature for the use of TPU and erosion resistance were used.

The original contribution of this paper lies in characterisation of unique TPU/CFRP hybrid laminate under high velocity impact conditions and in the numerical campaign aiming to identify the optimal thickness to minimise the impact damage.

The Statement of Authorship Form and the paper can be found next.

This declaration concerns the article entitled:	
High-Velocity Impact Investigation On Thermoplastic Polyurethane/CFRP T-Stiffened Panel	
Publication status (tick one)	
Draft manuscript	
Submitted	
In review	
Accepted	
Published	✓
Candidate's contribution to the paper (detailed, and also given as a percentage)	
The candidate contributed to/ considerably contributed to/predominantly executed the…	

Formulation of ideas:	80% The ideas were developed with the help of my supervisors.
Design of methodology:	80% I designed the experimental setup and developed the numerical model.
Experimental work:	80% The experimental tests were carried out by collaborator who collected the data. I elaborated and correlated this data with the numerical model. I interpreted the results and made conclusions.
Presentation of data in journal format:	90% I designed the manuscript structure, wrote all the drafts and realised all figures. Feedback on the draft and help for the paper submission, review and submission were provided by my supervisors.

Statement from Candidate			
This paper reports on original research I conducted during the period of my Higher Degree by Research candidature.			
Signed		**Date**	26/05/2020

HIGH-VELOCITY IMPACT RESPONSE ON ADVANCED HYBRID COMPOSITE STRUCTURES

Francesco RIZZO*, Tommaso D'AGOSTINO, Fulvio PINTO, Michele MEO

Materials and Structures Centre, University of Bath, Bath, Ba2 7AY, UK
*corresponding author: f.rizzo@bath.ac.uk

Keywords: CFRP, impact, high-velocity, damage suppression, impact resistance, TPU, damage.

ABSTRACT

In this work, an experimental and numerical study of the High Velocity Impact (HVI) behaviour for hybrid structures was presented. HVI at different velocities were carried out on the structures, evaluating failure phenomena and impact damage using high-speed camera and ultrasound techniques (C-scan). In order to predict the complex impact response and damage extension in the structure, a 3D explicit Finite Element Model (FEM) was developed for each structure using a commercial LS-DYNA software. Experimental and numerical results were then presented showing a good correlation with an error between the 6% and 17% in terms of absorbed energy and damage extension. Afterwards, an optimisation analysis was carried out on the numerical model in order to identify the best design parameters when a TPU layer is introduced in the lamination sequence of the material for damage mitigation purposes. Results were presented reporting a reduction of at least 54% in absorbed energy, damage extension and maximum indentation respectively when 1mm thick Thermoplastic Polyurethane (TPU) layer is applied on the Carbon Fibre Reinforced Polymer (CFRP)impact surface.

1. Introduction

Over the last 30 years, the diffusion of composite materials allowed numerous improvement for several industrial sectors including railways [4], aerospace [5, 6] and automotive [7] in terms of performance, payload, durability and manoeuvrability due to their high specific performance and low weight [1, 2]. However, low out-of-plane impact resistance makes these materials particularly susceptible to damage and delamination that can negatively affect the global mechanical properties of the entire structure [8-10]. Analysing the different and most frequent causes of Low and High Velocity Impact (LVI and HVI) in all aforementioned industries, Foreign Object Debris (FOD) have been found to be the most limiting and detrimental for the use of composite in advanced applications. The term "Foreign Object Debris" is used to describe any alien or external substance (stones, asphalt, ice) on a surface that if accelerated by the aerodynamic of the moving structure and/or runway lofting [11], can cause considerable damage to structures [11-13]. Consequently, it is clear that a detailed investigation on the phenomenology and characterisation of this class of impact phenomena is required in order to reduce their detrimental effects on the laminated structure and guarantee an acceptable safety factor for the entire mechanical system.

As described in literature [14], threats and the consequences of debris impact on aircraft structures are accurately studied analysing their frequency, size and impact probability in function of projectile mass and velocity. An analysis of this type of impact events and the response of the composite structure was investigated by Onder et al. [15, 16], who studied the phenomenon from the railways prospective evaluating the resistance of composite materials against debris (flying ballast) and reporting a detailed discussion on its ballistic aspect with experimental and numerical results. In several works [17-19], multiple possible causes of DOF acceleration were studied in depth, reporting analytical, experimental and numerical comparisons between different impacts scenarios and the probability for a structure to be involved in these events.

Based on the results from these studies, the impact velocity of FOD are identified in a range of 70-150 m/s for objects with a mass in a range of 0.1-10 g, and therefore, severe impact damage can be generated into the composite body with a consequent loss of mechanical properties and considerable risk for the entire system. Thus, an extensive research investigation on HVI is required to investigate these consequences, to increase the impact performance of composite materials and to reduce the safety issue due to HVI events.

Several researchers [20-22] studied the experimental behaviour of composite materials under HVI conditions and compared the results with Finite Element Models (FEMs). In particular, Cantwell [20] et al. investigated the effect of high velocity impacts on composite materials underlying the substantial detrimental effect between small projectiles and drop-weight projectiles with equal impact energy, demonstrating the necessity of a protection system especially against HVIs to prevent inner damage generation. In this context, impact performance of composite structures can be improved following several approaches including modification of single components [23-25], modification of the inner morphology of the composite structure [26-28] and introduction of a secondary reinforcement [29-31]. In particular, Cuomo and al. [32] focussed their attention on this last solution by introducing a Thermoplastic Polyurethane (TPU) layer on the impact surface of conventional Carbon Fibre Reinforced Polymer (CFRP) during the lamination phase using a “one-step” manufacturing procedure. It was demonstrated that TPU/CFRP hybrid material is a very promising solution for the mitigation of LVI damage, showing no damage for impact energies of 5J in contrast with traditional laminates.

In this work, TPU/CFRP hybrid plates were fabricated using the “one-step” manufacturing process illustrated in the aforementioned work in order to investigate its impact performance under HVI conditions (~100 m/s) corresponding to DOF impact velocity for airplanes take-off phase and cruise speed of high-speed trains [33, 34]. Impact data and morphological damage analysis were obtained using a

high-speed camera and visual inspection. This information was then used to calibrate a FEM analysis developed in DYNA3D in order to predict CFRP and TPU/CFRP material behaviours also when applied to complex geometries. A TPU/CFRP T-Stiffened panel was designed and simulated using the same FEM code to evaluate the influence of the three different TPU thicknesses on its impact response.

2. Design, modelling and manufacturing of TPU/CFRP

Both traditional and TPU/CFRP plates used during FEM calibration campaign were fabricated using the "one-step" manufacturing [32]. These were manufactured using a carbon fibres prepreg system (Tanax-E IMS65 E23 and CYCOM 977-2 thermoset epoxy resin) cut 150 mm x100 mm x 0.25 mm in size. Single plies were laminated using a cross ply lamination sequence ([0/90/0/90/0/(90)¯]s with 11 plies in total. An additional TPU layer (1 mm of thickness) was directly introduced on the uncured CFRP surface in order to optimise the bonding between the epoxy resin and the TPU during curing. A metal mould was then used to ensure good finishing and dimensional accuracy. Plates were cured in autoclave at 120 °C and 100 Psi with a ramp of 0.2° C/min for 8 hours. The final samples thickness was around 2.8 mm (CFRP+TPU) In Figure 1, a schematisation of TPU/CFRP sample is reported.

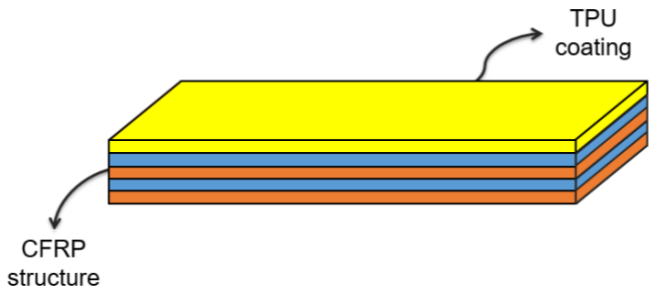

Figure 1-schematisation of TPU/CFRP hybrid material layup

Two different lamination sequences were considered to design the panel (850 x 450 mm in size) and the T-stiffener respectively. The lamination sequence for all the elements is reported in Table 1.

Table 1- Lay-up sequence of the different regions for the T-stiffened panel

Section	Number of Plies	Ply Thickness (mm)	Stacking Sequence
Panel	24	0.25	$[+45/-45/0_2/90/0_2/90/+45/-45/0_2]_S$
Flange	18	0.25	$[0/90/+45/-45/0/+45/-45/90/0]_S$
Web	36	0.25	$[0/90/+45/-45/0/+45/-45/90/0]_{2S}$
Bracket	24	0.25	$[0/90/-45/45]_{3S}$

A schematisation of the structure is reported in Figure 2.

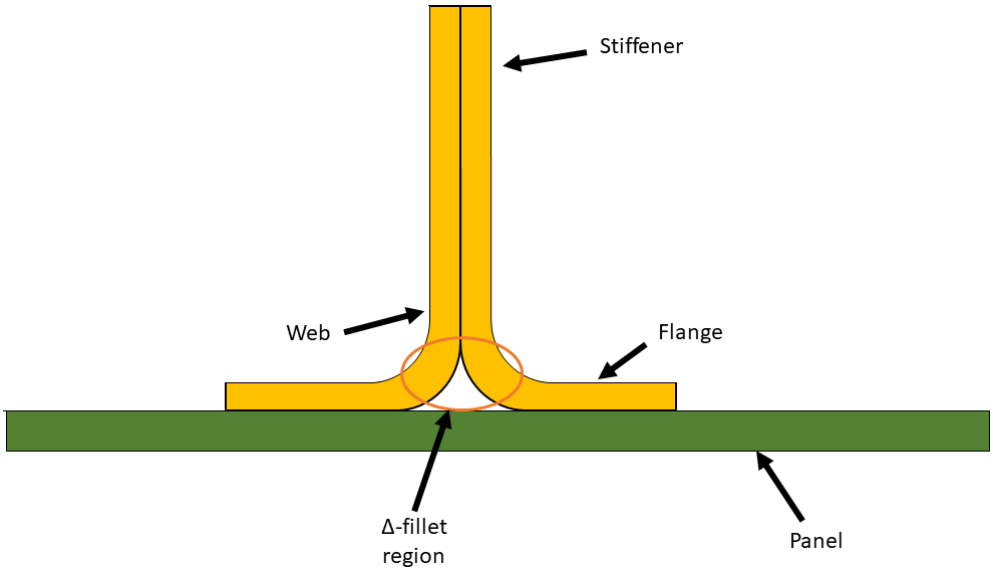

Figure 2- T-Stiffened panel manufacturing layout

In order to predict the impact behaviour of TPU/CFRP material and its application in more complex structures (T-Stiffened panel), a Finite Element Model (FEM) code was developed using a DYNA3D software [35, 36]. The projectile was simulated as a steel 2.5-mm-diameter sphere using 3D brick elements and a PLASTIC_KINEMATIC material model (see Table 2) in order to simulate the possible plastic deformation of the projectile. In order to simulate the CFRP behaviour, an orthotropic progressive damage material model (MAT_261) was implemented to model the damage initiation and propagation for the single lamina

during the impact. Fibre breakage (tension and compression) and matrix failure (tensile and shear) are computed using Pinho fracture-based criteria [37]. In the computational evaluation of the damage for each single element, a fringe colour map is defined associating numerical values to the damage evolution: 0 (blue) for the absence of damage and 1(red) for damage initiation. When the fracture criteria are met, the relative element is removed (eroded) by the calculation. Material properties are reported in Table 2 and Table 3. TPU behaviour was implemented using a hyperplastic material model using the Mooney-Rivlin formulation [36, 38] since literature data showed good correlation in predicting rubber-like material behaviour for strain around 250%-300%. The particularity of this material model is the evaluation of the strain energy density as a linear combination of the two invariants of the left Cauchy-Green deformation tensor that allows an increased numerical stability in the impact area for HVI. Mechanical properties of TPU were implemented using literature data [39, 40]. In order to predict delamination and its propagation during the impact event, a TIEBREAK contact (option 6) was used to simulate the matrix interface between two adjacent layers. This contact implements linear failure criteria (tensile and shear) that deletes the contact law between the layers when satisfied. It is possible to show its status for each element using a fringe colour map where 0 (blue) corresponds to the tied (undamaged) areas, while 1 (red) corresponds to the untied (delaminated) ones.

Table 2 MAT_261 orthotropic material card paramters:RO: density, modulus of elasticity (E11, E22, E33), poisson's ratios (PR12 ,PR31, PR32), shear modulus (G12, G23, G31), normal and transverse strenght under traction and compression (X1t, X1c, X2t, X2c), shear strenght (S12, S23, S31), compresisve fibre failure energy (ENKINK), tensile fibre failure energy (ENA), Intralaminar matrix tensile energy failure (ENB), Intralaminar matrix trasnverse shear energy failure (ENT) and Intralaminar matrix longitudinal shear energy failure (ENL).

MAT	RO (Kg/m3)	E11 (GPa)	E22 (GPa)	E33 (GPa)	PR21	PR31	PR32	G12 (GPa)	G23 (GPa)	G31 (GPa)	X1t (MPa)	X1c (MPa)
CFRP	1530	183	9	9	0.035	0.035	0.25	4	4	4	1500	950
MAT	X2t (MPa)	X2c (MPa)	S12 (MPa)	S23 (MPa)	S31 (MPa)	ENKINK (J/m2)	ENA (J/m2)	ENB (J/m2)	ENT (J/m2)	ENL (J/m2)		
CFRP	70	200	80	80	80	75100	50100	478	900	900		

Table 3- Material properties of steel used for FEA model. RO: density, modulus of elasticity (E), poisson's ratios (PR), yeild strenght (UY), tangent modulus (ETAN), effective plastic strain at failure(FAIL).

PART	RO (Kg/m3)	E (GPa)	PR	UY (MPa)	ETAN (GPa)	FAIL
Steel	7830	210	0.3	215E6	4E8	/

Two different FE meshes (quarter-symmetric) were modelled using these parameters for plates and the T-stiffened panel. TPU/CFRP plates were designed as 150 mm x 100 mm in size with a variable element size to improve the solution accuracy in the impacted area and thickness of 3 mm (11 CFRP layers and 1 TPU layer). T-stiffened panel FE mesh was designed following the aforementioned design parameters. In order to analyse the influence of TPU thickness on impact response, three different thicknesses (0.25 mm, 0.5 mm and 1 mm) were implemented on the T-stiffened panel. Traditional CFRP plate (thickness 2.5 mm for 11 CFRP layers) and uncoated T-stiffened panel were modelled and simulated as references. In Figure 3, images of hybrid TPU/CFRP meshes are reported.

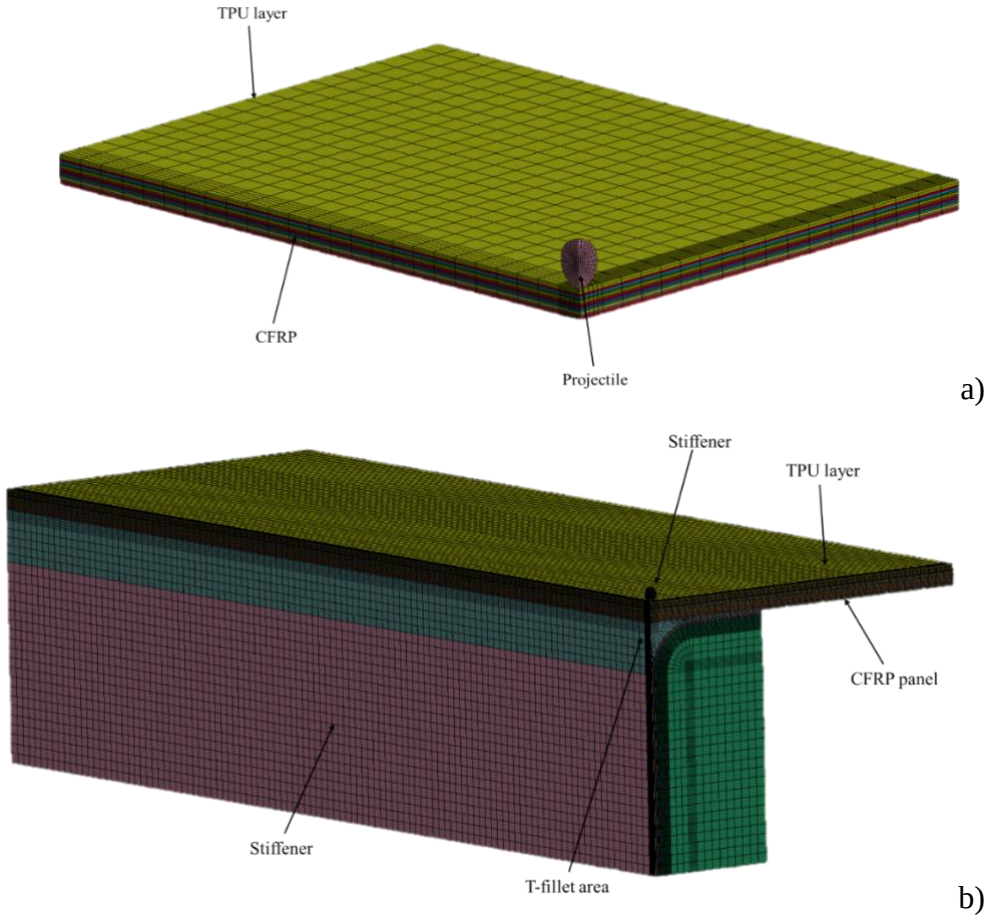

Figure 3- FE mesh of hybrid TPU/CFRP plate (a) and T-stiffened panel (b).

In order to guarantee an accurate contact between the projectile and the composite part, a penalty-based contact was set between the two parts. Two different set of boundary conditions were applied on the two geometries. Plates were fully constrained along the edges to model the support used during the experimental tests while the T-stiffened panels were fully constrained on the edge far from the impact area.

3. Experimental setup

In order to carry out HVI, a custom single stage pressure gun was designed and manufactured in order to guarantee an impact velocity between ~100-150 m/s to simulate runway debris impacts on airplanes during take-off and on high-speed railways structures at cruise speed.

The schematic layout of the device is reported in Figure 4.

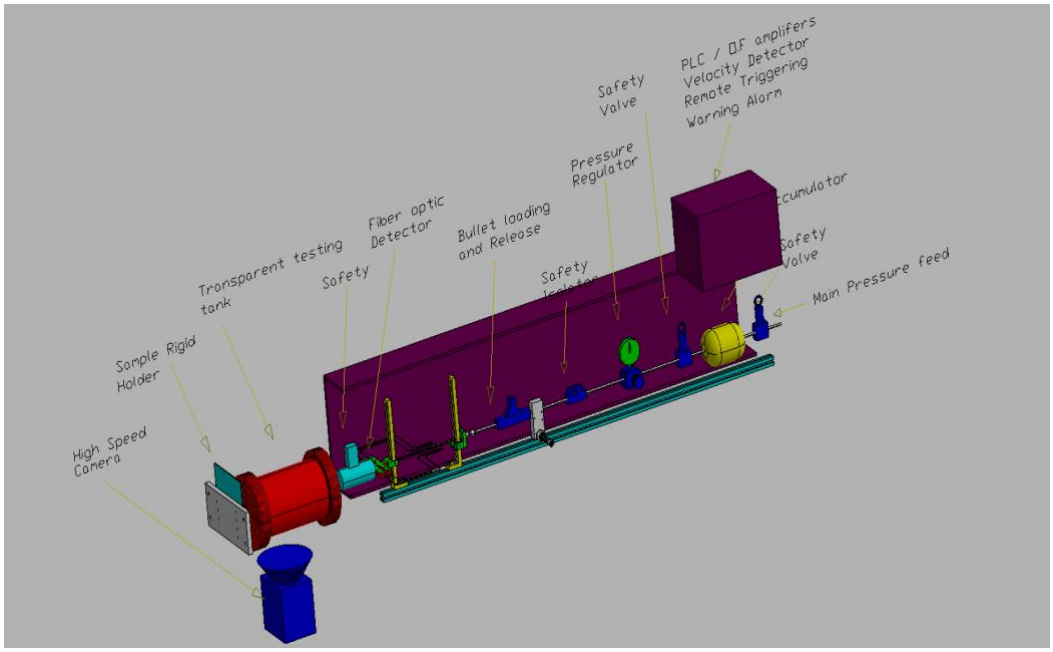

Figure 4-Layout of the single stage pressure gun used during the experimental setup

A centrifugal compressor was used to build-up air into the pressure chamber and a barometer was used to regulate the pressure for the required impact velocity. An estimation of the linear output velocity *u* [41,42] can be calculated using equation (1) considering the kinetic energy of the projectile (chrome steel sphere, 2.5mm diameter, 0.06g) as the work done by the expanding gas to move it into the barrel:

$$u = \sqrt{\left(V + \frac{\pi d^4}{4} L\right)^{(1-\gamma)} - V^{(1-\gamma)}} \cdot \sqrt{2 \frac{m_g}{m_p} RTV^{(\gamma-1)}} \cdot \frac{}{(1-\gamma)}. \qquad (1)$$

Where: V is the volume of the pressure chamber, d is the diameter of the barrel, L is the barrel length, γ is the ratio of specific heats, m_g and m_p are ratio of mass of gas and projectile respectively, R is specific gas constant, T is and temperature. Assumptions of ideal gas and no frictions conditions are taken into account. A high speed camera Phantom MIRO LAB 310 was used to record impact images and calculate the projectile velocity using the dedicated post-processing software. A pressure of 6 bar was necessary to obtain an average impact velocity of 105.2 m/s

(impact energy: ~0.32J). TPU/CFRP samples were placed onto a steel support with a square window of 85mm x 85 mm and then fixed to a steel block. The assembly was placed 30 mm from the pressure gun with the TPU surface facing the exit barrel. The T-stiffened panel was clamped to a rigid support in order to avoid displacement and vibrations, and impacted on its flat surface.

Internal damage extension was analysed using a 5MHz Phased-Array Transducer (National Instrument) with a beam length for each probe of 0.58 mm with a total length of 225 pixels. C-scan images were displayed in a 16-bit amplitude colour-map (0-40 V in range).

4. Results and discussion

The results of the HVI campaign on TPU/CFRP and traditional plates are reported in Figure 5 where the experimental impact damage is morphologically compared to numerical one. Experimental data were collected by high speed camera while numerical ones are obtained analysing impact frames from LSDYNA3D post-processing software.

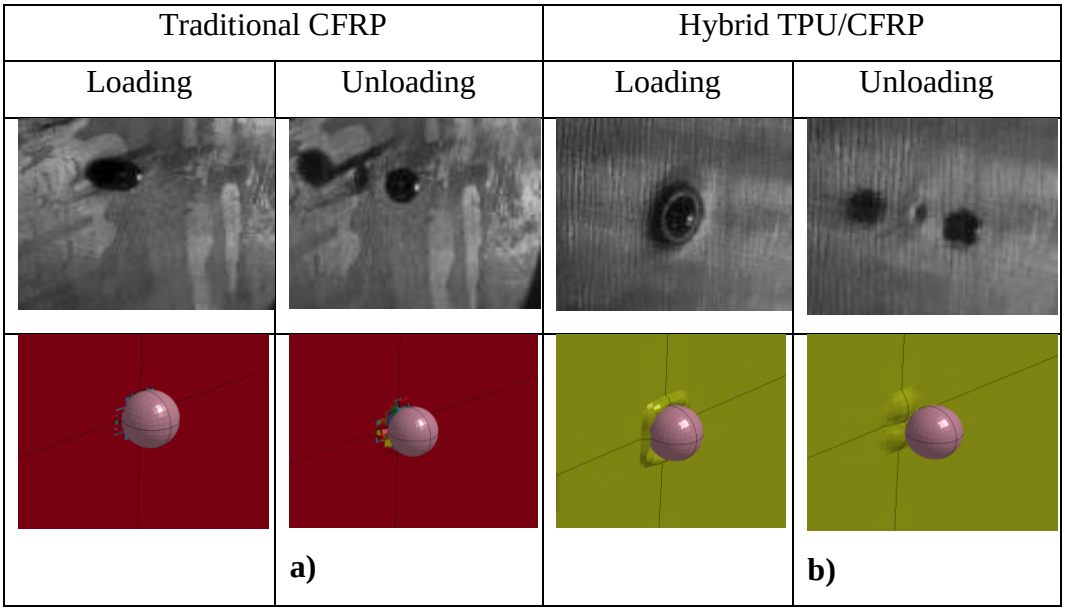

Figure 5-Comparison between experimental (top row) and numerical (bottom row) for traditional and hybrid CFRP plates

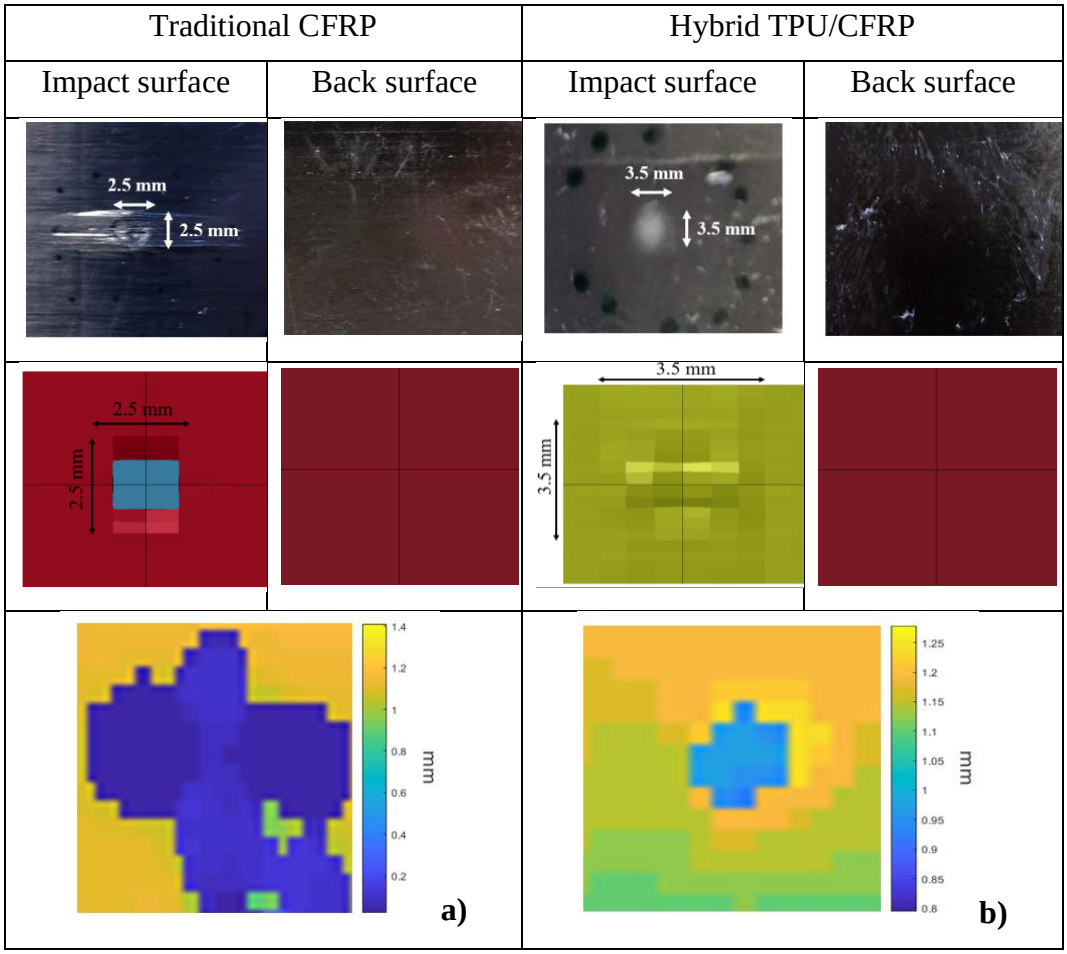

Figure 6-Impact damage after HVI on traditional (a) and Hybrid TPU/CFRP (b) plates both for experimental (first row) and numerical (second row) cases. C-scan images (Time of Flight-TOF) (third row) are reported analysing the surface far from the impact.

Analysing damage morphology (Figure 5.b and Figure 6.a) of traditional CFRP, the numerical model calibration and the experimental results show similar damaged areas (~2mm2 for numerical and ~2.4mm2 for experimental). No fibre fragmentation is reported in the visual analysis of the numerical model due to the complexity in evaluating transversal matrix failure in dynamic events. Nevertheless, this phenomenon can be evaluated using the dedicated fringe plot for matrix failure [36] reported in In Figure 7.a and Figure 7.b. Analysing the fringe images, it is possible to compare this fringe output with experimental fragmented area reporting a similar extension (~9.5mm for numerical and ~10.5mm). No sign of damage is identified on the back surface in the simulated and experimental results

as confirmed in Figure 6. Similarly, C-scan images report small delaminated areas (~10.8mm) with the predominate presence of superficial damage in the impact location. Another parameter that proves the numerical and experimental correlation is the maximum indentation recorded by the numerical analysis (~0.8mm) and the one measured on the impacted samples (~0.5 mm). It is possible to conclude, thus, that the experimental results are comparable to the numerical ones (error of ~9%) demonstrating an optimal calibration for traditional CFRP plate model.

As for the coated samples, no visual damage is detected on CFRP body of TPU/CFRP plates (Figure 5.b and Figure 6.b) due to TPU opacity as well as no sign of damage on the surface far from impact. C-scan images are then used for damage evaluation of experimental plates while matrix fringe for TPU/CFRP composite samples are reported in Figure 7.c and Figure 7.d with colour map illustrating values for CFRP body only. Comparing the results, a similar affected area extension (~3.8 mm and ~4.1 mm for experimental) is shown for the two cases reporting no damage in the CFRP body. Based on these results, then it is possible to confirm the potentiality of the FEM code to predict the CFRP material behaviour and rubber-like TPU mechanical characteristics with an error of 6% between the extension of the affected measured areas.

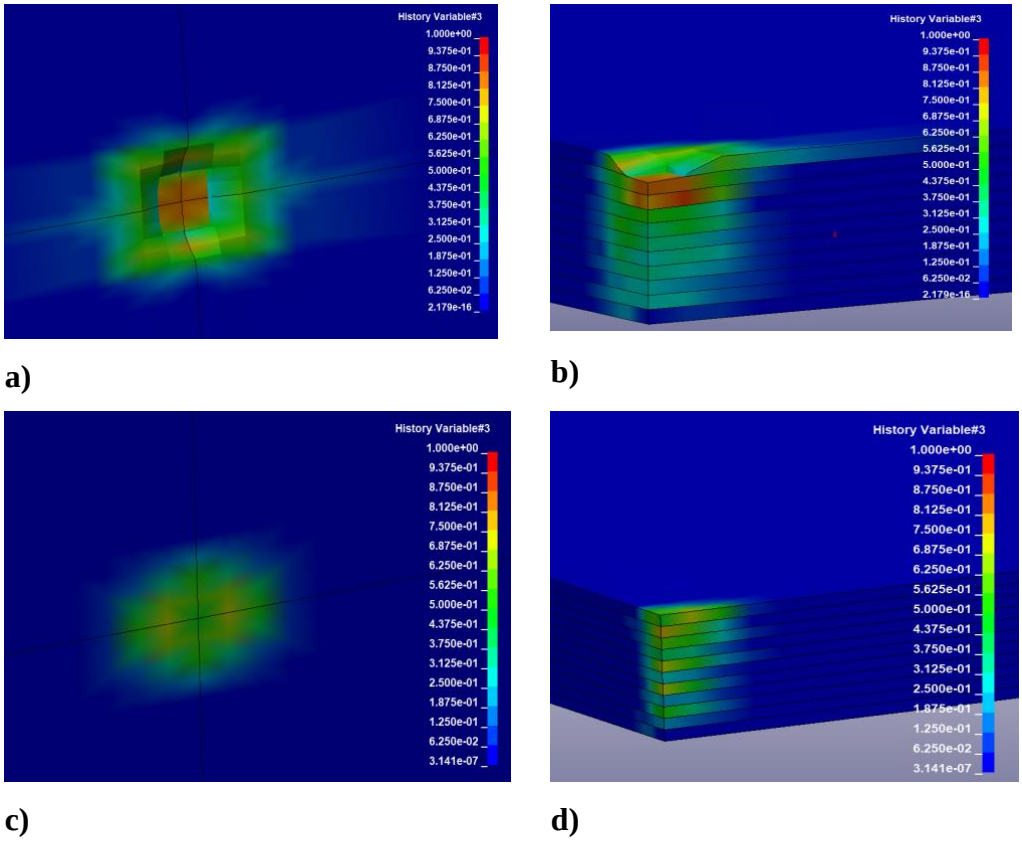

Figure 7- Matrix failure fringe map for full-model and quarter section of traditional CFRP (a and b) and TPU/CFRP plates (c and d).

In terms of impact resistance, analysing the extension of the internal damage between the traditional CFRP laminate and the TPU coated one, it is clear that the polymeric coating is able to reduce the extent of the internal delamination within the laminate.

By comparing the damaged area morphology and extension between TPU/CFRP (no damage) and traditional samples (~10.5mm), it is clear that TPU addition is able to prevent the generation of a considerable damage into the CFRP body. Indeed, as shown from numerical results, damage presence is in at least 1 ply of the traditional sample while, for TPU/CFRP material, no plies are involved in the erosion algorithm. This means that the presence of TPU offers damage-suppression feature to the CFRP structure allowing to reduce the damaged area and, consequently, to reduce the mechanical properties detriment with an increase in confidence and reliability on the composite material.

In order to demonstrate the validity of this concept on complex structures, the impact response of a T-stiffened panel towards HVI was simulated using TPU/CFRP and compared with a traditional CFRP part.

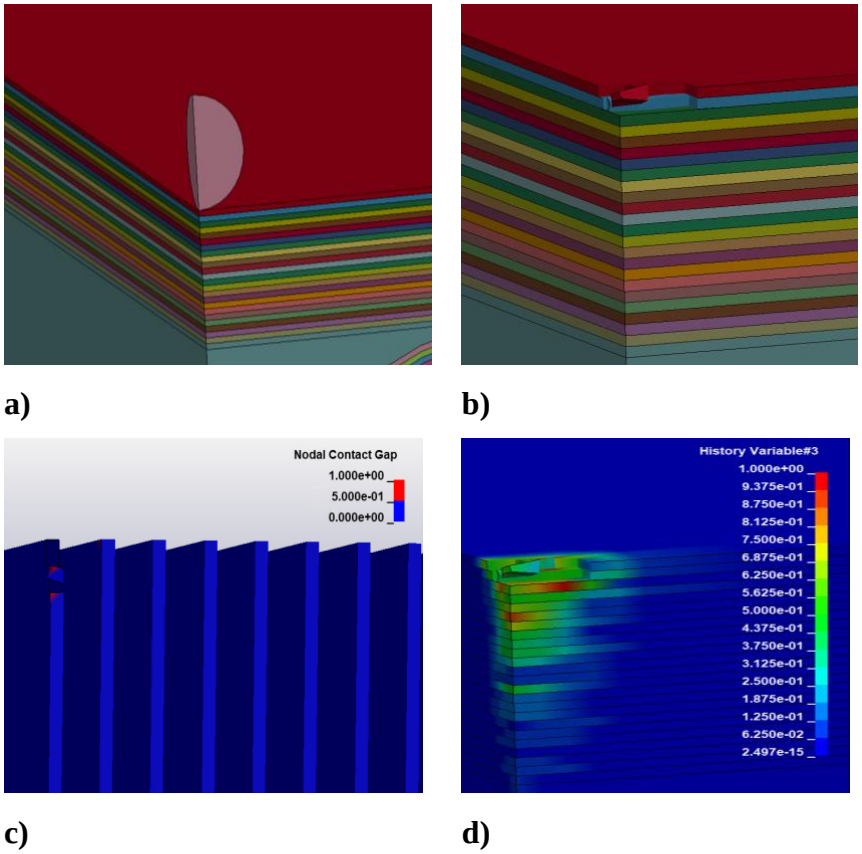

Figure 8-Impact model output of traditional CFRP: first frame (a), visual damage evaluation (b), delamination (c) and matrix failure (d).

As it is possible to see from the results from the traditional CFRP structure (Figure 8.a and Figure 8.b), the impact behaviour of this structure is very similar to the one illustrated in the plate case. From visual damage evaluation, 1st ply and 2nd ply are interested by damage (erosion) with an area of 1.14mm2 and 1.10mm2 respectively. Matrix failure fringe map (Figure 8.c) however displays a distributed portion where it is clear that matrix failure is initiated especially in 3rd and 6th plies with a total in-plane area of ~6mm2. On the contrary, delamination evaluation (Figure 8.d) shows no sign of delamination outside the area where elements are removed (eroding algorithm) from the calculation. Based on these results, it is clear that no penetration is showed and only compression damage to fibres and matrix is reported

without any the presence of delaminated areas due to low energy (~0.32J) involved during the impact event [20, 43].

In order to reduce the CFRP sensitivity against HVI, a TPU layer is added on this structure and an optimisation study is carried on evaluating the optimal thickness to apply on the structure. Images of the hybrid structure with three different thicknesses of TPU are shown in Figure 9.

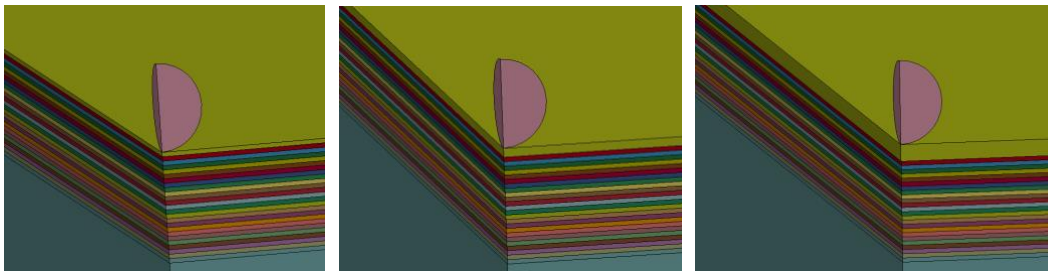

a) **b)** **c)**

Figure 9-TPU/CFRP hybrid T-stiffened panel using three different TPU thicknesses: 0.25mm (a), 0.5mm (b) and 1 mm (c).

Results of visual damage, delamination and matrix fringe plot for the three different simulations are shown in Figure 10.

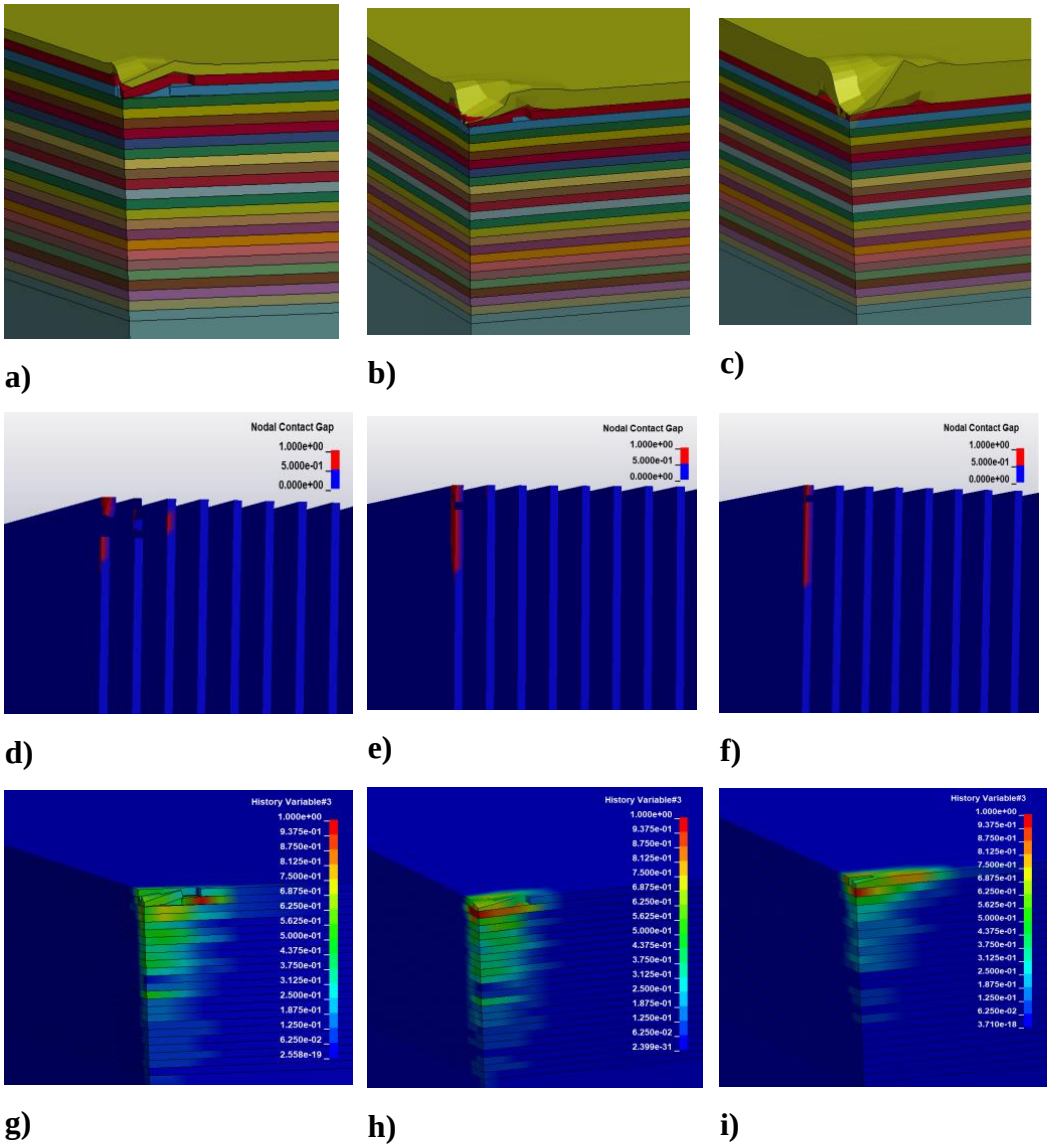

Figure 10-Impact results (visual damage) of TPU/CFRP T-stiffened panel reporting the frame at maximum displacement: 0.25mm (a), 0.5mm (b) and 1mm (c); delamination: 0.25mm (d), 0.5mm (e) and 1mm (f); and matrix failure fringe plot: 0.25mm (g), 0.5mm (g) and 1mm (i).

It is clear from the FEM images that the damage-suppression ability of the TPU layer is directly dependent on the thickness of the coating. Indeed analysing more in detail Figure 10.a (0.25 mm), visual damage (elements erosion) is identified in the 1st ply (~1.008 mm^2) and 2nd ply (~0.74 mm^2). Matrix failure initiation (Figure 10.g) is identified especially in the 2th ply with an affected area of around 1.5mm^2 while delamination (Figure 10.d) is localised at interface between TPU and CFRP (2.89mm^2) and in a minimal portion (~0.03 mm^2) between the 1st and 2nd ply.

Analysing Figure 10.b (0.5 mm), instead, visual damage evaluation is reported only in the 1st ply with a reduced damaged area of 0.76 mm^2 compared to the previous case (-32%). Matrix failure (Figure 10.e), instead, is identified for an affected area of 2.88mm^2. It is important to notice that matrix failure is located where visual damage was detected in the 0.25 mm case (Figure 10.g). Analysing delaminated area (Figure 10.h), a greater interface separation (7.5mm^2) between TPU and CFRP is evaluated in comparison with the 0.25 mm case (+158%) due to the different impact response of the hybrid material for this value of thickness. No further interface separations between CFRP plies are reported.

In 1 mm case Figure 10.c, only a small damaged area is detected (0.132 mm^2) with a reduction of -432% in comparison with 0.5mm case. The area of interest for matrix failure initiation (Figure 10.g) is also reduced (1.8mm^2) and limited to the 1st ply of the panel without any further affection in other layers. Greater TPU/CFRP delamination (Figure 10.g), instead, is evaluated (8.5mm^2) with no affection for further interfaces of CFRP layers. Total damaged area as sum on all the plies (eroded elements) and delamination (TPU/CFRP interface separation only) are reported in Figure 11 for the three different TPU/CFRP and the traditional CFRP T-stiffened panels.

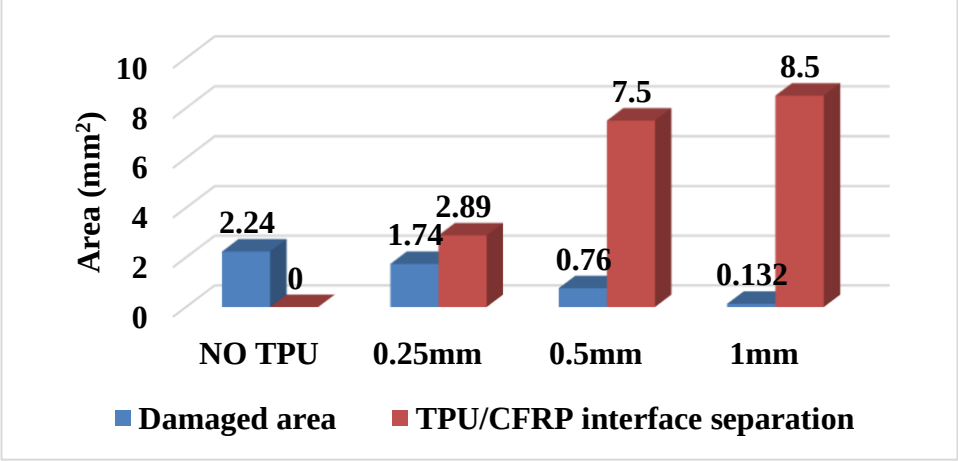

Figure 11-Damaged and delaminated area from impact results of traditional CFRP and TPU/CFRP T-stiffened panel

Comparing these results to the traditional CFRP ones, it is possible to see an evident damage-suppression effect of TPU against HVI with a reduction of the damaged area of -22%, -66% and -94% for TPU thickness of 0.25mm, 0.5mm and 1mm respectively when compared to traditional CFRP. This is due to damping properties of TPU that improves the impact response of the entire structure [32]. It is important to notice that the calculation of delaminated area values is identified increasing the TPU thickness, but they correspond to interface separation between TPU and CFRP.

Another indication of the TPU positive effect on CFRP protection is observed analysing the projectile velocity in relation with time and the maximum displacement recorded on the CFRP panel (without the TPU layer) for each test typology reported in Figure 12.

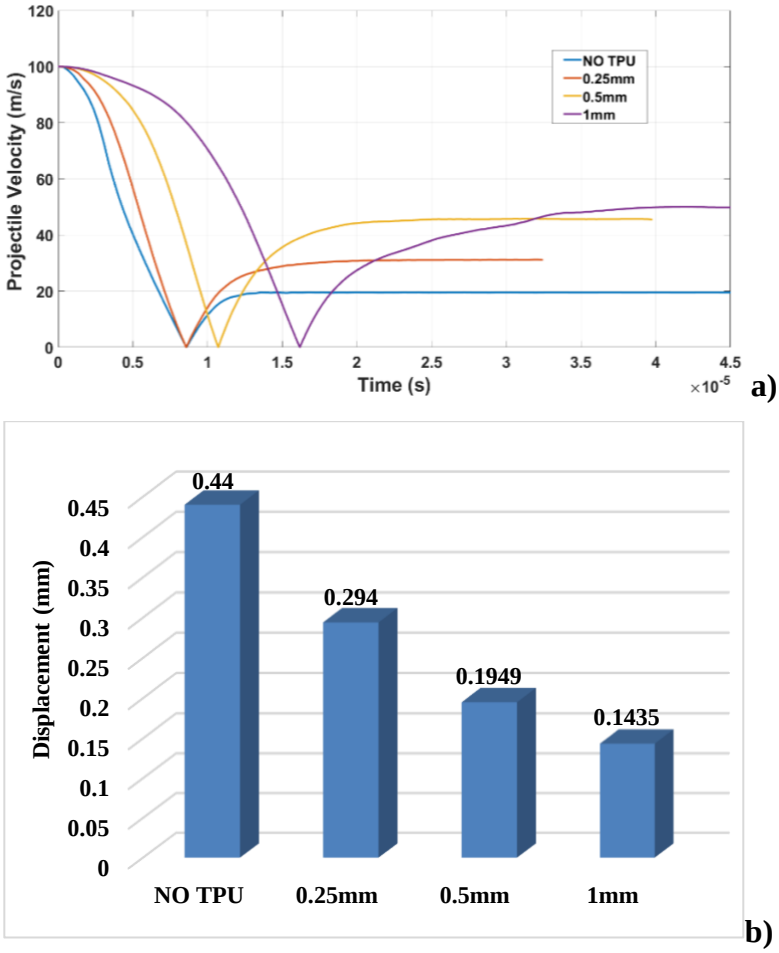

Figure 12- Velocity –time plot (a) and maximum indentation on the CFRP panel (b) detected on the TPU/CFRP T-stiffened panel and traditional T-stiffened panel.

The projectile velocity during the impact event is strongly influenced by the presence of TPU that changes its profile in time. Indeed, from Figure 12.a it is possible to notice a variation for the rebound velocity when TPU is applied on the structure with an increase of +62%, +134% and +156% for 0.25mm, 0.5mm and 1 mm respectively if compared with the traditional material. This phenomenon is due to TPU hyper-elastic properties that, during impact, allows a higher elastic deformation of the entire structure. Since the threshold for elastic energy storage is increased, less impact energy is dissipated by the material as damage and a higher amount of energy is transferred back to the projectile (higher rebound velocity). Increasing the TPU amount, it is demonstrated that this effect is amplified [32, 44, 45]. Another positive effect of TPU on damage mitigation can be evaluated

analysing the maximum indentation of projectile on the CFRP panel. The values reported in Figure 11.b are calculated analysing the global projectile displacement along the impact direction and subtracting the relative TPU thickness value for each case. Results show that the maximum displacement applied on the panel is progressively reduced by increasing the TPU thickness with variations of -33%, -57% and -68% for 0.25mm, 0.5mm and 1mm respectively compared to traditional material. Similarly, to the rebound velocity analysis, also in this case TPU greatly affects the impact behaviour of the material increasing the elastic energy threshold and reducing to a smaller amount, the impact energy transferred to the CFRP for damage generation. These results confirm that the damage-suppression ability of TPU material can be used to mitigate HVI damage extension and its effectiveness increases for higher values of thickness. A further trade-off in terms of TPU thickness is then necessary in order to understand the optimal amount of TPU necessary to minimise the increase in weight and maximise the damage mitigation effect offered by this material.

5. Conclusions

In this work, the design and numerical simulation of a TPU/CFRP hybrid T-stiffened panel were carried out in order to investigate the potentialities of a TPU layer for HVI damage mitigation on aeronautic and railways structures studying the effect of TPU thickness on the impact behaviour of the structure. The first part of this study involved the manufacturing of TPU/CFRP plates introducing an additional TPU superficial coating in the lamination sequence, and the HVI experimental tests, carried out using a custom single-stage pressure gun with 2.5 mm chrome steel spheres as impact projectiles. A high-speed camera was used to record projectile impact velocity and impact data. Results for traditional CFRP showed the presence of damage of around ~10mm in the location where the impact took place while no external damage was detected on the structure for TPU/CFRP plates. C-scans analyses were carried out and the damaged area extension was assessed showing delaminated areas for traditional CFRP and only interface

separation between TPU and CFRP for the hybrid material. Collected impact data were then used to calibrate a LSDYNA3D FEM code to predict mechanical behaviour of a TPU/CFRP T-stiffened panel under HVI conditions. Simulations showed a considerable impact resistance increase when a TPU layer of 0.25 mm is applied on the panel surface with a variation of damaged area, rebound velocity and maximum indentation of -22%, +62% and -33% respectively indicating a positive effect of the TPU hyper-elastic behaviour on structure impact response. This effect is amplified considering TPU thicknesses of 0.5 mm and 1 mm with a reduction of damaged area of -66 and -94% respectively, an increase of +134% and +156% in rebound velocity and a reduction of maximum indentation of -57% and -68% respectively. A further trade-off between the different properties is required in order to tune impact resistance improvement and minimise the weight increments.

Acknowledgments

This paper has been funded by the EXTREME project of the European Union's Horizon 2020 research and innovation programme under grant agreement No. 636549.

References

1. Baker, A.A., et al., An affordable methodology for replacing metallic aircraft panels with advanced composites. Composites Part A: Applied Science and Manufacturing, 2002. 33(5): p. 687-696.
2. Marsh, G., Composites fight for share of military applications. Reinforced Plastics, 2005. 49(5): p. 18-22.
3. Cheng, W.L., S. Langlie, and S. Itoh, High velocity impact of thick composites. International Journal of Impact Engineering, 2003. 29(1): p. 167-184.
4. Robinson, M., E. Matsika, and Q. Peng, Application of Composites in Rail Vehicles. Reference Module in Materials Science and Materials Engineering, 2016.

5. Soutis, C., Carbon fiber reinforced plastics in aircraft construction. Materials Science and Engineering: A, 2005. 412(1-2): p. 171-176.

6. Tenney, D., G. Sykes, and D. Bowles, Composite materials for space structures. 1985.

7. Mouti, Z., et al., An experimental investigation into localised low-velocity impact loading on glass fibre-reinforced polyamide automotive product. Composite Structures, 2013. 104: p. 43-53.

8. Ishai, O. and A. Shragai, Effect of impact loading on damage and residual compressive strength of CFRP laminated beams. Composite Structures, 1990. 14(4): p. 319-337.

9. Shim, V. and L. Yang, Characterization of the residual mechanical properties of woven fabric reinforced composites after low-velocity impact. International Journal of Mechanical Sciences, 2005. 47(4-5): p. 647-665.

10. Schubel, P.M., J.-J. Luo, and I.M. Daniel, Impact and post impact behavior of composite sandwich panels. Composites Part A: applied science and manufacturing, 2007. 38(3): p. 1051-1057.

11. Nguyen, S.N., et al., Modeling the lofting of runway debris by aircraft tires. Journal of Aircraft, 2008. 45(5): p. 1701-1714.

12. Patterson Jr, J., Foreign object debris (FOD) detection research. International Airport Review, 2008. 11(2): p. 22-7.

13. Kim, H., D.A. Welch, and K.T. Kedward, Experimental investigation of high velocity ice impacts on woven carbon/epoxy composite panels. Composites Part A: applied science and manufacturing, 2003. 34(1): p. 25-41.

14. Greenhalgh, E., et al., Characterisation of the realistic impact threat from runway debris. The Aeronautical Journal, 2001. 105(1052): p. 557-570.

15. Onder, A., C. ONeill, and M. Robinson, Flying ballast resistance for composite materials in railway vehicle carbody shells. Transportation Research Procedia, 2016. 14: p. 595-604.

16. Önder, A. and M. Robinson, Harmonised method for impact resistance requirements of E-glass fibre/unsaturated polyester resin composite railway car bodies. Thin-Walled Structures, 2018. 131: p. 151-164.

17. Nguyen, S.N., E.S. Greenhalgh, and R. Olsson, Analytical Modeling of Runway Stone Lofting. Journal of Aircraft, 2011. 48(4): p. 1412-1421.

18. Nguyen, S., et al., Runway debris impact threat maps for transport aircraft. The Aeronautical Journal, 2014. 118(1201): p. 229-266.

19. Nguyen, S., et al., Improved models for runway debris lofting simulations. The Aeronautical Journal, 2009. 113(1148): p. 669-681.

20. Cantwell, W. and J. Morton, Comparison of the low and high velocity impact response of CFRP. Composites, 1989. 20(6): p. 545-551.

21. Villanueva, G.R. and W. Cantwell, The high velocity impact response of composite and FML-reinforced sandwich structures. Composites Science and Technology, 2004. 64(1): p. 35-54.

22. Chen, J., F.A. Allahdadi, and T.C. Carney, High-velocity impact of graphite/epoxy composite laminates. Composites science and technology, 1997. 57(9-10): p. 1369-1379.

23. Russell, A.J. and K.N. Street, The effect of matrix toughness on delamination: static and fatigue fracture under mode II shear loading of graphite fiber composites, in Toughened composites. 1987, ASTM International.

24. Ning, J., et al., Fabrication and mechanical properties of SiO2 matrix composites reinforced by carbon nanotube. Materials Science and Engineering: A, 2003. 357(1-2): p. 392-396.

25. Cho, J., J. Chen, and I. Daniel, Mechanical enhancement of carbon fiber/epoxy composites by graphite nanoplatelet reinforcement. Scripta materialia, 2007. 56(8): p. 685-688.

26. Rizzo, F., F. Pinto, and M. Meo. Bioinspired pseudo-ductile composite laminates with hierarchical energy absorption mechanism. in Bioinspiration, Biomimetics, and Bioreplication VIII. 2018. International Society for Optics and Photonics.

27. Pinho, S.T., P. Robinson, and L. Iannucci, Fracture toughness of the tensile and compressive fibre failure modes in laminated composites. Composites science and technology, 2006. 66(13): p. 2069-2079.

28. Czél, G., et al., Demonstration of pseudo-ductility in unidirectional discontinuous carbon fibre/epoxy prepreg composites. Composites Science and Technology, 2015. 106: p. 110-119.
29. Pinto, F., et al., Multifunctional SMArt composite material for in situ NDT/SHM and de-icing. Smart Materials and Structures, 2012. 21(10): p. 105010.
30. RIZZO, F., et al., Structural Hybrid Layer for Critical Strain Detection in Composite Parts: A Multifunctional Approach. Structural Health Monitoring 2017, 2017.
31. Paine, J.S. and C.A. Rogers, The response of SMA hybrid composite materials to low velocity impact. Journal of Intelligent Material Systems and Structures, 1994. 5(4): p. 530-535.
32. Cuomo, S., et al. A Thermoplastic Polymer Coating for Improved Impact Resistance of Railways CFRP Laminates. in European Conference on Composite Materials-18th Conference on Composite Materials. 2018.
33. Standard, B., Railway applications G structural requirements of railway vehicle bodies. BS EN, 2000. 12663.
34. EN15227, S.E., Railway applications—crashworthiness requirements for railway vehicle bodies. English Version, European Committee for, 2008. 7.
35. Hallquist, J.O., LS-DYNA theory manual. Livermore software Technology corporation, 2006. 3: p. 25-31.
36. Manual, L.-D.K.U.s., vol. II. Livermore Software Technology Corporation (LSTC), 2013.
37. Pinho, S., L. Iannucci, and P. Robinson, Physically based failure models and criteria for laminated fibre-reinforced composites with emphasis on fibre kinking. Part II: FE implementation. Composites Part A: Applied Science and Manufacturing, 2006. 37(5): p. 766-777.
38. Marckmann, G. and E. Verron, Comparison of hyperelastic models for rubber-like materials. Rubber chemistry and technology, 2006. 79(5): p. 835-858.
39. Qi, H.J. and M.C. Boyce, Stress–strain behavior of thermoplastic polyurethanes. Mechanics of Materials, 2005. 37(8): p. 817-839.

40. Bartolomé, L., et al., Experimental characterization and modelling of large-strain viscoelastic behavior of a thermoplastic polyurethane elastomer. Rubber Chemistry and Technology, 2013. 86(1): p. 146-164.
41. Lamberson, L. and P. Boettcher, Compressed gas combined single-and two-stage light-gas gun. Review of Scientific Instruments, 2018. 89(2): p. 023903.
42. Seigel, A.E., The theory of high speed guns. 1965, Advisory Group for Aerospace Research and Development Neuilly-sur-seine (France).
43. Sastry, Y.S., et al., Studies on ballistic impact of the composite panels. Theoretical and Applied Fracture Mechanics, 2014. 72: p. 2-12.
44. Williams, K.V. and R. Vaziri, Application of a damage mechanics model for predicting the impact response of composite materials. Computers & Structures, 2001. 79(10): p. 997-1011.
45. Delfosse, D. and A. Poursartip, Energy-based approach to impact damage in CFRP laminates. Composites Part A: Applied Science and Manufacturing, 1997. 28(7): p. 647-655.

8 CHAPTER: Conclusions and Future Works

8.1 Conclusions

Laminated composites are materials with excellent high in-plane mechanical properties and low weight which fully satisfy the advanced industry requirements. However, their intrinsic fragile nature and the absence of reinforcement along the out-of-plane direction means these materials are prone to damage generation within the laminate's body as a consequence of an impact event. This can lead to the weakening of the part and the possible catastrophic collapse of the structure without any warning signs of failure. Based on this premise, the original contribution contained within this thesis consist of the improvement of the impact proprieties of laminates and the activation of non-structural benefits for improving the impact properties and the reliability of the structure by hybridising the laminated structures using three different approaches. The approaches followed for hybridisation, their structural benefits with percentage variation in comparison with conventional laminates, and non-structural features are summarised in Table 5:

Table 5-Summary of hybridisation processes used in this work

HYBRIDISATION	PROCEDURE USED	STRUCTURAL BENEFIT	NON-STRUCTURAL BENEFIT
METAL	Introduction of copper wires	Increase of maximum contact force (~6%)	SHM, anti-icing and de-icing
BRICK-AND-MORTAR	Introduction of discontinuities	Increase of toughness (+67%)	Increase of drapability
POLYMER	Introduction of polymeric layer	Decrease of extent of damaged area (-100% LVI and -66% HVI)	Increase of erosion resistance

The aim of this first approach is to obtain an optimised embodiment of metal wires within traditional CFRP creating a Multifunctional composites in which the hybrid phase not only works as an additional reinforcement improving the maximum tolerated force (~+6%) but is also able to enable new additional features by exploiting its thermo-electrical properties such as strain sensing, in-situ IR damage detection and de-icing techniques.

The second approach involves the introduction of a 3D hierarchical pattern of discontinuities within the fibrous reinforcement to increase the amount of impact energy that the material is able to absorb (~+67%) and increase of the drapability of the material during the manufacturing process.

The third and final approach considered in this thesis consists of the use of a Thermoplastic Polyurethane (TPU) coat introduced within the lamination sequence to reduce damage generated whilst promoting improved erosion resistance, allowing the material to be employed in harsh environments. Both Low Velocity

and High Velocity Impact conditions were investigated reporting no damage generation at 5J and reduction of 66% of damaged area respectively.

Based on the results of these works, it is clear that these hybridisation approaches are effective in increasing the appeal and the safety of composite structure in advanced sectors. Furthermore, these works show that composite materials can be tuned and adapted to a wide range of applications by modifying (hybridising) only the fibrous reinforcement. Applications for these materials (Figure 47) can be found in leading edge of wind blades, motorsport back and front wings, ballistic armour and protections, and the vehicles panels for high-speed trains where the high impact reliability is required alongside specific and unique characteristics.

Figure 47-Advanced applications for hybrid FRP: aerospace (Image from Quora), ballistic protection (image from pngimg) and motorsport (image from GrabCad)

8.2 Future Works

In this thesis, the improvement of impact properties of composite materials and the activation of non-structural properties was carried out by hybridising the lamination sequence of the material using three different approaches. However,

each of the hybridisation processes can still be improved by investigating further developments representing a future opportunity for research. Firstly, it is necessary to investigate the corrosion and fatigue behaviour of these hybrid materials to understand their resistance in harsh environments and under continuous dynamic loading conditions. Considering the metal-carbon nature of hybrid materials, further investigation into developing a numerical model able to optimise the number of wires and their geometrical parameters and maximise impact behaviour and non-structural abilities in function of the geometry where the hybrid material is used would be highly beneficial. Another future work that can be considered for this material is its use to manufacture prototypes of front wing and back wing for racing cars, testing its performance under operative conditions. Analysing instead the 3D hierarchical hybrid material, a further investigation could be carried out by varying the geometrical parameters of the discontinuity pattern to enhance the hierarchical failure mechanisms and absorb more energy during the impact. Also, this material can be used to realise a 3D hierarchical laminated material using a quasi-isotropic lamination sequence to investigate whether toughness enhancement can also be verified for this structure.

TPU coatings have already be demonstrated to be effective in protecting both plate samples and aircraft structures such as the T-stiffened panel. However, further tests are required to demonstrate the effectiveness of the TPU layer to resist in corrosive environments. Also, it is necessary to evaluate the adhesion between TPU and composite materials and maximise this adhesion to guarantee the efficiency of the material when repeated impacts are carried out on its surface.

Finally, a combination of these three hybridisation processes can also represent an interesting research area for future works. In particular, the combination of the structural benefits of the three processes can be potentially achieved by hybridising the material using metal wires, brick-and-mortar and polymeric layers at the same time. In other words, all three structural benefits can be virtually achieved at the same time in the same material. However, this combined hybridisation process

could limit the activation of all the non-structural benefits since some conflicts could occur. For example, considering the potential of using metal wires as a heat source for thermography and the TPU layer as an abrasion protective layer, the resolution of the technique may be significantly affected by the low heat conductivity of TPU compared to the laminate's layers. Thus, a further investigation of this approach may be considered for the further development of hybrid materials with enhanced impact properties and non-structural features.

PhD Activities

In this is section, the manuscripts submitted to international peer-reviewed journals and conference proceedings of research works presented at international conferences during the PhD period at University of Bath are listed. Only parts of these works were used in this thesis.

Peer-reviewed Journals (ordered by date published):

1. **Rizzo, F**., Pinto, F. & Meo, M. (2019). Development of multifunctional hybrid metal/carbon composite structures. *Composite Structures 222, 110907*.

2. **Rizzo, F**., Pinto, F. & Meo, M. (2019). 3D bio-inspired hierarchical discontinuous CFRP with enhanced ductility. *Composite Structures 226, 111202*.

3. **Rizzo, F**., Cuomo, S., Pinto, F., Pucillo, G., & Meo, M. (2019). Thermoplastic polyurethane composites for railway applications: Experimental and numerical study of hybrid laminates with improved impact resistance. *Journal of Thermoplastic Composite Materials, 0892705719856049.*

4. **Rizzo, F**., Pinto, F. & Meo, M. (2020). Investigation of silica-based shear thickening fluid in enhancing composite impact resistance. *Applied Composite Materials*.

5. Flora, F., **Rizzo, F**., Pinto, F. & Meo, M. (2020). Ultrasonic Consolidation (UC) debulking of thermosetting prepreg for autoclave curing of composite laminates. *Composites: Part B.* (Submitted)

6. **Rizzo, F**., Porter, M., Pinto, F., & Meo, M. (2020). Bioinspired helicoidal composite structure featuring variable ply pitch. (Draft)

7. **Rizzo, F**., Pinto, F. & Meo, M. (2020), Investigation on the design of hybrid CFRP/Titanium single shear lap joint. (Draft)

Conference Papers (ordered by date published):

1. Pinto, F., **Rizzo, F**. & Meo, M. (2017). Impact resistant smart hybrid laminates. *Behavior and Mechanics of Multifunctional Materials and Composites* Vol. 10165, p. 101650W

2. **Rizzo, F**., Iervolino, O., Pinto, F. & Meo, M. (2017). Structural Hybrid Layer for Critical Strain Detection in Composite Parts: A Multifunctional Approach. *IWSHM 2017: Real-Time Material State Awareness and Data-Driven Safety Assurance* (pp. 1-8).

3. **Rizzo, F**., Pinto, F. & Meo, M. (2018). Bioinspired pseudo-ductile composite laminates with hierarchical energy absorption mechanism *Bioinspiration, Biomimetics, and Bioreplication* VIII 10593, 105930G.

4. Cuomo, S., **Rizzo, F**, Pucillo, G., Pinto, F. & Meo, M. A Thermoplastic Polymer Coating for Improved Impact Resistance of Railways CFRP Laminates. *European Conference on Composite Materials-18th Conference on Composite Materials.*

5. **Rizzo, F**., D'Agostino, T., Pinto, F. & Meo, M. (2019). High-velocity impact response on advanced hybrid composite structures. *Smart*

Structures and NDE for Energy Systems and Industry 4.0 10973, 109730T.

6. **Rizzo, F**., D'Agostino, T., Cuomo, S., Pinto, F. & Meo, M. (2020). High-velocity impact investigation on TPU/CFRP T-stiffened panel. *Materials Today: Proceedings*. **(Peer-reviewed)**

7. Flora, F., **Rizzo, F**., Pinto, F. & Meo, M. (2020). Ultrasonic Consolidation (UC) debulking of thermosetting prepreg for autoclave curing of composite laminates. *Materials Today: Proceedings*. **(Peer-reviewed)**

My research at the University of Bath was granted by EXTREME; a project organised by the European Union as part of the Horizon 2020 research and innovation programme under grant agreement No. 636549.

.

References

[1] Prabhakar MM, Rajini N, Ayrilmis N, Mayandi K, Siengchin S, Senthilkumar K, et al. An overview of burst, buckling, durability and corrosion analysis of lightweight FRP composite pipes and their applicability. Composite Structures. 2019:111419.

[2] Vassilopoulos AP. Fatigue life prediction of composites and composite structures: Woodhead publishing, 2019.

[3] Kernin A, Wan K, Liu Y, Shi X, Kong J, Bilotti E, et al. The effect of graphene network formation on the electrical, mechanical, and multifunctional properties of graphene/epoxy nanocomposites. Composites Science and Technology. 2019;169:224-31.

[4] Jones RM. Mechanics of composite materials: CRC press, 2014.

[5] Johnson T. History of Composites. ThoughtCo; 2018.

[6] Nagavally RR. Composite materials-history, types, fabrication techniques, advantages, and applications. International Journal of Mechanical and Production Engineering. 2016;5:87-92.

[7] Gordon J. The new science of strong materials, 1968. Penguin.

[8] Gordon J. The New Science of Strong Materials. 2 nd eEdition., Rrepr. int. Penguin Books, London; 1991.

[9] Marsh G. 50 years of reinforced plastic boats. Reinforced plastics. 2006;50:16-9.

[10] Goldsworthy WB. Pultrusion machine and method. Google Patents; 1971.

[11] Starr T. Pultrusion for engineers: Elsevier, 2000.

[12] Aftalion F, Kent JA. Handbook of industrial chemistry and biotechnology. 2012.

[13] Callister WD, Rethwisch DG. Materials science and engineering: an introduction: John wiley & sons New York, 2007.

[14] Friedrich K. Application of fracture mechanics to composite materials: Elsevier, 2012.

[15] He K, Hoa S, Ganesan R. The study of tapered laminated composite structures: a review. Composites Science and Technology. 2000;60:2643-57.

[16] DF O'Regan M, Meenan B. A comparison of Young's modulus predictions in fibre-reinforced-polyamide injection mouldings. Composites Science and Technology. 1999;59:419-27.

[17] Mohammed U, Lekakou C, Dong L, Bader M. Shear deformation and micromechanics of woven fabrics. Composites Part A: Applied Science and Manufacturing. 2000;31:299-308.

[18] Peng X, Cao J. A continuum mechanics-based non-orthogonal constitutive model for woven composite fabrics. Composites Part A: Applied Science and Manufacturing. 2005;36:859-74.

[19] Akkerman R. Laminate mechanics for balanced woven fabrics. Composites Part B: Engineering. 2005;37:108-16.

[20] Barbero EJ, Damiani TM, Trovillion J. Micromechanics of fabric reinforced composites with periodic microstructure. International Journal of Solids and Structures. 2005;42:2489-504.

[21] Hahn H, Pandey R. A micromechanics model for thermoelastic properties of plain weave fabric composites. 1994.

[22] Jiang Y, Tabiei A, Simitses GJ. A novel micromechanics-based approach to the derivation of constitutive equations for local/global analysis of a plain-weave fabric composite. Composites Science and Technology. 2000;60:1825-33.

[23] Sjoblom PO, Hartness JT, Cordell TM. On low-velocity impact testing of composite materials. Journal of composite materials. 1988;22:30-52.

[24] Cantwell W, Morton J. Comparison of the low and high velocity impact response of CFRP. Composites. 1989;20:545-51.

[25] Liu D, Malvern LE. Matrix cracking in impacted glass/epoxy plates. Journal of composite materials. 1987;21:594-609.

[26] Robinson P, Davies G. Impactor mass and specimen geometry effects in low velocity impact of laminated composites. International Journal of Impact Engineering. 1992;12:189-207.

[27] Shivakumar K, Elber W, Illg W. Prediction of impact force and duration due to low-velocity impact on circular composite laminates. 1985.

[28] Abrate S. Impact on laminated composite materials. Appl Mech Rev. 1991;44:155-90.

[29] Abrate S. Impact Dynamics. Impact Engineering of Composite Structures: Springer; 2011. p. 71-96.

[30] Yang S, Sun C. Indentation law for composite laminates. Composite Materials: Testing and Design (6th Conference): ASTM International; 1982.

[31] Davies G, Zhang X, Zhou G, Watson S. Numerical modelling of impact damage. Composites. 1994;25:342-50.

[32] Tao J, Sun C. Influence of ply orientation on delamination in composite laminates. Journal of composite materials. 1998;32:1933-47.

[33] Agrawal S, Singh KK, Sarkar P. Impact damage on fibre-reinforced polymer matrix composite–a review. Journal of composite materials. 2014;48:317-32.

[34] Shah S, Karuppanan S, Megat-Yusoff P, Sajid Z. Impact resistance and damage tolerance of fiber reinforced composites: A review. Composite Structures. 2019.

[35] Léonard F, Stein J, Soutis C, Withers PJ. The quantification of impact damage distribution in composite laminates by analysis of X-ray computed tomograms. Composites Science and Technology. 2017;152:139-48.

[36] Shyr T-W, Pan Y-H. Impact resistance and damage characteristics of composite laminates. Composite Structures. 2003;62:193-203.

[37] Zhang Z, Shen J, Zhong W, Sun Z. A dynamic model of ceramic/fibre-reinforced plastic hybrid composites under projectile striking. Proceedings of the Institution of Mechanical Engineers, Part G: Journal of Aerospace Engineering. 2002;216:325-31.

[38] Kim J-S, Chung S-K. A study on the low-velocity impact response of laminates for composite railway bodyshells. Composite Structures. 2007;77:484-92.

[39] Yeh H-Y, Kim CH. The Yeh-Stratton criterion for composite materials. Journal of composite materials. 1994;28:926-39.

[40] Liu X, Wang G. Progressive failure analysis of bonded composite repairs. Composite Structures. 2007;81:331-40.

[41] Sela N, Ishai O. Interlaminar fracture toughness and toughening of laminated composite materials: a review. Composites. 1989;20:423-35.

[42] Garg AC, Mai Y-W. Failure mechanisms in toughened epoxy resins—A review. Composites Science and Technology. 1988;31:179-223.

[43] Tang Y, Ye L, Zhang Z, Friedrich K. Interlaminar fracture toughness and CAI strength of fibre-reinforced composites with nanoparticles–A review. Composites Science and Technology. 2013;86:26-37.

[44] Saghafi H, Minak G, Zucchelli A, Brugo T, Heidary H. Comparing various toughening mechanisms occurred in nanomodified laminates under impact loading. Composites Part B: Engineering. 2019;174:106964.

[45] Kostopoulos V, Baltopoulos A, Karapappas P, Vavouliotis A, Paipetis A. Impact and after-impact properties of carbon fibre reinforced composites enhanced with multi-wall carbon nanotubes. Composites Science and Technology. 2010;70:553-63.

[46] Wang J, Dong S, Wang D, Yu X, Han B, Ou J. Enhanced impact properties of concrete modified with nanofiller inclusions. Journal of Materials in Civil Engineering. 2019;31:04019030.

[47] Francesconi L, Aymerich F. Numerical simulation of the effect of stitching on the delamination resistance of laminated composites subjected to low-velocity impact. Composite Structures. 2017;159:110-20.

[48] Francesconi L, Aymerich F. Effect of Z-pinning on the impact resistance of composite laminates with different layups. Composites Part A: Applied Science and Manufacturing. 2018;114:136-48.

[49] Zhang H, Wang M, Wen W, Xu Y, Cui H, Chen J. A Full-Process Numerical Analyzing Method of Low-Velocity Impact Damage and Residual Strength for Stitched Composites. Applied Sciences. 2018;8:2698.

[50] Seltzer R, González C, Muñoz R, LLorca J, Blanco-Varela T. X-ray microtomography analysis of the damage micromechanisms in 3D woven composites under low-velocity impact. Composites Part A: Applied Science and Manufacturing. 2013;45:49-60.

[51] Stig F, Hallström S. Influence of crimp on 3D-woven fibre reinforced composites. Composite Structures. 2013;95:114-22.

[52] Swolfs Y, Gorbatikh L, Verpoest I. Fibre hybridisation in polymer composites: a review. Composites Part A: Applied Science and Manufacturing. 2014;67:181-200.

[53] Safri SNA, Sultan MTH, Jawaid M, Jayakrishna K. Impact behaviour of hybrid composites for structural applications: A review. Composites Part B: Engineering. 2018;133:112-21.

[54] Fukuda H. Micromechanical strength theory of hybrid composites. Advanced Composite Materials. 1991;1:39-53.

[55] Kretsis G. A review of the tensile, compressive, flexural and shear properties of hybrid fibre-reinforced plastics. Composites. 1987;18:13-23.

[56] Selmy A, Elsesi A, Azab N, El-Baky MA. In-plane shear properties of unidirectional glass fiber (U)/random glass fiber (R)/epoxy hybrid and non-hybrid composites. Composites Part B: Engineering. 2012;43:431-8.

[57] Marom G, Fischer S, Tuler F, Wagner H. Hybrid effects in composites: conditions for positive or negative effects versus rule-of-mixtures behaviour. Journal of Materials Science. 1978;13:1419-26.

[58] Saka K, Harding J. A simple laminate theory approach to the prediction of the tensile impact strength of woven hybrid composites. Composites. 1990;21:439-47.

[59] Zweben C. Tensile strength of hybrid composites. Journal of Materials Science. 1977;12:1325-37.

[60] Zhang J, Chaisombat K, He S, Wang CH. Hybrid composite laminates reinforced with glass/carbon woven fabrics for lightweight load bearing structures. Materials & Design (1980-2015). 2012;36:75-80.

[61] Naik N, Ramasimha R, Arya H, Prabhu S, ShamaRao N. Impact response and damage tolerance characteristics of glass–carbon/epoxy hybrid composite plates. Composites Part B: Engineering. 2001;32:565-74.

[62] Kowsika MV, Mantena PR. Static and low-velocity impact response characteristics of pultruded hybrid glass-graphite/epoxy composite beams. Journal of Thermoplastic Composite Materials. 1999;12:121-32.

[63] Sarasini F, Tirillò J, D'Altilia S, Valente T, Santulli C, Touchard F, et al. Damage tolerance of carbon/flax hybrid composites subjected to low velocity impact. Composites Part B: Engineering. 2016;91:144-53.

[64] Jawaid M, Khalil HA. Cellulosic/synthetic fibre reinforced polymer hybrid composites: A review. Carbohydrate polymers. 2011;86:1-18.

[65] Jawaid M, Alothman OY, Paridah M, Khalil HSA. Effect of oil palm and jute fiber treatment on mechanical performance of epoxy hybrid composites. International Journal of Polymer Analysis and Characterization. 2014;19:62-9.

[66] Ahmad Z. Principles of corrosion engineering and corrosion control: Elsevier, 2006.

[67] Tucker WC, Brown R, Russell L. Corrosion between a graphite/polymer composite and metals. Journal of composite materials. 1990;24:92-102.

[68] Vogelesang L, Marissen R, Schijve J. A new fatigue resistant material: Aramide Reinforced Aluminium Laminate (ARALL). 1981.

[69] Gunnink J, Vogelesang L, Schijve J. Application of a new hybrid material (ARALL) in aircraft structures. Proceedings of the 13th Congress of the International Council of the Aeronautical Sciences (ICAS), Washington1982. p. 990-1000.

[70] Vlot A. Glare: history of the development of a new aircraft material: Springer Science & Business Media, 2001.

[71] Vlot A, Gunnink J, Alderliesten R, Van der Hoeven W, de Boer A, Hart W, et al. Towards technology readiness of fibre metal laminates- Glare Technology Development(GTO) 1997-2000. ACUN- 3 International Composites Conference, Proceedings, Sydney, Australia, Feb 5-9, 2001, Sydney 2052, Australia, University of New South Wales, 20012001. p. 243-56.

[72] Dhaliwal GS, Newaz GM. Modeling low velocity impact response of carbon fiber reinforced aluminum laminates (CARALL). Journal of Dynamic Behavior of Materials. 2016;2:181-93.

[73] Amooyi Dizaji R, Yazdani M. Low Velocity Impact Response of CARALL composites reinforced with nano particles. Modares Mechanical Engineering. 2017;17:58-64.

[74] Bradley P, Harris S. Strategic reinforcement of hybrid carbon fibre-reinforced polymer composites. Journal of Materials Science. 1977;12:2401-10.

[75] Bradley SJHaPD. AIME Conference on Composite Materials. Geneva and Boston1976. p. p. 327.

[76] Dawood M, Rizkalla S. Environmental durability of a CFRP system for strengthening steel structures. Construction and Building Materials. 2010;24:1682-9.

[77] Angioni SL, Meo M, Foreman A. Impact damage resistance and damage suppression properties of shape memory alloys in hybrid composites—a review. Smart Materials and Structures. 2011;20:013001.

[78] Rim M-S, Kim E-H, Lee I, Choi I-H, Ahn S-M, Koo K-N, et al. Low-velocity impact characteristics of composite plates with shape memory alloy wires. Journal of theoretical and applied mechanics. 2011;49:841-57.

[79] Meo M, Antonucci E, Duclaux P, Giordano M. Finite element simulation of low velocity impact on shape memory alloy composite plates. Composite Structures. 2005;71:337-42.

[80] Hallquist JO. LS-DYNA keyword user's manual. Livermore software Technology corporation. 2007;970:299-800.

[81] Nagai H, Oishi R. Shape memory alloys as strain sensors in composites. Smart Materials and Structures. 2006;15:493.

[82] Abry J, Bochard S, Chateauminois A, Salvia M, Giraud G. In situ detection of damage in CFRP laminates by electrical resistance measurements. Composites Science and Technology. 1999;59:925-35.

[83] Cui D, Song G, Li H. Modeling of the electrical resistance of shape memory alloy wires. Smart Materials and Structures. 2010;19:055019.

[84] Pinto F, Maroun F, Meo M. Material enabled thermography. NDT & E International. 2014;67:1-9.

[85] Suzuki Y, Todoroki A, Mizutani Y. Diagnosis for CFRP aircraft by Joule heating using lightning protection system. Proceedings of 12th Japan International SAMPE Symposium & Exhibition: Japan SAMPE; 2011.

[86] Orłowska A, Kołakowski P, Holnicki-Szulc J. Detecting delamination zones in composites by embedded electrical grid and thermographic methods. Smart Materials and Structures. 2011;20:105009.

[87] Zhang Q, Yu Y, Yang K, Zhang B, Zhao K, Xiong G, et al. Mechanically robust and electrically conductive graphene-paper/glass-fibers/epoxy composites for stimuli-responsive sensors and Joule heating deicers. Carbon. 2017;124:296-307.

[88] Lin AY-M, Meyers MA. Interfacial shear strength in abalone nacre. Journal of the mechanical behavior of biomedical materials. 2009;2:607-12.

[89] Li X, Wang J, Du J, Cao M, Liu K, Li Q, et al. Spear and shield: survival war between Mantis Shrimps and Abalones. Advanced Materials Interfaces. 2015;2.

[90] Barthelat F, Tang H, Zavattieri P, Li C-M, Espinosa H. On the mechanics of mother-of-pearl: a key feature in the material hierarchical structure. Journal of the Mechanics and Physics of Solids. 2007;55:306-37.

[91] Zimmermann EA, Gludovatz B, Schaible E, Dave NK, Yang W, Meyers MA, et al. Mechanical adaptability of the Bouligand-type structure in natural dermal armour. Nature communications. 2013;4:2634.

[92] Sun J, Bhushan B. Hierarchical structure and mechanical properties of nacre: a review. Rsc Advances. 2012;2:7617-32.

[93] Jackson A, Vincent JF, Turner R. The mechanical design of nacre. Proc R Soc Lond B. 1988;234:415-40.

[94] Meyers MA, Lin AY-M, Chen P-Y, Muyco J. Mechanical strength of abalone nacre: role of the soft organic layer. Journal of the mechanical behavior of biomedical materials. 2008;1:76-85.

[95] Currey JD. Mechanical properties of mother of pearl in tension. Proceedings of the Royal society of London Series B Biological sciences. 1977;196:443-63.

[96] Song J, Fan C, Ma H, Liang L, Wei Y. Crack deflection occurs by constrained microcracking in nacre. Acta Mechanica Sinica. 2018;34:143-50.

[97] Anderson TL. Fracture mechanics: fundamentals and applications: CRC press, 2017.

[98] Cox H. The elasticity and strength of paper and other fibrous materials. British journal of applied physics. 1952;3:72.

[99] Laspalas M, Crespo C, Jiménez M, García B, Pelegay J. Application of micromechanical models for elasticity and failure to short fibre reinforced composites. Numerical implementation and experimental validation. Computers & Structures. 2008;86:977-87.

[100] Zak G, Haberer M, Park C, Benhabib B. Mechanical properties of short-fibre layered composites: prediction and experiment. Rapid Prototyping Journal. 2000;6:107-18.

[101] Narducci F, Pinho S. Exploiting nacre-inspired crack deflection mechanisms in CFRP via micro-structural design. Composites Science and Technology. 2017;153:178-89.

[102] Pimenta S, Pinho ST. Hierarchical scaling law for the strength of composite fibre bundles. Journal of the Mechanics and Physics of Solids. 2013;61:1337-56.

[103] Malkin R, Yasaee M, Trask RS, Bond IP. Bio-inspired laminate design exhibiting pseudo-ductile (graceful) failure during flexural loading. Composites Part A: Applied Science and Manufacturing. 2013;54:107-16.

[104] Gu GX, Takaffoli M, Hsieh AJ, Buehler MJ. Biomimetic additive manufactured polymer composites for improved impact resistance. Extreme Mechanics Letters. 2016;9:317-23.

[105] Tsuji N, Springer GS, Hegedus I. The drapability of aligned discontinuous fiber composites. Journal of composite materials. 1997;31:428-65.

[106] Huang S-L, Lai J-Y. Structure-tensile properties of polyurethanes. European polymer journal. 1997;33:1563-7.

[107] Albozahid M. Design of novel high modulus TPUs for nanocomposite applications: University of Manchester, 2018.

[108] Pichaiyut S, Nakason C, Vennemann N. Thermoplastic elastomers-based natural rubber and thermoplastic polyurethane blends. Iranian Polymer Journal. 2012;21:65-79.

[109] Bajsic EG, Rek V, Sendijarevic A, Sendijarevic V, Frisch K. DSC study of morphological changes in segmented polyurethane elastomers. Journal of Elastomers & Plastics. 2000;32:162-82.

[110] Saldivar-Guerra E, Vivaldo-Lima E. Handbook of polymer synthesis, characterization, and processing: John Wiley & Sons, 2013.

[111] Seefried Jr C, Koleske J, Critchfield F. Thermoplastic urethane elastomers. I. Effects of soft-segment variations. Journal of Applied Polymer Science. 1975;19:2493-502.

[112] Yoon KH, Yoon ST, Park OO. Damping properties and transmission loss of polyurethane. I. Effect of soft and hard segment compositions. Journal of Applied Polymer Science. 2000;75:604-11.

[113] Weibo H, Fengchang Z. Studies on the dynamic mechanical and vibration damping properties of polyether urethane and epoxy composites. Journal of Applied Polymer Science. 1993;50:277-83.

[114] Qi HJ, Boyce MC. Stress–strain behavior of thermoplastic polyurethanes. Mechanics of Materials. 2005;37:817-39.

[115] Arruda EM, Boyce MC. A three-dimensional constitutive model for the large stretch behavior of rubber elastic materials. 1993.

[116] Bergström J. 8 - Viscoplasticity Models. In: Bergström J, editor. Mechanics of Solid Polymers: William Andrew Publishing; 2015. p. 371-436.

[117] Boyce MC, Parks DM, Argon AS. Large inelastic deformation of glassy polymers. Part I: rate dependent constitutive model. Mechanics of Materials. 1988;7:15-33.

[118] Miller SG, Roberts GD, Kohlman LW, Heimann PJ, Pereira JM, Ruggeri CR, et al. Impact behavior of composite fan blade leading edge subcomponent with thermoplastic polyurethane interleave. 2015.

[119] Russo P, Langella A, Papa I, Simeoli G, Lopresto V. Thermoplastic polyurethane/glass fabric composite laminates: Low velocity impact behavior under extreme temperature conditions. Composite Structures. 2017;166:146-52.

[120] Tilly GP. A two stage mechanism of ductile erosion. Wear. 1973;23:87-96.

[121] Zhang N, Yang F, Li L, Shen C, Castro J, Lee LJ. Thickness effect on particle erosion resistance of thermoplastic polyurethane coating on steel substrate. Wear. 2013;303:49-55.

[122] Gagné M, Therriault D. Lightning strike protection of composites. Progress in Aerospace Sciences. 2014;64:1-16.